Quantum Gas Microscopy of Fluctuating Hydrodynamics in Optical Ladders

Julian F. Wienand

München 2024

Quantum Gas Microscopy of Fluctuating Hydrodynamics in Optical Ladders

Dissertation an der Fakultät für Physik
Ludwig-Maximilians-Universität München

vorgelegt von

Julian Florian Wienand

aus Aschaffenburg

München, den 4. April 2024

Tag der mündlichen Prüfung: 17.05.2024
Erstgutachterin: Prof. Monika Aidelsburger
Zweitgutachter: Prof. Sarang Gopalakrishnan
Weitere Kommissionsmitglieder: Prof. Thomas Birner, Prof. Alexander Högele

Abstract

We demonstrate the emergence of *fluctuating hydrodynamics* in chaotic quantum many-body systems using quantum simulation experiments in large tunable ladders of hard-core bosons. Using a ^{133}Cs quantum gas microscope with single-site resolution, we examine the post-quench build-up of fluctuations and density-density correlations, starting from a highly excited state. The ladder systems can be tuned from integrable to fully chaotic, allowing to study the crossover between ballistic and diffusive transport. We find a separation of equilibration timescales between the local expectation values and non-local fluctuations, suggesting that systems may appear thermalized even though fluctuations continue to grow. We show that, from a macroscopic point of view, the relaxation dynamics are described by fluctuating hydrodynamics and entirely determined by the linear response coefficients. This profound insight allows for the extraction of the equilibrium diffusion constant from non-equilibrium experiments, offering a new approach for testing fluctuation-dissipation relations in far-from-equilibrium chaotic quantum systems. Besides these main results about the relaxation of isolated quantum many-body systems, this thesis reports on the current state of our ^{133}Cs quantum gas microscope, describing and characterizing the experimental setup, including optical superlattices and imaging techniques. Furthermore, it reports on a new theoretical approach for understanding the bulk-boundary correspondence in higher-order symmetry-protected topological phases, demonstrated using the 2d superlattice Bose-Hubbard model.

Zusammenfassung

Wir demonstrieren das Auftreten von *fluktuierender Hydrodynamik* in chaotischen Quantenvielteilchensystemen mittels Quantensimulationsexperimenten in großen einstellbaren Leitern mit Hard-Core-Bosonen. Mit einem ^{133}Cs-Quantengasmikroskop mit Einzelplatzauflösung untersuchen wir den Aufbau von Fluktuationen und Dichte-Dichte-Korrelationen nach einem Quench, ausgehend von einem hochangeregten Zustand. Die Leitersysteme können von integrierbar bis vollständig chaotisch eingestellt werden, was es uns ermöglicht, den Übergang zwischen ballistischem und diffusivem Transport zu beobachten. Wir beobachten eine Separation der Zeitskalen für das Erreichen des Gleichgewichtzustands zwischen den lokalen Erwartungswerten und den nicht-lokalen Fluktuationen, was darauf hindeutet, dass Systeme thermisch erscheinen können, obwohl die Fluktuationen weiter wachsen. Wir zeigen, dass aus makroskopischer Sicht die Relaxationsdynamik durch fluktuierende Hydrodynamik beschrieben wird und vollständig durch die Linear-Response-Koeffizienten bestimmt ist. Dieses weitreichende Ergebnis ermöglicht die Extraktion der Gleichgewichts-Diffusionskonstante aus Nichtgleichgewichtsexperimenten und bietet einen neuen Ansatz zum Testen von Fluktuations-Dissipations-Beziehungen in weit vom Gleichgewicht entfernten chaotischen Quantensystemen. Neben diesen Hauptergebnissen hinsichtlich der Relaxation von isolierten Quanten-Vielteilchensystemen berichtet diese Arbeit auch über den aktuellen Stand unseres ^{133}Cs-Quantengasmikroskops und beschreibt den experimentellen Aufbau, einschließlich der optischen Übergitter und Abbildungstechniken. Darüber hinaus wird über einen neuen theoretischen Ansatz zur Beschreibung der Bulk-Boundary-Korrespondenz in symmetriegeschützten topologischen Phasen höherer Ordnung berichtet, demonstriert am 2d-Übergitter-Bose-Hubbard-Modell.

Contents

Introduction

Believing in science means, to some degree, believing in *reductionism*: the paradigm that every phenomenon in the universe can *in principle* be traced back to the most fundamental laws of physics. Whatever dictates the properties and behavior of the smallest constituents of matter, must also *somehow* explain the complexity which emerges at larger scales, ranging from atoms, molecules and proteins to life, meteorology and dark matter in the universe [1, 2]. However, even if there was complete knowledge about the fundamental laws of physics, understanding the universe in its entirety would probably still remain elusive. The relationship between emergent behavior and first principles can be highly non-trivial [1] and evade any systematic description. For instance, while a two-body problem in classical mechanics is exactly solvable, a three-body problem is generally not and the complexity of a general n-body problem grows as $O(n^2)$ [3]. For *quantum* many-body problems, the complexity of the system scales exponentially with the particle number, limiting computational methods down to a few particles [4]. This highlights the importance of finding simplifications and approximations or giving up on the idea of reductionism altogether.

In many cases, a system can be described phenomenologically without any knowledge about the underlying microscopic physics: Water flowing through a pipe is modelled by the Navier-Stokes equations which dictate the time evolution of fluids in the continuum limit based on locally conserved quantities [5]. The fact that water is composed of $\gg 10^{23}$ water molecules is irrelevant: Instead, the microscopic physics is simply absorbed into a few characteristic constants such as the viscosity. This approach is called *hydrodynamics* and generally applies to systems that are *chaotic* at the microscopic level, usually due to *interactions* between the constituent particles and due to a large number of excitations at high temperature. Hydrodynamics has been jokingly referred to as a *theory of everything* [6] due to its widespread use in various fields, including high-energy physics [7], astrophysics and cosmology [8–10], solid-state electron dynamics [11–13] and ultracold atoms [14–16]. It is a powerful tool for capturing the essential macroscopic dynamics of microscopically highly complex systems, turning their microscopic complexity into a feature: At its heart lies the assumption that whatever the dynamics are, randomness will eventually take the system to the same thermal equilibrium state described by statistical physics. Thus, as long as the perspective on the system is sufficiently coarse-grained, the system's state can be approximated as locally thermal, allowing to write down continuous differential equations that define the time evolution of macroscopic continuous quantities. This makes hydrodynamics a theory describing the late-time and long-wavelength dynamics of the system [17].

The framework of hydrodynamics has been widely extended to various scenarios which go beyond simple chaotic systems and its macroscopic description using the diffusion equation: These include integrable systems with infinitely many conserved quantities (generalized hydrodynamics or GHD [18–20]) and chaotic systems in which not only the evolution of mean quantities but also the dynamics of fluctuations play an important role (fluctuating hydrodynamics or FHD). It was originally proposed by Landau and Lifshitz in the 1950s [21], but it can also be derived from kinetic theory [22–24]. In FHD, the standard hydrodynamic equations are extended by a noise term, introducing random uncorrelated fluctuations. Fluctuations provide a glimpse of the microscopic scale from a macroscopic point of view

because they are observable effects of the random, discrete events that occur at the microscopic level. In particular, these are of importance in mesoscopic systems as well as systems near criticality [25] Fluctuations are tied to dissipative currents through the fluctuation dissipation theorem (FDT) [26, 27] and (if they are not of thermal origin) can reveal phase transitions, both in classical and quantum many-body systems [28, 29]. In out-of-equilibrium systems, fluctuations are expected to exhibit even richer features [30] and provide new means for studying the relaxation of many-body systems [31]. For instance, they can be used to characterize turbulent flow [32]. Besides in fluid dynamics, fluctuations are important for modeling thermal noise in nano-electronics, structural changes of proteins, DNA mutations [33], lipid membranes [34], molecular motors [35] and nucleation in metastable materials [36–38]. Another example concerns the question how isolated quantum systems thermalize without contact to a thermal bath: The answer is considered to be the maximization of local entanglement entropy, leading to locally thermal states with maximum subsystem fluctuations [39, 40], as described by the eigenstate thermalization hypothesis [41, 42].

Strikingly, FHD predicts that the macroscopic time evolution of a chaotic system is completely determined by a few equilibrium transport coefficients such as, for instance, the diffusion constant. This would imply that the well-known FDT has implications reaching far beyond the equilibrium case. To what extent this hypothesis applies to all chaotic systems is an open question, particularly in light of known exceptions such as dipole-conserving fluids [43]. Its applicability to chaotic *quantum* many-body systems has been even less explored and only from a theoretical point of view [44, 45]. The microscopic origins of fluctuations in quantum systems are of very different nature compared to a classical system and root in spatial entanglement spreading during the thermalization process [39]. If a quantum many-body system could be macroscopically approximated using FHD, many predictions about the system's behavior would not require computationally expensive simulations of the full many-body problem. Due to a large amount of entanglement building up during thermalization, even advanced numerical methods like time-dependent variational principle (TDVP) algorithms [46–49] are limited to short evolution times. In turn, testing the applicability of FHD in the quantum regime would amount to an equally challenging task: It requires computing the time evolution of both mean quantities and fluctuations in a many-body system and comparing it quantitatively with the predictions of an FHD model.

As foreseen by Yuri Manin and Richard Feynman [50, 51], one solution to this problem is not to use a classical computer for these simulations, but, instead, a quantum computer. Such a device can naturally capture quantum effects like entanglement without mapping them to classical bits, avoiding the need for large amounts of storage and computational power. While universally programmable quantum computers are in their infancy [52], so-called quantum simulators with restricted programmability and highly-specialized capabilities have been producing remarkable results by probing ground states and out-of-equilibrium dynamics [53]. In the last two decades a large variety of quantum simulation platforms has emerged, including superconducting qubits, polar molecules, ions and ultracold atoms [54, 55]. Ultracold atoms in optical lattices mimic electrons moving in the periodic electrostatic potential of a real solid [54]. In contrast to the real solid, the artificial cold atom system is highly controllable, easier to measure and manipulate (thanks to slower dynamics and larger lengthscales) and can be imaged with single-particle resolution [56–58]. This technique, called quantum gas microscopy, provides access to novel observables like fluctuations and density-density correlations [59–62] and can reveal intriguing details about the state of the quantum many-body system [55]. For instance, this platform has provided powerful means for studying ground states in exotic phases of matter [54, 63], ranging from antiferromagnets [64] to quantum Hall physics [65, 66]. However, the high degree of controllability in the optical lattice also allows to conduct quench experiments and study relaxation dynamics, both in presence or absence of thermalization [39, 40, 67–79]. So far, fluctuation dynamics have only been studied in relatively small quantum systems, insufficient for extracting slow hydrodynamic timescales and gaining a macroscopic point of view on the out-of-equilibrium quantum system [39, 40, 70, 80, 81].

In this work we employ ultracold ^{133}Cs atoms in optical lattices for analog quantum simulation experiments with hard-core bosons in ladder systems. We construct and operate a quantum gas microscopy setup with single-site resolution [82, 83] to study the relaxation of an isolated quantum system after a quench. The dynamics of the system can be smoothly tuned from purely integrable to fully chaotic, allowing to explore the onset of chaos and the crossover between ballistic and diffusive dynamics. We track the equilibration of both local mean quantities and fluctuations in the system, obtaining a rich picture of the timescales on which hydrodynamic modes relax. In doing so, we answer the following questions:

- How do the fluctuations of local subsystems relax in an isolated quantum system? How does the growth speed depend on the size of the subsystem and how does it compare with the equilibration timescales of local mean quantities like the local density?
- How does hydrodynamic behavior emerge as the dynamics of the system are tuned from integrable to chaotic?
- Does the relaxation behavior agree with predictions from FHD? Can a chaotic quantum many-body system indeed be described by a classical macroscopic continuum model? Are the entire non-equilibrium dynamics, therefore, determined by a few equilibrium transport coefficients?
- Obtaining values of transport coefficients from mean quantities, such as the local density, is typically a very challenging task and requires working in the linear-response regime close to equilibrium. Can a quantum simulator be used to experimentally extract them from the far-from-equilibrium fluctuations in the system?

In answering these questions, we extend the reach of FHD to a quantum regime which is, in general, not only analytically intractable but also hard to access numerically: In conventional condensed matter theory we usually assume near-equilibrium and low temperature conditions with a dilute gas of excitations governing transport. In contrast, the experiment we are conducting is about the relaxation from far-from-equilibrium initial states to maximally entangled final states. On the one hand, this makes it difficult to benchmark the experimental results with numerical methods on classical computers based on microscopic models. On the other hand, it sets the stage for quantum simulation to shine and provide solutions for complex quantum many-body problems that otherwise would be hard to obtain.

Bulk-boundary correspondence in higher-order symmetry-protected topological phases

Besides exploring fluctuations in quantum many-body systems, this thesis reports on a theoretical contribution to the understanding of higher-order symmetry-protected topological (HOSPT) phases. It is motivated by the capabilities of our apparatus to realize strongly-interacting topological matter in optical superlattices, such as the bosonic equivalent of the Su–Schrieffer–Heeger (SSH) model. In 1d, this model features symmetry-protected topological (SPT) phases which can carry topologically protected fractional boundary charges [84]. Intriguingly, in 2d, it features *higher-order* SPTs (of second order) which can carry topologically protected corner charges [85]. Generally, the boundary states in topologically non-trivial matter of order n are n-dimensions lower than the bulk of the system [86, 87]. Such higher-order topological phases have been realized in solids and classical metamaterials [88–98] with applications in electronics and photonics [99], e.g., for topological nanolasers [100–102].

In 1d, quantized edge states can be understood as the consequence of bulk polarization. Within the framework of the modern theory of polarization (MTP), polarization is related to Berry phase of the Bloch bands [103, 104] and the many-body position operator [105]. Similar to a dielectric material, a

change of the bulk polarization leads to the buildup of charge at the boundary, as described by Thouless pumps [106–108]. There have been attempts to generalize these concepts to the higher-order case [87, 98, 109–115] but understanding the bulk polarization in HOSPT phases has so far remained elusive. In particular, the question how exactly topological invariants can be defined in systems with periodic boundary conditions and how they can be used to track the charge transport in higher-order Thouless pumps has been a subject of recent debates [109–111].

In this thesis (Chapter 7), we directly address this question and present a new approach for describing HOSPT phases using the 2d superlattice Bose-Hubbard model (2d-SL-BHM) as a concrete example. We define four Berry phases, which (combined) provide full information about the polarization of the bulk. We use them to track the charge transport in different Thouless pumps. In doing so, we establish a clear correspondence between the quantized fractional charge emerging at the corners and the quantized change of the bulk polarization which can be either dipolar or quadrupolar, depending on the pump. Our approach provides easily adaptable tools for describing HOSPT phenomena in a wide range of matter and contributes to understanding higher-order topology from the point of the MTP.

Outline of this thesis

- In Chapter 1 we introduce the basic concepts underlying the thermalization of isolated quantum systems both in the classical and in the quantum case. These include chaos, ergodicity and the eigenstate thermalization hypothesis, shedding light on thermalization from a microscopic point of view. We also highlight why ultracold atoms in optical lattices are an ideal platform for studying the relaxation of a quantum many-body system to thermal equilibrium and explain the role of quench experiments.
- Chapter 2 introduces *fluctuating hydrodynamics* which combines conventional hydrodynamics with noise. This theory provides a (classical) coarse-grained description of chaotic many-body systems, absorbing the details of the microscopic physics into a few macroscopic quantities. Quantitatively testing the validity of this theory in the quantum regime is one of the main goals of this thesis.
- Chapter 3 introduces the experimental apparatus and its construction, highlighting tools relevant for the quantum simulation experiments in Chapter 5. In particular, we highlight technical details concerning the optical superlattices and the imaging techniques behind achieving single-site resolution.
- Chapter 4 is about the methods and techniques for calibrating the apparatus and characterizing its performance. Further, we discuss the sequence used for preparing Mott insulating initial states.
- Chapter 5 is the key chapter of this thesis and discusses the quench experiments for studying the growth of local mean densities, fluctuations and density-density correlations, both in the integrable and the chaotic regime. In the chaotic case, we observe the emergence of fluctuating hydrodynamics.
- Chapter 6 provides supplementary information about the experiments, including the benchmarking of experimental imperfections like disorder, finite-size effects and other evaluation details.
- In Chapter 7 we switch topics and present a theoretical framework for understanding the bulk-boundary correspondence in higher-order symmetry protected topological phases, using the 2d

superlattice Bose-Hubbard model as an example. This could pose an interesting future research direction for our quantum gas microscope.

- Finally, we summarize the main results of this work, propose follow-up experiments and point out further interesting directions to be studied in the future.

Publications

Featured in this thesis:

- **J. F. Wienand**, S. Karch, A. Impertro, C. Schweizer, E. McCulloch, R. Vasseur, S. Gopalakrishnan, M. Aidelsburger, I. Bloch, "Emergence of fluctuating hydrodynamics in chaotic quantum systems", arxiv:2306.11457 [16]
- **J. F. Wienand**, F. Horn, M. Aidelsburger, J. Bibo, F. Grusdt, "Thouless pumps and bulk-boundary correspondence in higher-order symmetry-protected topological phases", Phys. Rev. Lett. (2022) [116]

Closely related work:

- A. Impertro, S. Karch, **J. F. Wienand**, S. Huh, C. Schweizer, I. Bloch, M. Aidelsburger, "Local readout and control of current and kinetic energy operators in optical lattices", arxiv:2312.13268 [117]
- A. Impertro, **J. F. Wienand**, S. Häfele, H. v. Raven, S. Hubele, T. Klostermann, C. R. Cabrera, I. Bloch, M. Aidelsburger, "An unsupervised deep learning algorithm for single-site reconstruction in quantum gas microscopes", Nat. Comm. Phys. (2023) [83]
- T. Klostermann, C. R. Cabrera, H. v. Raven, **J. F. Wienand** , C. Schweizer, I. Bloch, M. Aidelsburger, "Fast long distance transport of cold cesium atoms", Phys. Rev. A (2022) [118]

CHAPTER 1

Quantum simulation of non-equilibrium dynamics with ultracold atoms in optical lattices

In this Chapter we highlight fundamental concepts underlying out-of-equilibrium systems, including chaos and ergodicity, both from a classical and a quantum point of view. Using the statistical ensembles, we define what thermalization means and illustrate the mechanisms and conditions underlying system reaching thermal equilibrium. We also elaborate on why ultracold atoms in optical lattices pose an excellent platform for probing out-of-equilibrium dynamics and introduce the idea of quantum quench experiments.

1.1 Ultracold atoms in optical lattices

Ultracold atoms in optical lattices are a key platform for the analog simulation of quantum many-body systems [63]: Just like electrons in the electrostatic potential of the nuclei in a real solid, they act as quantum particles in a periodic potential, naturally emulating condensed matter systems. Optical lattices are realized by standing waves of monochromatic light generated from counter-propagating laser beams at the same frequency [119, 120]. Due to the AC Stark shift, the time-independent light intensity has a trapping or anti-trapping effect on the ultracold atoms (see Fig. 1.2a). In simplest terms, when a ground state atom is exposed to a light field of intensity $I(\mathbf{r})$ in vicinity of a transition of linewidth γ at frequency ω_0, it experiences a potential described by [121]:

$$U(\mathbf{r}) = \frac{3\pi c^2}{2\omega_0^3}\frac{\gamma}{\Delta}I(\mathbf{r}), \tag{1.1}$$

where γ is the linewidth of the transition and $\Delta = \omega - \omega_0$ is the detuning of the laser frequency ω with respect to the transition frequency ω_0. More generally, if the laser frequency is close to multiple transitions, their contributions to the overall potential have to be added [121]. Importantly, the sign of the detuning Δ determines whether the potential is attractive ($\Delta < 0$, *red detuning*) or repulsive ($\Delta > 0$, *blue detuning*). Thus, in a red (blue) detuned lattice, the atoms are trapped at the intensity maxima (minima). In 1d, the lattice potential can be written as:

$$V(x) = V_0 \cos^2(kx), \tag{1.2}$$

where k is the wavenumber (depending on the wavelength λ) and V_0 is the amplitude of the potential. If two optical lattices of wavenumbers k_1, k_2 and amplitudes V_1, V_2 are combined, the result is called a *superlattice* parametrized by:

$$V(x) = V_1 \cos^2(k_1 x) + V_2 \cos^2(k_2 x + \phi/2), \tag{1.3}$$

where ϕ is the phase between the two lattices, see Sec. 3.3 for details.

In addition to experiencing a potential, the atoms scatter lattice light photons at a rate of

$$\Gamma(\mathbf{r})_{\mathrm{sc}} = \frac{1}{\hbar}\frac{\gamma}{\Delta} U(\mathbf{r}). \tag{1.4}$$

While the scattering rate scales as $\Gamma_{\mathrm{sc}} \sim 1/\Delta^2$ with the detuning, the potential does so as $U(\mathbf{r}) \sim 1/\Delta$. Thus, in order to minimize heating of the atoms due to scattering while achieving deep potentials, one usually chooses both high lattice light intensity and large detuning [121].

1.2 Quantum gas microscopy

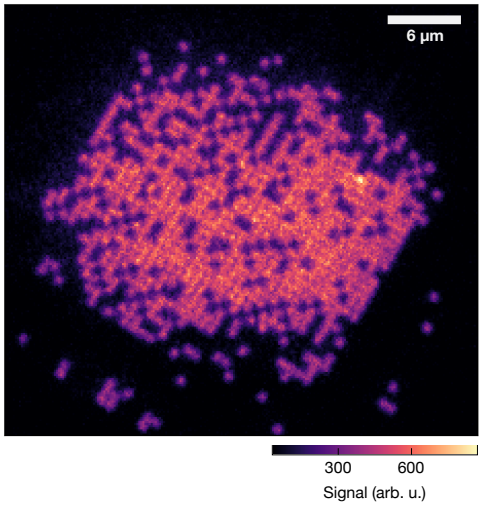

Figure 1.1 | **Quantum gas microscopy.** High-resolution image of a fluorescing array of atoms in a 2d optical square lattice (wavelength $\lambda = 1534\,\mathrm{nm}$, spacing $a = \lambda/2 = 767\,\mathrm{nm}$). Quantum gas microscopy allows to study systems at the single-particle level and obtain more (local) information about the many-body wavefunction.

The field of analog quantum simulation with ultracold atoms experienced a major revolution when the technique of *quantum gas microscopy* was developed: It allows to image atoms trapped in an optical lattices with single lattice site resolution [56, 122]. The concept is simple: First, the optical lattice is abruptly ramped up to very large depth, pinning the atoms down in their respective lattice sites. Next (usually as part of a cooling process) the atoms are illuminated with (near-)resonant light, leading to the emission of fluorescence photons. Finally, the fluorescence light is collected by a high-NA objective providing a resolution that is on the order of the lattice spacing (cf. Sec. 4.3).

Fig. 1.1 depicts a typical image produced using this technique, showing an array of ^{133}Cs atoms in a square optical lattice potential. This image is a *snapshot* of the many-body wavefunction realizing an incompressible Mott insulator in a harmonic trap (cf. Sec. 1.3). By pinning the atoms in place, the many-body wavefunction collapses into the (parity projected) local Fock basis of the individual lattice sites [123]. Parity projection results from light-assisted collisions during the imaging process, eliminating all local pairs of atoms. The snapshot shows a density distribution *sample*, drawn from the superposition of a possibly large number of many-body eigenstates. Thanks to single-site resolution, we gain access to novel observables, including:

- **Full counting statistics**: By taking many snapshots we can obtain the full counting statistics (FCS) of local- and non-local observables [45, 64, 124–134]. As a simple example, consider the total atom number in a certain region of the system. Interesting physics might not only be found in the mean of this quantity but also in the fluctuations or in the higher moments of the FCS, as discussed in Chapter 5.
- **Multi-point correlation functions**, exploring connections between the occupation (spin) of one site and the occupation (spin) of other sites [59, 60, 62, 81].
- **Second-order Renyi-entropy**, measured by letting two identical systems interfere and realizing the Hong-Ou-Mandel effect [39, 70, 135], see Ref. [136] for details and further applications.
- **Local kinetic energy and current**, measured using basis rotations in a superlattice potential [117]. This novel technique goes beyond conventional density measurements and, further, also allows to measure current-current, energy-energy correlations and entanglement [137].

Importantly, the high-NA microscopy setup does not only allow to read-out the many-body system but also to manipulate it at the single particle level using programmable light patterns [138] (cf. Sec. 3.4).

1.3 The Bose-Hubbard model

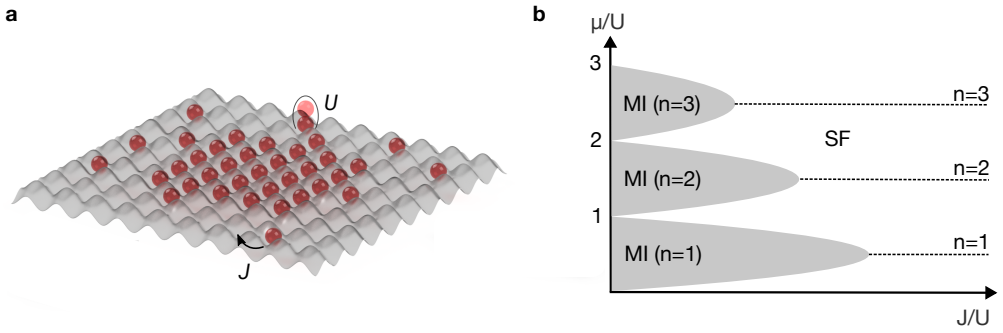

Figure 1.2 | The Bose-Hubbard model. a, The Bose-Hubbard model is implemented by ultracold atoms placed in an optical lattice. The atoms can tunnel to nearest-neighbor sites with a rate of J. The interaction energy U is the energetic cost for placing pairs of particles on the same lattice site. **b**, Sketch of the phase diagram of the Bose-Hubbard model, spanned by the ratio J/U and the chemical potential μ/U, exhibiting Mott insulator (MI) phases of integer filling n and superfluid (SF) phases [139].

Placing ultracold bosonic atoms in an optical lattice (cf. Eq. 1.2) naturally implements the Bose-Hubbard model [140] (see Fig. 1.2a). It is defined by the Hamiltonian

$$\hat{H}_{\mathrm{BHM}} = -J\left(\sum_{\langle i,j\rangle} \hat{a}_i^\dagger \hat{a}_j + \mathrm{h.c.}\right) + \frac{U}{2}\sum_i \hat{n}_i(\hat{n}_i + 1), \tag{1.5}$$

with $\langle i, j\rangle$ denoting all nearest-neighbor pairs. Here, J denotes the tunnel strength and U is the on-site interaction strength, as illustrated in Fig. 1.2. Originally proposed in the 1960s [141, 142], it was meant to provide a simplified description of transition metal monoxides (like FeO, NiO, CoO), which were found to be insulators but predicted to be metals [143]. As it turns out, the insulating properties of these materials do not originate in their band structure but in the strong interactions between the electrons.

Fig. 1.2b shows the ground state phase diagram of the Bose-Hubbard model, spanned by the ratio of tunnel strength and interaction strength on the horizontal axis and the chemical potential (controlling the density of particles in the system) on the vertical axis. In the limit of weak interactions ($J/U \gg 1$) the system is in a superfluid phase independent of the filling. However, if the on-site interactions are sufficiently strong ($J/U \lesssim 1/16$ in 2d), a Mott insulator phase emerges for integer filling fractions. For instance, consider the case of filling $n = 1$ when every single site in the lattice is occupied by an atom. In order to add a second atom to any of the sites, one would have to pay the on-site interaction energy U. Thus, over a wide range of chemical potentials, the filling remains constant until the chemical potential is sufficiently high for overcoming the energy barrier (Mott gap) for creating doubly occupied sites. While in the superfluid phase atoms can tunnel freely from site to site, in the Mott insulator phase particle transport is completely suppressed and the state is incompressible.

The direct observation of the superfluid-to-Mott transition using ultracold bosonic atoms in optical lattices [144] is considered one of the most important quantum simulation experiments in the history of the field [53] and gained remarkable interdisciplinary attention [53, 54]. It beautifully illustrated how interactions can give rise to insulating properties in an artificial quantum material, mimicking the physics at play in a real solid. Later, the same experiment was conducted using a quantum gas microscope [57] to showcase the advantages of single-site resolution (cf. Sec. 1.2).

1.4 Quantum quench experiments

In the previous Section we have discussed the ground state phase diagram of the Bose-Hubbard model which has been extensively studied using quantum gas microscopy [145]. The atoms trapped in the optical lattice constitute an isolated quantum many-body system in equilibrium. Intriguingly, quantum simulators can also be used to measure the relaxation behavior of out-of-equilibrium quantum systems [39, 40, 67–79].

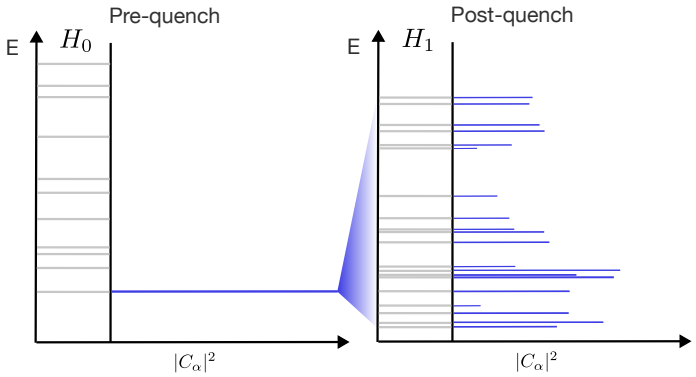

Figure 1.3 | Quantum quench. When the Hamiltonian of a system H_0 is abruptly changed to a different Hamiltonian H_1, the energy eigenstates of H_0 are projected onto the energy eigenstates of H_1, generally producing a highly excited state, followed by a relaxation process [39].

One way to achieve that is to take the system to a highly-excited initial state and, subsequently, watch it relax back to equilibrium. This is called a quench experiment: The system is first prepared in the ground state of a Hamiltonian H_0, as depicted in Fig. 1.3a:

$$|\psi\rangle_{\text{pre}} = |g\rangle_{H_0} \tag{1.6}$$

Subsequently, the Hamiltonian is changed abruptly to become H_1. As a consequence, the ground state

of H_0 (an eigenstate) is projected onto the eigenstate manifold of H_1. The post-quench state is then a superposition of eigenstates of the new Hamiltonian H_1 with each component given by the overlap of the pre-quench ground state with the post-quench eigenstates (see Fig. 1.3b) [39, 146, 147]:

$$|\psi\rangle_{\text{post}} = \sum_{\alpha} {}_{H_1}\langle\alpha|g\rangle_{H_0} \, |\alpha\rangle_{H_1} \, . \tag{1.7}$$

The mean energy of the post-quench state in H_1 typically lies close to the middle of the many-body spectrum. Thus, the effective temperature of the post-quench state can be considered infinite [148, 149]. After the quench, the relaxation behavior of the state will strongly depend on whether the system is *integrable* or *chaotic*, as defined in the next Section.

1.5 Chaos vs integrability

As an intuition, the dynamics of integrable systems are constrained in phase space due to a large number of conserved quantities. In contrast, non-integrable systems behave irregularly in some way, cannot be exactly solved and have (at least partially) chaotic properties. A rigorous universally applicable definition of *integrability* and *chaos* has so far remained elusive and these terms are often used as notions rather than mathematical concepts [150].

In classical systems, it can generally be stated that chaotic behavior of a system is caused by a low number of conserved quantities. Let us assume a classical system is described by the Hamiltonian $\mathcal{H}(\mathbf{q}, \mathbf{p})$ with generalized coordinates $\{q_i\}$ and $\{p_i\}$ with $i = 1, \dots, N$. The system, therefore, has N degree of freedoms and the phase space is $2N$-dimensional, spanned by $\{q_i\}, \{p_i\}$. Each conserved quantity leads to a restriction of the system's dynamics: For instance, if only the total energy is conserved, all possible trajectories must lie on the $(2N-1)$-dimensional equal-energy surface. If there are M conserved quantities in the system, the dimensionality of the accessible phase space is reduced to $2N - M$. This allows to classify systems as follows:

- A system is said to be *chaotic* if the number of conserved quantities is smaller than the number of degrees of freedom [151]. In that case, the restrictions imposed on the phase space trajectories are usually insufficient for preventing exponential sensitivity of the system's time evolution to the initial conditions, as discussed in Sec. 1.6. Thus, the system behaves chaotically and movement of the particles due to repeated scattering resembles that of random walkers, leading to diffusive transport [152]. Examples include Brownian motion (cf Sec. 2.3), heat transfer [153] and the communication between neurons via diffusive neurotransmitters [154].

- In contrast, if the number of conserved quantities is equal to or exceeds the number of degrees of freedom, the system is called *integrable*. This usually means that the dynamics of a system are analytically tractable and that the trajectories in phase space are periodic. This often leads to ballistic forms of transport [155], where the scattering length of (quasi)particles is comparable to the system size. As an example, integrability is closely related to the theory of solitons [156] which provides descriptions for nonlinear optics phenomena, tsunami waves and localized condensed matter excitations [157]. Integrable systems can be analytically tractable, while chaotic systems are generally not and are more likely to require computationally expensive numerical simulations [158].

In quantum mechanics, the number of conserved quantities is also a good indicator for whether a quantum system is integrable or chaotic [159]. For instance, the 1d Heisenberg model is integrable due to an infinite set of conservation laws that can be expressed as the sum of polynomials of spin

variables [160]. However, adding long range interactions to the model breaks integrability and results in a chaotic Hamiltonian [161]. Note that the picture of phase space trajectories does not easily carry over to the quantum case, as the Heisenberg uncertainty principle forbids simultaneous measurements of both position and momentum. Instead, signatures for distinguishing quantum chaos and quantum integrability are found in the distribution of energy level spacings: In case of chaotic models, this distribution is found to be of a Wigner-Dyson type, as predicted by random matrix theory (RMT). For integrable models, we find a Poisson distribution, instead, see Ref. [162] for details.

1.6 Classical thermalization

In general, chaotic dynamics are required for a system to thermalize. In the following we will define what thermalization means and shed light on the role of chaos in this process.

Piercing an air-filled balloon inside a vacuum chamber will always lead to the same result: The released gas particles will eventually become equally distributed in the chamber and their velocities will follow a Maxwell-Boltzmann distribution. Surprisingly, we can expect this final state irrespective of where the balloon was located, what shape the balloon had or at what point on its surface it was pierced [163]. This simple observation hints at a universal principle underlying the time evolution of chaotic systems in the universe: Governed by the interactions between particles and their physics, they will relax to a final state corresponding to *thermal equilibrium* and lose all memory about their initial state: It is impossible for any observer to reverse the time evolution and reconstruct the initial state once thermal equilibrium is approached. The quantity that captures this loss of information is called entropy and quantifies randomness in the system. In an isolated system, thermal equilibrium corresponds to a maximum entropy state. It is maximally random in a sense that the particle and energy density is homogeneously spread out across the entire system, as opposed to the initial state, when all particles are confined to the volume of the balloon.

The most direct way one could think of for studying the thermalization and the thermal equilibrium of this gas in the vacuum chamber would be to track both position and momentum of every particle over time, as they collide with each other. Assuming that the system is described by a classical Hamiltonian $\mathcal{H}(\mathbf{q}, \mathbf{p})$, the generalized coordinates $\{q_i\}$ and $\{p_i\}$ would evolve as:

$$\frac{dq_i}{dt} = \{q_i, \mathcal{H}\}, \quad \frac{dp_i}{dt} = \{p_i, \mathcal{H}\}, \tag{1.8}$$

where $\{ \dots \}$ is the Poisson bracket. However, the sheer amount of particles ($\gg 10^{23}$) and their interactions with each other make this approach unfeasible, both from an analytical and a numerical point of view. Fortunately, in many cases knowing the microscopic physics of the system is not necessary for making predictions about its future behavior. Instead, one can focus on macroscopic descriptions of the system's bulk parameters: For instance, we can measure the pressure or temperature of a vapor without measuring the velocity of each individual particle. The theory which deals with the relationships between these macroscopic properties of matter in equilibrium is called (classical) *thermodynamics*. It provides a framework for understanding and predicting the behavior of systems in equilibrium in terms of energy transformations and heat transfer [164]. On microscopic scales, describing the behavior of particles means dealing with a complex many-body system that has a very large number of states. *Kinetic theory* aims to derive the collective behavior of particles, starting from the fundamental laws that dictate their trajectories and interactions. The field of *statistical physics* (or statistical thermodynamics) analyzes the statistics of possible states and is concerned with the distribution of energy, velocity and positions of particles in a system. Both aim to derive the thermodynamic properties from behavior of individual particles, and, in doing so, bridge the gap between macroscopic and microscopic descriptions of matter

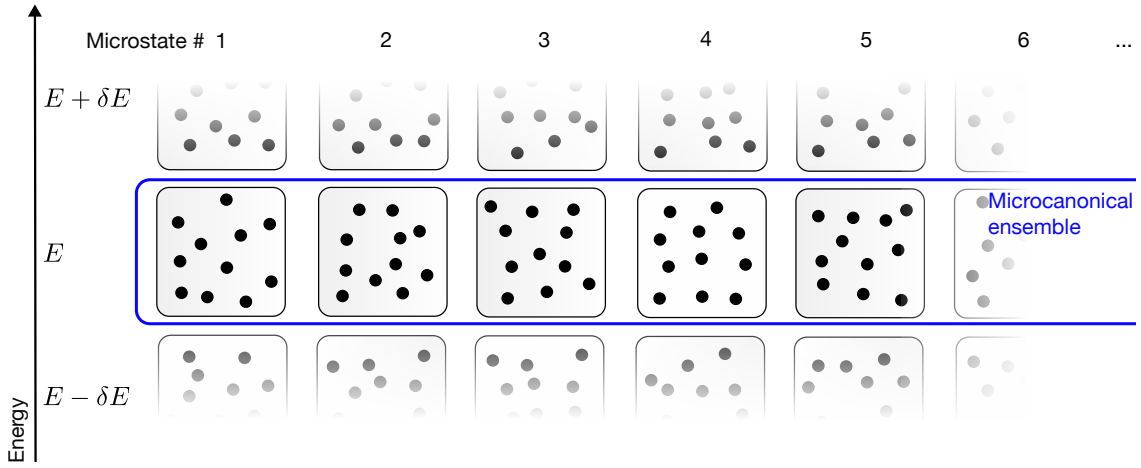

Figure 1.4 | The microcanonical ensemble. Taking repeated snapshots of a system in phase space ultimately reveals all possible microstates. If the system is completely isolated such that particle number, volume and energy are conserved, all observed microstates will have the same energy $E \in]E - \delta E, E + \delta E[$. The complete collection of microstates in this energy class is called the microcanonical ensemble, a subset of the canonical ensemble which includes all energies.

[165]. In the following, we employ the statistical approach and define thermal equilibrium using the *microcanonical ensemble*.

The microcanonical ensemble

Even in thermal equilibrium, the particles collide randomly and their velocities and positions fluctuate. Every time we take a snapshot of the system, we would find a different configuration of particle positions and velocities. If we kept taking snapshots until we have seen *all possible* configurations, then we would have generated an ensemble of microstates (see Fig. 1.4). Assuming that the vacuum chamber does not allow any particle or energy transfer across its boundaries, all observable microstates will have the same energy $E \in]E - \delta E, E + \delta E[$ and the same particle number. The ensemble of microstates at one particular energy is called the *microcanonical ensemble*.If the system was not isolated and allowed energy transfer across its boundaries, the entirety of observed microstates would constitute the *canonical ensemble*. If additionally, particles could leave and enter the system, we would get the *grand canonical ensemble*. These thermodynamic ensembles are also called *Gibbs ensembles*.

Since all microstates have the same energy, it is reasonable to assume that all microstates are equally likely to be observed. This is expressed by the phase space probability

$$\rho(p,q) = \begin{cases} \frac{1}{\Gamma(E,V,N)} & E - \delta E < H(q,p) < E + \delta E \\ 0 & \text{otherwise,} \end{cases} \tag{1.9}$$

where $\Gamma(E,V,N)$ is the volume occupied by the microstates within the (infinitesimally small) energy shell $]E - \delta E, E + \delta E[$ at constant volume V and particle number N. In thermal equilibrium, the (Boltzmann) entropy of the system is maximal and can be computed from the number of (equally probable) microstates [166]:

$$S(E,V,N) = k_B \ln \Gamma(E,V,N). \tag{1.10}$$

The microcanonical ensemble average of any quantity $A(p,q)$ is given by [167]:

$$\langle A\rangle_{\mathrm{mc}} = \frac{1}{\Gamma(E,V,N)} \int dq \int dp\ \rho(p,q)\, A(q,p)\ \delta(E - H(q,p)) \tag{1.11}$$

and its variance is obtained from evaluating:

$$\sigma_A^2 = \langle A^2\rangle_{\mathrm{mc}} - \langle A\rangle_{\mathrm{mc}}^2. \tag{1.12}$$

Thus, in thermal equilibrium, we are able to compute any quantity in the system from statistics only, without knowledge about the microscopic physics that govern the interactions between the particles. This is a very powerful tool for predicting measurements in fully thermalized states. The ensemble, however, does not provide any information about *how* the system relaxes toward thermal equilibrium and how the measured quantity time-evolves during the thermalization process. Another open question is: What mechanism underlies Eq. 1.11, leading to mean quantities that are in agreement with the assumption that all microstates are equally likely (cf. Eq. 1.9)? What dynamics are necessary for a system to reach thermal equilibrium, as defined by the microcanonical ensemble? The answer is generally chaos.

Chaos and ergodicity

While a classical system is intrinsically deterministic, i.e. the time evolution is, in principle, predictable using Eq. 1.8, it can be deterministically chaotic when its space trajectory at long times is infinitely sensitive to the initial conditions. Let us assume that two initial states are separated by a small difference vector $\delta\mathbf{k}_0$ in phase space. If the system is chaotic, this difference will grow exponentially over time (the so-called *butterfly effect*), i.e.

$$|\delta\mathbf{k}(t)| = |\delta\mathbf{k}_0| e^{\lambda t}. \tag{1.13}$$

Here, $\lambda > 0$ is the Lyapunov exponent that quantifies the predictability of the system [168].

As an example, consider the dynamical billiard depicted in Fig. 1.5a: A single particle moves freely inside the billiard and its direction of movement is only altered by elastic collisions with the elliptical billiard wall. As illustrated by the two trajectories in black and red, any small difference in the initial velocity vector of the particle will grow large over time, as expressed by Eq. 1.13. One can imagine that, if there are no *special* initial state vectors that do not lead to divergence, the particle will always ultimately explore every point of the billiard and every velocity vector of constant length, generating all possible microstates. In that case averaging the position of the particle over time (from $t = 0$ until $t \to \infty$) will yield the same result as taking the average of many snapshots at a constant late time $t = t^* \gg 1$. In this case the system is called *ergodic*. For comparison, consider the rectangular billiard depicted in Fig. 1.5b. Here, the initial angle of the particle's velocity vector is conserved. Thus, while the particle might still visit every point of the billiard's area it will do so only with certain velocity components. The dynamics of the particle are, therefore, restricted to a subregion of the overall phase space and ergodicity is broken.

The notion of ergodicity can be more rigorously defined as follows: When measuring an observable A, we expect to obtain the mean value predicted by the microcanonical ensemble according to Eq. 1.11. However, a measurement typically takes a finite amount of time τ that is long compared to the average interaction time of the particles. Thus, we can picture the measurement result as a finite time integral over the time-evolution of the actual quantity:

$$\bar{A}_\tau = \frac{1}{\tau} \int_0^\tau dt\ A(q,p,t) \tag{1.14}$$

Ergodicity means that Eq. 1.11 and Eq. 1.14 are equivalent in the limit of long measurements $\tau \to \infty$.

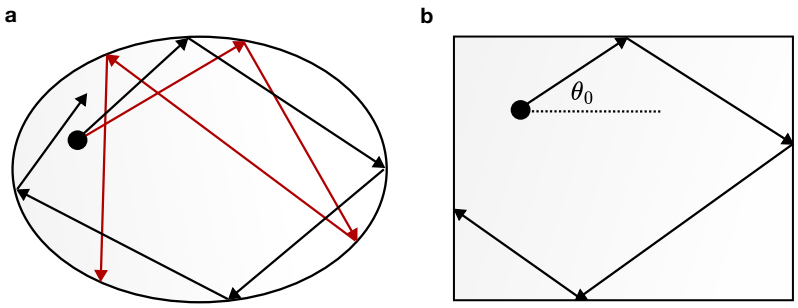

Figure 1.5 | **Ergodicity illustrated using dynamical billiards. a,** Elliptical billiard (ergodic). The trajectories of two particles with slightly different initial velocity vectors diverge quickly over time, indicating that, according to the ergodic hypothesis, each individual trajectory will eventually explore the entire billiard surface with all possible velocity vectors of constant length. **b,** Rectangular billiards restrict the velocity of the particle to certain vectors, preventing a full exploration of the phase space and breaking ergodicity.

This assumption is known as the *ergodic hypothesis* [169]: A system is ergodic if the microcanonical ensemble average $\langle A \rangle_{\text{mc}}$ is identical to the infinite-time average $\bar{A}$ over the evolution of A:

$$\bar{A} = \lim_{\tau \to \infty} \bar{A}_\tau(q, p) = \langle A \rangle_{\text{mc}}. \tag{1.15}$$

The latter is independent of the initial conditions which only matter at short times. Intuitively, this equivalence means that, as the system evolves over time, it eventually visits all microstates in the microcanonical ensemble (which are all equally likely, as stated by Eq. 1.9), producing measurement result in agreement with thermal equilibrium as defined by Eq. 1.11.

All systems require chaos to become ergodic. However, not all chaotic systems are necessarily ergodic: It is possible for a system to exhibit both chaotic and regular regions in phase space, such that trajectories launched in the chaotic region do not enter the regular zones. For instance, the Chirikov standard map falls into this special category [170].

1.7 Thermalization of isolated quantum systems

In quantum systems the microscopic physics governing the microscopic motions of particles and their interactions are fundamentally different compared to classical systems. Important concepts in quantum mechanics like superpositions, unitarity and entanglement require us to understand relaxation and thermalization of a system from the viewpoint of wavefunctions, operators and density matrices. Let us consider an isolated quantum system in an initial state $|\psi\rangle(t = 0)$. This state will time-evolve under the Hamiltonian $\hat{H}$ as:

$$|\psi\rangle(t) = \hat{U}\,|\psi\rangle(t = 0), \tag{1.16}$$

where

$$\hat{U} = e^{-\frac{i}{\hbar}\hat{H}t} \tag{1.17}$$

is the time-evolution operator that acts as a unitary transformation. This means that if the initial state of the isolated quantum system is a pure state, it will remain a pure state for all eternity and

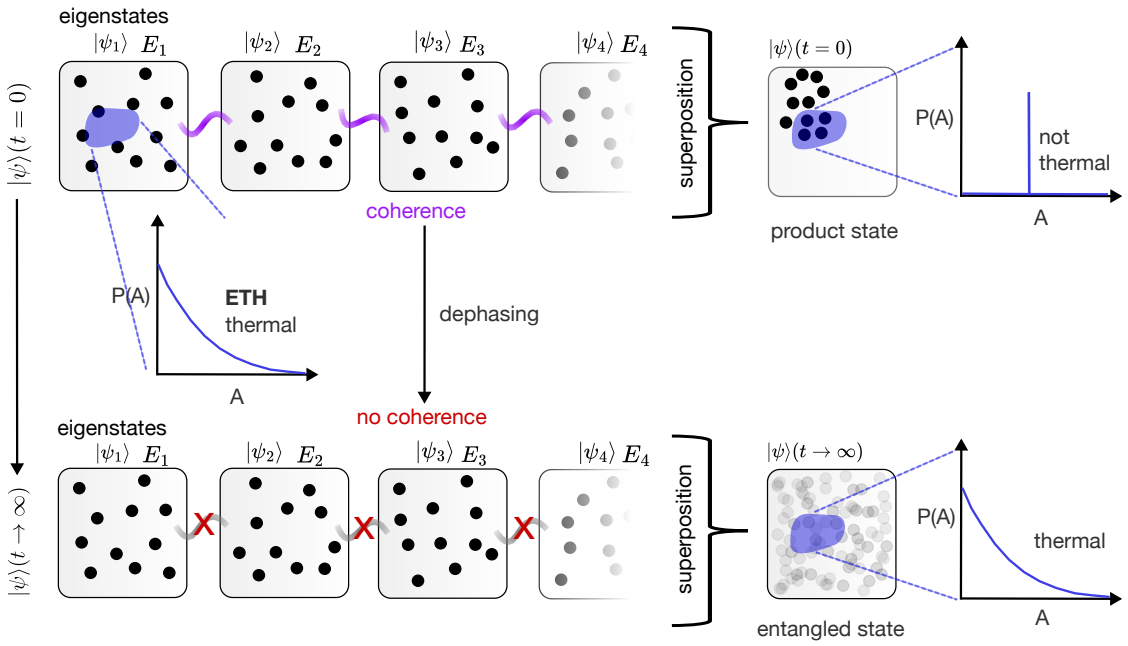

Figure 1.6 | Thermalization of an isolated quantum system. The initial state of the quantum system $|\psi\rangle(t=0)$ is a superposition of eigenstates, forming a product state. Each eigenstate is thermal according to the eigenstate thermalization hypothesis (ETH). This means that the measured distribution of any local observable in any eigenstate will match the prediction from statistical physics in the microcanonical ensemble. However, due to fixed phase relations (coherence) between the eigenstates in the superposition, measuring the observable in the initial state will not yield a thermal distribution. As the system time-evolves, the coherence between the eigenstates in the superposition vanishes, such that not only the eigenstates individually but also the superposition $|\psi\rangle(t\to\infty)$ appears thermal [163].

dynamical chaos as in the classical case cannot emerge. This suggests that the process of thermalization unfolds in a fundamentally different way.

Let us write the initial state as a superposition of (energy) eigenstates of $\hat{H}$:

$$|\psi\rangle(t=0)=\sum_\alpha C_\alpha|\psi_\alpha\rangle, \tag{1.18}$$

with $C_\alpha=\langle\psi_\alpha|\psi\rangle(t=0)$ and $\sum_\alpha|C_\alpha|^2=1$. The time-evolution can then be expressed as:

$$|\psi\rangle(t)=\sum_\alpha C_\alpha e^{-\frac{i}{\hbar}E_\alpha t}|\psi_\alpha\rangle, \tag{1.19}$$

where E_α are the energy eigenvalues fulfilling the time-independent Schrödinger equation $H|\psi_\alpha\rangle=E_\alpha|\psi_\alpha\rangle$. Let A be an observable. Using the eigenstate decomposition in Eq. 1.19, the time evolution of A is given by [171]:

$$\langle A\rangle(t)=\langle\psi|A|\psi\rangle(t)=\sum_{\alpha,\beta}C_\alpha^* C_\beta e^{-\frac{i}{\hbar}(E_\alpha-E_\beta)t}A_{\alpha,\beta}. \tag{1.20}$$

Similar to Eq. 1.14, we can define the long-time average as:

$$\bar{A}=\lim_{\tau\to\infty}\frac{1}{\tau}\int_0^\tau\langle A\rangle(t)dt. \tag{1.21}$$

The relaxation process of the system is called thermalization if the long-time average matches the prediction from statistical physics in the microcanonical ensemble belonging to the energy shell $I = [E - \delta E, E + \delta E]$:

$$\bar{A} = \langle A \rangle_{\mathrm{mc}}(E \in I), \tag{1.22}$$

where

$$\langle A \rangle_{\mathrm{mc}}(E \in I) = 1/N_{E \in I} \sum_{\alpha : E_\alpha \in I} A_{\alpha\alpha}, \tag{1.23}$$

in analogy with Eq. 1.11. Here, $N_{E \in I}$ is the number of microstates in the energy shell I.

Eigenstate Thermalization Hypothesis

According to Eq. 1.20, off-diagonal elements of A (i.e. $A_{\alpha,\beta}$ with $\alpha \neq \beta$) will oscillate at a frequency $(E_\alpha - E_\beta)/\hbar$ and dephase and, thus, average out to zero in Eq. 1.21. Therefore, one could expect that A relaxes to

$$\bar{A} = \sum_\alpha |C_\alpha|^2 A_{\alpha\alpha}. \tag{1.24}$$

However, this is not generally true as, depending on the exact spectrum of $\hat{H}$, a high density of states at a certain value of $E_\alpha - E_\beta$ might prevent dephasing. Further, the relaxation described by Eq. 1.24 does not necessarily mean thermalization in a sense that all initial states will reach the same thermal equilibrium: In general, $\bar{A}$ depends on details of the initial state through the coefficients C_α (cf. Eq. 1.24). This suggests that more information about the spectrum of $\hat{H}$ is needed and that not all operators A can relax or thermalize. Considering the unitarity of the time evolution and, as a consequence, the inability of the *global* system to relax, we can assume that the thermalization only happens locally and we need to restrict ourselves to *local* operators [171]: If the operator A describes a local measurement in a subsystem $\mathcal{A}$, information about the remainder of the overall system is lost and the idea of different initial states relaxing to the same local equilibrium (according to Eq. 1.24) seems possible.

Random matrix theory approaches [41, 42, 172] support the claim that the diagonal elements of A are given by the average of the microcanonical ensemble of the corresponding eigenenergies:

$$A_{\alpha\alpha} = \langle A \rangle_{\mathrm{mc}}(E_\alpha), \tag{1.25}$$

and $A_{\alpha\alpha}$ is not expected to vary much between the eigenstates that are energetically similar. The statement in Eq. 1.25 is called the eigenstate thermalization hypothesis (ETH) because it suggests that thermalization occurs at the level of individual eigenstates and that each eigenstate already looks locally thermal. It means that if the system is in an energy eigenstate of the Hamiltonian and we measure A (e.g. in the density basis), we find a thermal distribution as expected from statistical physics. Then, the question whether we would also measure a thermal distribution in a general quantum state ψ (which is a superposition of energy eigenstates) must be answered by the phase relations C_α between the eigenstates (see Fig. 1.6). If we prepare a specific initial state, the coefficients C_α are highly non-trivial and coherently combine into a state in which A is not thermal. However, as time passes and the system evolves, coherence between the energy eigenstates is lost. Then, due to dephasing, $\langle A \rangle(t)$ will yield a thermal value, consistent with the prediction from statistical physics and the microcanonical ensemble.

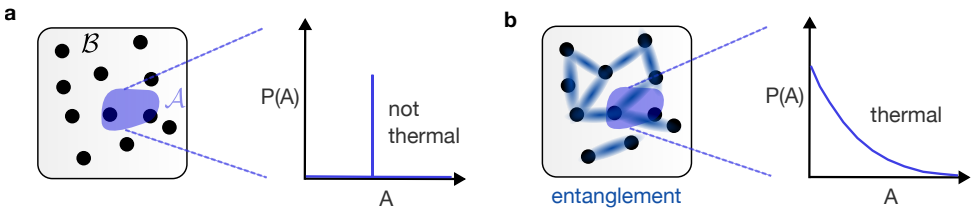

Figure 1.7 | Entanglement entropy. a If a subsystem $\mathcal{A}$ is not entangled with the remainder of the overall system $\mathcal{B}$, the subsystem's state is pure and measurements of operators in the subsystem will generally have non-thermal distributions. **b**, In presence of maximal entanglement between the subsystem and the remainder of the overall system, the subsystem's state becomes fully mixed. Then, repeated measurements of subsystem observables will yield a thermal distribution.

Entanglement entropy

How thermal statistics emerge in isolated quantum systems from out-of-equilibrium dynamics is an intricate question which has been answered only recently [39, 171, 173]. In the classical microcanonical ensemble the entropy is defined as in Eq. 1.10 and maximized by the uniform distribution of microstate probabilities, which corresponds to a thermal equilibrium state at late times. From an information point of view, the knowledge about what microstate the system will be found in is minimal, indicating that memory about the initial state is maximally lost.

For a state of an isolated quantum system which is described by the density matrix ρ, we can define the von Neumann (entanglement) entropy [174]:

$$S = -\mathrm{Tr}(\rho \ln \rho). \tag{1.26}$$

As stated by Eq. 1.19, a closed quantum system initialized in a pure state will undergo a unitary time evolution and stay pure. If the system is pure, information about the state is maximal and we obtain an entropy of zero at all times. Thus, Eq. 1.26 cannot be the maximized thermal entropy belonging the the microcanonical ensemble from statistical physics, according to the ETH.

The solution to finding a thermodynamical entropy in a quantum system lies in the notion of locality, similar to the restrictions applied to A in the preceding paragraph: Instead of describing the entire isolated system, we focus on a subsystem $\mathcal{A}$ (and calling the remainder of the overall system $\mathcal{B}$) [173]. The reduced density matrix for subsystem $\mathcal{A}$ reads:

$$\rho_{\mathcal{A}} = -\mathrm{Tr}_{\mathcal{B}}(\rho \ \ln \rho) \tag{1.27}$$

If there is no entanglement between $\mathcal{A}$ and $\mathcal{B}$, measuring $\mathcal{A}$ will reveal a pure state with $\mathrm{Tr}(\rho_{\mathcal{A}}^2) = 1$. If, however, $\mathcal{A}$ and $\mathcal{B}$ are entangled, $\rho_{\mathcal{A}}$ becomes mixed. The entanglement entropy is defined as:

$$S_E(\mathcal{A}, \mathcal{B}) = -\mathrm{Tr}(\rho_{\mathcal{A}} \ln \rho_{\mathcal{A}}), \tag{1.28}$$

quantifying the amount of entanglement between $\mathcal{A}$ and $\mathcal{B}$, or, from an information theory point of view, the uncertainty about the quantum state of $\mathcal{A}$ due to its entanglement with $\mathcal{B}$, when only $\mathcal{A}$ is measured.

Recent analytical [175] and numerical studies [173] suggest that the thermodynamic entropy of the subsystem $\mathcal{A}$ is equivalent to the entanglement entropy between this subsystem and its environment:

$$S(\mathcal{A}) = -\mathrm{Tr}(\rho_{\mathcal{A},\mathrm{mc}} \ln \rho_{\mathcal{A},\mathrm{mc}}) = -\mathrm{Tr}(\rho_{\mathcal{A}} \ln \rho_{\mathcal{A}}) = S_E(\mathcal{A}, \mathcal{B}). \tag{1.29}$$

Further, in thermal equilibrium, the reduced density matrix $\rho_{\mathcal{A}}$ of subsystem $\mathcal{A}$ is equivalent to the

mixed density matrix expected from statistical physics in the microcanonical ensemble $\rho_{\mathcal{A},\mathrm{mc}}$. Eq. 1.29 essentially extends the ETH to entropy and explains how subsystems of an isolated quantum system can appear thermal, even though the overall system remains in a pure state: through maximal entanglement between the subsystem and its surroundings which acts as a thermal bath, as illustrated in Fig. 1.7. Thus, from the perspective of the global system, the information about the initial state is not lost, but scrambled in the form of many-body entanglement.

Thermalization through entanglement

In conclusion, in order for an isolated quantum system to reach thermal equilibrium described by Eq. 1.29 or Eq. 1.22 after a quench (cf. Sec. 1.4), the particles in the system build up entangled with each other over growing distances, until the entanglement entropy is locally maximized. The maximum speed at which entanglement (or quantum information) can spread is the speed of light in the system, also called the Lieb-Robinson velocity [176]. In most systems (both integrable and chaotic, excluding localized systems) entanglement spreads ballistically at constant speed [177–181]. An important consequence of entanglement is the emergence of density-density correlations [59] and fluctuations as the system relaxes. Quantum gas microscopes provide access to these observables and we will study them in Chapter 5, looking out for signatures of fluctuating hydrodynamics (see next Chapter).

CHAPTER 2

Fluctuating hydrodynamics

This Chapter introduces the framework of fluctuating hydrodynamics (FHD), a classical macroscopic theory combining hydrodynamics with random noise. We start by introducing hydrodynamics in general and discuss the implications of adding fluctuations. We illustrate the most important concepts of this theory using two simple analytically solvable diffusive systems: Brownian motion of a single particle and the symmetric simple exclusion process (SSEP). The purpose of this Chapter is to provide the theoretical context for Chapter 5 where the applicability of FHD (an effective classical description) to an isolated chaotic out-of-equilibrium quantum system is experimentally tested.

2.1 Hydrodynamics

When we want to describe how water flows through a tube (cf. Fig. 2.1a), we do not have to know about the chemistry and physics of water molecules. Instead, we can make use of a set of partial differential equations, called the Navier-Stokes equations (NSE) [182], which dictate the time evolution of the fluid flow velocity. The NSE are just one example of a much more universal theory, called *hydrodynamics*: It treats a fluid as a continuous medium with locally well-defined macroscopic quantities, such as density or pressure and locally averages the behavior of the constituent particles rather than attempting to describe their individual trajectories [183] (see Introduction for more context).

Length- and timescales

Hydrodynamics is a theory which is exact but only in the late-time and long-wavelength limit of the system [17]. This is visualized in Fig. 2.1b: At the microscopic scale (average particle-particle distance d), we encounter a many-body problem consisting of interacting particles colliding in complex ways (i). This problem is generally analytically intractable and the complexity grows unfavorably with the number of particles, making a microscopic description of the system unfeasible. In contrast, if we zoom out by a lot (iii), the many-body character of the problem vanishes: we do not detect the presence of individual particles anymore but, instead, measure continuous quantities, such as the density $\bar{n}(x,t)$, which varies on a lengthscale $l_{\text{macro}} = \bar{n}(x,t)/\partial_x \bar{n}(x,t)$ (macroscopic scale). For a clear separation of lengthscales we require:

$$d \ll l_{\text{meso}} \ll l_{\text{macro}}. \tag{2.1}$$

This defines an intermediate lengthscale l_{meso} on which the density is homogeneous and the system appears to be in (local) thermal equilibrium (homogeneous density) [184]. In the following, we will refer to the segments corresponding to this lengthscale as *fluid cells* and imagine that the overall system (macroscopic process) is partitioned into a finite number of fluid cells (cf. Fig. 2.1b (iii)).

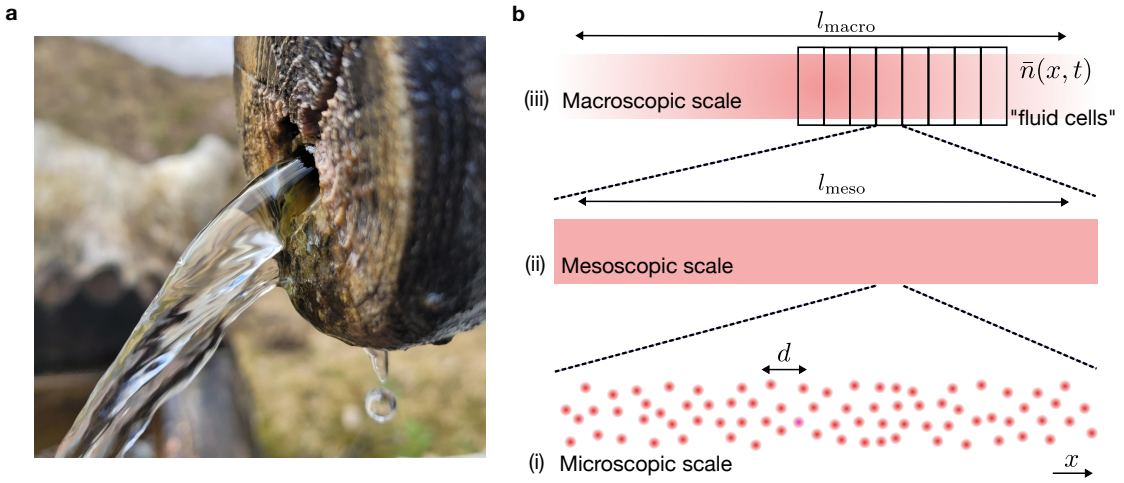

Figure 2.1 | **Hydrodynamics. a**, Understanding and describing flow of a water through a pipe does not require knowledge about the chemistry of water molecules. Instead, one can find a macroscopic continuum description in the framework of hydrodynamics. **b**, Hydrodynamics provides equations for the coarse-grained (macroscopic) time evolution of conserved quantities, assuming that local mesoscopic segments ("fluid cells") have already thermalized. This allows to conveniently ignore the details of the microscopic physics and absorb them into few effective variables of the macroscopic model [184].

The mesoscopic lengthscale is not static but grows in time as the system relaxes over larger and larger distances and thermal equilibrium is reached in larger and larger segments (cf. Secs. 1.6 and 1.7). Let τ_{relax} be the local relaxation time on the microscopic level. Then there is mesoscopic relaxation time, defined as:

$$\tau_{\mathrm{relax}} \ll t_{\mathrm{meso}} \ll \bar{n}(x,t)/\partial_t \bar{n}(x,t), \tag{2.2}$$

where $\bar{n}(x,t)/\partial_t \bar{n}(x,t)$ is the relaxation timescale on which the macroscopic density variations vanish and *global* thermal equilibrium is reached. The local equilibrium in individual fluid cells is reached within t_{meso}. Importantly, if t_{meso} has passed and a fluid cell has fully relaxed, the average quantity $\bar{O}$ representing a late-time measurement of the fluid cell is equivalent to that obtained from the Gibbs ensemble average in statistical physics (cf. Eq. 1.15 and Eq. 1.22):

$$\bar{O} = \langle O \rangle_{\mathrm{stat}}. \tag{2.3}$$

Assuming that all fluid cells are in local thermal equilibrium means that we can simply work with the mean quantities of the fluid cells directly rather than describing the microscopic physics governing the thermalization process of each fluid cell. Moving to larger scales and increasing the level of coarse-graining, the number of fluid cells approaches infinity and the local mean quantities become a continuous field.

In the following we will assume that the system is 1d. However, the formalism can be easily generalized to higher dimensions by substituting $x \to \mathbf{r}$ and $\partial_x \to \nabla_{\mathbf{r}}$.

Conservation laws

As discussed in Sec. 1.5, a chaotic system is generally characterized by a small number of (locally) conserved quantities Q_i ($i = 1, \ldots, N$), such as particle number and energy. These can be expressed

as integrals of local densities $q_i(x,t)$, such as particle density or energy density. For each conserved quantity, we can write down a continuity equation:

$$\partial_t q_i(x,t) + \partial_x j_i = 0, \tag{2.4}$$

expressing the fact that any change of the local density must be accompanied by a corresponding current $j_i(x,t)$ at the microscopic level. On a timescale t_{meso} the system is expected to thermalize on a lengthscale l_{meso}, defining the fluid cells, as described earlier. As stated by Eq. 2.3, the local mean density in a fluid cell (on the mesoscopic scale) is equal to the ensemble average [19]:

$$\bar{q}_i = \langle q_i \rangle_{\text{stat}}, \tag{2.5}$$

By zooming out even more (to the macroscopic scale), the density of fluid cells diverges and we can generalize the continuity equation to:

$$\partial_t \bar{q}_i(x,t) + \partial_x \bar{j}_i(x,t) = 0, \tag{2.6}$$

with initial conditions $\bar{q}_i(x, t_{\text{meso}}) = \langle q_i \rangle_{\text{stat}}(x)$ and $\bar{j}_i(x, t_{\text{meso}}) = \langle j_i \rangle_{\text{stat}}(x)$. Eq. 2.6 expresses that any change of the density in a fluid cell must be accompanied by a current between adjacent fluid cells. Thus, the microscopic conservation laws have translated to macroscopic conservation laws for a coarse-grained density field $\bar{q}_i(x,t)$. In contrast, all information about other laws of physics driving the thermalization of the fluid cells is lost. Yet, we can maintain an exact description on large time- and lengthscales, just by assuming that the fluid cells are locally thermal, and, as discussed below, by absorbing the details of the model into the definition of the coarse-grained density current $\bar{j}_i(x,t)$.

Density current

In general, the density current $\bar{j}_i(x,t)$ can be expressed as a function of the density $\bar{q}_i(x,t)$ and its derivatives. This is because the state of the system is expected to be fully defined by the information about all local densities in what is a bijection [19]. The equation defining the density current is called the *equation of state*:

$$\bar{j}_i = F(\bar{q}_i, \partial_x \bar{q}_i, \partial_x^2 \bar{q}_i, \dots), \tag{2.7}$$

and is, in general, highly model-dependent [184]. A common way of expanding the density current is writing it out as a gradient expansion [185]:

$$\bar{j}_i(x,t) = \sum_j A_{ij}(\{\bar{q}_i(x,t)\})\, \bar{q}_j(x,t) - \frac{1}{2} \sum_j D_{ij}(\{\bar{q}_i(x,t)\})\, \partial_x \bar{q}_j(x,t) + \dots . \tag{2.8}$$

If only the first order term is non-zero ($A_{ij} \neq 0, D_{ij} = 0$), we obtain *Euler scale* hydrodynamics. The matrix A_{ij} is called the *flux Jacobian* and encodes the response of the system to spatial density gradients. In general, Euler scale hydrodynamics describes ballistic transport of conserved quantities.

In many cases the current does not depend on the density but on the gradient of the density ($A_{ij} = 0, D_{ij} \neq 0$). This is captured by the second term in Eq. 2.8, which gives rise to phenomena like diffusion and can reproduce *Navier-Stokes hydrodynamics*. The entries of $D_{ij}(\{\bar{q}_i(x,t)\})$ are called diffusion constants, heat conductivities or viscosity, depending on whether particle transport, energy transport or momentum transport is considered, respectively [186]. In general, they depend on the density, just as the laws of physics governing the interactions between the particles are density-dependent [187]. If the particle number is the sole (locally) conserved quantity in the system, simple particle diffusion would be described by *Fick's law*. It states that the particle current is proportional to the gradient of the density:

$$\bar{j}(x,t) = -D(\bar{n}(x,t))\frac{\partial \bar{n}(x,t)}{\partial x} \tag{2.9}$$

with a density-dependent *linear-response* diffusion constant $D(\bar{n})$. If only energy was conserved, we could write down Fourier's law of heat conduction stating that the heat current is proportional to the temperature gradient:

$$\bar{j}(x,t) = -k\frac{\partial \bar{T}(x,t)}{\partial x}. \tag{2.10}$$

Here, k denotes the thermal conductivity. Eq. 2.9 and Eq. 2.10 are also called *constitutive relations* [188]. Note that, if there are multiple conserved quantities in the system, their transport, in general, is coupled, as expressed by the sum in Eq. 2.8. This means, for instance, that the particle current can depend on both the spatial density gradient (or an external field) and the spatial energy gradient, leading to a set of coupled differential equations describing thermoelectric coupling [189].

Generalized hydrodynamics

Hydrodynamics applies to systems with very few conserved quantities and (infinitely) many fast decaying modes, a situation which generally characterizes chaotic systems. In contrast, integrable systems have (infinitely) many conserved quantities which prevent relaxation to a state described by the Gibbs ensemble and conventional hydrodynamics breaks down (cf. Sec. 1.5). In order for the theory of hydrodynamics to also describe integrable systems, an extended approach is necessary which takes into account all infinitely many conservation laws resulting in an infinitely large system of continuity equations and density currents. This framework is called *generalized hydrodynamics* (GHD) and, just like standard hydrodynamics, can provide significant numerical advantages, see Refs. [18–20, 185] for more details.

2.2 Fluctuating hydrodynamics

At a macroscopic level, hydrodynamic fields emerge from the assumption of local thermal equilibrium. However, in practice, the level of coarse-graining might still be small enough to be able to *detect* the discretized nature of the microscopic particles in the form of *fluctuations*. Imagine a volume homogeneously filled with a dense gas. If a bullet is shot into the volume, the bullet will slow down due to countless collisions with gas molecules until it comes to a complete stop. So where did the kinetic energy of the bullet go? It has dissipated into the gas, i.e. it transferred to the microscopic degrees of freedom of the individual gas molecules, increasing the amplitude of fluctuations in the system. In this sense, dissipative fluxes can be understood as the macroscopic consequence of fluctuating dynamics in the system [190]. The extended hydrodynamics theory which takes such fluctuations into account is called *fluctuating hydrodynamics* (see Introduction for more context and applications).

The key step establishing *fluctuating* hydrodynamics is to add a random noise term to the equation of state:

$$\bar{j} = F(\bar{q}, \partial_x \bar{q}, \partial_x^2 \bar{q}, \dots) + \xi. \tag{2.11}$$

As a consequence, the continuity equations (Eq. 2.6) become a system of *stochastic* differential equations. The noise term ξ takes the role of random statistical forces affecting the density currents. In a classical system, these forces can be envisioned as the consequence of random collisions between the constituent particles of the system. In a quantum system, fluctuations emerge due to measurement projection noise in the presence of entanglement (cf. Sec. 1.7). Irrespective of what the microscopic origins

of the random fluctuations exactly are, the term ξ aims to universally capture them as white noise. Generally, we assume that

$$\begin{aligned} \langle \xi \rangle &= 0 \\ \langle \xi(x,t)\xi(x',t') \rangle &= \eta\ \delta(x-x')\,\delta(t-t'), \end{aligned} \tag{2.12}$$

with noise amplitude η (see Sec. 2.4 for details). These expressions state that the noise is zero on average and is completely uncorrelated, as expected from random collisions between the particles in the system at the microscopic level [190].

With random fluctuations introduced in the model, a natural question to ask would be: How do the fluctuations transfer to measurable observables? One way to answer this question is to use the framework of macroscopic fluctuation theory (MFT) [31]. MFT provides methods for analyzing the FCS in non-equilibrium systems, complementing FHD and its description of the dynamics. For more information, see Appendix A. In the following, however, we will compute correlations and fluctuations by solving the stochastic differential equations (SDEs) of FHD using standard methods.

2.3 Brownian motion

One of the simplest examples illustrating the macroscopic effects of microscopic fluctuations is *Brownian motion*: the shaky random movement of a tracer particle in liquids or gases, e.g. pollen grains immersed in water [191]. The grains have a typical size on the order of 10 µm and weigh about ≈ 1 µg. They are sufficiently small and light in order to experience significant velocity changes from collisions with individual water molecules at room temperature, leading to visible erratic movements (fluctuations) under the microscope [192]. If the tracer particle was too heavy, though, the fluctuation amplitude would be undetectable.

Let us picture a single particle, initially located at position $x_0 = 0$ at time $t = 0$, performing a discretized random walk (a chaotic process). At each time step Δt, the particle moves right or left with a probability of 50% each. After T steps the position of the particle is

$$x_T = \sum_{t=1}^{T} d_t, \tag{2.13}$$

where $\mathbf{d} = (d_1, d_2, \ldots, d_T)$ is a sequence of random steps of length a to the left ($d_t = -a$) and to the right ($d_t = +a$).

Probabilistic description

As the process is random, we can only make probabilistic predictions about the position of the particle. The mean position of the particle is:

$$\langle x_T \rangle = \left\langle \sum_{t=1}^{T} d_t \right\rangle = \sum_{t=1}^{T} \langle d_t \rangle = 0, \tag{2.14}$$

independent of the number of time steps T, suggesting that on average the particle does not move. However, for the variance of the particle position we find:

$$\langle x_T^2 \rangle = \left\langle \sum_{t=1}^{T} d_t^2 + 2 \sum_{t \neq t'} d_t d_{t'} \right\rangle = \sum_{t=1}^{T} \langle d_t^2 \rangle = \sum_{t=1}^{T} a^2 = a^2 T, \tag{2.15}$$

i.e. the range of likely positions $[-l, l]$ continues to expand according to a square root law:

$$l = \sqrt{x_T^2} = \sqrt{a^2 T}. \tag{2.16}$$

Using $T = t/\Delta t$, we can rewrite Eq. 2.15 as:

$$\langle x_t^2 \rangle = 2Dt, \tag{2.17}$$

Here,

$$D = a^2/(2\,\Delta t) \tag{2.18}$$

denotes the diffusion constant which effectively quantifies the mobility of the particle (cf. Sec. 2.1). It absorbs the randomness in the particle's micromotion into a single number.

Langevin-type description

More generally, in continuous space and time we can describe Brownian motion by assuming that the velocity of the tracer particle randomly fluctuates (due to the random collisions in the bath) [193]:

$$\dot{x}(t) = \xi(t), \tag{2.19}$$

with white noise $\xi(t)$ of amplitude η fulfilling (cf. Eq. 2.12):

$$\langle \xi(t) \rangle = 0; \quad \langle \xi(t) \xi(t') \rangle = \eta\, \delta(t - t'). \tag{2.20}$$

This is a very simple example for a Langevin-type equation [194] which describes a system that is subject to fluctuating forces. The motion of the particle is parametrized by:

$$x(t) = x_0 + \int_{t_0}^{t} d\tau\, \xi(\tau), \tag{2.21}$$

assuming the initial condition $x(t = 0) = x_0$. Since ξ is random, it averages out to zero and we find:

$$\langle x(t) \rangle = x_0 + \left\langle \int_{t_0}^{t} d\tau \xi(\tau) \right\rangle = x_0 \tag{2.22}$$

For the equal-time correlator we get:

$$\langle x(t_1)\, x(t_2) \rangle = x_0^2 + \left\langle \int_{t_0}^{t_1} d\tau_1 \int_{t_0}^{t_2} d\tau_2 \xi(\tau_1) \xi(\tau_2) \right\rangle = x_0^2 + \int_{t_0}^{t_1} d\tau_1 \int_{t_0}^{t_2} d\tau_2 \langle \xi(\tau_1) \xi(\tau_2) \rangle, \tag{2.23}$$

and substituting Eq. 2.20 for $\xi(\tau)$, gives:

$$\langle x(t_1)\, x(t_2) \rangle = x_0^2 + \int_{t_0}^{t_1} d\tau_1 \int_{t_0}^{t_2} d\tau_2\, \eta\, \delta(\tau_1 - \tau_2) = x_0^2 + \eta \min(t_1, t_2). \tag{2.24}$$

Thus, the variance of the particle position is:

$$\langle x(t)^2 \rangle = \eta t. \tag{2.25}$$

Comparing this result with Eq. 2.17 yields that the noise amplitude and the diffusion constant are related through:

$$\eta = 2D. \tag{2.26}$$

In this Langevin-type description, the randomness of the microscopic motion is taken into account by the amplitude of the generic white noise. In contrast to the probabilistic description presented first, no information about the details of the underlying stochastic process is included. Thus, we now have a macroscopic theory of Brownian motion that goes beyond the picture of collisions experienced by the tracer particles in the bath of surrounding molecules. The diffusion constant is the only model parameter required for an exact description of the random walk in the limit of long time- and lengthscales compared to the microscopic collisions. It depends on the amplitude of the noise in agreement with our intuition that larger velocity fluctuations should lead to a faster spreading of the mean particle position.

2.4 Many-body random walks

Brownian motion describes the fluctuating behavior of a single tracer particle in a bath. However, in general, we want to describe the many-body physics of a large volume of gas or liquid, containing $\sim 10^{23}$ particles. Switching from one to many random walkers will not change the fact that the system is chaotic. Further, keeping up the spirit of the Langevin-type description, we do not want to tackle the full many-body problem. Instead, we choose a macroscopic description, which does not require us to know about the microscopic physics of the system, and employ FHD (cf. Sec. 2.2).

Assuming only particle number conservation, we can write down the *continuity equation* for the density $n(x,t)$ and the associated current $j(x,t)$:

$$\partial_t n(x,t) + \partial_x j(x,t) = 0. \tag{2.27}$$

Any inhomogeneous density distribution is expected to lead to a diffusive particle current $j(x,t) \neq 0$, as postulated by Fick's law (cf. Eq. 2.9). This is due to the system's natural tendency to maximize its entropy in equilibrium. Additionally, we add a noise term in order to include fluctuations originating in the random interactions between the particles:

$$j = -D(n)\, \partial_x n - \xi, \tag{2.28}$$

where $D(n)$ is the (generally density-dependent) diffusion coefficient. Note that the noise term must be in the expression for the current in order to ensure that the particle number is conserved. The noise is assumed to be uncorrelated in both time and space as expressed by Eq. 2.12. Then, Eq. 2.28 combined with the continuity equation (Eq. 2.27) yields a SDE, the fluctuating diffusion equation:

$$\partial_t n(x,t) = D(n)\, \partial_x^2 n(x,t) + \partial_x \xi, \tag{2.29}$$

which describes the time evolution of the macroscopic density field $n(x,t)$.

Fluctuation-dissipation relation

Fourier transforming Eq. 2.29 yields [195]:

$$(i\omega + D(n)q^2)\, n(q,\omega) = i\, q\, \xi(q,\omega) \tag{2.30}$$

and allows to solve for $n(q,\omega)$:

$$n(q,\omega) = \frac{-iq\, \xi(q,\omega)}{i\omega + D(n)\, q^2}. \tag{2.31}$$

We then can compute the disconnected density-density correlator $\tilde{C}(x,x',t,t')_{\text{eq}}$ in equilibrium by applying the inverse Fourier transformation to $\langle n(q,\omega)n(q',\omega')\rangle$, yielding [195]:

$$\tilde{C}(x,x',t,t')_{\text{eq}} = \langle n(x,t)n(x,',t')\rangle = \frac{\eta}{2D(n)} \frac{\exp\left(-\frac{|x-x'|^2}{8D(n)|t-t'|}\right)}{\sqrt{4\pi\, D(n)\,|t-t'|}}. \tag{2.32}$$

In the limit $t \to t'$ this expression becomes:

$$\tilde{C}(x,x')_{\text{eq}} = \frac{\eta}{2D(n)}\delta(x-x'). \tag{2.33}$$

The (disconnected) density-density correlations in equilibrium are equivalent to the equilibrium fluctuations. For a conserved quantity, they are generally expected to be related to the susceptibility $\chi(n)$ of the system and have the form [196]:

$$\tilde{C}(x,x')_{\text{eq}} = \chi(n)\, \delta(x-x'). \tag{2.34}$$

Comparing Eq. 2.33 and Eq. 2.34 yields that the amplitude of the fluctuations η is related to the susceptibility as

$$\eta = 2D(n)\chi(n), \tag{2.35}$$

a manifestation of the FDT [27, 197].

Out-of-equilibrium correlations and hydrodynamic tails

In order to solve the SDE and compute the out-of-equilibrium dynamics, we define the Green's function $G(x,t)$ as the solution of Eq. 2.27 in response to a Delta-perturbation:

$$\partial_t G(x,t) - D(n)\, \partial_x^2 G(x,t) = \delta(x)\, \delta(t). \tag{2.36}$$

Fourier-transforming this expression gives:

$$G(k,\omega) = \frac{1}{i\omega + D(n)k^2}. \tag{2.37}$$

The Green's function in real space, therefore, reads:

$$G(x,t) = \Theta(t)\frac{\exp\left(-\frac{x^2}{4D(n)t}\right)}{\sqrt{4\pi D(n)t}} = \Theta(t)\, g(x,t), \tag{2.38}$$

where $\Theta(t)$ is the Heaviside step function. Then, the time evolution of the density field $n(x,t)$ can be expressed as [196]:

$$n(x,t) = \Theta(t) \int dx' g(x-x')n_0(x') + \int dx' \int_0^t dt' g(x-x',t-t')\, \partial_{x'}\xi(x',t'), \tag{2.39}$$

with initial condition $n_0 = n(x,0)$. We assume that the initial state lacks any long-range correlations, such that $\langle n(x,t=0)\, n(x',t=0)\rangle = B(n)\,\delta(x,x')$, where $B(n)$ is the (disconnected) autocorrelator amplitude. One can show using Eq. 2.39 and Eq. 2.34 that the (disconnected) equal-time density-density correlations away from equilibrium yield [196]:

$$\tilde{C}(x,x',t) - \tilde{C}(x,x')_{\text{eq}} = \langle n(x,t)\, n(x',t)\rangle - \langle n(x,t)\, n(x',t)\rangle_{\text{eq}} = (B(n) - \chi(n))\, \frac{\exp\left(-\frac{|x-x'|^2}{8D(n)t}\right)}{\sqrt{8\pi D(n)t}}. \tag{2.40}$$

This expression corresponds to a Gaussian cone, indicating that the correlation front expands as a square root function with a σ-envelope of $\sigma(t) = \sqrt{4Dt}$. Note that compared to the Green's function in Eq. 2.38 there is a factor of two in the denominator of the exponential. In the limit of large evolution times $t \gg |x-x'|^2/(8D(n))$, Eq. 2.40 simplifies to:

$$\tilde{C}(x,x',t) \to \frac{B(n) - \chi(n)}{\sqrt{8\pi D(n)t}}. \tag{2.41}$$

Thus, the correlations are expected to decay according to a square root law $\sim t^{-1/2}$. This is a common characteristic in hydrodynamic systems called a *hydrodynamic tail* [198–202]. It was originally discovered in studies of molecular dynamics [203, 204]. Note that this is a feature captured only by FHD as compared to standard hydrodynamics, going beyond simple diffusion.

Particle number fluctuations

As shown in Appendix D, the density-density correlations are closely related to the particle number fluctuations. In a discrete 1d system, the fluctuations are quantified by the variance of the total particle number in a subsystem of length L sites (cf. Eq. D.3):

$$\text{Var}_L(t) = LC_0(t) + 2\,(L-1)\,C_1(t) + 2\,(L-2)\,C_2(t) + \cdots + 2\,C_{L-1}(t), \tag{2.42}$$

where $C(t)$ are the connected density-density correlators belonging distance d, as defined in Eq. 2.47. The sum can be rewritten as:

$$\text{Var}_L(t) = LC_0(t) + 2L\sum_{d=1}^{L-1} C_d(t) - 2\sum_{d=1}^{L-1} d\, C_d(t). \tag{2.43}$$

In the continuum limit ($d = ia, i \in \mathbb{N}_0$, $a \to 0$, $L \to \infty$ with $L/a = \text{const.}$) we get:

$$\text{Var}_L(t) = LC_0(t) + 2L\int_0^\infty dx\, C_x(t) - 2\int_0^\infty dx\, x\, C_x(t). \tag{2.44}$$

Next, assuming a homogeneous mean density, we have $C_d = \tilde{C}_d + \text{const.}$ and we can substitute Eq. 2.40 for C_x and solve the integrals. In the limit of short times $t \ll L^2/D$, but long enough for the autocorrelator $C_0(t)$ to saturate to $C_0(\infty)$ the variance yields:

$$\text{Var}_L(t) = 2\,C_0(\infty)\sqrt{\frac{2Dt}{\pi}} + \text{const.} \approx \sqrt{\frac{2Dt}{\pi}} \tag{2.45}$$

The last step assumes that the fluctuations in the initial state are negligibly small, i.e. $\text{Var}_L(t=0) \approx 0$. Thus, the variance growth for all subsystems of different sizes L is the same (at times significantly smaller than the saturation timescale of a respective subsystem). This is due to the presence of a fixed number of bonds through which the particles can move in and out of the subsystem, independent of the

subsystem size L. Although Eq. 2.45 does not depend on L, the saturation timescale t_{sat} still does. This is because $\mathrm{Var}_L^{\mathrm{sat}} = \mathrm{Var}_L(t \to \infty) \approx \sqrt{(2\,D\,t_{\mathrm{sat}})/\pi}$ and $\mathrm{Var}_L^{\mathrm{sat}} \propto L$ and therefore $L \propto \sqrt{t_{\mathrm{sat}}}$.

Importantly, Eq. 2.40 and Eq. 2.45 suggest that the out-of-equilibrium dynamics of both the density and the fluctuations are completely determined by the diffusion constant. As shown later in Section 5.7, we can use either a generalized form of Eq. 2.45 or the expression for the density-density correlations in Eq. 2.40 to extract the diffusion constant from experimental data. In the following, we will first apply these concepts to a simple classical chaotic model called the symmetric simple exclusion process (SSEP).

2.5 The symmetric simple exclusion process (SSEP)

Consider particles in a one-dimensional lattice, as shown in Fig. 2.2a. In every timestep, each particle attempts to hop to the right and to the left with a probability of 50% each. However, the movement only happens if the target site is not already occupied by another particle (*exclusion*). This chaotic classical hard-core model is called the symmetric simple exclusion process (SSEP).

The SSEP is a special case of the asymmetric simple exclusion process (ASEP) [205], where the probabilities of the particle moving left or right are generally not equal. The ASEP has applications in, for instance, traffic flow models [206], protein synthesis [207] and electrophoresis [208]. It is considered a testbed for studying the non-equilibrium dynamics of classical many-body systems, particularly because, at least in 1d, it can be solved analytically [209, 210]. Methods for that include the Bethe ansatz [211, 212], matrix formulations [213] and MFT [210].

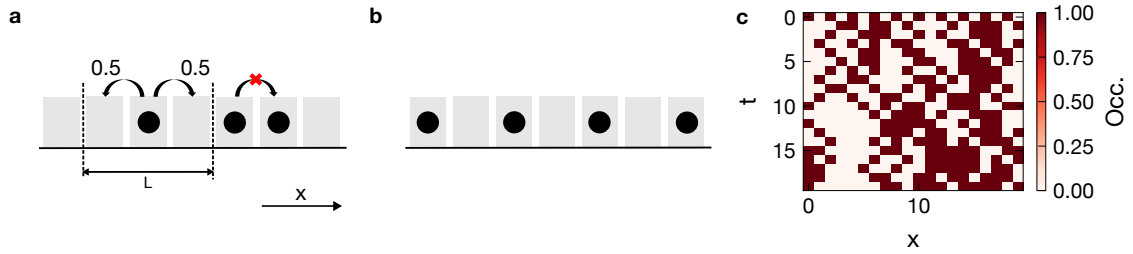

Figure 2.2 | **The symmetric simple exclusion process in 1d. a**, In every time step each particle attempts to move forth or back by one site with equal probability, but the movement succeeds only if the target site is not occupied by another particle. **b**, The initial state is a density wave at half filling with particles occupying every second site. **c**, Single simulation run showing how the initial occupation quickly randomizes within a few timesteps.

Macroscopic description using FHD

In the following, we opt for coarse-grained description of the SSEP in the hydrodynamic limit with the particle number as the only conserved quantity. The SSEP is essentially a many-body random walk: Even though exclusion restricts the movement of the particles at the microscopic level, the randomness of the dynamics is expected to carry over to the macroscopic scale. Thus, using FHD, we can assume that the system is described by the SDE introduced in Eq. 2.28 and Eq. 2.27. The susceptibility (cf. Eq. 2.35) is given by [45]:

$$\chi(\bar{n}) = \bar{n}(1-\bar{n}), \tag{2.46}$$

where $\bar{n}$ is the mean filling of the system. The susceptibility corresponds to the variance of the particle number of a single randomly occupied site. It must be zero both in the limit of zero and unity filling (no fluctuations in empty or completely filled systems) and symmetric around $\bar{n} = 1/2$.

Simulation

We simulate the dynamics of the SSEP in a system containing 800 sites with open boundary conditions. As an initial state, we choose a far-from-equilibrium density wave at half filling where every second site of the lattice is occupied and every other site is empty (see Fig. 2.2b). In each time step, the position of every particle is updated exactly once and the order in which particles are moved is random. In order to enable a robust statistical analysis of the stochastic dynamics, we run more than 1000 simulations with 2000 time steps. Fig. 2.2c shows the occupation dynamics of a single run. While the initial state is characterized by a regular arrangement of equally spaced particles, the particle distribution quickly randomizes within a few timesteps and and relaxes to an average value of $1/2$. Fig. 2.3a shows the time evolution of the local mean density $\langle n_i(t)\rangle$ measured on a particular site located in the center of the system. It can be seen oscillating first before equilibrating quickly within $t < 10$ timesteps.

At first sight this could suggest that the system thermalizes very quickly and loses memory of the initial state on the same timescale as the local mean density decays. However, if we do not focus on the mean density alone but also take into account the particle fluctuations in the system, a very different picture emerges. The important role of fluctuations can already be surmised from the late-time behavior in Fig. 2.2c, which shows that particles appear to be more likely to bunch up at later times. This means that, if we consider a certain section of the system of length L (cf. Fig. 2.2a), the variance of the particle number (or the fluctuation amplitude) in this section is expected to grow.

Fig. 2.3a also shows the variance of the total particle number $\mathrm{Var}_L(t)$ in subsystems of sizes $L = 2, 4, 6$ sites in the center of the overall system. Intriguingly, while the local mean density equilibrates quickly, the particle number fluctuations relax on much longer timescales. Thus, there is a separation of equilibration timescales between local mean densities and fluctuations which is particularly pronounced in large subsystems. This is due to the finite speed at which density-density correlations can spread through the system, as discussed below. As a consequence, large subsystems take longer to become fully correlated with the environment. The variance is expected to saturate at the value corresponding the maximum possible fluctuations. This coincides with the scenario that the occupation of each of the L sites in the subsystem is random, leading to a saturation variance of $L\chi(\bar{n}) = L/4$.

The slow fluctuation growth can be thought of as a manifestation of the hydrodynamical tail in the density-density correlations discussed in Sec. 2.4. In fact, as shown in Appendix D, the density-density correlations can be calculated from the particle number fluctuations and vice versa. Fig. 2.3b depicts the connected density-density correlations

$$C_d(t) = \langle n_i(t) n_j(t)\rangle - \langle n_i(t)\rangle\langle n_j(t)\rangle, \tag{2.47}$$

for distance $d = |i - j| = 2$ as a function of time. Here, $n_i(t)$ is the occupation of site i. The solid line is a fit to the simulation result using the function $C_2(t) = \alpha\, x^{-\delta} + \gamma$. It yields $\delta = 0.4972(95)$ and, therefore, reveals a correlation decay consistent with $t^{-1/2}$ and the hydrodynamic tail paradigm.

Extracting the diffusion constant

Fig. 2.3c shows the time-evolution of connected density-density correlations C_d for distances up to $d = 55$. The plot reveals a cone with a square-root envelope, suggesting fast equilibration spreading at short times, followed by slower spreading at later times. This is in agreement with our expectation that, due to chaos in the SSEP, the correlation spreading is diffusive, as discussed in Sec. 2.4. The correlations have negative sign (for $0 < d \lesssim 2\sigma(t)$), such that finding an atom on a site implies a reduced probability for finding a second particle at any other distance from that site within the cone. By fitting the cone using Eq. 2.40 we can obtain a value for the diffusion constant. The fit yields $D = 0.722(8)$, consistent with the value $D = 0.724$ obtained from Bethe ansatz calculations [213].

As suggested by Eq. 2.45, we can extract the diffusion constant also from the early time evolution of

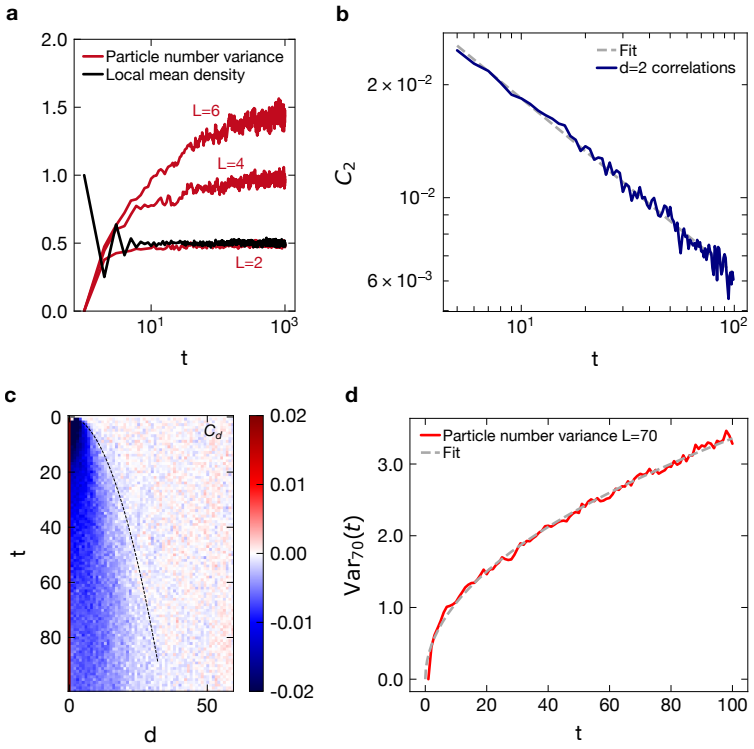

Figure 2.3 | Fluctuating hydrodynamics in the symmetric simple exclusion process. a, While the local mean density on some particular site equilibrates quickly (blue trace), the variance of the total number of particles in a subsystem of length $L = 6$ continues to grow on much longer timescales (red trace). **b**, Density-density correlations at distance $d = 2$ as a function of evolution time. The dashed line is fit to the simulated data, yielding a polynomial decay coefficient of approximately 0.5, indicating a hydrodynamic tail. **c**, The density-density correlations as a function of time and distance $d = |i - j|$ form a diffusive cone with a square-root envelope. The dashed line is the 2σ-envelope of the Gaussian fit (Eq. 2.40) with $\sigma(t) = \sqrt{4Dt}$. **d**, Time-evolution of the particle number variance in a $L = 70$ subsystem. The dashed line is a fit of short-time regime ($t < 100$) using Eq. 2.45.

the particle number variance in a large subsystem. Fig. 2.3d depicts $\mathrm{Var}_{L=70}(t)$ for $t < 100$, revealing a square-root fluctuation growth. Fitting the trace using Eq. 2.45 yields $D = 0.711(2)$, in very good agreement with the value obtained from the density-density correlations.

The diffusion constant (a linear-response transport coefficient) is the only information we need in order to fully describe our system macroscopically using FHD, even in out-of-equilibrium situations. No further knowledge about the details of the SSEP is required as all the microscopic laws are absorbed by the diffusion constant D and the noise term ξ (cf. Eq. 2.29). As discussed in Sec. 2.1, the diffusion constant is generally density-dependent. However, due to the small-spaced density variations in the initial state, the mean density quickly equilibrates to $1/2$ and all fluctuation dynamics unfold on a homogeneous density background.

In this Section, we have invoked the SSEP to illustrate the concepts behind FHD and the capabilities it provides for describing and analyzing chaotic many-body systems. In Chapter 5 we will apply these concepts to a real *quantum* many-body system and investigate whether the FHD description holds even though the microscopic physics are fundamentally different (cf. Sec. 1.7).

CHAPTER 3

Experimental setup

Our experimental apparatus is a novel quantum gas microscope for neutral (bosonic) ^{133}Cs atoms. In this Chapter, we show the characteristics of this element and present the experimental setup. We discuss the tools recently added for studying quantum thermalization in large systems, including a high-NA objective, optical superlattices and a digital micromirror device (DMD).

3.1 Analog quantum simulation using ^{133}Cs

All elements used in utracold atom experiments come with an individual set of states, scattering characteristics and magnetic and optical properties. The question which element is the best choice can only be answered in light of the scientific goals that a particular experiment aims to achieve. Our quantum gas microscope experiment in Munich utilizes bosonic ^{133}Cs, the only stable isotope of cesium. Cesium is an Alkali metal with a single electron in the outer shell, weighs 133 atomic units and its nucleus counts 55 protons. Its long-lived hyperfine ground states are used to define the second in the International System of Units (SI) [214]. It features a large magnetic moment which allows to introduce large Zeeman shifts with relatively small magnetic fields [215].

Choosing ^{133}Cs is motivated by our goal to study the physics of strongly-interacting topological quantum many body systems. When it comes to topology, it is the competition between strong interactions and the filling of topologically non-trivial bandstructures which gives rise to new exotic phases of matter, including fractional Chern insulators (FCIs) [216], topological Kondo insulators [217] and bosonic HOSPT phases [218]. Cesium is believed to be an excellent candidate for quantum simulating these phases: It stands out as the only stable element which combines two important characteristics that are expected to benefit the realization of artificial strongly-interacting topological matter:

- The ability to control the scattering length by means of an external magnetic field, taking advantage of a broad Feshbach resonance at low field. In an optical lattice, this allows to tune the on-site interaction strength U in the Bose-Hubbard model [219].

- The possibility to engineer robust state-dependent lattices that are less prone to heating due to the large hyper-fine splitting in the energetic structure of ^{133}Cs [220]. These state-dependent lattices are expected to allow for engineering robust artificial gauge fields which set the stage for topologically non-trivial quantum Hall physics. [221, 222]

The relatively large mass of ^{133}Cs compared to other popular elements such as lithium or rubidium comes with both advantages and disadvantages. In the following, we will discuss these properties and their implications for quantum simulation experiments in more detail.

Feshbach resonance

Feshbach resonances provide a means to tune the interactions between ultracold atoms. In general, the interaction strength of two cesium atoms depends on the background scattering length a_{bg}, which is set by the s-wave molecular potential depth, a property of the energetic structure of two scattering atoms. In presence of an external magnetic field, the energetic structure is altered due to Zeeman shifts. Whenever, as a consequence of that, the energy of the colliding particles (open channel) gets close to the energy of a bound molecular state (closed channel), the scattering length diverges as described by $a(B) = a_{bg}(1 - \Delta/(B - B_0))$, where B denotes the magnetic field strength. This phenomenon is called a Feshbach resonance at B_0 of width Δ.

Fig. 3.1a shows the scattering length $a(B)$ as a function of the magnetic field strength for the absolute ground state $|F = 3, m_F = 3\rangle$ of ^{133}Cs as well as for $|F = 3, m_F = 2\rangle$ and mixed pairs thereof [223, 224]. These states are important candidates for realizing two-component systems with tunable interspecies interactions which, for instance, allow to implement the Heisenberg XXZ model [225]. The behavior of the scattering length in the low-field regime (between 0 G and 100 G) is dominated by a very broad Feshbach resonance at −11.7 G [226] with a zero-crossing of the scattering length at 17.12 G [227]. At this field the atoms become non-interacting. Additional (narrow) resonances are located at, for instance, 19.84 G and 47.97 G [228]. While, in principle, the Feshbach resonance allows us to tune the scattering length within a large range exceeding $[-1000\, a_0, 1000\, a_0]$, care must be taken as three-body collisions can occur and, as a consequence, the lifetime of the system is diminished. Inelastic two-body processes are forbidden in $|F = 3, m_F = 3\rangle$. In contrast, the three-body loss rate scales with a^4 and is affected by so-called Efimov resonances [229], leading to an overall three-body-loss minimum at around 21 G [230]. For instance, tuning the field close to this minimum is important for producing a ^{133}Cs Bose-Einstein condensate [82].

Besides harnessing the $|F, m_F\rangle = |3, 3\rangle$ and $|3, 2\rangle$ states as spin states for two-component systems, other more common choices are $|3, 3\rangle$ and $|4, 3\rangle$ [231, 232] or $|3, 3\rangle$ and $|4, 4\rangle$ [233]. Here, however, the tunability of interactions is more restricted, as the scattering lengths for $|4, 4\rangle \leftrightarrow |4, 4\rangle$, $|4, 3\rangle \leftrightarrow |4, 3\rangle$ and $|3, 3\rangle \leftrightarrow |4, 4\rangle$ are roughly constant with values $2860\, a_0$, $\approx 1300\, a_0$ (weak dependence on the magnetic field below 40 G) [223] and, $2500\, a_0$ [234] respectively.

Energetic structure and large hyperfine splitting

The most important transitions in the energetic structure of ^{133}Cs are depicted in the inset of Fig. 3.1b. The D1 line connects the ground state $6s_{1/2}$ with the $6p_{1/2}$ state at $\lambda_{\mathrm{D1}} = 894$ nm and the D2 line connects the ground state with the $6p_{3/2}$ state at $\lambda_{\mathrm{D2}} = 852$ nm [215]. The only transitions featuring a shorter visible wavelength are $6s_{1/2} \leftrightarrow 7p_{1/2}$ and $6s_{1/2} \leftrightarrow 7p_{3/2}$ at 459 nm and 456 nm (blue) , respectively [235]. The most common transition used for imaging is the (closed) D2 line at $\lambda = 852$ nm. In principle, using the (open) blue transitions would mean a better resolution in diffraction-limited imaging setups. However, efforts in this direction have so far been unsuccessful, probably due to the presence of multiple decay paths via intermediate states and the enhanced heating resulting from that [236].

One of the main features of ^{133}Cs is the large hyperfine-splitting of 42 nm, particularly in comparison with lighter Alkali atoms such as lithium, sodium and rubidium [237–239]. This characteristic is useful for engineering state-dependent lattices, which emerge, e.g., when the lattice light is circularly polarized and if its wavelength matches the so-called antimagic wavelength λ_{AM} located between the D1 line and the D2 line. Here, atoms in two different m_F-states (denoted $|\uparrow\rangle$ and $|\downarrow\rangle$, respectively) experience the lattice potential with equal amplitude but opposite sign (see Fig. 3.1b). The exact value of λ_{AM} depends on the chirality of the light and the magnetic moment of the state. Importantly, due to the large hyper-fine splitting in ^{133}Cs, the off-resonant scattering rate $\Gamma_{\mathrm{sc}} \sim \Delta^{-1}$ remains low. Thus, heating is suppressed, increasing the accessible timescales of quantum simulation experiments.

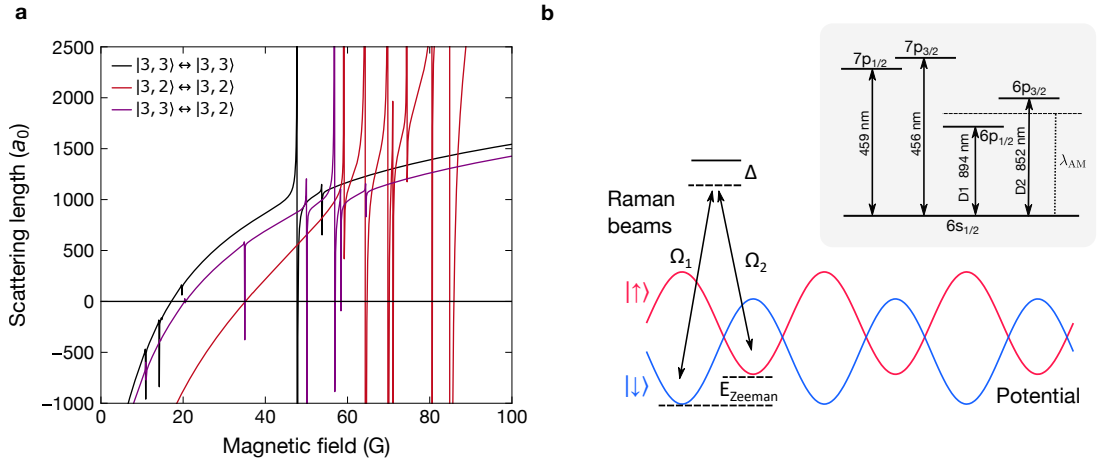

Figure 3.1 | ^{133}Cs **for quantum simulation experiments.** **a**, A broad low-field Feshbach resonance allows to widely tune the scattering rate using a magnetic field, here shown for pairs of atoms in the absolute ground state $|F = 3, m_F = 3\rangle$, in $|F = 3, m_F = 2\rangle$ and for mixed pairs of these two states (data taken from Refs. [223, 224]). **b**, Illustration of a state-dependent lattice potential realized at the anti-magic wavelength λ_{AM} (located between the D1 and the D2 line). The inset depicts an energy level diagram of ^{133}Cs, highlighting the most important transitions in the visible and near-infrared range as well as the anti-magic wavelength.

Aligned with the original goal of our experiment, state-dependent lattices are expected to facilitate the realization of artificial gauge fields in a way that is more robust to heating [220] compared to previously implemented schemes [65, 240]. The main ingredient for realizing artificial gauge fields is restoring the tunnelling between adjacent lattice sites of opposite spin (suppressed by the necessity to flip the spin) using a two-photon Raman process (Raman assisted tunnelling). The detuning of the two Raman beams must match the energy offset between the $|\uparrow\rangle$-lattice and the $|\downarrow\rangle$-lattice which is given by the Zeeman shift. This shift is on the order of MHz and, thus, very different from the other energy scales of the lattice potential in the kHz regime. I is the decoupling of these energy scales that mitigates parametric heating in presence of the artificial gauge field and is expected to pose a significant advantage compared to earlier schemes [65, 240].

Large mass

The relatively large mass of ^{133}Cs compared to other Alkali atoms like potassium or rubidium has ambiguous consequences: On the one hand, it allows to achieve larger trap depths with less laser power. This can prove advantageous, e.g., during fluorescence imaging when the atoms need to be pinned in place by a deep three-dimensional lattice potential. It facilitates the collection of more fluorescence photons in a shorter time and makes it easier to achieve a high signal-to-noise ratio. On the other hand, a large mass means smaller tunnel coupling between adjacent sites in an optical lattice. As a consequence, smaller lattice spacings are required to keep the timescale of the quantum dynamics in an experimentally feasible regime. This can pose challenges to single-site resolved imaging, particularly in case of ^{133}Cs where the standard imaging transition (D2 line) has a comparably long wavelength of 852 nm (see Sec. 3.4 for details).

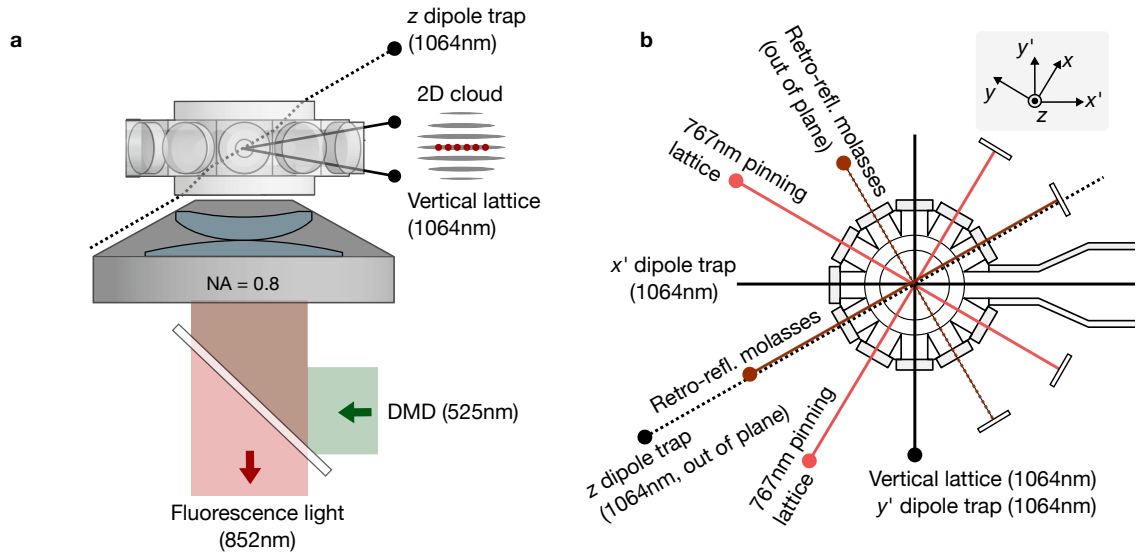

Figure 3.2 | Science chamber overview. Orientation of optical lattices, dipole traps, molasses beams and imaging-related light passing through the science chamber to prepare, manipulate and detect a two-dimensional quantum system of ultracold ^{133}Cs atoms. The dots indicate the direction of origin for each beam. **a**, Side view. **b**, Top view.

3.2 Setup overview

The construction of this experiment started in 2017. For a detailed documentation of the overall vacuum system, the basic laser cooling techniques, transport schemes and BEC production steps, see Refs. [82, 118]. The timing software and hardware in use for controlling the machine as well as magnetic field stabilization methods are described in Ref. [224]. The following Sections will focus on the science chamber and all new ingredients which have been added to prepare large high-quality quantum many-body systems and to perform the thermalization experiments presented in Chapter 5.

Science chamber and objective – The science chamber is a glass cell of a dodecagonal shape (manufactured by *Precision Glassblowing* with nanostructure coating by *TelAztec*). It has eleven small side windows with a diameter of 12 mm and two larger windows with a diameter of 30 mm, one at the top and one at the bottom. Our high-resolution objective (manufactured by *Special Optics*) is characterized by a numerical aperture (NA) of 0.8 and a working distance of 25 mm. It is directly positioned beneath the glass cell and optical access to the atoms is provided by the bottom window, as depicted in Fig. 3.2a. We use the objective both to collect fluorescence photons produced during imaging at the end of the sequence and to project green light (λ_{DMD}) onto the atoms to create programmable potentials with a DMD. The optical setups for imaging and programmable potentials are discussed in Sec. 3.4.

Dipole traps – There are three dipole traps providing harmonic confinement in all directions. The x'- and y'-dipole traps have waist radii measuring 100 µm × 100 µm and 370 µm × 110 µm, respectively. They are arranged orthogonally in the horizontal plane, creating a crossed dipole trap at the center of the glass chamber, where the atoms are situated. The z-dipole trap enters the glass cell under a steep angle of 60° through the top window and closely passes by the objective lens, as shown in Fig. 3.2a. Its waist radius (110 µm × 53 µm) is chosen such that the confinement it provides, when projected into the horizontal plane, is round.

Lattices – In the z-direction we have *shallow-angle* vertical lattice created by two 1064 nm beams which enter the glass cell from the side in y'-direction and interfere under a small half-angle of 4°. The resulting vertical planes are spaced by 8 µm, only one of which is loaded for creating an effectively

two-dimensional quantum system. In the horizontal direction we use two perpendicular retro-reflected superlattices, created by overlapped retro-reflected beams of wavelengths $\lambda_{\text{short}} = 767\,\text{nm}$ (*short lattice*)and $\lambda_{\text{long}} = 1534\,\text{nm}$ (*long lattice*). For more details about the superlattices, see Sec. 3.3.

Molasses for fluorescence imaging – The imaging fluorescence photons are produced as a side product of molasses cooling on the D2-line ($\lambda_{\text{D2}} = 852\,\text{nm}$). The molasses cooling is realized by two retro-reflected near-resonant cooler beams (waist diameter 2 mm) as well as a repumper beam. The first cooler beam enters the glass cell from the same side as the z dipole trap but propagates in the horizontal plane. The second cooler beam enters the glass cell out-of-plane under an angle of 60°, similar to the z dipole trap but from a direction perpendicular to the first cooler beam. The two cooler beams together create a polarization gradient lattice in which Sisyphus cooling takes place. In order to ensure similar scattering rates on all sites in the two-dimensional horizontal lattice, it is crucial to modulate the retro-mirrors and spatially wash out the polarization gradient lattice [241]. More details can be found in Sec. 3.4.

Coils for gradient and offset fields – The glass cell is surrounded by two pairs of x coils, two pairs of y coils and one pair of z coils, each of which can be operated in either Helmholtz or anti-Helmholtz-configuration for generating offset and gradient fields at the position of the atoms. In addition, the experimental table is located inside a coil cage that is used for compensating environmental magnetic field fluctuations. The coil setup and the active magnetic field stabilization are not discussed in this thesis but more information can be found in Ref. [224].

Microwave – We have a microwave horn pointing at the glass cell for driving transitions between the $F = 3$ and $F = 4$ ground state manifolds at $\approx 9.192\,\text{GHz}$. The electronics built for generating and controlling the microwave radiation are described in Ref. [224].

3.3 Optical superlattices

Superlattices realize a periodic potential with two frequency components (called *long* and *short*) that differ by a factor of two, as depicted in the inset of Fig. 3.3. This leads to a periodic double well structure featuring two tunnel couplings J_{dw} and J_{long} that occur in alternation. Further, there can be an energy offset Δ between the left and the right side of each double well. The three parameters J_{dw}, J_{long}, Δ depend on the depths of the short and the long lattices as well as the relative phase ϕ between the two lattice potentials.

Our superlattice is created by overlapping a $\lambda_{\text{short}} = 767\,\text{nm}$ lattice beam with a $\lambda_{\text{long}} = 1534\,\text{nm}$ lattice beam and retro-reflecting both. The choice of these wavelengths is, on the one hand, motivated by the good availability of lasers. On the other hand, choosing a small wavelength of $\lambda_{\text{short}} = 767\,\text{nm}$ makes sense keeping in mind that ^{133}Cs is a relatively heavy element and a lower tunnelling rate. However, in order be able to observe system dynamics on long timescales, large tunnel couplings are required to lower the system's susceptibility to heating and disorder. Thus, small lattice spacings are generally preferable as long as they can still be resolved by the imaging setup.

The superlattice setup in vicinity of the science chamber is shown in Fig. 3.3. In each of the two perpendicular lattice axes in x- and y-direction, the light for the long and the short lattice is supplied by separate fibers from the preparation table (see Sec. 3.4) and is intensity-stabilized independently. Shortly before entering the science chamber the two beams are overlapped using a dichroic mirror. Lenses before and after the glass cell (in front of the common retro-mirror) ensure that the vertical beam waist radius of both the incoming beams and the retro-reflected beams at the position of the atoms is 140 μm.

Initial alignment of the short lattice beams is achieved by first coarse-aligning the beam through the science chamber by eye. Subsequently, we block the retro-mirror and load the atoms into the compressed y-dipole trap after BEC production and subject them to a brief pulse. Scanning the pointing of the lattice beam then allows to observe how the cloud is pushed away from the dipole trap center.

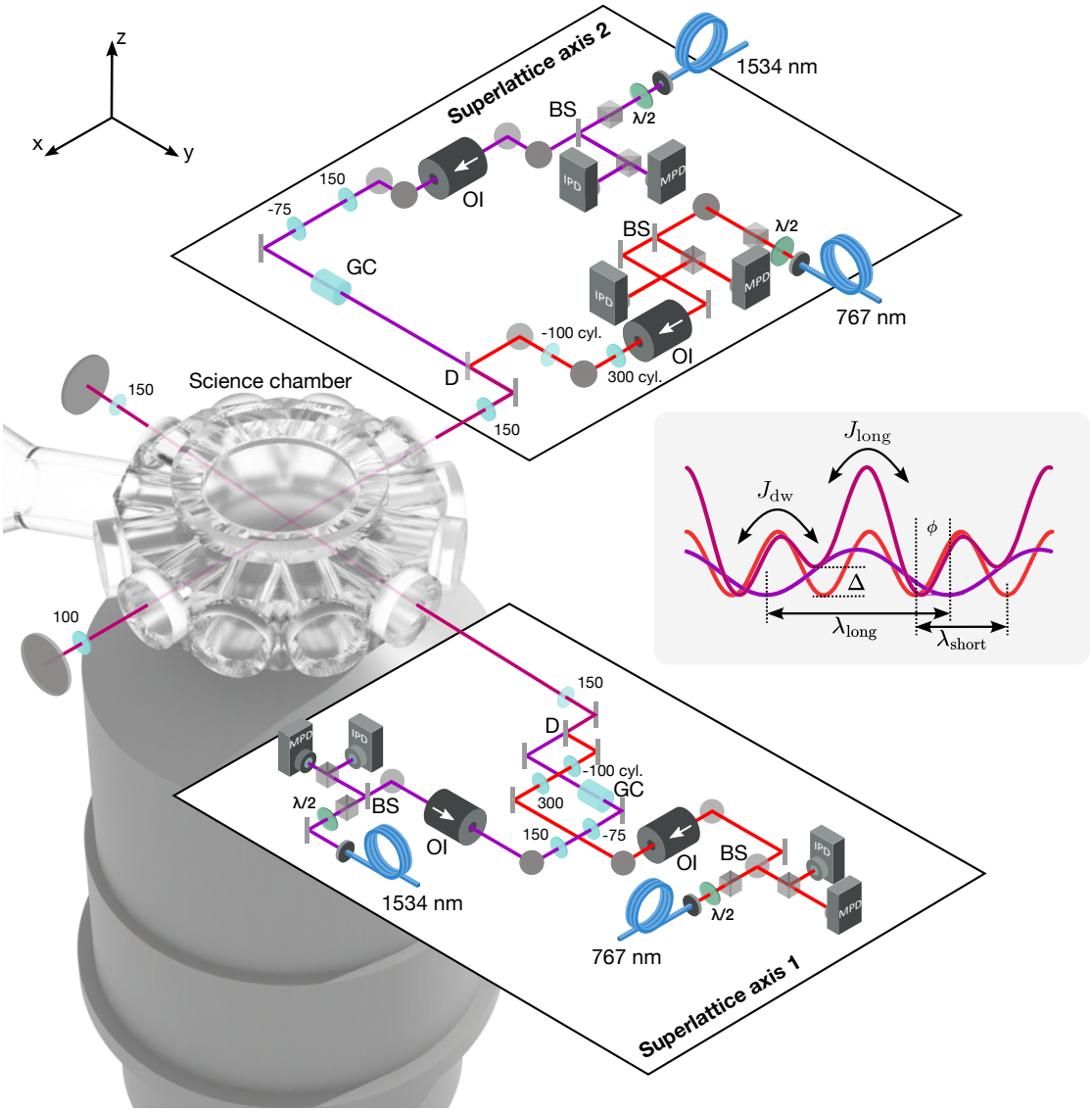

Figure 3.3 | Optics setup for realizing superlattice potentials. Each of the two perpendicular superlattices is generated by overlapping two beams of wavelengths differing by a factor of 2 ($\lambda_{\mathrm{short}} = 767\,\mathrm{nm}$ and $\lambda_{\mathrm{long}} = 1534\,\mathrm{nm}$). The common beam bath starts at a dichroic before science chamber and is retro-reflected by a multi-wavelength mirror on the opposite site. The setup includes lenses (blue), waveplates (green), mirrors and polarizing beam splitters (grey), dichroic mirrors (D), beam samplers (BS), optical isolators (OI), photo diodes for monitoring (MPD) and stabilizing the intensity of the lattice light (IPD). The focal lengths of all lenses are given in millimeters. Glass cylinders (GC) in the long lattice beam paths allow to tune the angle between the short and the long lattice at the position of the atoms in the science chamber. **Inset**: Resulting superlattice potential characterized by a double well structure with two tunnelling strengths J_{dw}, J_{long}. The tilt of the double well Δ can be adjusted by tuning the superlattice phase φ.

Using this signal, we can center the beam on the atomic cloud. Next, we unblock the retro and try to observe a Bragg diffraction signal which is used to optimize the alignment of the retro-mirror. After that, we perform a parametric heating scan to confirm that the alignment is good (cf. Sec. 4.8). Once the short lattices are aligned, we overlap the long lattice beams with the short lattice beams at two points after the dichroic. We usually place a temporary mirror somewhere between the dichroic and the

last lens before the glass cell and reflect both lattice beams out. This way we can let them propagate for several meters and pick two points very far away from each other for the overlapping procedure. In order to overlap the beams as precisely as possible, we use a *Wincam* beam profiling camera that is sensitive to both 767 nm and 1534 nm light. After multiple iterations of optimizing the overlap at the first and the second point in alternation, the long lattice should be aligned. We confirm that with a parametric heating scan (cf. Sec 4.8).

In order to achieve an excellent superlattice potential quality it is crucial to ensure good overlapping along the entire common beam bath after the dichroic. Initial alignment can lead to a situation where the beams are well overlapped at the position of the atoms but cross there under a small non-zero angle. This leads to a tilt gradient of the double wells perpendicular to the direction of the lattice [242]. In order to correct for that, a rotatable glass cylinder is placed before the dichroic in the beam path of the long lattice. By rotating this glass cylinder in the horizontal plane we can adjust the angle under which the long and short lattice cross at the position of the atom and tune it to zero (see Sec. 4.9 for details).

Note that the short lattice is used for both physics and pinning during fluorescence imaging, while the long lattice is used for physics only. The maximum power delivered to the atoms is about 3 W in the short lattice and 300 mW in the long lattice, leading to maximum depths of 400 μK and 4 μK, respectively. Thus, only the short lattice is deep enough to keep the atoms in place during the fluorescence imaging process (cf. Sec. 3.4).

Stabilizing the superlattice phase

The superlattice phase is geometrically fixed by the position of the retro-mirror. Thus, the most feasible way of controlling the superlattice phase is changing the frequency of either the short or the long lattice light. We choose to adjust the long lattice frequency, as this leaves the position of the sites in the short lattice (which acts as the pinning lattice during fluorescence imaging) untouched and does not further complicate reconstruction efforts (cf. Sec. 4.3). Let $\Delta\nu = \nu_{\text{long}} - 0.5\nu_{\text{short}}$ be the difference between the frequency of the long lattice and half the frequency of the short lattice. Then, the superlattice phase at distance L from the retro-mirror reads:

$$\phi = \frac{2\pi L}{c}\Delta\nu \tag{3.1}$$

The further the retro-mirror is placed away from the atoms, the more sensitive the superlattice phase is to the frequency of the lattice light. In our case $L_x = 200\,\text{nm}$ and $L_y = 300\,\text{nm}$ in the two lattice axes, such that a superlattice phase rotation of π corresponds to a frequency change of approximately 750 MHz and 500 MHz in ν_{long}, respectively.

The short lattice light is generated by two 8W TiSa laser (*Sirah Matisse + Spectra Physics Millenia eV*), one for each axis. The long lattice light ($\lambda_{\text{short}} = 1534\,\text{nm}$) comes from a *NKT Boostik + Adjustik* system in one axis and from a *Nufern* Amplifier + *Rio* Seed combination in the other axis. The setup for preparing the lattice light is shown in Fig. 3.4. In order to control and stabilize the superlattice phase we employ a frequency-offset-lock: A portion of the short lattice light ($\lambda_{\text{short}} = 767\,\text{nm}$) is combined with a small amount of frequency-doubled long lattice light ($\lambda_{\text{short}} = 1534\,\text{nm}$). The resulting beat note is detected by an ultrafast photodiode (*Thorlabs DX12CF*), amplified twice (*Kuhne KU0180A*) and delivered to a servo (*Vescent D2-135*). The servo compares the beat note frequency to a reference signal from a DDS board and computes a feedback voltage. The feedback controls the piezo of the laser seeding the 1534 nm-amplifier, modulating the frequency of the long lattice light. The superlattice phase is, therefore, stabilized to the reference and can be controlled by the DDS board. The DDS board is programmed to output a frequency that is proportional to an analog voltage signal with a conversion factor of 1.6 GHz/V after a frequency multiplier. The inset in Fig. 3.4 shows a typical beat note spectrum when the superlattice phase is stabilized by the lock. From the FWHM of the beat note (170(3) kHz)

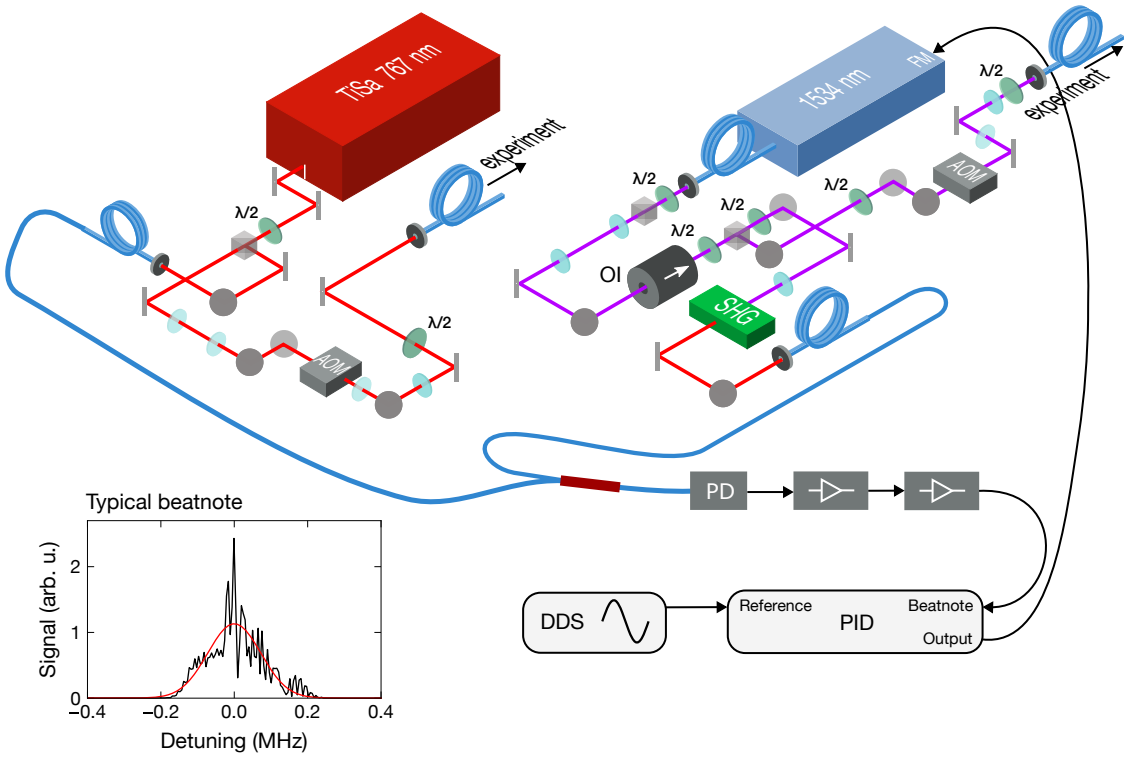

Figure 3.4 | **Superlattice phase stabilization.** In order to stabilize the relative phase between the short lattice ($\lambda_{\text{short}} = 767\,\text{nm}$) and the long lattice ($\lambda_{\text{short}} = 1534\,\text{nm}$), we use a frequency-offset-lock based on beating a small fraction of the short lattice light with a small amount of frequency-doubled long lattice light. The frequency doubling is realized using second harmonic generation (SHG) in a nonlinear crystal. The beat note is amplified twice and supplied to a PID controller which compares the beat note to a reference signal and computes a response voltage. The latter modulates the frequency of the long lattice laser which alters the phase of the superlattice. Optical elements are labelled as in Fig. 3.3. **Inset**: Typical beat note spectrum (black) fitted using a Gaussian (red). The FWHM is 170(3) kHz, corresponding to a phase noise amplitude of approximately 1 mrad.

and Eq. 3.1 we can conclude that the superlattice phase fluctuations are on the order of 1 mrad. That is about one order of magnitude smaller compared to the situation when the lock is not engaged.

The maximum rate $\Delta\phi/\Delta t$ at which the superlattice phase adapts in response to controlled ramps of the reference frequency is about $\pi/500\,\text{ms}$, limited by the PID. We can accelerate that to about $\pi/6\,\text{ms}$ taking advantage of the feed forward input of the servo lock, which allows to directly modulate the piezo. If the voltage applied to the feed forward input is chosen such that the superlattice phase is already very close to its target value (the lock point), the lock stabilizes within a few milliseconds and does not have to slowly adjust the servo output until the lock point is reached.

3.4 Fluorescence imaging and potential shaping

Fluorescence imaging in optical lattices usually requires to pin the atoms in place while producing fluorescence photons. Pinning is achieved by ramping up the depths of the optical lattices in all spatial directions to the highest possible values. This ensures that when the atoms heat up during the imaging process, they do not hop to other lattice sites, as this would compromise the image. Fluorescence

photons are usually produced as a side product of a laser cooling process (either Raman sideband cooling or molasses cooling) which aims to counteract the heating during imaging [58].

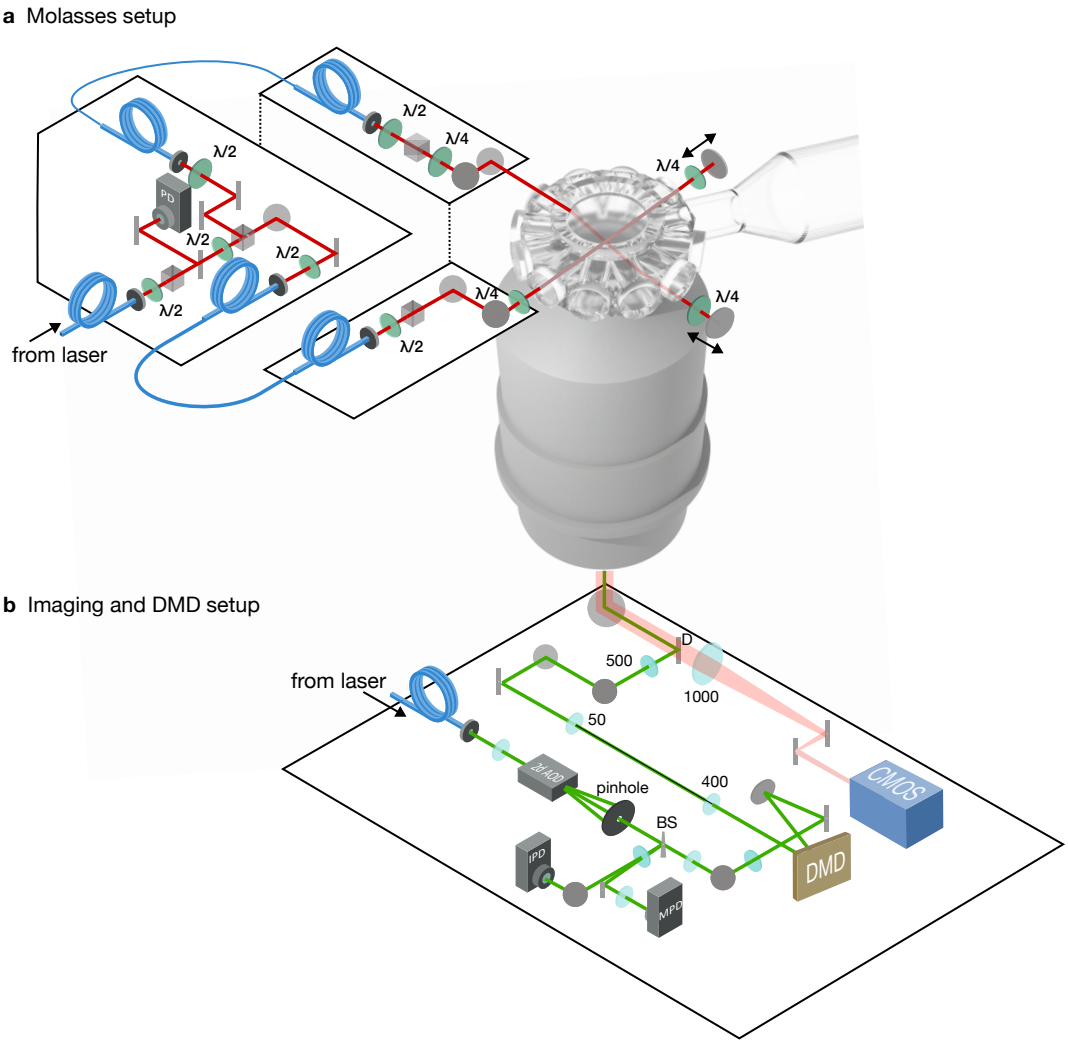

Figure 3.5 | Setups for fluorescence imaging and programmable potentials.. **a**, Molasses cooling setup. The fluorescence photons are generated as a side product of molasses cooling on the D2 line, turned on while the atoms are pinned in the short optical lattice. Two roughly perpendicular retro-reflected molasses beams enter the science chamber through the horizontal and vertical viewports. The light originates from the D2 cooling laser in the basic laser setup (see [82] for details). All optical elements are labelled as in Fig. 3.3. **b** The fluorescence photons are collected by the high-NA objective located underneath the science chamber and focused on a CMOS camera. The objective is also used to project green 525 nm light controlled by a DMD into the atom plane for realizing programmable potentials.

Imaging setup

The imaging setup is located underneath the science chamber, as shown in Fig. 3.5b. Its purpose is to focus the fluorescence photons collected by the high-resolution objective onto a CMOS camera (*Teledyne Photometrics Kinetix*). This is achieved by a $f = 1000\,\text{mm}$ tube lens (*Thorlabs ACT508-1000-B*, 2 in diameter) which, together with the working distance of the objective (25 mm), leads to a magnification of about 40. This means that the actual area of a lattice site ($383.5\,\text{nm} \times 383.5\,\text{nm}$) in the atom plane

corresponds to an area of (15.3 μm × 15.3 μm) on the camera chip. The camera has a pixel size of 6.5 μm, i.e. each lattice site is mapped onto 5.5 camera pixels. The alignment procedure for the objective is described in detail in [82, 243]. It makes use of a reference beam that is aligned with the atoms and perpendicular to the vertical windows of the science chamber.

DMD

Besides for collecting fluorescence photons coming from the atoms, we also use the objective for projecting green light ($\lambda_{\mathrm{DMD}} = 525\,\mathrm{nm}$) into the atom plane. This light is overlapped with the fluorescence imaging path via a custom dichroic (manufactured by *Optoman*) in the Fourier plane between the objective and the tube lens. One of the mirrors in this path is a DMD (model *Texas Instruments DLP6500*, interfaced by *bbs Bild- und Lichtsysteme GmbH*). The mask displayed on the chip is demagnified by a factor of 160 and imaged into the atom plane. This allows us to shape the green beam and create custom potentials for the atoms. In order to minimize wavefront errors due to deformation of the optics, all mirrors have been glued to their mounts. The last lens in the DMD path before the dichroic is mounted on a picomotor-controlled stage for convenient focusing. Initial alignment of the DMD is achieved by overlapping the green light in the DMD path with the reference beam (set up for aligning the objective, see Ref. [82]) along the entire distance between the dichroic mirror and the DMD. Assuming that the distance between the optics in DMD setup is correct according to the specified focal lengths, this pre-alignment is sufficient for observing a push-away movement of the atoms when projecting a large illuminated box with ca. 200 mW of green light. For focusing we ask the DMD to project a distinct shape onto the atoms, e.g. a box of reasonable size. We choose a large dense atom cloud, such as the BEC after single plane loading, so that we can observe the interaction between the atoms and the DMD potential over a large area. Next, we adjust the position of the last lens in the DMD setup before the dichroic to move the focus into the atom plane. The closer we are to the focus, the sharper the features of the mask in the atom density become (e.g. the edges of the box). For fine-alignment of the DMD, see Sec. 4.6.

For smooth custom potentials in the atom plane it is important to reduce the spatial coherence of the green light as much as possible in order to prevent potential corrugations due to speckles [244]. A common way to achieve that is to use superluminescent laser diodess (SLDs) a light source which feature a broad spectral width. However, these diodes have not been available for wavelengths $< 670\,\mathrm{nm}$. Shorter wavelengths are preferred for this application as they provide a better resolution and maximize the sharpness of the potential's features in the atom plane. Thus, instead of an SLD, we use a multimode laser outputting 5 W of $\lambda = 525\,\mathrm{nm}$ light (*Wavespectrum WSLX- 525-005-400M-H*). This laser not only has a broad spectrum (15 nm width) but also provides a large amount of power, eliminating the need for further amplification stages. The temporal incoherence of this light is converted into spatial incoherence by means of a square core fiber (150 μm core size) [245] which guides the light from the laser to the experiment table depicted in Fig. 3.5. Using a square core fiber (as compared to using no fiber) improves the speckle contrast from 15 % to 7 %. For further reduction of the speckle contrast the setup includes a two-dimensional acusto-optic deflector (AOD) after which only the (1, 1)-order passes through a beam block and propagates to the DMD. It allows us to wiggle the pointing of the beam at very large frequencies up to 1 MHz, much faster than any relevant atomic energy scales. This washes out any remaining speckles and reduces the speckle contrast to < 1 %. For more details about the DMD including calibration and alignment techniques, see Sec. 4.6 or Ref. [246].

Molasses cooling

The atoms are imaged by performing molasses cooling with circularly polarized light on the D2 line at $\lambda_{\mathrm{D2}} = 852\,\mathrm{nm}$, similar to [241], and collecting the fluorescence photons using the high-NA objective which is positioned underneath the class cell. The molasses light is generated by the basic laser setup

discussed in Ref. [82]. The cooler beams are red detuned by 78 MHz with respect to the ($F = 4 \leftrightarrow F' = 5$)-transition and the repumper beam is resonant with the ($F = 3 \leftrightarrow F' = 4$)-transition. As shown in Fig. 4.3a, the cooler light is split up in two paths for the two retro-reflected cooler beams that are approximately perpendicular to each other. One lies in the horizontal plane and enters the glass cell under an angle of 30° with respect to the x' transport axis (cf. Sec. 3.2). The other is 60° out-of-plane and passes through the top and bottom windows of the glass cell. There used to be a third molasses beam propagating like the second one but entering through the top window from the opposite side. However, it was removed after we found that the fluorescence signal is more homogeneous without it. The repumper beam (not shown) co-propagates with the x'-dipole trap (cf. Sec. 3.2).

The polarization of the cooler light is controlled by the $\lambda/4$-plates before and after the glass cell. In theory, the polarization of the incoming beam and the retro-beam should be right-handed and left-handed circular, respectively. Further, the cooling scheme requires zero magnetic field, such that all environmental fields need to be compensated within a range of approximately 200 mG. The interference of the two cooler beams creates a polarization gradient lattice which drives a Sisyphus cooling process. However, since this lattice is not commensurate with the pinning lattice, the scattering rate is spatially modulated, leading to visible fringes in the fluorescence image [241] (see Sec. 4.4). In order to wash these fringes out, the retro-mirrors of the two cooler beams are mounted on piezos with a travel range of about 3 μm. Their position is modulated at prime number frequencies around 100 Hz, typically 97 Hz and 149 Hz which is fast compared to the typical exposure time of 300 ms. In addition to the piezo modulation, the frequency of the cooler beams is also modulated, typically with an amplitude of 14% of the detuning and with a frequency of 50 Hz. For more details and optimization procedures, see Sec. 4.4.

CHAPTER 4

Calibration, preparation and measurement techniques

This Chapter summarizes all preparatory steps for the thermalization measurements presented in Chapter 5. It includes calibration and optimization procedures concerning the superlattices, the programmable DMD potential and the imaging. The corresponding setups and basic alignment procedures are introduced in Chapter 3. Here, we focus on fine-alignment techniques and characterization methods and, further, discuss the initial state preparation.

4.1 Initial state preparation

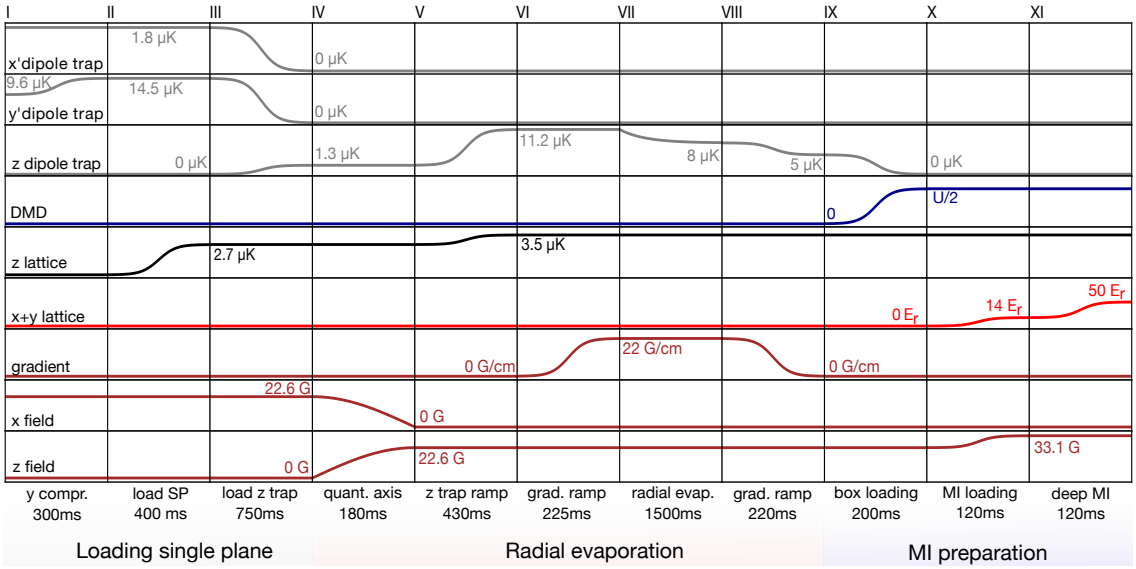

Figure 4.1 | Experimental sequence for preparing initial product states. Starting from a BEC in a dipole trap (not discussed here), we load the atoms into a single plane of the shallow vertical lattice. Next, we perform radial evaporation using a gradient field and load a box potential with wall height $U/2$, generated by a DMD. Finally, the Mott insulator is prepared by adiabatically ramping up the horizontal lattices.

Starting point for the quantum simulation experiments in this work is a two-dimensional Mott insulator product state in a box potential. This Section is about the experimental sequence that takes us from the BEC to this initial state (see Fig. 4.1). The steps explained below can be grouped in three

stages: (I-III) loading the BEC into a single plane of the vertical lattice, (IV-VIII) performing evaporation cooling to obtain a superfluid in a box, and (IX-XI) converting the superfluid into a high-quality Mott insulator. Preceding parts of the overall sequence responsible for the BEC production are not discussed here, see [82, 118, 224] for details.

The BEC is confined in the crossed dipole trap (created by two 1064 nm beams in x' and y' direction, see Fig. 3.2). The first step towards preparing a Mott insulator is to load the BEC into a single plane of the vertical lattice and create a quasi-2d system. We start by compressing the atoms vertically by ramping up the y' dipole trap power (I), followed by a ramp-up of the vertical lattice (II), see Fig. 4.1. The y'-trap compression is necessary in order to ensure that the vertical size of the atom cloud becomes sufficiently small such that only one plane of the vertical lattice is loaded (efficiency $> 95\%$). Next, the z dipole trap is turned on while the crossed dipole trap is turned off, switching to roughly isotropic harmonic confinement in the horizontal plane. This is important in order to perform efficient radial evaporation cooling using a magnetic gradient in the next step.

In preparation for applying a gradient force in the x-y-plane, we rotate the quantization axis from vertical to horizontal (IV) and further ramp up the z dipole trap and the vertical lattice (V). Just like during BEC production, the magnetic field strength is kept constant at 22.6 G which is the three-body-loss minimum of ^{133}Cs (cf. Sec. 3.1). We found that the best cooling results are achieved by first ramping up the gradient field to a value that just falls short of pulling atoms out of the trap (VI), followed by a long exponentially decreasing ramp of the z dipole trap power (VII) which allows only the hottest atoms to escape. The evaporation process is ended by ramping the gradient back down to zero and reducing the z dipole trap depth to a lower value (VIII). We now have a cold superfluid in the z dipole trap. Provided that most atoms have been loaded into a single plane in step (II), any small fraction of atoms in other planes will be cooled less efficiently and escape the trap during evaporation. This is due to a reduced thermalization rate in low density clouds.

As a last step, we turn the two-dimensional superfluid into a Mott insulator state: We first replace the horizontal harmonic confinement of the z dipole trap with a box potential provided by the DMD (IX). Typically, the region inside the box is 50×50 sites large and fully surrounded by a wall of 10 sites thickness. The wall height is $U/2$ at the inner edge of the box and decreases outwards with a typical slope of $U/24\,\mu$m. Here, U is the on-site interaction strength in the 2d lattice potential that is activated in the next step. The lattice depths are ramped up in two segments, such that $U/J = 16$ after the first ramp (X) and $U/J > 50$ after the second ramp (IX), where J is the nearest-neighbor tunnelling strength in the lattice. This ensures that the SF-to-MI phase transition is crossed slowly, avoiding heating. Since the maximum wall height of the box potential was chosen to match $U/2$, the interactions force any excessive atoms to spill out of the box, making the Mott insulator more robust to atom number fluctuations (cf Sec. 4.5) [15]. Simultaneously with the first ramp (IX), we also increase the scattering length from $280a_0$ to $580a_0$ by ramping up the offset field to 33.1 G. In doing so, we increase U and become less sensitive to temperature and residual harmonic confinement.

The result of this sequence is a Mott insulator in the 2d short horizontal square lattice as shown in Fig. 4.2a. The total cycle time of the experiment up to this point is ca. 18 s. We typically achieve a size of up to 60×60 sites and an average filling of 98%. Note that instead of ramping up the two short lattices, we can also produce Mott insulating states in either the long lattices only (Fig. 4.2c, filling up to $\sim 85\%$) or in a rectangular lattice potential with one axis being short and the other one being long (Fig. 4.2b, filling up to $\sim 90\%$). The latter configuration means that, from the perspective of the short lattice, only every second row is occupied, corresponding to a charge density wave (CDW) with a period of two sites. This state will play an important role in the thermalization measurements in Chapter 5. Further, using the DMD in combination with stripe potentials that are projected into the atom plane during Mott insulator preparation, we can prepare CDWs of larger period and in arbitrary directions. For instance, Fig. 4.2b shows a 11001100-CDW aligned with the x axis (filling up to $\sim 85\%$). Note that

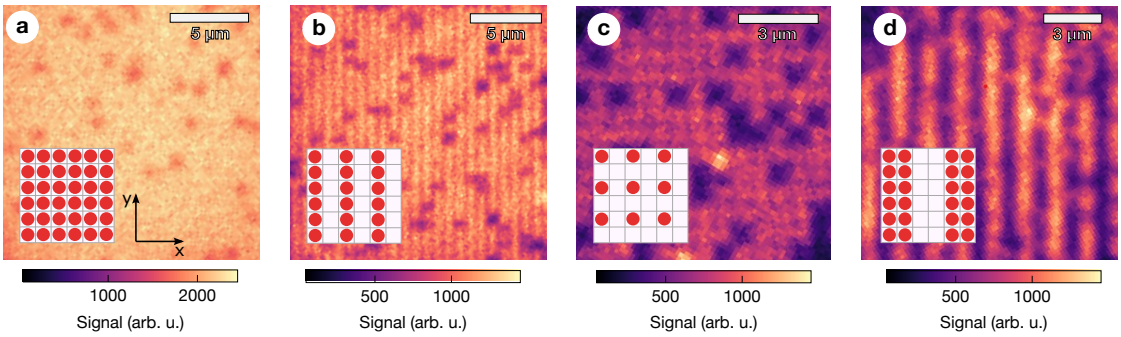

Figure 4.2 | **Initial product states. a**, Mott insulator in a short-short lattice configuration with a spacing of 383.5 nm in both *x* and *y* direction. **b**, Mott insulator in a long-short lattice configuration, consisting of a tilted superlattice in *x* direction and a simple lattice in *y* direction. We also refer to this state as a 101010 charge density wave (CDW). **c**, Mott insulator in a long-long configuration with 767 nm spacing in both *x* an *y* direction. **d** A 11001100 charge density wave (CDW) created using simple lattices with spacing 383.5 nm in *x* and *y* direction, combined with a stripy DMD potential which prevents the occupation of every second pair of columns.

in lattices involving larger spacings than $\lambda_{\mathrm{short}} = 383.5\,\mathrm{nm}$, the on-site interactions are generally weaker. This can lower the efficiency of the spilling process and the Mott insulator becomes more susceptible to atom number fluctuations and temperature. Further, the target density in Mott insulators in long lattices can be very different from the initial density distribution before loading the box, requiring more mass transport and possibly causing more heating.

4.2 Fluorescence imaging characterization

Experimental sequence

In order to read out the final state of the quantum simulation experiment we quench the horizontal short lattices to the highest possible powers, typically close to 3 W in each lattice. Simultaneously, the vertical lattice power is quenched to approximately 13 W, such that the potential depth in all directions reaches $\approx 400\,\mu\mathrm{K}$. This pins the atoms in place and projects the many-body wave function into the local Fock basis of each individual lattice site. About 10 ms after pinning, we turn on compensation fields in all spatial directions in order to ensure that the overall field strength of the atoms is zero within typically 50 mG, a condition required for molasses cooling. Due to the vicinity of an ion pump to the glass cell, the compensation field strengths are typically on the order of 100 mG. The cooling process and the production of fluorescence photons is then initiated by turning on the cooler beam and the repumper beam at the same time. A brief moment after that (typically a few milliseconds) we begin exposing the camera chip to the fluorescence light, taking the actual image. The piezos shifting the molasses retro-mirrors and washing out the polarization gradient lattice for better signal homogeneity are always on. In addition, the detuning of the cooler beam is modulated (cf. Sec. 4.4). The optimal cooler detuning typically lies between 70 MHz and 80 MHz with about 3 mW of power in each beam. The repumper power typically does not exceed 500 µW. The exposure time is 300 ms. Following the exposure, the lattices and the molasses beams are turned off. The sequence is completed, the machine is reset and a new run can be started.

Point spread function (PSF)

In order to characterize the resolution of our imaging system, we take several hundred images of very dilute clouds, such that the probability of finding two atoms close to each other is very low (see Fig. 4.3). We cut quadratic crops with exactly one atom in the center (orange region in Fig. 4.3a). By averaging over these crops, we obtain the mean signal of an individual atom which corresponds to the PSF of the imaging system (see Fig. 4.3b). We then fit the radial profile of the PSF using an Airy disk profile and obtain $r \approx 850\,\mathrm{nm}$ for the resolution of our imaging system, according to the Rayleigh criterion. This is almost 30% larger than the diffraction limit $r = 1.22\,\lambda_{D2}/(2\,\mathrm{NA}) \approx 650\,\mathrm{nm}$ that we expect from our high-resolution objective (NA=0.8) and our imaging wavelength of $\lambda_{D2} = 852\,\mathrm{nm}$. One possible reason could be insufficient confinement in the vertical direction during imaging, leading to a significant part of the atomic wave function getting imaged out-of-focus. We are planning to improve the resolution in the near future, as mentioned in the Outlook.

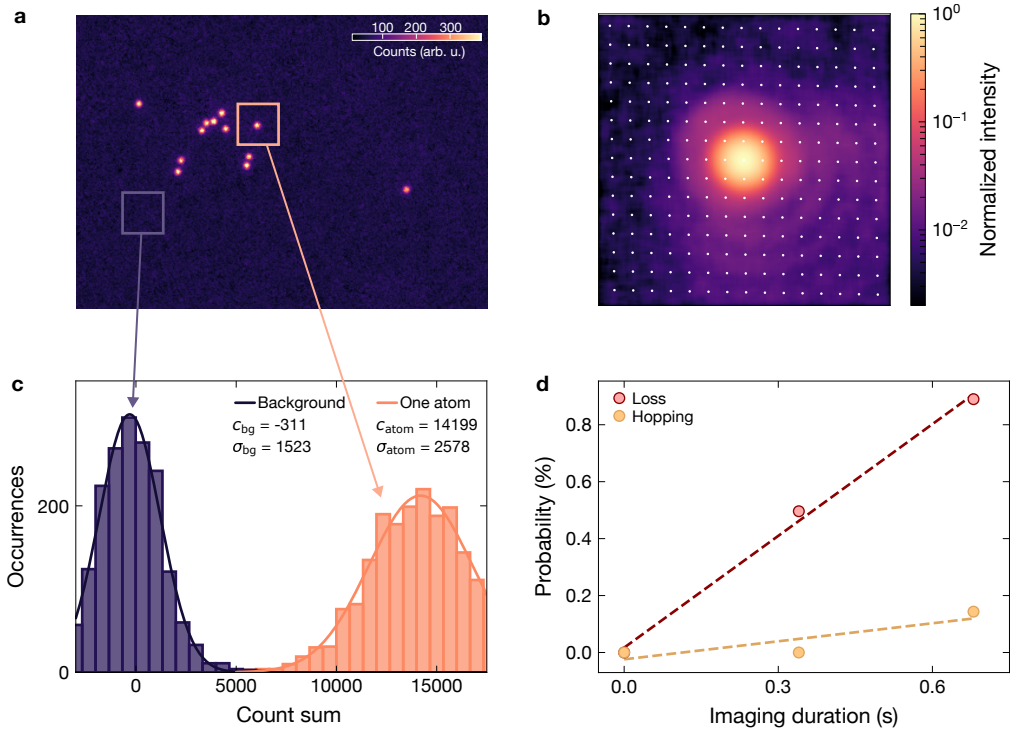

Figure 4.3 | Fluorescence imaging characterization. a, Fluorescence image of a dilute cloud of atoms. Each atom appears as the PSF of the imaging system. We cut quadratic crops containing exactly one atom in the center (orange) and crops containing no atoms (violet) for obtaining an averaged PSF and performing signal count statistics. **b**, Mean fluorescence signal of a single atom averaged over ca. 2000 crops. The intensity has been normalized with respect to the maximum signal at the symmetry point of the PSF. The white dots mark the lattice sites in the short lattice with a spacing of 383.5 nm. **c**, Histogram of total fluorescence signal counts in empty background crops (violet) and crops containing exactly one atom (orange). By fitting both peaks with a Gaussian and obtaining the mean and the variance of the background counts and the atom counts, we can compute the signal-to-noise ratio (SNR) as defined in Eq. 4.1. Negative counts occur since we first subtract the mean background signal from all fluorescence images. **d**, Probability that an atom hops to a different site or is lost entirely, as a function of the fluorescence imaging exposure time. Dashed lines are linear fits to the experimental data for extracting the hopping rate and the loss rate.

Signal-to-noise ratio (SNR)

Dilute clouds as shown in Fig. 4.3a are also suitable for extracting the signal-to-noise ratio (SNR) in our images. The SNR is defined as

$$\mathrm{SNR} = \frac{c_{\mathrm{atom}} - c_{\mathrm{bg}}}{\sigma_{\mathrm{atom}} + \sigma_{\mathrm{bg}}}, \tag{4.1}$$

where c_{atom} and σ_{atom} are the mean and the variance of the fluorescence signal counts of a single atom, respectively. Analogously, c_{bg} and σ_{bg} denote the mean and the variance of the background counts. Experimentally, the fluorescence signal of the atoms is influenced by the exposure time, the molasses parameters (which affect the rate of scattered photons) as well as the NA and the optics in the imaging setup (cf. Sec. 3.4). Due to residual fringes in the intensity of the molasses light, the strength of the fluorescence signal will spatially vary, increasing σ_{atom}. Further, the noise characteristics of the camera chip as well as stray light from the molasses beams can increase c_{bg} and σ_{bg}.

In addition to cutting crops containing single atoms which we have used to characterize the PSF (Fig. 4.3b), we also cut crops containing no atoms (violet region in Fig. 4.3a) to characterize the background. Fig. 3.4c shows the histogram of signal counts detected in both the background and the single atom crops. Fitting the peaks using a Gaussian yields c_{atom}, σ_{atom}, c_{bg} and σ_{bg} and, using Eq. 4.1, allows to determine the SNR. For an exposure time of 300 ms we get a SNR of 5.2. As pointed out in Sec. 4.3, we rely on a comparatively high SNR in order for the reconstruction algorithm to work with high fidelity.

Loss and hopping rate

During imaging, the atoms heat up and acquire an equilibrium temperature on the order of several 10 μK, depending on the efficiency of the molasses cooling process. At the same time, the depth of our pinning lattice is approximately 400 μK. Thus, we expect a small but non-zero probability that an atom performs thermal hopping during the exposure time, decreasing the integrity of the fluorescence image. The rate of this process is described by the Arrhenius law $\Gamma_{\mathrm{h}} = \Gamma_{\mathrm{a}} \mathrm{erfc}\left(\sqrt{V_{\mathrm{latt}}/k_B T}\right)$, where Γ_a is an experimentally or theoretically obtained constant, V_{latt} is the depth of the pinning lattice and T is the equilibrium temperature of the atoms during molasses cooling [247, 248]. In order to keep Γ_{h} low, it is important to either cool efficiently to smaller T or to increase the depth of the pinning lattice and suppress the hopping process. In case a very weak signal and a small SNR can be tolerated, another option would be to reduce the exposure time to values much smaller than $1/\Gamma_{\mathrm{h}}$. In addition to hopping processes, atoms can also get lost entirely due to collision events with residual gas particles in the vacuum.

In order to measure the hopping and loss rates in our setup, we take four images of the same dilute cloud (as shown in Fig. 4.3a) in quick succession and track the movement of the atoms from image to image. Fig. 4.3d shows what fraction of atoms in the first image has moved away from its original position in the later images (but is still detected somewhere on the image) and what fraction of atoms has vanished entirely, as a function of exposure time. Here, the first image (reference) corresponds to zero exposure time. Fitting the slope of the linear probability growth yields a hopping rate of $\gamma_{\mathrm{hopp}} = 2.1(1.2)$ mHz and a loss rate of $\gamma_{\mathrm{loss}} = 13(1)$ mHz, comparable to other state-of-the-art experiments [147]. This means that during our typical exposure time of 300 ms, about 0.5% of atoms either hop or get lost. Note that atoms which undergo hopping over distances larger than the region of interest (ROI) or in out-of-plane direction of the vertical lattice are also counted as loss events. This might explain why the measured loss rate is more than seven times larger than the measured hopping rate.

4.3 Machine-learning based reconstruction algorithm

As pointed out in Sec. 3.3, achieving large tunnel couplings with a heavy element like ^{133}Cs requires short-spaced optical lattices. The spacing of the short lattices (which also serve as pinning lattices during imaging) is just $a_{\mathrm{short}} = \lambda_{\mathrm{short}}/2 = 383.5\,\mathrm{nm}$. This is more than a factor of two smaller than the resolution of our imaging system $r \approx 850\,\mathrm{nm}$, as described by the ratio $\beta = r/a_{\mathrm{short}} \approx 2.2$, and puts us in a challenging resolution regime: The ratio β in other quantum gas experiments typically does not exceed 1.6 [241]. Existing reconstruction algorithms, such as threshold reconstruction or Richardson-Lucy deconvolution, fail to provide us with a state-of-the-art imaging fidelity that is necessary for obtaining high-quality data within a reasonable amount of time. Thus, we have developed a new reconstruction method, opting for a machine-learning driven approach. In the following, we will briefly discuss the main ideas of this novel algorithm. For more details, see Refs. [83, 249].

Idea and implementation

The algorithm is based on a convolutional neural network embedded in an autoencoder architecture, as visualized in Fig. 4.4a. The input consists of a 16×16 sites snippet of an experimental fluorescence image which has been rescaled to match the exact size of 256×256 pixels. The image is first processed by the encoder part of the network consisting of three convolutional layers: Each layer down-samples the image and reduces the number of pixels by a factor of 4 down to a size of just 16×16 pixels, exactly as many pixels as there are lattice sites in the image. The step-wise reduction of pixels is implemented using learnable kernels that sweep across the image and serve as a blueprint for how pixel values in the previous image combine into the fewer number of pixels in the next image. The encoder part is followed by the bottleneck: Here, a binarization step is carried out, i.e. all pixel values above a threshold are set to 1 and all other pixel values are set to 0. Finally, the image gets upsampled again by the decoder part of the network which inversely mirrors the encoder. It reverses the down-sampling until the image has acquired its original size of 256×256 pixels (output image).

During training, the network is asked to minimize the difference between the output image and the input image. This means that the kernels in the convolutional and deconvolutional layers are adjusted until the output side of the network reproduces the original image. Because of the special structure of the network all image information is forced through the bottleneck between the encoder and the decoder part. The idea here is that the 16×16 binary matrix at the bottleneck *must* contain the minimal information required to recover the original image on the output side; and this minimal information can only be the occupation of the 16×16 lattice sites.

Importantly, training is unsupervised, i.e. it does not require any simulated fluorescence images for which the true occupation is known. This avoids the necessity to include more sophisticated imaging phenomena, including density-dependent effects like superradiance, in the simulation. Instead, the training data consist of experimental fluorescence images which depict random homogeneous lattice fillings ranging from zero to one. They are created by first preparing an $n = 1$ Mott insulator (cf. Sec. 4.1), followed by the random removal of a variable fraction of atoms in the Mott plateau using microwave and blowout pulses.

After training, only the encoder part and the bottleneck are needed for reconstructing new images that were not part of the training data. The occupation, i.e. the result of the reconstruction algorithm, is then read off from the binary bottleneck matrix. To get insight into decision-making process of the network, we can plot the histogram of deconvoluted counts just before the binarization step, as depicted in Fig. 4.4b, showing two peaks. The left (right) peak corresponds to the unoccupied (occupied) sites which get assigned negative (positive) deconvoluted pixel values by the trained network. The threshold should be adjusted to the value that separates the two peaks best. Any overlap region of the two peaks means that even for the best threshold choice the overall fidelity of the algorithm is reduced.

The reconstruction is carried our for all remaining 16×16-sites snippets, until all lattice sites in the fluorescence image have been reconstructed, as shown in Fig. 4.4c.

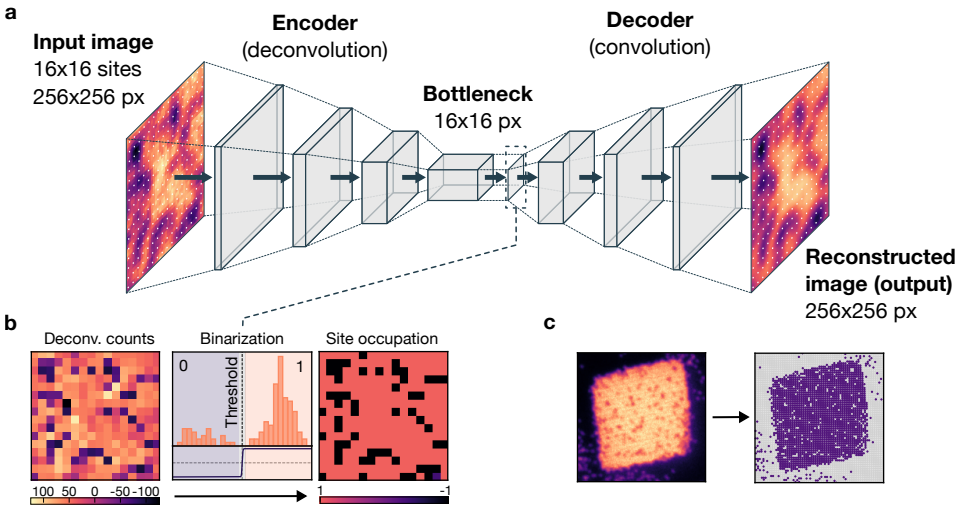

Figure 4.4 | Autoencoder-type convolutional neural network for high-fidelity reconstruction in challenging resolution regimes. a, Network structure consisting of an encoder part, a bottleneck and a decoder part. The encoder part downsamples the input image (showing 16×16 lattice sites) to a small image of just 16×16 pixels. The decoder part upsamples it back to the original size at the output. The network is trained to make the output image replicate the input image, forcing all image information through the low-dimensional bottle neck, which, consequently, must store direct information about the occupation of the lattice sites. **b**, Threshold binarization in the bottleneck. The downsampled pixel values are set to zero and one, based on a carefully chosen threshold that aims at separating the two peaks in the bimodal distribution of the pixel count histogram before the binarization. **c**, Combining the reconstruction results of all 16×16 lattice sites snippets, we obtain th reconstruction result of an entire fluorescence image.

Reconstruction fidelity estimation

The reconstruction fidelity is defined as the fraction of correctly determined site occupations. Its is limited by the finite SNR of the fluorescence image (noise). In addition, there are systematic errors resulting from a spatially varying signal strength in the image (molasses fringes, large number of atoms in other planes of the vertical lattice showing up as a blurry background). Also, the reconstruction algorithm could be internally biased due ro reasons rooted in its structure and its way of functioning. Lastly, while not a matter of the reconstruction algorithm itself, the integrity of the reconstruction result also relies on low thermal hopping and atom loss rates during imaging.

In general, the true occupation of the lattice sites in the fluorescence images is unknown. Thus, there is no direct way of assessing the reconstruction performance. Testing the algorithm with simulated images can be an option but might lead to conclusions that do not translate to real images. That is because it is challenging to write a simulation which takes all imaging effects into account, such as density-dependent superradiance which is particularly relevant in our β-regime. Instead, we rely on two indirect methods for estimating the reconstruction fidelity from the reconstruction result:

- **Histogram of deconvoluted counts**: We can estimate the fidelity from the histogram of deconvoluted pixel counts obtained from the bottleneck before binarization (Fig. 4.4b). Here, the presence of a bimodal distribution indicates distinguishability between empty and occupied sites,

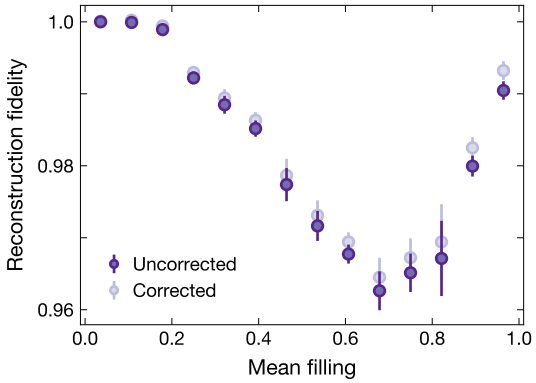

Figure 4.5 | Reconstruction fidelity estimated from comparative multi-imaging. Fidelity as a function of the mean filling in the fluorescence image, showing near-optimal performance for dilute clouds and Mott insulator states and at least 96% fidelity in all other filling ranges. Dark markers assume that there is no hopping and loss during imaging, while the bright markers take these effects into account via a calibrated probability $p_\delta(n)$ (cf. Eq. 4.2).

and the level of distinguishability (and, therefore, the fidelity) is related to the overlap area of the two peaks: The fidelity can be defined as $\mathcal{F} = 1 - (A_0 \bigcap A_1)/(A_0 \bigcup A_1)$, where A_0 and A_1 are the areas of the left (unoccupied sites) and right (occupied sites) peak, respectively. In practice, the reconstruction process is highly non-linear and the shape of the peaks in the histogram is not known. This complicates efforts to quantify the peak areas and determine the fidelity. Assuming that the peaks are Gaussian, however, we obtain a filling-depending fidelity of $\mathcal{F} \gtrsim 99\%$ with the smallest value at half filling.

- **Comparative multi-imaging**: Another way to estimate the reconstruction fidelity is to take two images of the same atom distribution and compare the reconstruction results. Under perfect conditions (infinite SNR, no thermal hopping), sites which are classified as empty or occupied in the first image should also be classified as empty and occupied in the second image. However, due to different random noise and due to hopping and loss events during or in between the exposures, different reconstruction results can emerge. Let δ denote the measurable probability that a site is classified differently in the second image compared to the first one. Then the reconstruction fidelity can be estimated from

$$\mathcal{F} = \frac{1}{2}\left(1 + \sqrt{\frac{1-2\delta}{1-2\,p_\delta(n)}}\right). \tag{4.2}$$

Here, $p_\delta(n)$ is the filling-dependent probability that occupation differences emerge due to non-zero hopping and loss rates (see Appendix B for a derivation). The latter can be calibrated independently, as shown in Sec. 4.2. Fig. 4.5 shows the estimated reconstruction fidelity as a function of the mean filling in the fluorescence image, both with ($p_\delta(n) \neq 0$) and without ($p_\delta(n) = 0$) the correction for hopping and loss events. We find that the reconstruction algorithm performs the worst at intermediate fillings ($\bar{n} \approx 0.7$) with a fidelity of about 96%. In contrast, for near-unity filling or dilute clouds the fidelity approaches 1.

In conclusion, we have estimated a reconstruction fidelity exceeding 96% at all fillings, indicating that the performance of our imaging setup is comparable to that of other experiments in the field [83] and sufficient for performing state-of-the-art quantum simulation experiments. Both methods are expected to be mostly sensitive to random noise and the SNR rather than systematic errors. We are aware that some of the errors in the reconstruction result ($\lesssim 1 - \mathcal{F}$) are of a systematic kind, showing

up as unphysical density-density correlations in the data. This small artefact and the question how it can be corrected is addressed in Sec. 6.4.

4.4 Molasses optimization

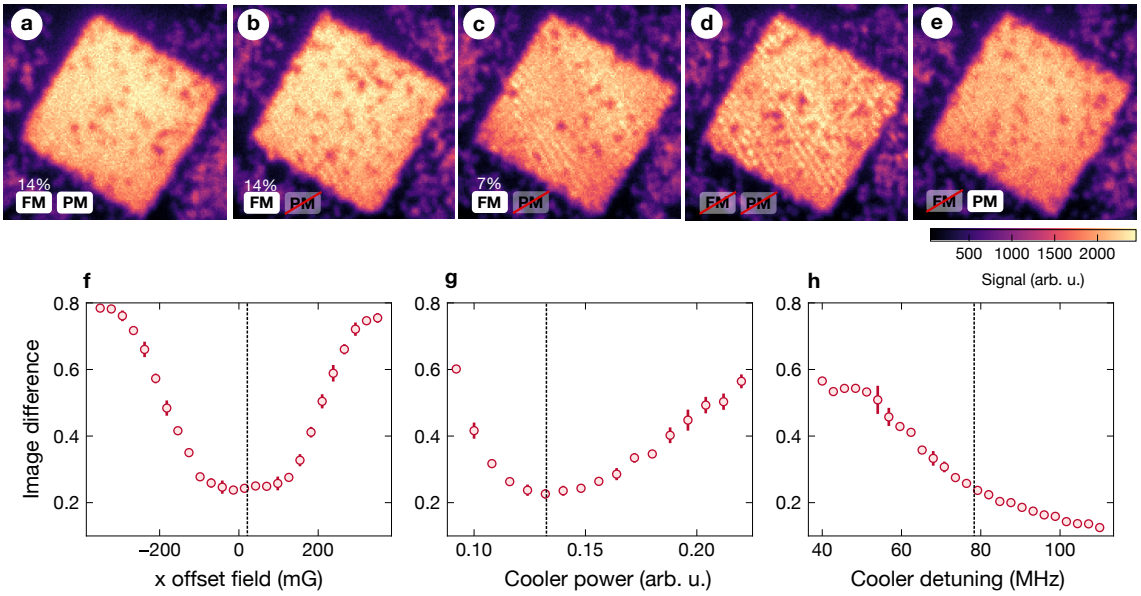

Figure 4.6 | **Molasses optimization. a-e**, Raw fluorescence images of an $n = 1$ Mott insulator, taken for different combinations and strengths of molasses modulation: spatially via piezo (PM) and in frequency (FM). If either modulation type is turned off, undesirable fringes appear in the image. **f-h**, Normalized difference between the first and and the second image of the same atom distribution (as defined in Eq. 4.3), taken ca. 600 ms apart, as a function of important molasses parameters: the compensation field (molasses power and detuning fixed at 0.13 and 78 MHz, respectively), the molasses beam power (offset field and detuning fixed at 50 mG and 78 MHz, respectively) and the cooler detuning (offset field and molasses beam power fixed at 50 mG and 0.13, respectively).

Piezo and frequency modulation

The cooling process relies on a polarization gradient lattice created by the molasses beams. This lattice is not commensurate with the pinning lattice, leading to a spatial variation of the scattering rate which appear as fringes in the imaging signal (Fig. 4.6d). In order to remove these fringes, we modulate the phase of the polarization gradient lattice using both the position of the retro-mirrors which are mounted on piezos (piezo modulation or PM) and the frequency of the molasses beams (FM). The peak-to-peak amplitude of the frequency modulation is usually set to 14% of the cooler detuning (typically between 70 MHz and 80 MHz), a value that has been found to be a good compromise between removing most of the fringes effectively without compromising the cooling by altering the detuning to much (Fig. 4.6b). The modulation frequency is 50 Hz. However, in order to remove the fringes entirely, frequency modulation needs to be combined with piezo modulation (Fig. 4.6a). The PM amplitude is chosen such that the retro-mirrors move by several microns, more than the wavelength of the polarization gradient lattice. Both molasses beams are piezo modulated and the modulation frequencies are prime numbers in the 100 Hz − 200 Hz range, faster than the exposure time during

fluorescence imaging. Note that in our two-molasses-beam configuration both modulation types need to be turned on at the same time in order to effectively remove the fringes. In an earlier version of the molasses setup with three beams, piezo modulation alone was sufficient.

Optimization of the cooling parameters

In order to optimize the molasses parameters (i.e. compensation field strength, polarization, cooler detuning, cooler power and repumper power), we prepare an n=1 Mott insulator (cf. Sec. 4.1) and minimize the number of defects in the density plateau after long imaging times. Here, we assume that these defects are predominantly caused by hopping during the image process as a consequence of suboptimal molasses settings. In particular, we compare multiple images of the same atom number distribution, taken in succession. The same method is used to quantitatively determine the hopping and loss rates in our system, see Sec. 4.3 for more details.

Fig. 4.6(f-h) shows typical optimization scans for the most important molasses parameters: the offset field, cooler beam power and the cooler detuning. Here, we take two images of the same atom distribution about 600 ms apart, each of which has an exposure time of 300 ms. Between the two images the pinning lattices and cooler beams are kept on. Let S_1 and S_2 be the total fluorescence signal in the first and the second image, respectively. Then, we can define the normalized difference between the two images as:

$$\mathrm{Diff} = \frac{S_1 - S_2}{S_1}. \tag{4.3}$$

The idea is that for optimal molasses parameters the difference between the two images is minimal, leading to similar fluorescence signals, as loss and hopping events are suppressed. Fig. 4.6f shows the image difference as a function of the x compensation field strength with a clear minimum at ca. 10 mG. The data was taken with the detuning value and the cooler power value indicated by dashed lines in Fig. 4.6(g-h). The minimum is a broad plateau with a width of ca. 200 mG, meaning that the molasses cooling process can tolerate environmental field changes up to an absolute strength of ca. 100 mG. Scans of the compensation fields in other directions look very similar (not shown). The optimization of the cooler power (Fig. 4.6g) and the detuning (Fig. 4.6h) is closely coupled as a larger detuning can, to some extent, be traded in for a higher cooler power and vice versa. In general, for a fixed detuning we find an optimum cooler power. In contrast, for a fixed cooler power, the optimal detuning seems to be outside the measurement range, suggesting that very large detunings are the best choice (Fig. 4.6h). However, larger detunings reduce the fluorescence signal and, as a consequence, the SNR. Thus, as a compromise between optimal cooling and a decent SNR obtained within a reasonable exposure time, we typically settle at a moderate detuning of 78 MHz. Increasing the power to very large values at very large detuning or reducing the power to small values at small detunings was not found to improve the overall cooling performance.

The same optimization technique was also used to optimize the repumper power as well as the polarization of the molasses beams which is controlled by the $\lambda/4$-plates in the beam path (cf. Fig.. 4.3). The cooling efficiency appears to be very insensitive to the repumper power as long as the power is sufficiently large, typically on the order of a few 100 μW. Optimizing the rotation angles of the waveplates empirically using the image difference signal did not lead to a configuration consistent with the theoretically ideal circular polarization. Instead, we operate with an uncharacterized elliptical polarization that has proven to work best.

4.5 Mott insulator optimization

Sequence considerations

Obtaining a high-quality Mott insulator plateau requires careful optimization of the field, gradient and lattice ramps that make up the sequence discussed in Sec. 4.1. The list below provides the most important optimization knobs which are most likely to make a difference. Note these clues apply to all Mott insulator initial states that can be prepared in the final part of the sequence (cf. Sec. 4.1 and Fig. 4.2), not only to the short-short Mott insulator with unity filling in the short lattice.

- **BEC quality**: The larger the BEC is, the more cold atoms remain after radial evaporation and the more (colder) atoms are available for filling the box and forming a Mott insulator. We typically work with a BEC of at least 10000 atoms (ideally 20000) visible after 75 ms time-of-flight (with levitation on). Atom number below this threshold can lead to unstable conditions dominated by atom number fluctuations which translate to filling fluctuations in the Mott insulator plateau.

- **Single plane loading**: If the atoms are distributed among multiple planes, the atom density in the central plane can be insufficient for efficient thermalization during evaporation, leading to atom loss. Further, too many atoms in adjacent planes appear as background artefacts on the fluorescence images, rendering reconstruction impossible. In order to make sure that only a single plane is loaded, we either use matter-wave-focussing techniques [82, 250, 251] in the vertical direction with absorption imaging or optimize on the absence of background artefacts in the fluorescence images directly.

- **Offset field**: Success of both the BEC production and the radial evaporation is very sensitive to the strength of the offset field. On the one hand, the field strength needs to be close to the three-body-loss minimum (cf. Sec. 3.1) at ca. 21 G [230]. On the other hand, larger offset fields increase the interaction strength and, therefore, the thermalization speed during evaporation. Thus, for best results, a compromise between these two opposing trends needs to be found. For the Mott insulator preparation, i.e. at a point during the lattice ramps when the probability of finding more than two atoms on the same site is already very low, we increase the scattering length to a value far higher than the three-body-loss minimum, leading to a larger on-site interaction strength U. This makes the Mott insulator more robust against finite temperature and potential corrugations.

- **Gradient strength and z dipole trap depth**: We found that a better Mott insulator quality is achieved when performing radial evaporation with an initially deep z dipole trap (providing strong harmonic confinement) and a large horizontal gradient rather than a weak gradient in combination with a shallow z dipole trap.

- **Ramp durations**: We have carefully optimized all ramp durations in the sequence using the mean filling of the $n = 1$ Mott insulator plateau as an observable. Besides the exponential evaporation ramp of the z dipole trap, the ramp durations in steps (III), (IX) and (XI) (see Fig. 4.1) have the highest impact on the final Mott insulator quality, as they implement the transfer of atoms from one trap to another. In general, the ramp durations are chosen as short as possible in order to avoid heating and as long as necessary to ensure the adiabaticity of the transfer and loading operations.

- **Trap overlapping**: The quality of the Mott insulator is affected by how well the box potential is aligned horizontally with the trap center of the vertical lattice. Further, the z dipole trap needs to be aligned with the DMD box and all horizontal lattices need to be horizontally aligned with the position of the compressed cloud in the y' dipole trap at the end of step (I) in Fig. 4.1. When

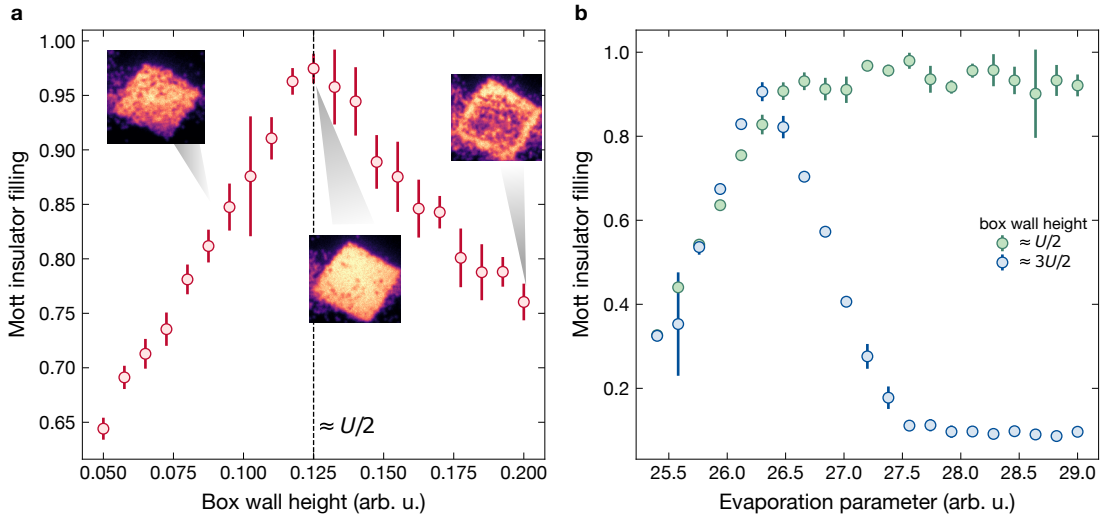

Figure 4.7 | Calibrating the box potential height for spilling. a, Filling inside the box potential versus height of the box wall averaged over five fluorescence images. If the box potential is too low, too many atoms escape. If the box potential is too high, excessive atoms cannot escape and form doublons which become holes during imaging. At the optimal point in between, where the wall height roughly matches $U/2$, spilling occurs in such a way that only excessive atoms leave the box, leading to a high-quality $n = 1$ Mott insulator. Error bars denote the standard deviation. **b** Filling inside the box potential as function of the final z trap power controlling the amount of atoms left after evaporation, averaged over five fluorescence images. If spilling is not working (because the DMD walls are too high, e.g. $3U/2$), the atom number needs to be just right in order to achieve a high-quality Mott insulator plateau. If, however, spilling is working (wall height $U/2$), variable (but not too high) amounts of excessive atoms leave the box without creating doublons, making the Mott insulator very robust against atom number fluctuations. Error bars denote the standard deviation.

pre-aligning the lattices using push sequences, one should work with the cloud in the compressed y'-dipole trap, as emphasized in Sec. 3.3.

- **Thermal hopping during imaging**: Even a perfect Mott insulator with near-unity filling can appear suboptimal due to detection issues. Hopping and loss events during fluorescence imaging cause holes in the $n = 1$ plateau and doublons which appear as empty sites due to parity projection. In order to check whether the hopping and loss rates during imaging are sufficiently low, we use the multi-imaging method outlined in Sec. 3.4.

- **Spilling**: For excessive atoms to spill out during Mott insulator preparation, the wall height of the box potential needs to be set to roughly $U/2$. This trick is crucial for making the Mott insulator robust against atom number fluctuations, as detailed below.

Spilling

One of the most helpful tricks for obtaining large robust high-quality $n = 1$ density plateaus is preparing a Mott insulator in a box potential and choosing the wall height of the box to match $U/2$ [15]. This allows excessive atoms to spill out of the box due to the on-site interaction energy, while only those required to form the $n = 1$ Mott insulator phase remain. In order to find the optimal wall height, we prepare a Mott insulator in a box but use the final power of the z dipole trap to set the chemical potential to a high value leading to more atoms in the box than there are available lattice sites (ca. 50×50 sites). Then, we observe the Mott insulator density plateau filling as a function of the DMD light intensity which controls the wall height of the box potential, as shown in Fig. 4.7a. We find that, on the one hand,

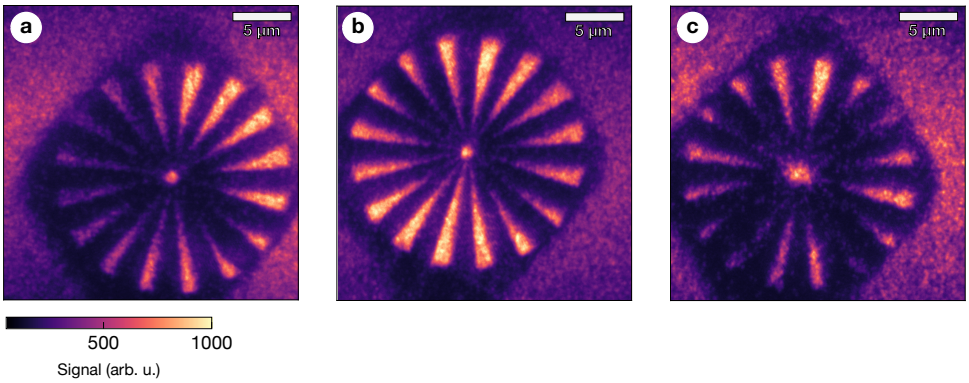

Figure 4.8 | Siemens star for fine-aligning the DMD. Average of 10 fluorescence images of a BEC in a single plane of the vertical lattice in presence of the Siemens star mask projected onto the atoms using the DMD. **a**, After initial alignment of the DMD imaging system with aberrations. **b**, After fine-alignment (walking the DMD imaging path) leading to reduced aberrations. **c**, Out-of-focus.

if the wall height is too low, too many atoms leave the box and the number of atoms is insufficient to fill all lattice sites. On the other hand, if the box wall is too high, too many atoms are trapped in the box leading to doubly occupied sites which, due to parity projection, appear as holes in the fluorescence image. If, however, the wall height is just right, the atoms that spill out of the box are those which do not find any remaining free lattice sites. This is because it is energetically more favorable to leave the box rather than paying interaction energy U by occupying an already occupied site.

The robustness resulting from spilling is demonstrated in Fig. 4.7b: Here, we show the filling inside the box as a function of the evaporation parameter that controls the atom number loaded into the box. One finds that if the wall height is too large, the filling is very sensitive to the atom number and one needs to carefully optimize the final power of the z dipole trap in order to achieve a high quality Mott insulator. However, if the box potential is set to $U/2$ (corresponding to the maximum in Fig. 4.7a), the mean filling of the box is always excellent, provided that the number of loaded atoms is sufficiently high. This makes the initial state preparation robust to atom number fluctuations caused by fluctuations in earlier parts of the sequence and leads to better data quality.

4.6 Potential flattening for large system sizes

DMD alignment optimization

After pre-aligning the DMD (see Sec. 3.4), fine-adjustments are necessary to ensure that the projection of the DMD mask on the atoms is free of aberrations. If a bright box is projected onto the atoms and not all four edges of the box appear sharp simultaneously, the DMD image in the atom plane is probably aberrated by astigmatism. This means that the DMD light is not perfectly aligned with the optical axis of the objective or that there are aberrations caused by the DMD imaging optics. For sensing the direction and the strength of the aberrations we project a Siemens star mask on the atoms. It consists of radially symmetric stripes that narrow down to zero in the center. The idea is that, depending on the resolution of the DMD imaging system, the stripes are only visible up to a certain distance away from the center, which decreases with better resolution. The presence of non-isotropic aberrations like astigmatism leads to certain stripes extending closer to the center than others, indicating an angular dependence of the resolution.

Fig. 4.8 shows mean fluorescence signals of a Siemens star projected into the atom plane (BEC in a single plane of the vertical lattice), averaged over ten images. After initial alignment of the DMD, we typically measure an atom distribution as shown in Fig. 4.8a which clearly suggests that there is a resolution gradient in the horizontal direction. In order to optimize the alignment of the DMD imaging system with respect to the optical axis of the objective, we walk the DMD light in the direction of this gradient using the last two mirrors before the dichroic mirror in the DMD setup (cf. Fig. 4.3). The last mirror is adjusted, such that the projected Siemens star moves in the direction of the aberrations and the second-last mirror is adjusted to move the Siemens star back to the trap center of the single plane in the vertical lattice. After each walking iteration we take a new averaged image of the projected Siemens star and eventually find a much more symmetric density pattern, as shown in Fig. 4.8b. Note that the intensity of individual stripes can also be influenced by the location of the Siemens star pattern with respect to the trap center where the atom bulk is located. This is why one should always move the Siemens star roughly back to the horizontal center of the single plane potential such that averaged images after individual iterations are comparable. The Siemens target can also be used to focus the DMD imaging system: If not focused properly, the projection of the star in the atom plane appears fragmented, as shown in Fig. 4.8c.

Pixel mapping

By default, any mask on the DMD chip will show up distorted in the atom plane. This is due to the fact that, in order to reflect the light in the right direction, the surface of the DMD chip is both rotated and tilted with respect to the optical axis of the DMD imaging system. Thus, precise controlling of custom repulsive potentials in the atom plane requires mapping the pixels of the DMD to the coordinates in the atom plane. This mapping can be approximately described by a linear transformation:

$$\begin{pmatrix} x \\ y \end{pmatrix}_{\text{cam}} = \begin{pmatrix} A_{xx} & A_{xy} \\ A_{yy} & A_{yy} \end{pmatrix} \begin{pmatrix} x \\ y \end{pmatrix}_{\text{DMD}} + \begin{pmatrix} C_x \\ C_y \end{pmatrix}, \tag{4.4}$$

where $(x, y)_{\text{cam}}$ and $(x, y)_{\text{DMD}}$ are the coordinates in the atom plane and on the DMD chip, respectively. The diagonal elements of the matrix A induce scaling and the off-diagonal elements control shearing, while (C_x, C_y) describes translation in the x and y direction.

In order to obtain A and C, which define the linear transformation, we project a mask containing a deformed grid of 36 dark points on a bright background into the atom plane, as shown in Fig. 4.9a. If we choose a large cloud that is distributed over an area comparable to the DMD chip size in the atom plane (e.g. in the single plane of the vertical lattice before radial evaporation), atoms are trapped by the potential wells created by the dark points. An averaged fluorescence showing that is depicted in Fig.4.9b. Thanks to the deformation, we can easily identify the points in the fluorescence image with those in the original mask and, using peak fitting, obtain DMD-to-camera coordinate pairs for all 36 points. These are then used for determining the coefficients of the linear transformation in Eq. 4.4 using a least-squares fit. After this calibration, whenever a custom potential needs to be projected onto the atoms, the mask to be sent to the DMD is first inversely-transformed according to Eq. 4.4, such that the image in the atom plane is distortion-free.

Potential compensation

A key application of the DMD is to create large homogeneous systems for quantum simulation experiments. In particular, we use the DMD to correct for large-scale potential corrugations as well as for the horizontal harmonic confinement of the vertical lattice beams. In order to find the box mask

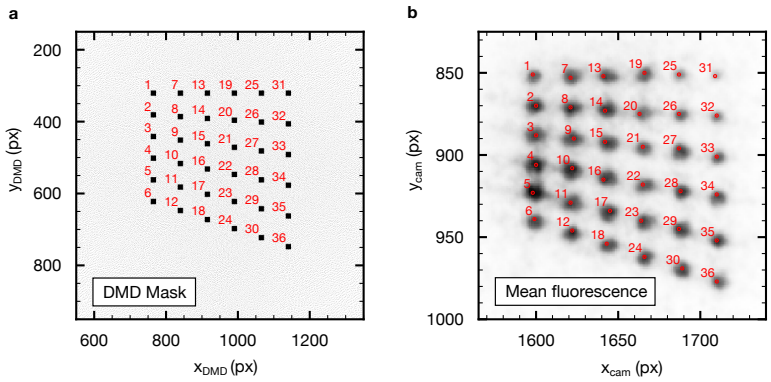

Figure 4.9 | **DMD-to-camera mapping.** **a**, A DMD mask containing a distorted grid of 36 dark points. **b**, Mean fluorescence image (ca. 20 images) of a BEC in a single plane of the vertical lattice, loaded into the potential wells created by the grid points. The positions of the atoms in the wells are fitted and mapped onto the grid points on the DMD mask. This defines an affine transformation which is used to transform a mask from the camera coordinate system into the DMD coordinate system and ensure that its projection in the atom plane is distortion-free.

that – if projected by the DMD imaging system – leads to a flat potential inside the box in the atom plane, we follow this procedure:

1. We define two quadratic regions: A box B_{ex} with a length of $d_{\mathrm{ex}} = 60$ short lattice sites, delimited by walls (solid lines in Fig. 4.10, top panel), and an inner box B_{in} with a length of $d_{\mathrm{in}} = 50$ short lattice sites, indicating the area that we aim to flatten.

2. We prepare the first DMD mask M_0: a box of width d_{ex} with maximum wall height of considerable thickness (e.g., 5 short lattice sites). The floor of the box mask is flat and set to a brightness of 25%. This value needs to be chosen carefully considering the maximum available DMD light power as well as the amplitude of the potentials to be corrected. For instance, in our case the maximum DMD light intensity corresponding to 100% reflectivity creates a repulsive potential of ca. $2\,U$, meaning that a box floor of 25% allows to correct for harmonic confinement or corrugations with a maximum amplitude of $0.5\,U$. Outside the box the mask is dark.

3. We load a dilute superfluid ($\bar{n} \approx 0.05$) into the box created by M_0 and wait more than 100 ms for the superfluid density to equilibrate. Then, we take at least 10 images (Fig. 4.10, top panel) and compute the mean fluorescence signal I_i. We also apply a Gaussian filter to I_i with a window size of three sites, smoothening the averaged image, so that random short-scale fluctuations of the local density are ignored.

4. We predict the next mask M_{i+1} which (when projected into the atom plane) should lead to a flatter density distribution inside the box. Let μ be the mean of I_i inside B_{in}, then the next mask (only inside B_{in}) is computed from:
$$M_{i+1}|_{B_{\mathrm{in}}} = \left(\frac{I_i}{\mu}\right)^{k_I} M_i|_{B_{\mathrm{in}}}, \tag{4.5}$$
where $k_I = 0.15$ is a feedback parameter. All other regions outside B_{in} in the new mask remain unchanged.

5. The new mask M_{i+1} is projected into the atom plane for the next iteration. We repeat steps 3-5 until the mean fluorescence signal inside B_{in} has flattened out.

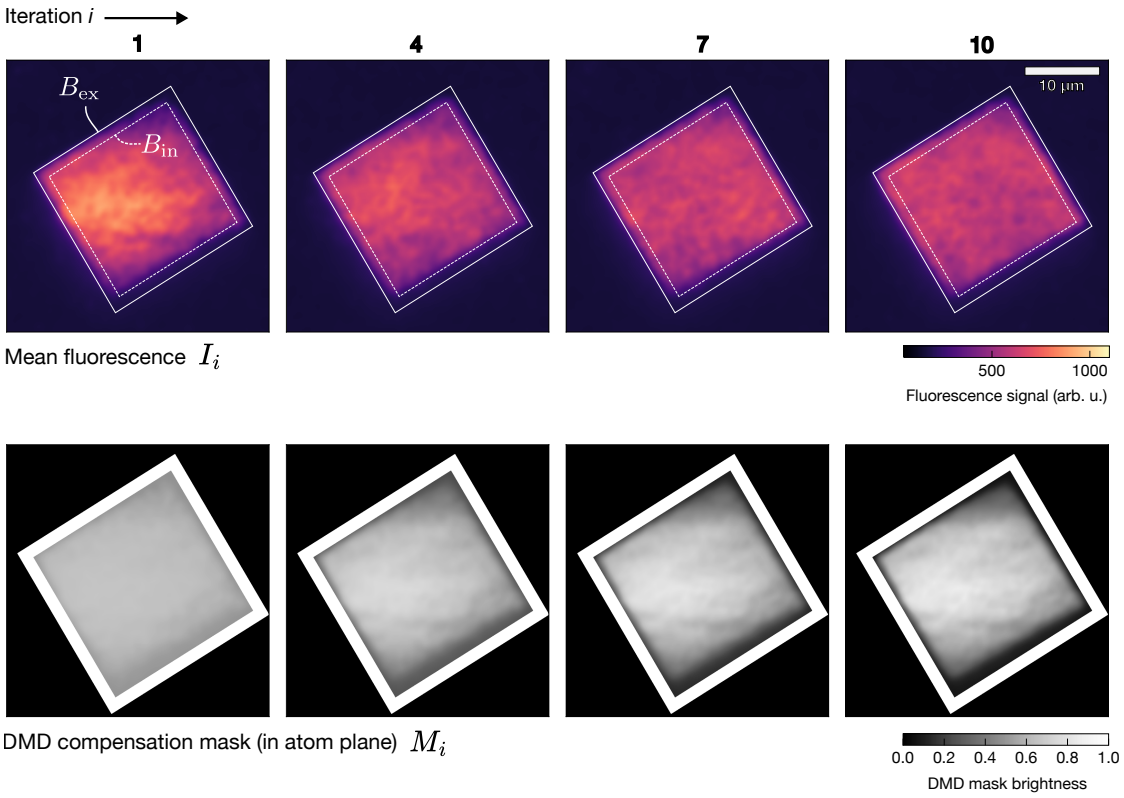

Figure 4.10 | Potential flattening using the DMD. A low-density superfluid ($\bar{n} \approx 0.05$) is used to probe the inside of the box for potential inhomogeneities. In a series of iterations (left to right, typically 10) the floor of the box potential (bottom panel) is adjusted according to Eq. 4.5, such that the mean superfluid density (top panel) becomes homogeneous inside the box. In order to mitigate edge effects, only the region B_{in} inside the actual box B_{ex} is stabilized, delimited by the dashed line. The location of the walls of the box is indicated by the solid white lines. Once the compensation mask has been found, it is applied as the floor of a new box potential with the same size as B_{in}.

Fig. 4.10 shows how the mean fluorescence signal I_i evolves as the number of iterations increases (top panel) and how the compensating mask M_i gradually adapts to the initial density distribution (bottom panel). Once this procedure is completed (typically after $N = 10$ iterations), we use the compensating mask $M_N|_{B_{\mathrm{in}}}$ inside B_{in} as the floor of a new box of width d_{in}. We found that giving the superfluid some extra space during the compensation procedure (B_{ex}) while compensating only inside a smaller region of the box (B_{in}), leads to better results, possibly due to imperfect alignment of the DMD imaging system and the resulting blurriness of certain box edges.

Note that here our compensation mask is generated in absence of any horizontal lattices. However, the horizontal lattices can contribute a small additional harmonic confinement, depending on their depth. If necessary, they can be turned on during the procedure as long as the tunnelling strength remains large enough for the atoms to move in the box. Nevertheless, we found the potential compensation without horizontal lattices to work very well for the experiments presented in Chapter 5. While other methods are primarily designed for removing harmonic potentials [81], our method is additionally able to eliminate potential corrugations (such as fringes created by the vertical lattice beams).

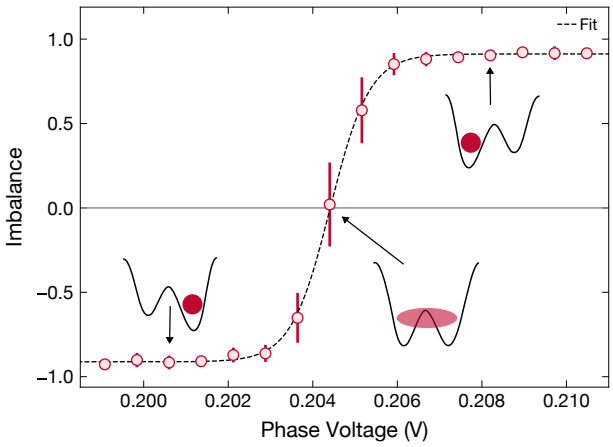

Figure 4.11 | Calibration of the superlattice phase. Imbalance versus the analog output voltage controlling the reference frequency of the frequency-offset-lock and, therefore, the superlattice phase. Goal of this calibration measurement is to find the phase voltage for which the double wells are symmetric and the imbalance is zero. The dashed line is a fit to the experimental data using a sigmoid function in order to obtain the symmetric phase. Each data point is the mean of six measurements, error bars denote the standard deviation.

4.7 Superlattice phase calibration

Imbalance traces

When working with phase-tunable superlattices, we can distinguish between two important configurations that differ by a phase shift of $\pi/2$ and occur periodically for $\phi = \phi_0 + n\pi, n \in \mathcal{Z}$: symmetric double wells with $\Delta = 0$ (no tilt) and maximally tilted double wells with $\Delta = \Delta_{\max}$. As described in Sec. 3.3, the phase is tuned by adjusting the laser frequency of the long lattice. In order to find a laser frequency corresponding to a symmetric configuration, we load a rectangular Mott insulator with short spacing in one axis and long spacing in the other axis, as depicted in Fig. 4.2b. Next, we adiabatically ramp up the short lattice belonging to the axis with the long lattice, therefore splitting the long lattice sites and turning them into double wells. Depending on the superlattice phase, the double well is either tilted or not tilted. Hence, the single atom in that double well will either become localized on one side (right $|R\rangle$ or left $|L\rangle$) or stay delocalized in a superposition of left and right $1/\sqrt{2}\,(|L\rangle + |R\rangle)$. This is captured by the imbalance

$$I = \frac{n_{\text{even}} - n_{\text{odd}}}{n_{\text{even}} + n_{\text{odd}}}, \tag{4.6}$$

which compares the filling of even and odd sites (n_{even} and n_{odd}, respectively) along the superlattice axis [67, 68]. In the symmetric configuration we expect the imbalance to be zero, otherwise it should approach $+1$ (all atoms in even sites) or -1 (all atoms in odd sites).

Fig. 4.11 shows the imbalance (averaged over the entire cloud in a box containing 40×40 lattice sites) as a function of the superlattice phase that is controlled by an analog voltage signal (cf. Sec. 3.3). There is a clear transition from negative to positive imbalance corresponding to a change of the tilt direction of the double wells. We obtain the symmetric superlattice phase by fitting the imbalance trace using a sigmoid function, yielding a phase control voltage of 0.203 41(16) V. The uncertainty of 160 µV corresponds to about 1 mrad which matches the width of the beatnote of the phase lock, presented in Sec. 3.3. Note that a finite slope of the imbalance close to the symmetric point can also be caused by inhomogeneities in the superlattice potentials, leading to different parts of the cloud becoming symmetric for different control

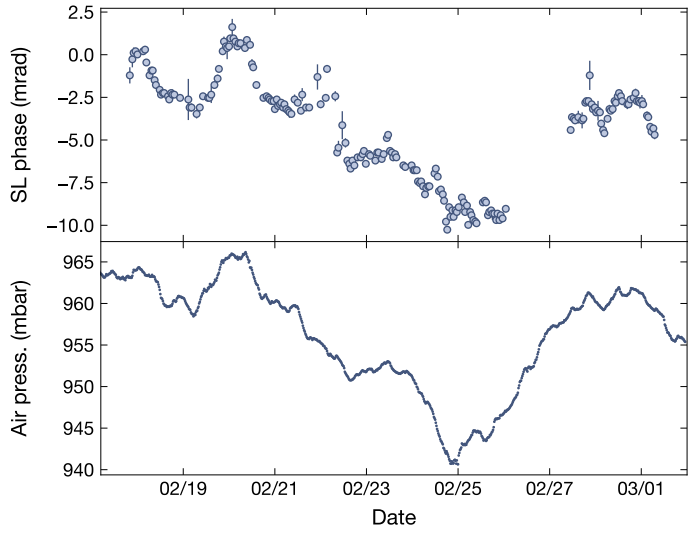

Figure 4.12 | Long-term drifts of the superlattice phase. Calibrated superlattice phase as a function of time (top panel) in 2023, showing strong correlations with the ambient air pressure (bottom panel). Error bars denote the standard error of the fit.

voltage values. In our experiment, this is usually a strong indicator for a significant angle between the short and the long lattice at the positions of the atoms, as discussed in Sec. 4.9.

Long-term phase drift

The relative phase of the short and the long lattice is expected to drift in response to changes in environmental conditions like temperature and air pressure. This is because the lattice beams propagate through air between the retro-mirror and the atoms in the center of the glass cell, and the wavelength of the light $\lambda = c(n_a)/\nu$ depends on the refractive index n_a of the traversed medium. In our experiment, temperature fluctuations are reduced to about 0.2° by the air conditioning system. However, the ambient air pressure is dictated by the weather. Fig. 4.12 shows the long-term evolution of the superlattice phase (upper panel) over a period of 12 days. For comparison, the lower panel shows the air pressure as recorded by meteorological sensors in our lab. One finds a clear correlation between superlattice phase and air pressure, revealing air pressure variations as the primary source of superlattice phase drifts with a sensitivity of about 0.4 mrad/mbar. For the experiments presented in Chapter 5, it is crucial that the superlattice stays in the symmetric configuration within < 1 mrad. In order to ensure phase stability over days and correct for long-term drifts, we have an automatic script running which takes and fits imbalance traces (as the one shown in Fig. 4.11) at least once every 45 min.

4.8 Calibration of on-site interactions and tunnel couplings

This section describes methods for calibrating the parameters of the (superlattice) Bose-Hubbard model implemented by the horizontal lattices (cf. Sec. 1.3). These include the on-site interaction strength U, the tunnelling strength J between short lattice sites and the double well tunnelling strength J_{dw} inside long lattice sites split by the short lattice (cf. Sec. 3.3).

On-site interactions

The most convenient knob for controlling the scattering rate $a(B)$ and the interaction strength $U \sim a(B)$ is the offset field, thanks to a low-field Feshbach resonance (cf. Sec 3.1). We can spectroscopically measure U in the short lattice by first preparing a deep $n = 1$ Mott insulator (short lattice depth ca. $60\,E_\mathrm{r}$, vertical lattice depth 3.5 μK), as described in Sec. 4.1. Then, after setting the offset field to the desired strength, we perform a sine modulation of the two-dimensional lattice depth (10% amplitude) for 300 ms. If the modulation frequency matches $|U|$, resonant tunnelling to already occupied sites occurs, doublon excitations are created and the measured filling of the Mott plateau decreases as a consequence of parity projection. The inset of Fig. 4.13 shows the mean fluorescence signal of the Mott insulator plateau as a function of the modulation frequency at an offset field of 11 G in the attractive regime (meaning negative U). There is a clearly visible $|U|$-resonance at a fitted offset field of 1405(12) Hz.

We repeat this measurement for offset fields in a range from 9 G in the attractive regime to 34 G in the repulsive regime and plot the fitted on-site interaction strength as a function of the offset field (see Fig. 4.13). The solid line is a fit to the experimental data using a hyperbolic function [252]:

$$U(B) = U_0 \left(1 - \frac{\delta}{B - B_0}\right), \tag{4.7}$$

where B_0 and δ denote the position and the width of the Feshbach resonance and U_0 is the background value of the on-site interaction strength far away from the resonance. The fit yields $U_0 = 1333(45)$ Hz, $\delta = 10.28(48)$ G and $B_0 = 5.97(34)$ G and the interaction strength zeros out at an offset field of approximately 16.25 G. These results differ significantly from the values reported in the literature ($\delta = 28.7$ G and $B_0 = -11.7$ G) [228]. One possible reason for that could be an incorrect calibration of the offset field. In addition, the experimental scattering length in the repulsive regime is limited by confinement-induced resonances due to the large trap anisotropy caused by the large spacing of the vertical lattice [253]. Generally, the on-site interaction strength $U(B)$ is proportional to the scattering length $a(B)$, as depicted in Fig. 3.1. However, In our case, he vertical lattice provides us with a typical confinement of just $f_z \sim 1$ kHz. As a consequence, even though the scattering length continues to increase when ramping up the offset field beyond 30 G, the on-site interaction strength does not. We can increase the vertical lattice power by up to a factor of two in order to increase U by up to 40% at large field strengths of $B \approx 40$ G. However, this also amplifies potential corrugations introduced by the vertical lattice.

Tunnel coupling in simple lattices

Similar to the calibration of U, we can also measure J in the short lattice spectroscopically by sine-modulating the corresponding lattice depth. Fig. 4.14 shows the average filling of an $n = 1$ Mott insulator as a function of the modulation frequency (lattice power is 30 mW, modulation amplitude is 3% with 400 ms duration). If the modulation frequency equals the parametric heating resonance between the first and the third lattice band, atoms can be promoted to higher bands which leads to strong heating. As a consequence, atom loss occurs and the fluorescence signal drops. We obtain the position $f^* = 40.32(17)$ kHz of this peak using a Lorentzian fit (an empirical choice) and compare it to numerical exact diagonalization (ED) calculations. These relate f^* to the lattice depth from which we can estimate J. Typically, the measured lattice depth is about 30% lower than the value expected for the applied power, considering the size of the lattice laser beam at the position of the atoms. Possible reasons for this discrepancy include beam shaping uncertainties, beam reflections on the glass cell windows and an imperfect alignment of the retro-beam. Note that an alternative way to calibrate J is observing the relaxation of a CDW and extract the frequency of the imbalance oscillations, see Sec. 5.3 for details.

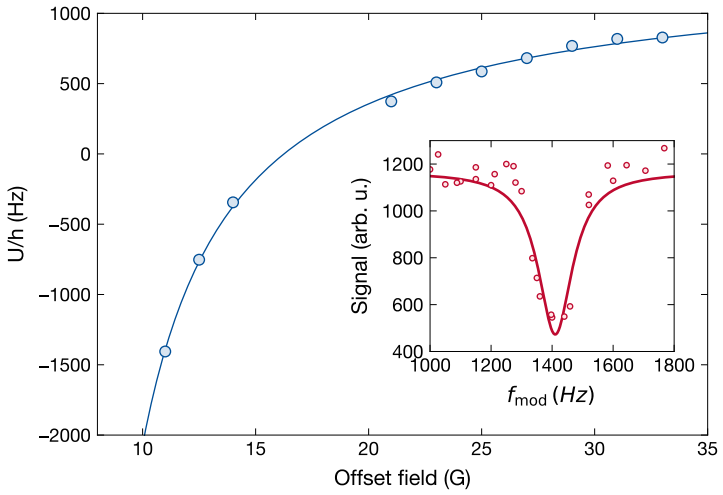

Figure 4.13 | Calibrating the on-site interaction strength U. On-site interaction strength U as function of the offset field strength, measured using modulation spectroscopy. The solid line is a hyperbolic fit of the Feshbach resonance (see Eq. 4.7). Error bars (fit errors) are smaller than the marker size. The inset shows an individual modulation spectroscopy scan for $B = 11$ G with attractive interactions (no repetitions). The mean fluorescence signal of an $n = 1$ Mott insulator plateau is measured as a function of the modulation frequency. When the resonance condition $f_{\text{mod}} = |U|$ is fulfilled, atom loss occurs and the fluorescence signal drops. The resonance is fitted using a Lorentzian function (solid line) to obtain U.

Tunnel coupling in superlattices

In a superlattice potential the tunnelling strength alternates between J_{long} and J_{dw}, where J_{long} is the tunnelling strength between adjacent double wells and J_{dw} denotes the tunnelling strength between the right and the left side of each double well (cf. inset in Fig.3.3). In order to calibrate J_{dw}, we perform tunnel oscillation experiments: We start by loading a rectangular Mott insulator with an asymmetric double well configuration, such that only the even (or odd) rows of the short lattice are occupied (cf. Sec. 4.1). The long lattice is deep enough ($V_{\text{long}} > 40E_r$) so that we can assume that all double wells are isolated from each other. Next, we also ramp up the short lattice to a large depth (to freeze out all dynamics) and adiabatically ramp the superlattice phase to the symmetric configuration. We then abruptly turn on the dynamics by quenching down the short lattice power to a variable value. As a consequence, the asymmetric initial state, an eigenstate of the tilted double well, starts to time-evolve in the symmetric double well potential, leading to density oscillations between the right and the left side of the double well at a frequency of $f = 2J_{\text{dw}}$. These oscillations are captured by the imbalance (cf. Eq. 4.6), as shown in Fig. 4.15 as a function of evolution time after the quench. The tunnelling strength $J_{\text{dw}} = f/2 = 484.3(5)$ Hz is then obtained using a sine fit. In practice, we measure J_{dw} for at least three pairs of $(V_{\text{short}}, V_{\text{long}})$ and fit this data using an exact-diagonalization-based numerical function $J_{\text{dw}}(V_{\text{short}}, V_{\text{long}})$. The free parameters are $V_{\text{short}}, V_{\text{long}}$ which denote the short and long lattice depths, respectively. By establishing a relationship between the double well tunnelling strength and the depths of both the long and the short lattice, J_{dw} is calibrated.

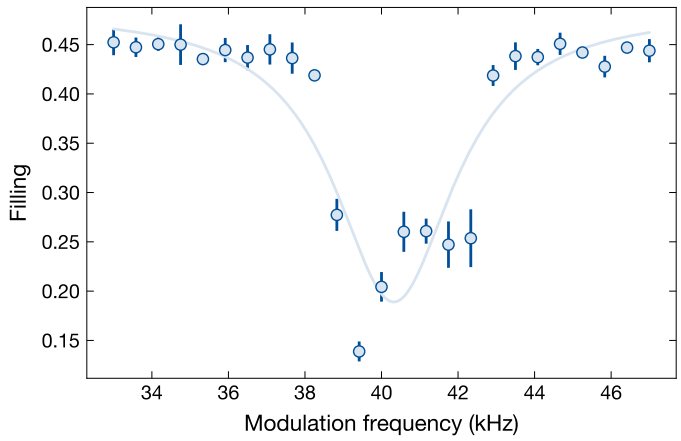

Figure 4.14 | **Parametric heating scan**. Mean filling of the Mott insulator plateau as a function of the frequency at which the short lattice depth is modulated. The modulation takes 400 ms and has an amplitude of 3%. The mean lattice power is 30 mW. When the parametric resonance between the first and the third lattice band is hit, atom loss occurs. This allows to relate the lattice depth to the experimental beam power and calibrate J. The solid line is a fit to the experimental data using a Lorentzian. Error bars denote the standard deviation.

4.9 Superlattice angle optimization

The superlattice angle θ is the angle between the short lattice and the long lattice at the position of the atoms. As shown in Fig. 4.16a, this leads to a superlattice phase gradient perpendicular to the superlattice axis which is, to first order [242], described by:

$$\phi(x) = \phi_0 + 4\pi\theta x/\lambda_{\text{long}}. \tag{4.8}$$

Even a small superlattice angle of $\theta = 1$ mrad leads to a superlattice phase change of $\Delta\phi = 126$ mrad across a typical ROI spanning over 20 long or 40 short lattice sites. While this inhomogeneity can be useful for certain experiments [242], it is undesirable when aiming for identical conditions in the entire ROI.

After initial alignment of the superlattice by overlapping the short and the long lattice beams at two points in the beam path (cf. Sec. 3.3), we check the inhomogeneity of the superlattice potential by measuring spatially resolved tunnel oscillations. Fig. 4.16b shows the imbalance (cf. Eq. 4.6) as a function of time and position perpendicular to the superlattice axis. We find that the oscillation frequency is the slowest in the center of the ROI and increases toward its edges. For each position, we obtain J_{dw} by fitting the time evolution of the imbalance using a sine function (just as in the previous Section) and plot $J_{\text{dw}}(x)$ in Fig. 4.16e (red markers). The quadratic spatial variation of $J_{\text{dw}}(x)$ (see red solid line) is consistent with a linear tilt gradient of 14(1) Hz/λ_{short} (cf. Eq. 6.4) which corresponds to a phase gradient of 0.4 mrad/λ_{short} for the superlattice depths used in this experiment. Using Eq. 4.8, we are then able to estimate a superlattice angle of $\theta = 0.005°$ or 0.1 mrad.

For the experiments presented in Chapter 5 we aim for a homogeneous superlattice potential without phase gradients in any direction and, thus, would like to minimize the superlattice angle θ. For this purpose, the 1534 nm beam path of our superlattice setup contains a glass cylinder plate which introduces an adjustable parallel shift in the horizontal plane (cf. Fig. 3.3). The last lens before the science chamber which focusses the lattice beam onto the atoms translates this parallel shift into a change of the angle under which the long lattice beam hits the atoms. Hence, by adjusting the orientation of the glass cylinder, we can minimize the superlattice angle θ and remove the phase gradient.

As a first step of this procedure, we prepare a rectangular Mott insulator (cf. Sec. 4.1) and adiabatically

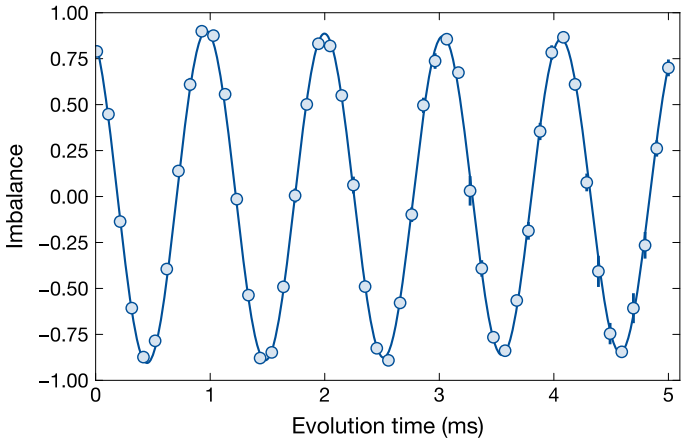

Figure 4.15 | Tunnel oscillation in isolated double wells. Mean imbalance as a function of evolution time after quenching on the tunnel coupling inside symmetric double wells, starting with an asymmetric occupation (imbalance 1). The solid line is a sine fit to the experimental data for obtaining the oscillation frequency f and calibrating $J_{\mathrm{dw}} = f/2$.

split the double wells by slowly ramping up the short lattice in the symmetric configuration. If the superlattice angle is non-zero, only part of the ROI will show zero imbalance (symmetric region), flanked on either side by regions where the imbalance approaches $+1$ and -1, as depicted in Fig. 4.16a. Next, we start rotating the glass cylinder, trying to increase the size of the symmetric region and, therefore, lowering the phase gradient across the cloud. Fig. 4.16c demonstrates how the spatial imbalance profile changes when the glass cylinder is rotated in the right direction, showing a growth of the symmetric region toward later shots. Since the long lattice beam is not perfectly focused on the atoms, the glass cylinder rotation not only makes the symmetric region broader but also shifts it, such that the symmetric superlattice phase needs to be occasionally adjusted (cf. Sec. 4.7).

After several iterations of glass cylinder rotation and phase recalibration, the superlattice angle is minimized and the spatial tunnel oscillations acquire a spatial profile as depicted in Fig. 4.16d. We find that the superlattice potential is now much more homogeneous with a residual J_{dw} gradient that is on the order of the error bars (cf. Fig. 4.16e, blue markers).

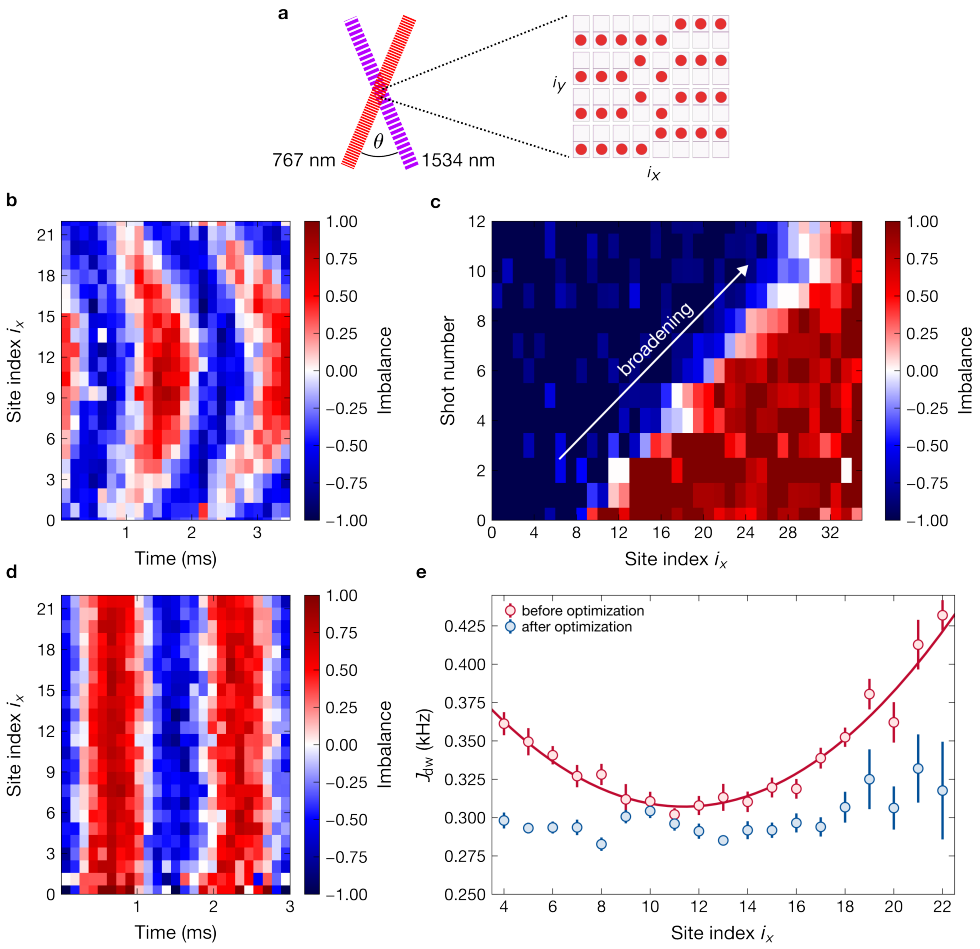

Figure 4.16 | Superlattice angle optimization. a If the long and the short lattice cross under a non-zero angle ϑ at the position of the atoms, the superlattice potential will exhibit a tilt gradient perpendicular to the lattice axis. Thus, only a part of the cloud can be in the symmetric configuration and the regions on either side will exhibit tilts of opposite sign. **b**, Spatially resolved tunnelling oscillations before optimization, averaged along the superlattice axis. Due to the tilt gradient, the tunnelling oscillation frequency varies spatially. **c**, Using a glass cylinder in the long lattice beam path, the superlattice angle ϑ can be systematically tuned to zero. We repeatedly measure the spatially resolved imbalance profile, averaged along the superlattice axis, and gradually turn the glass cylinder to increase the width of the zero-imbalance region (white). Since turning the glass cylinder also alters the superlattice phase, the white region will occasionally move out of the ROI and a phase recalibration becomes necessary. **d**, After optimization, the tilt gradient is removed and the tunnelling oscillations are spatially homogeneous. **e**, Fitted tunnelling oscillation frequency from (**b**) and (**d**) (using a sine function) as a function of position perpendicular to the superlattice axis, comparing the profiles before and after optimization. The red solid line is a parabolic fit to the frequency profile before optimization, revealing a superlattice phase gradient of $0.4\,\mathrm{mrad}/\lambda_{\mathrm{short}}$.

CHAPTER 5

Emergence of fluctuating hydrodynamics in a chaotic quantum ladder

In this Chapter we present the main experimental results of this thesis and observe the emergence of FHD in a chaotic quantum system. We shed light on the role that fluctuations play in the thermalization process after a quench and study the timescales on which they grow and equilibrate. We do so in a ladder system of hard-core bosons that can be tuned from fully integrable to chaotic, allowing to realize a crossover from ballistic to diffusive dynamics. Using single-site resolution, we find evidence that the large-scale fluctuation growth in chaotic, far-from equilibrium systems can be described by the simple macroscopic classical theory of FHD (cf. Chapter 2). This suggests that the entire non-equilibrium dynamics of an intractable chaotic quantum systems are effectively governed by a single quantity, the linear-response diffusion constant, extending the idea of fluctuation-dissipation relations to far-from-equilibrium situations. We show that the diffusion constant, which, in general, is hard to obtain using computational methods, can be extracted from the fluctuation and correlation dynamics.

5.1 The model

Ladder BHM

The model of interest in this work is the Bose-Hubbard model (BHM) in a ladder geometry. Similar to the fully two-dimensional BHM introduced in Eq. 1.5, it is defined by the Hamiltonian:

$$\hat{H} = -J\left(\sum_{\alpha,i} \hat{a}^\dagger_{\alpha,i}\hat{a}_{\alpha,i+1} + \text{h.c.}\right) - J_\perp\left(\sum_{i} \hat{a}^\dagger_{1,i}\hat{a}_{2,i} + \text{h.c.}\right) + \frac{U}{2}\sum_{\alpha,i} \hat{n}_{\alpha,i}(\hat{n}_{\alpha,i}+1). \tag{5.1}$$

Here, $\hat{a}_{\alpha,i}$, $\hat{a}^\dagger_{\alpha,i}$ are the bosonic annihilation and creation operators, respectively, and $\hat{n}_i = \hat{a}^\dagger_{\alpha,i}\hat{a}_{\alpha,i}$ is the particle number operator for site i in leg $\alpha \in \{1,2\}$ of the ladder [254, 255]. The tunnelling strength along (perpendicular to) the ladder is denoted by J ($J_\perp$) and U is the on-site interaction strength. We work at half filling, i.e. $\bar{n} = 1/2$, and we assume that the particles occupying the lattice are hardcore bosons, i.e. $U/J_{(\perp)} >> 1$. This means that it is energetically unfavorable for a lattice site to be occupied by more than one atom. Similarly to the purely one- or fully two-dimensional BHM, the hard-core BHM on a ladder possesses Mott insulator phases and superfluid phases, depending on the ratio $J_\perp/J$ and the mean filling. At half filling, the ground state is a superfluid for $J_\perp/J \leq 1$ and crosses over to a rung-MI for $J_\perp/J > 1$, where each rung of the ladder is occupied by one delocalized particle [255–257].

The relevance of this model for studying quantum thermalization roots in its tunability: The kind of dynamics governing the system in out-of-equilibrium situations depends on the tunnelling strength between the legs of the ladders (see also Sec. 1.5):

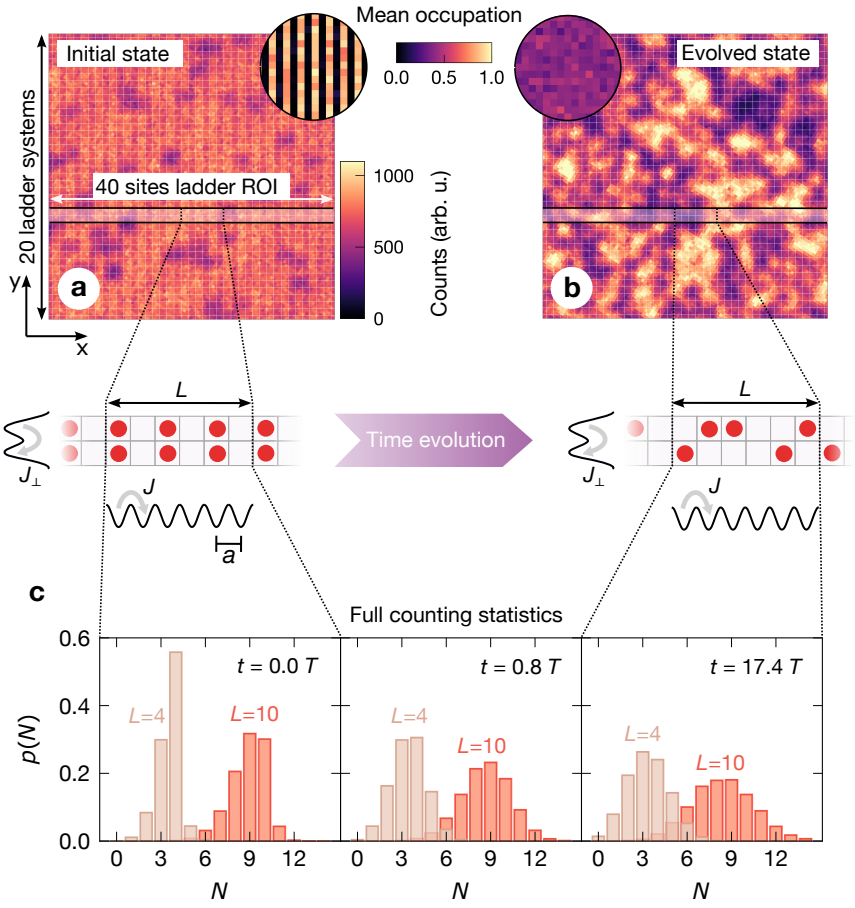

Figure 5.1 | **Quench experiment.** An optical superlattice in the *y*-direction in combination with simple lattice in the *x*-direction realizes multiple adjacent copies of large homogeneous ladder systems with a length of up to 50 sites. The edges of the system are provided by the walls of a DMD box potential which is also used to make the system as homogeneous as possible by removing harmonic confinement and large-scale corrugations. In order to mitigate edge effects, only the innermost 40×40 sites are used in the data analysis and define the ROI. By adjusting $J_\perp/J$ we can tune the ladder systems from decoupled and integrable ($J_\perp/J = 0$) to fully coupled and chaotic ($J_\perp/J = 1$). **a**, As an initial state for the quench thermalization experiment, we prepare a CDW with a period of two lattice sites using a superlattice potential in the *x*-direction. **b**, After quenching on the dynamics in the system, the CDW decays and a time-evolved state with uniform mean filling and slowly growing fluctuation emerges. The insets show the mean reconstructed occupation in the initial and evolved state, averaged over 32 images. **c**, Thanks to single-site resolving quantum gas microscopy, we can study the FCS of the total particle number in subsystems of various sizes and track the relaxation dynamics triggered by the quench.

- If $J_\perp/J = 0$ the legs of the ladder are fully decoupled. As a consequence, the motion of the hard-core bosons is restricted to 1d and the many-body problem can be mapped to the *integrable* free-fermion limit, as shown in Appendix C, effectively reducing it to a single particle problem [255, 258]. In 1d neither hard-core bosons nor fermions can exchange themselves and the fundamental difference in their statistics can usually be neglected [255]. This dynamics of the system are then generally ballistic and, in principle, analytically solvable.

- If $J_\perp/J \neq 0$, there are non-zero interactions between the two legs of the ladder. Since the system is not purely one-dimensional anymore, particle exchange is now allowed and the physics of

free-fermions and hard-core bosons becomes very different. As a consequence, the free-fermion mapping is not possible anymore [255, 259]. Integrability is broken and the system is expected to behave chaotically with diffusive dynamics. This configuration is much harder to simulate on classical computers, particularly for larger system sizes (> 20 lattice sites) and long evolution times (> 4 tunnelling times).

Note that a small but non-zero tunnelling strength $J_\perp$ between the legs of the ladder means that it will take a finite amount of time for the system to probe its dimensionality. So while the system's dynamics may seem integrable and ballistic at short times, they eventually will become diffusive on longer timescales $\sim 1/J_\perp$ [260–263], as observed in Sec. 5.5. Typically we consider $J_\perp/J = 1$ to be the *fully* diffusive case where hydrodynamic behavior plays out in its clearest and simplest form. Note that increasing $J_\perp/J$ to values beyond 1 can (for specific initial states) result in ballistic dynamics driven by correlated hopping processes [264]. However, this is part of ongoing investigations and might be addressed in future work.

Experimental implementation

We realize the ladder Hamiltonian in Eq. 5.1 using optical superlattices (cf. Sec. 3.3 for more information on the setup). As depicted in Fig. 5.1a, a deep long lattice ($\lambda_{y,\mathrm{long}} = 1534\,\mathrm{nm}$) in y direction cuts the ROI into about 20 decoupled ladder systems. The short lattice depth in y direction ($\lambda_{y,\mathrm{short}} = 767\,\mathrm{nm}$) sets the tunnelling strength $J_\perp$ between the legs of the ladder. In the x direction we use a simple optical lattice ($\lambda_{x,\mathrm{short}} = 767\,\mathrm{nm}$), the depth of which sets the tunnelling strength J along the ladder. The tunnelling strengths J and $J_\perp$ are calibrated using the methods introduced in Sec. 4.8. The maximum length of each ladder is about 50 sites with both ends provided by the walls of the DMD box potential (cf. Section 4.5). However, in order to mitigate finite-size effects arising from the presence of the edges we typically only evaluate the 40 most central sites which define the ROI.

5.2 The experiment

A common way to study the non-equilibrium dynamics of a system is to prepare it in a far-from-equilibrium state and then watch it relax. This is implemented by a quench experiment (see Sec. 1.4), where the Hamiltonian is changed so abruptly, that the ground state wavefunction in the pre-quench Hamiltonian becomes a highly-excited state in the post-quench Hamiltonian [39, 67, 147]. The time-evolution of this post-quench excited state is then subject to observation and measurements.

As discussed in Sec. 1.7, we expect entanglement entropy to build up after the quench, leading to a steady grow of fluctuations. In order to conduct a clean measurement of the fluctuation growth, unperturbed by large-scale particle currents, it is feasible to start with an initial state of small-scale density variations, such that local equilibrium of the mean density is achieved as quickly as possible. This idea is sketched in Fig. 5.2a using a short-wavelength charge density wave: While the density equilibrates very quickly, the spreading of entanglement and, therefore, the growth of fluctuations occurs on much longer hydrodynamic timescales (Fig. 5.2b). In this case we expect the later-time dynamics to play out on a constant density background and to be governed by a single spatially homogeneous diffusion constant, which simplifies the evaluation of the experimental data and the benchmarking of FHD. This setting is particularly advantageous in comparison to domain wall experiments [15], where the diffusion constant spatially depends on the local mean density which changes as the system evolves.

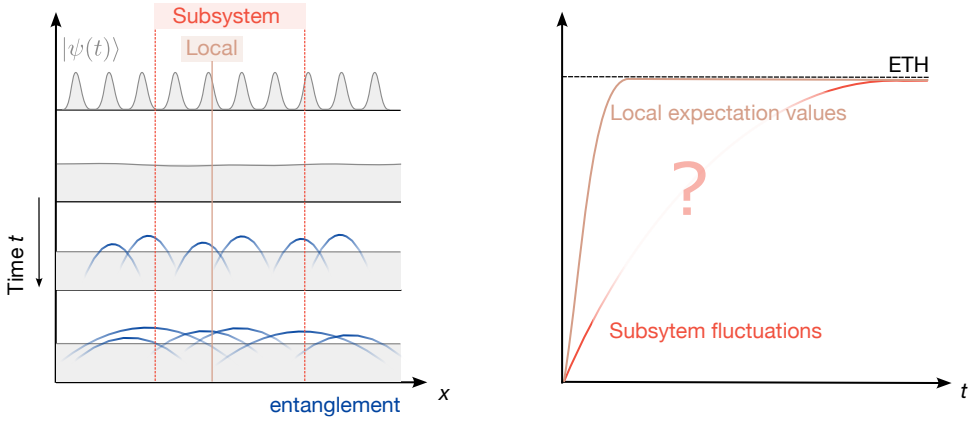

Figure 5.2 | Hydrodynamic fluctuations in a chaotic quantum system. **a** After quenching on the dynamics in a quantum system, any small-spaced initial density modulation will decay quickly and the local mean-density equilibrates fast. However, on longer timescales, entanglement starts to build up over longer and longer distances. As a consequence of entanglement, repeated measurements of quantities (like the number of particles) in a subsystem reveal fluctuations due to measurement projection noise. **b** These fluctuations grow on slow hydrodynamic timescales before eventually reaching their saturation value predicted by the ETH.

Initial state

The quench (cf. Sec. 1.4) is performed from a frozen product state (a short-spaced CDW) to a superfluid state. Following the sequence described in Sec. 4.1, we prepare a Mott insulator in a tilted x-superlattice configuration such that every second y-row is occupied and every other y-row is empty, producing a CDW as depicted in Fig. 5.1a. Both long and short lattice depths exceed $50E_r$ so that all dynamics are frozen, i.e. $J_\perp = J \approx 0$. This is the pre-quench state, lacking any coherence between the individual lattice sites. Choosing a CDW with a period of two sites is motivated by the following ideas:

1. It is an initial state with short-range density variations and we can expect the local mean density to decay quickly (see Section 5.3). Thus, as mentioned above, the growth of fluctuations will mostly occur on a homogeneous half-filling background (see Section 5.4) and is easier to compare with the predictions of FHD without adding further correction terms to this theory (cf. Chapter 2).

2. The CDW product state can be considered an infinite-temperature state in the post-quench ladder Hamiltonian [263]. As a consequence, the non-equilibrium chaotic system is expected to relax to a maximum-entropy (maximally entangled) state as predicted by the ETH [265, 266], see Sec. 1.7. This allows to compare the expected saturation values of observables with values measured at long times after the quench.

Quench preparation

So far, we have used a superlattice potential in x-direction and a simple lattice in y-direction, to prepare the CDW. However, for realizing the ladder system, we need a superlattice in y-direction and simple lattice in x-direction. Thus, while the dynamics are still frozen we adapt the 2d superlattice potential to realize the ladder Hamiltonian introduced in Sec. 5.1, as shown in Fig. 5.3: We first remove the long lattice along x and, at the same time, increase the long lattice depth in the y-direction to $17\,E_\mathrm{r}^{(\mathrm{l})}$ ($E_\mathrm{r}^{(\mathrm{l,s})} = h^2/(2m\lambda_{(\mathrm{l,s})}^2)$ is the recoil energy in the short and long horizontal lattice, respectively). The long lattice depth is sufficiently large for suppressing any significant coupling between adjacent ladder

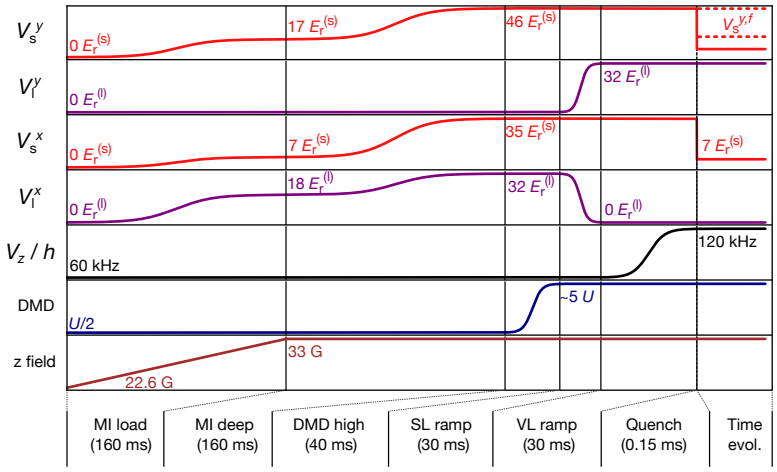

Figure 5.3 | Sequence for ladder preparation and the quantum quench. After using the superlattice in x direction to prepare a CDW as the pre-quench initial state, the dynamics are frozen and the ladder geometry is realized by the superlattice in y direction. For the quench, the short lattice powers are abruptly lowered to set J and $J_\perp$,according to the desired post-quench dynamics.

systems ($J_{\mathrm{y,long}}/J < 1\%$). We also ramp up the height of the DMD walls to $\sim 5\,U$ to prevent further spilling out of the box (cf. Section 4.5). Moreover, we increase the vertical lattice depth to about $V_z/h = 120\,\mathrm{kHz}$ to increase the on-site interaction strength and to ensure that we work sufficiently deep in the hard-core limit at all times ($U/J > 7$). For all values of $J_\perp/J$ investigated in this work, the doublon fraction does not exceed 3% (fraction of doubly-occupied sites), see Sec. 6.1 for details.

The quench

Finally, we abruptly turn on the dynamics in the system by quenching down the short lattice depths in both x- and y-direction, such that $J/h = 96(3)\,\mathrm{Hz}$ and $J_\perp/J = 0.0029(3), 0.55(2), 1.04(3)$, depending on the desired dynamics. This is the moment when the pre-quench MI product state is projected onto the eigenstate manifold of the post-quench Hamiltonian which is the ladder BHM as defined in Eq. 5.1. As the initial state is not an eigenstate of the new ladder Hamiltonian after the quench, what follows is a non-trivial time evolution. In the case of the chaotic ladder ($J_\perp/J > 0$), we expect a diffusive hydrodynamic equilibration process, eventually relaxing to a thermal equilibrium (thermalization). In the case of ballistic dynamics ($J_\perp/J = 0$), the relaxation of the system is expected to unfold in agreement with free fermion predictions (cf. Appendix C) without reaching thermal equilibrium. After the quantum system has evolved for a controllable time (up to $17.4\,\hbar/J$, see Fig. 5.1b), we instantly stop the evolution by ramping up the short lattice powers and image the atoms, as detailed in Sec. 3.4 and Sec. 4.3.

From the single-site resolved occupation data we are not only able to track the decay of the CDW (see Section 5.3) but have direct access to the FCS in the system. As shown in Fig. 5.1c, we can measure the particle number distribution in subsystems of variable size L. In particular, we will be interested in the particle number fluctuation growth (see Section 5.4) which corresponds to the variance of the FCS. Similarly, we can measure the spreading of density-density correlations following the quench (cf. Section 5.5).

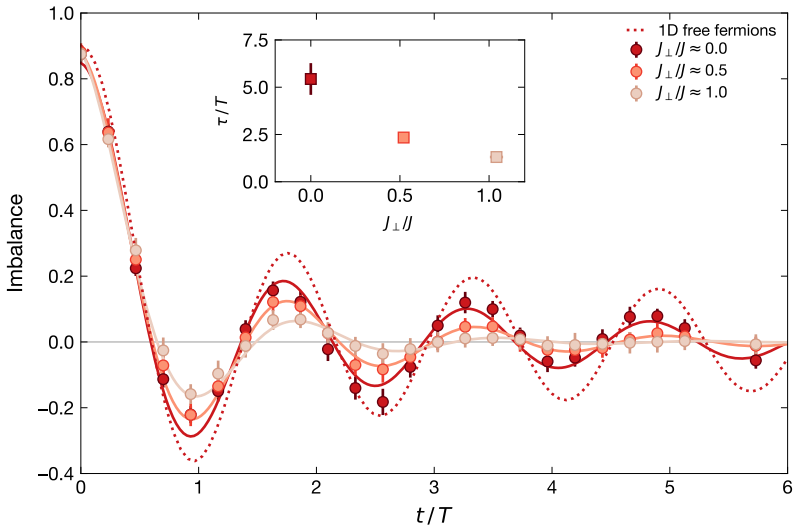

Figure 5.4 | Time evolution of the the local mean density (imbalance). Imbalance as a function of the evolution time after the quench for $J_\perp/J \approx 0.0, 0.5, 1.0$, where each data point was obtained from averaging over the entire 40×40 sites ROI in about 35 fluorescence images. The solid lines are fits to the data using an exponentially damped Bessel function (Eq. 5.4) and the dotted curve is the free fermion prediction, taking into account defects in the initial state (but not disorder in the lattice potential). The inset shows the fitted decay constant τ as a function of $J_\perp/J$. Error bars denote the standard deviation or the fit standard error (inset).

5.3 Local mean density decay

In the moment of the quench, the initial CDW becomes a highly excited state in the post-quench ladder Hamiltonian (Eq. 5.1) and will immediately start to decay. The perhaps simplest quantity for tracking the decay of the CDW is the imbalance which compares the mean occupation of even and odd rungs. It is defined as [67, 68]:

$$\mathcal{I} = (\langle \hat{n}_{\text{even}} \rangle - \langle \hat{n}_{\text{odd}} \rangle)/(\langle \hat{n}_{\text{even}} \rangle + \langle \hat{n}_{\text{odd}} \rangle) \tag{5.2}$$

Here, $\langle \hat{n}_{\text{even}} \rangle = \langle \hat{n}_{2i} \rangle_i$ and $\langle \hat{n}_{\text{odd}} \rangle = \langle \hat{n}_{2i+1} \rangle_i$ denote the average filling of even and odd sites in the ROI, respectively. For the ideal initial CDW state with all atoms occupying either only the even or only the odd rungs, $|\mathcal{I}| = 1$, corresponding to a maximum contrast. In turn, when the CDW has decayed and the atoms are equally distributed among even and odd ladder rungs, we expect $\mathcal{I} = 0$ (zero contrast). Since computing the imbalance, in principle, only requires information about the mean occupation of a single lattice site (ideally, $\langle \hat{n}_{\text{even}} \rangle = 1 - \langle \hat{n}_{\text{odd}} \rangle$), it can be regarded a *local* mean observable.

For the integrable configuration ($J_\perp/J = 0$), the analytical prediction for the time evolution of the imbalance is (cf. Appendix C):

$$\mathcal{I}(t) = \mathcal{J}_0(4\,t/T), \tag{5.3}$$

where $\mathcal{J}_0$ is the zeroth Bessel function of the first kind [267] and $T = \hbar/J$ is the tunnelling time along the ladder. Thus, the imbalance is expected to oscillate with an amplitude that decays polynomially. In contrast to the chaotic case, the dynamics are governed by infinitely many conserved quantities like the occupation numbers of each single-particle eigenstate, in analogy with Newton's cradle [258]. The relaxation of the system will lead to a state locally described by a generalized Gibbs ensemble (GGE) [268, 269] and can be further understood using the framework of generalized hydrodynamics (GHD)

(cf. Sec. 2.1 [270, 271]). In contrast, for chaotic configurations ($J_\perp/J > 0$) the number of conserved quantities is sharply reduced (to energy and particle number). Relaxation of the density variations is expected to occur on short timescales, faster than suggested by a simple Bessel function in the integrable case. The integrability-breaking interactions between the legs of the ladder dephase the oscillations that occur in the free-fermion limit and lead to further damping of the imbalance oscillation.

Fig. 5.4 shows the mean imbalance (averaged over the entire ROI) as a function of evolution time after the quench (in units of tunnelling times $T = J/\hbar$). For all three configurations $J_\perp/J$ it can be seen decaying on a timescale comparable to the tunnelling time. Notably, the decay is enhanced for the chaotic system ($J_\perp/J \approx 1.0$) compared to the integrable configuration ($J_\perp/J \approx 0.0$), in agreement with the expectation for a reduced number of conserved quantities. Motivated by the Bessel-type decay in the integrable limit, we fit the experimental data using an exponentially decaying Bessel function:

$$\mathcal{I}(t) = A\, \mathcal{J}_0(4\,t/T)\, e^{-t/\tau}, \tag{5.4}$$

where A is the amplitude and τ is the decay constant. This empirically chosen function aims to capture enhanced decay behavior beyond what the Bessel function describes. The inset in Fig. 5.4 shows the fitted decay constant τ as a function of $J_\perp/J$, indicating a decrease of τ toward the chaotic case for $J_\perp/J > 0$.

Note that, for the integrable case we, in theory, expect to find $A = 1$ and $\tau = \infty$ (a pure Bessel-type decay according to the free fermion prediction). However, due to defects in the initial state, the measured amplitude is reduced to about $A = 0.9$, consistent with our measured initial state quality. The measured finite decay constant $\tau < \infty$ is probably caused by disorder and inhomogeneities in our lattice potential. In Section 6.2 we run free-fermion simulations to show the connection between a reduced imbalance contrast and the presence of residual disorder in the system, and are able to estimate a disorder amplitude of $\Delta \approx J$.

5.4 Particle number fluctuations

If we want to probe FHD in the quantum regime we need to measure the particle number fluctuations in the system. The fluctuation amplitude is defined as the variance of the particle number distribution, i.e. the second moment of the FCS. For a subsystem of length L we define:

$$\mathrm{Var}_L \equiv \mathrm{Var}\left(\sum_i^L \hat{N}_i\right). \tag{5.5}$$

Here, $\hat{N}_i = \hat{n}_{1,i} + \hat{n}_{2,i}$ is the total particle number in the i-th rung of the ladder. Note that the subsystem contains $2\,L$ sites. The time evolution of fluctuations are a key indicator of how relaxation (thermalization) of the system unfolds beyond local observables. In a *quantum* system, the build-up of fluctuations is a consequence of many-body entanglement spreading (cf. Sec. 1.7).

Expected behavior

Under perfect conditions, the pre-quench CDW initial state is a defect-free product state of single particles that are localized and not entangled with each other. Repeated measurements of the particle number in any subsystem of this state would, therefore, always yield the same result and the particle number fluctuations would be zero. In practice, however, we expect to measure non-zero fluctuations even for the initial product state: They originate from defects which show up at random positions in every shot and, as a consequence, broaden the distribution of the total particle number measured in a fixed subsystem.

At long times after the quench the overall isolated chaotic quantum system is expected to ulti-

mately approach a maximally entangled state. Thus, due to density-density correlations resulting from entanglement, the measurement result for the particle number in any subsystem will depend on the measurement results in the remainder of the overall system and appear thermal in agreement with the ETH. As the subsystem is maximally entangled with its environment, the particle number fluctuation amplitude in the infinite-temperature post-quench system after long times is expected to take the maximum possible value. If just a single site is measured individually, one will find that it is occupied with a probability $\bar{n}$ and unoccupied with a probability $1-\bar{n}$, where $\bar{n} \approx 0.5$ is the mean filling of the system, yielding a variance of

$$\chi(\bar{n}) = \bar{n}\,(1-\bar{n}). \tag{5.6}$$

This expression defines the *susceptibility* χ. It quantifies the strength of the system's response to external fields. It is zero for $\bar{n} = 0$ (no particles) and $\bar{n} = 1$ (no mobility) and becomes maximal for $\bar{n} = 0.5$. Assuming that all site occupations are random, the maximum particle number variance for a subsystem of length L containing $2L$ sites reads:

$$\max(\mathrm{Var}_L) = 2L\,\chi(\bar{n}) = \mathrm{Var}_L(t \to \infty), \tag{5.7}$$

which is expected to be the late-time saturation value of $\mathrm{Var}_L(t)$. How fast the fluctuations grow, depends on how fast and through which channels entanglement spreads in the system following the quench, as discussed in Sec. 1.7. For the integrable case ($J_\perp/J \approx 0$), we expect the fluctuations to grow ballistically, while for the chaotic system ($J_\perp/J \approx 1$) the fluctuation growth is generally a diffusive hydrodynamic process.

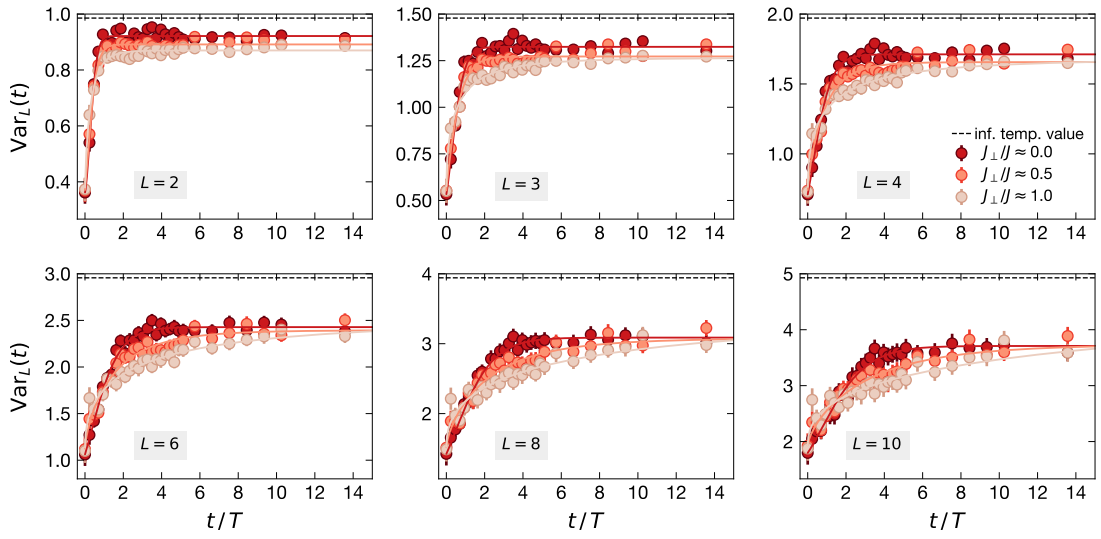

Figure 5.5 | Time evolution of particle number fluctuations sorted by subsystem size. Measured atom number variance in subsystems of various lengths $L = 2, 3, 4, 6, 8$ and 10 as a function of the evolution time after the quench (normalized to the tunnelling time $T = \hbar/J$) for $J_\perp/J \approx 0.0, 0.5, 1.0$. The solid lines are fits to the data using the empirical fit function introduced in Eq. 5.9. The dashed line is the infinite-temperature saturation value expected from ETH (Eq. 5.7). The discrepancy between the experimental and expected saturation levels can be predominantly attributed to disorder, as discussed in Sec. 6.2.

Measured fluctuation growth

Fig. 5.5 shows the particle number variance in different subsystem sizes ranging from $L = 2$ to $L = 10$ for $J_\perp/J = 0.0, 0.5, 1.0$, comparing integrable and chaotic configurations. The dashed black line indicates the infinite-temperature limit of the fluctuations given by Eq. 5.7. All traces start at a non-zero value at $t = 0$, which can be attributed to defects in the initial state, as discussed above. The fluctuations grow fast at the beginning and are then seen saturating at a value clearly below the infinite-temperature limit. This can be explained by experimental imperfections, such as imperfect initial state filling (cf. Eq. 5.7), disorder and finite size effects, and raises the question to what extent the (chaotic) system actually fully thermalizes, as discussed in Sec. 6.2 and Sec. 6.3.

Importantly, one finds that for larger subsystem sizes the fluctuation growth is slower. This is due to the fact that larger subsystems take longer to become correlated with their environment because of the finite speed at which entanglement and correlations can spread in the system. The fluctuation growth speed difference between the integrable and the chaotic case is particularly enhanced in large subsystems such as $L = 10$, consistent with the spreading of density-density correlations discussed in Sec. 5.5.

Fig. 5.6 provides an alternative perspective on the data shown in Fig. 5.5 and presents the time evolution of the variance sorted by $J_\perp/J$ instead of subsystem size L. Here, the variance

$$\overline{\mathrm{Var}}_L(t) = [\mathrm{Var}_L(t) - \mathrm{Var}_L(0)]/[\mathrm{Var}_L(\infty) - \mathrm{Var}_L(0)], \tag{5.8}$$

has been normalized with respect to the saturation value (red) and the initial state value (blue), directing particular attention to how the fluctuation growth speed scales with subsystem size and highlighting the slow fluctuation growth in large chaotic subsystems (right panel). In the following, we will quantify the fluctuation growth and discuss Fig. 5.6 in more detail.

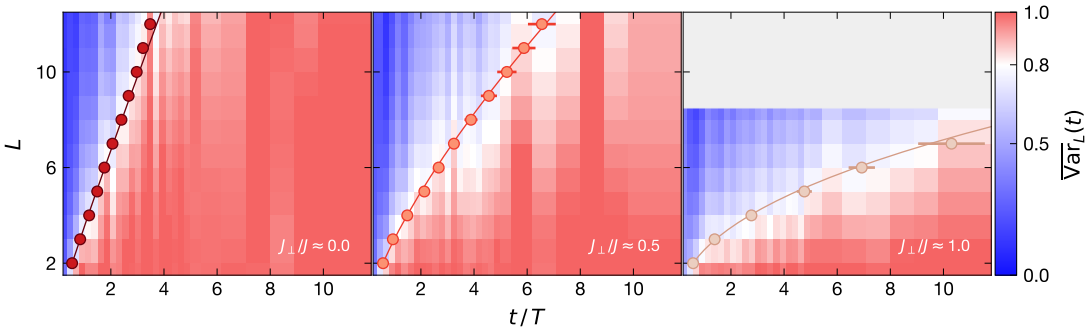

Figure 5.6 | Time evolution of particle number fluctuations sorted by $J_\perp/J$. Measured atom number variance in subsystems of various sizes for $J_\perp/J \approx 0.0, 0.5, 1.0$, normalized to the initial state value (blue) and the late time saturation value (red), as defined in Eq. 5.8. The data points show the saturation time t_{sat} of the fluctuations after which the variance has reached 80% of its saturation value. The solid lines are fits to these data points to obtain the scaling exponent z in $L \sim t_{\mathrm{sat}}^{1/z}$ as shown in Fig. 5.7. Error bars denote the uncertainty of the fit. The grey area in the right panel indicates the parameter regime where the fluctuation growth is too slow to reliably extract the saturation value by fitting the data.

Scaling

As a measure for the fluctuation growth speed, we define a saturation time t_{sat}: It is the time after which the particle number variance has reached 80% of its saturation value. We obtain t_{sat} from the experimental data by fitting the fluctuation growth traces in Fig. 5.5. The fit function is empirical and has a form which is reminiscent of the Fermi-Dirac distribution:

$J_\perp/J$	z
≈ 0.0	1.07(6)
≈ 0.5	1.4(2)
≈ 1.0	2.2(4)

Table 5.1 | Fluctuation growth scaling exponents. Scaling exponents z in Eq. 5.10 extracted from the data shown in Fig. 5.7 using the fit function in Eq. 5.9.

$$\mathrm{Var}(t, \mathrm{Var}_\infty, k, d) = (\mathrm{Var}_\infty - \mathrm{Var}_0)\left(\frac{2}{1+e^{-k\,t^d}} - 1\right) + \mathrm{Var}_0. \tag{5.9}$$

Here, $\mathrm{Var}_0 = \mathrm{Var}(t=0)$ and $\mathrm{Var}_\infty = \mathrm{Var}(t\to\infty)$. The free fit parameters are Var_∞, d and k, while Var_0 is fixed to the measured variance at $t=0$. We then determine the intersection of the fit result with the 80% threshold of the fitted saturation value, which defines the saturation time t_{sat} (i.e., 0% corresponds to Var_0 and 100% is corresponds to Var_∞). Both Fig. 5.6 and Fig. 5.7 show t_{sat} as a function of subsystem size for $J_\perp/J \approx 0.1, 0.5, 1.0$, with linear and logarithmic axes, respectively. The logarithmic plot reveals that there is a polynomial scaling between t_{sat} and L, as expressed by:

$$L \sim t_{\mathrm{sat}}^{1/z}, \tag{5.10}$$

with scaling exponent z [15, 272, 273]. Using a linear fit (solid lines in Fig. 5.7) we obtain the values shown in Tab. 5.1. These values agree with the expectation that, on the one hand, the dynamics in the decoupled chains ($J_\perp/J \approx 0.0$) are integrable ($z=1$), such that the speed at which a subsystem becomes correlated with the environment scales linearly with its size. On the other hand, the dynamics in the system with fully coupled legs ($J_\perp/J \approx 1.0$) are diffusive ($z=2$), such that the scaling is quadratic. For $J_\perp/J \approx 0.5$, we find a scaling exponent that lies between the ballistic and the diffusive limit and can be interpreted as a crossover situation between ballistic and diffusive dynamics. This special case is discussed in more detail in the following Section which focusses on the spreading of density-density correlations.

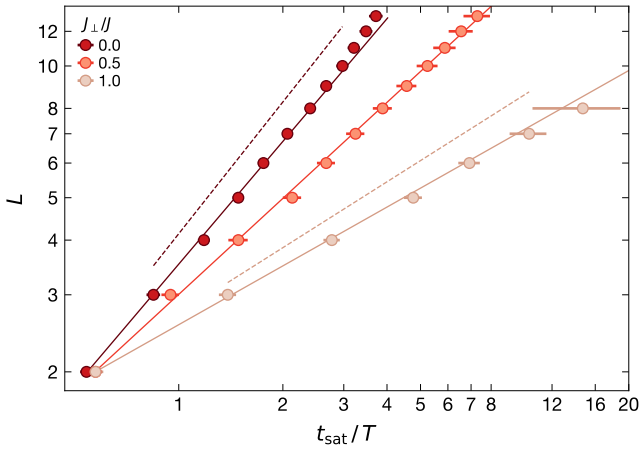

Figure 5.7 | Scaling of fluctuation growth timescales. Fluctuation saturation time t_{sat} as a function of subsystem size for $J_\perp/J \approx 0.0, 0.5, 1.0$. The solid lines are linear fits for extracting the scaling exponent z in $L \sim t_{\mathrm{sat}}^{1/z}$. The dashed lines are guide to the eyes, corresponding to ballistic dynamics ($z=1$, dark red) and diffusive ($z=2$, light red) dynamics.

5.5 Density-density correlations

While partitioning the overall systems in larger and larger subsystems is a form of coarse-graining toward a hydrodynamic point of view, the dynamics of the system eventually root in the microscopic laws that govern the interactions between the particles and how they become entangled with each other. An important consequence of spatial entanglement are density-density correlations. Thanks to our ability to resolve individual lattice sites, we can directly access them at equal times [59, 62, 73] (unequal time correlators are out of reach as taking a fluorescence image destroys the quantum state). The density-density correlations are closely related to the number fluctuations discussed in the previous Section. In fact, the particle number variance for a certain subsystem of length L can be expressed as a sum of density-density correlators involving distances up to $d = L$ (see Appendix D).

Definitions

The connected density-density correlator for two sites at position i and j in leg $\alpha = 1, 2$ and $\beta = 1, 2$, respectively, is defined as:

$$C_d^{\alpha,\beta} = \langle \hat{n}_{\alpha,i} \hat{n}_{\beta,j} \rangle - \langle \hat{n}_{\alpha,i} \rangle \langle \hat{n}_{\beta,j} \rangle , \tag{5.11}$$

where $\alpha, \beta = 1, 2$ denote the legs of the ladder and i, j label sites with distance $d = i - j$ along the ladder. Positive (negative) values mean that if there is an atom on site i in leg α the probability to find an atom (a hole) at position j in leg β is enhanced compared to what one would expect from the mean filling in the system. The average $\langle ... \rangle$ in Eq. 5.11 is taken, firstly, over all ladders in all fluorescence images (index k) in the ROI and then, secondly, over all possible pairs of site indices corresponding to the same distance $d = i - j$, i.e. $\langle ... \rangle = \langle \langle ... \rangle_k \rangle_d$.

In the following, we will focus on three different types of connected correlators in the ladder system:

- The density-density correlations within the same leg ($\alpha = \beta$), averaged over both legs:

$$C_d^I = \frac{1}{2} \left(C_d^{1,1} + C_d^{2,2} \right) . \tag{5.12}$$

- The density-density correlations between sites in different legs ($\alpha \neq \beta$):

$$C_d^{II} = \frac{1}{2} \left(C_d^{2,1} + C_d^{1,2} \right) . \tag{5.13}$$

- The density-density correlations of the rungs of the ladder:

$$C_d^{III} = \langle \hat{N}_i \hat{N}_j \rangle - \langle \hat{N}_i \rangle \langle \hat{N}_j \rangle . \tag{5.14}$$

  Here, $\hat{N}_i = \hat{n}_{1,i} + \hat{n}_{2,i}$, the total atom number in the rung at position i. One can show that

$$C_d^{III} = 2 \left(C_d^I + C_d^{II} \right) . \tag{5.15}$$

The third correlator C_d^{III} effectively treats the ladder system as one-dimensional and is the most natural choice when investigating the crossover from an integrable truly one-dimensional system (where it should match C_d^I) to a chaotic quasi-one dimensional ladder. Further, as C_d^{III} combines more two-site correlation terms, it is expected to have the highest signal-to-noise ratio. The autocorrelator C_0^{III} is equal to the particle number variance in a ladder subsystem of length $L = 1$. The second correlator C_d^{II} is interesting for studying how the two legs of the ladder become correlated over time due to the coupling between the legs of the ladder for $J_\perp / J > 0$.

Measured correlation spreading

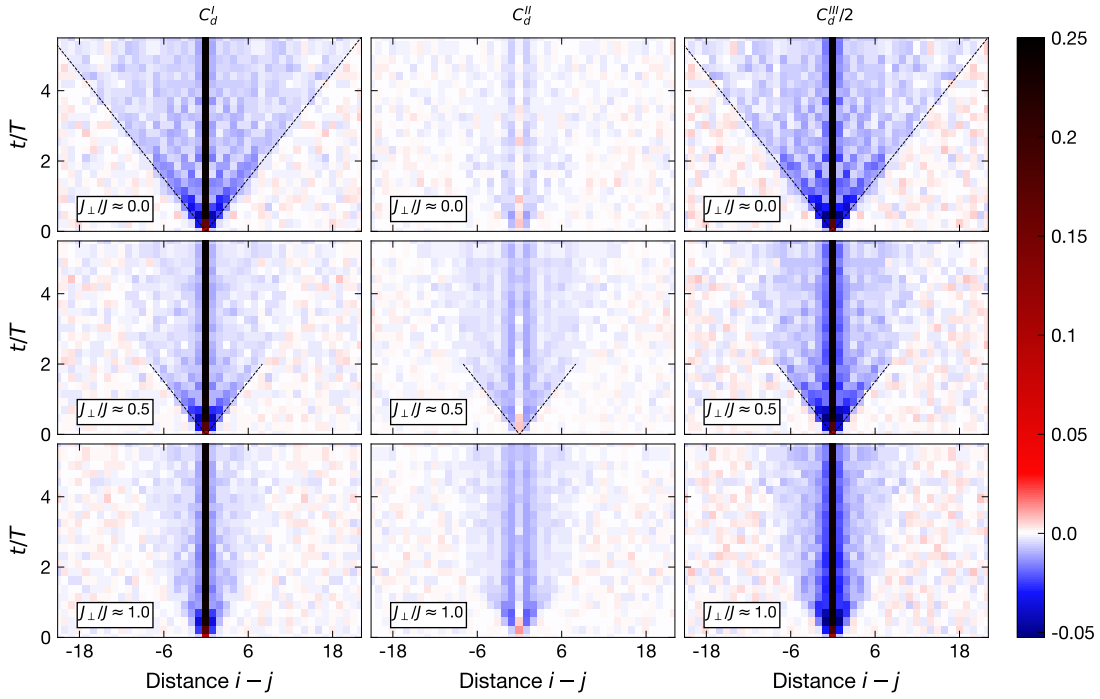

Figure 5.8 | Time-evolution of the density-density correlations. Density-density correlation profiles C_d^I (within 1d chains), C_d^{II} (between 1d chains) and C_d^{III} (rung correlations) as a function of evolution time after the quench for $J_\perp/J \approx 0.0, 0.5, 1.0$, obtained from 35 fluorescence images. The dashed lines indicate the maximum speed at which correlations can spread according to the Lieb-Robinson velocity ($4Ja/\hbar$).

Fig. 5.8 shows all three measured correlators as a function of distance $d = i - j$ and evolution time after the quench for $J_\perp/J = 0.0, 0.5, 1.0$. The emerging *cones* paint a clear picture of how correlations spread in the system depending on what kind of dynamics are at play: In the integrable case ($J_\perp/J \approx 0.0$, top row in Fig. 5.8), we find a correlation cone with a linear envelope, suggesting that the density-density correlation front spreads ballistically at constant speed. The slope of the cone's envelope is consistent with $4Ja/\hbar$ (dashed lines), where $a = a_{\text{short}} = 383.5\,\text{nm}$ is the lattice spacing in the short lattice. This is the Lieb-Robinson-velocity predicted by free fermion dynamics [176] (cf. Appendix C). It equals twice the group velocity of free fermions and corresponds to the maximum velocity that two fermions can have relative to each other [274, 275]. Also note the stripy inner structure of the cone, resulting from coherent quantum dynamics, similar to a single-particle quantum random walk.

In the chaotic case ($J_\perp/J \approx 1.0$, bottom row in Fig. 5.8), we find a cone with an inward-bending envelope that suggests faster correlation spreading at short times and slower spreading at late times. This is consistent with diffusive fluctuation growth which, as we have seen in Section 5.4, leads to a quadratic scaling between saturation time and subsystem size. If we take the scaling exponent obtained in the preceding Section ($z \approx 2$) and use the relationship between particle number fluctuations and density-density correlations (cf. Appendix D), we find that the envelope of the diffusive cone is described by a square-root function $\sigma_{\text{env}} = \sqrt{Bt}$, where σ_{env} is the Gaussian σ-width of the correlation cone and B is a scaling parameter that can be predicted using FHD (see Section 2.4). As shown in Sec. 5.7, we can use this property to obtain the diffusion constant.

In the crossover case of $J_\perp/J \approx 0.5$ (middle row in Fig. 5.8), the density-density correlations provide

intuition for what happens in a system where integrability is *weakly* broken [270]. We find a *mixed cone* with a ballistic onset at short times ($t < 2T$), followed by an inwards turning envelope at later times ($t > 2T$), which looks more similar to the diffusive cone observed for $J_\perp/J \approx 1.0$. The crossover, thus, turns out to be a crossover *in time* from ballistic to diffusive dynamics [276–278]. The timescale separating short-time ballistic and long-time diffusive behavior is set by $\hbar/J_\perp$ which determines how long it takes for the ladder system to realize that its two legs are coupled and to probe its dimensionality – and it is the coupling of the legs that leads to a break-down of the free fermion mapping and, therefore, to a breakdown of integrability. To our knowledge, our measurement constitutes the first direct observation of such a crossover situation using microscopic observables. It beautifully illustrates how the timescales on which hydrodynamics emerge depend on the level of integrability breaking and how long it takes for partially conserved modes with ballistic spreading to die out. Notably, the cone observed in the chaotic case ($J_\perp/J \approx 1.0$) also appears ballistic in the limit of very short evolution times, consistent with a square root envelope.

In comparison with C_d^{III}, the C_d^I correlator exhibits qualitatively the same behavior but has a worse signal-to-noise ratio for $J_\perp/J > 0$, as it only contains information from individual ladder legs. If there is a non-zero coupling between the two legs of the ladder, density-density correlations not only emerge along but also perpendicular to the chain. The density-density correlations between the two legs are captured by C_d^{II} (middle column), which is zero for $J_\perp/J \approx 0$ and grows in amplitude as $J_\perp/J$ approaches 1.

Hydrodynamic tail

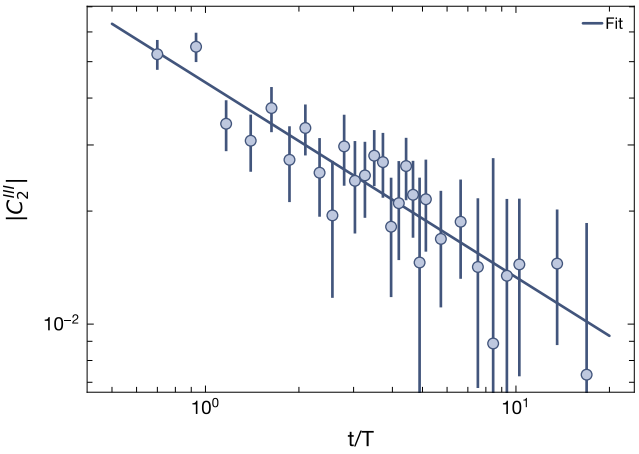

Figure 5.9 | Hydrodynamic tail. Magnitude of the rung density-density correlator C_2^{III} for distance $d = 2$ in the chaotic case ($J_\perp/J \approx 1.0$) as a function of the evolution time after the quench. The solid line is a fit to the experimental data to extract the exponent of the polynomial decay $|C_2^{III}(t)| \sim t^{-\xi}$, yielding $\xi = 0.519(41)$. This suggests that global equilibrium is approached slowly in what is known as a hydrodynamic tail. Error bars denote the standard deviation.

In a hydrodynamic system, the density-density correlations are expected to approach their equilibrium value algebraically as $\sim t^{-0.5}$, as discussed in Sec. 2.4. To check to what extent our quantum system follows this expectation, Fig. 5.9 plots the magnitude of the rung density-density correlator $|C_2^{III}(t)|$ for distance $d = 2$ as a function of the evolution time $t > 0.5\,T$ after the quench. Early times $t < 0.5\,T$ are excluded from this analysis due to the finite time it takes for correlations to spread to non-zero distances. We fit the data using a polynomial decay function:

$$|C_2^{III}(t)| = A\,t^{-\xi}, \tag{5.16}$$

where ξ is the decay exponent. The fit yields $\xi = 0.52(4)$, in excellent agreement with the expectation $\xi = 0.5$. This indicates the presence of a hydrodynamic long-time tail, a symptom of the system's slow diffusive path toward global equilibrium [195]. The hydrodynamic tail should appear in density-density correlators belonging to all distances. However, care must be taken when choosing larger distances as only the late-time behavior after local thermalization is hydrodynamic.

5.6 Separation of equilibration timescales

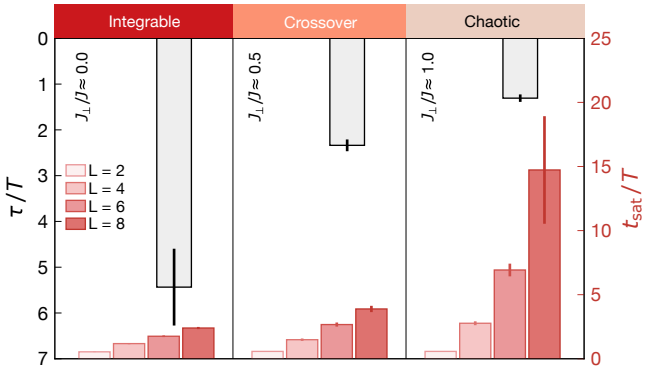

Figure 5.10 | Separation of equilibration timescales. Fluctuation saturation time t_{sat} for various subsystem sizes $L = 2, 4, 6, 8$ and imbalance decay constant in comparison with each other for $J_\perp/J \approx 0.0, 0.5, 1.0$. These quantities exhibit opposite behavior in the limits of $J_\perp/J \approx 0.0, 1.0$, indicating a separation of equilibration timescales. Error bars denote the standard error of the corresponding fits.

In Sec. 5.3 we have fitted the decay constant of the imbalance decay, which is the relaxation time of a mean local observable. In Sec. 5.4 we have obtained the fluctuation saturation timescales of the total particle number in subsystems of various sizes, which are relaxation times of coarse-grained quantities. Fig. 5.6 presents and compares all these measured equilibration timescales at a glance and, in doing so, visualizes an important feature of emerging FHD: As we tune the system from integrable ($J_\perp/J \approx 0.0$) to chaotic ($J_\perp/J \approx 1.0$), the imbalance decay is enhanced, while fluctuation growth is slowed down. Particularly in the chaotic case for large system sizes, there is a strong *separation of equilibration timescales*: While the local mean density decays quickly on the order of a single tunnelling time, the fluctuations in a subsystem of length $L = 8$ saturate on a timescale that is more than 10 times longer – and, as shown in Sec. 5.4, there is a quadratic scaling between the fluctuation saturation time and the subsystem size. As a consequence, while the system might look locally like it has already thermalized because the mean density has flattened out, it actually has not since the fluctuations are still growing. This underlines the importance of studying not only the mean but also higher moments of the FCS in order to obtain a complete picture of the non-equilibrium dynamics at play. In this work, we focus only on the mean and the fluctuations, limited by the the amount of data we are able to take and the quality of our data in light of experimental imperfections and initial state quality. However, measuring higher moments is in the scope of future experiments, as pointed out in the Outlook.

Note that both in the integrable and in the chaotic case the imbalance and the subsystem fluctuation will eventually reach the same saturation values, even though the integrable system does not thermalize. Thus, the FCS of the particle number (a real space observable) alone are generally insufficient for telling whether a late-time state is thermal or not – especially if the infinite number of conservation laws in the integrable case concern momentum space.

5.7 Extracting the diffusion coefficient

Experimental evidence for FHD

How fluctuations grow and particle density variations time-evolve in out-of-equilibrium systems are important questions that FHD tries to answer. FHD is a classical macroscopic theory which does not require knowledge about the microscopic physics of the system. Instead, FHD equations describe the time evolution of few coarse-grained conserved quantities in presence of random noise. Even though the ladder system under investigation in this Chapter is governed by the laws of quantum mechanics on a microscopic scale, we have found strong evidence for hydrodynamic behavior in agreement with the predictions from FHD:

- In Sec. 5.4, we have seen that, in the chaotic case ($J_\perp/J \approx 1.0$), the saturation timescale of the particle number fluctuations scales quadratically with system size, as expected in hydrodynamic systems.
- In Sec. 5.5, we have directly observed the diffusive spreading of correlations as a light cone shaped by a square root envelope.
- Also in Sec. 5.5, we have found that, in the chaotic case, the density-density correlations decay polynomially as $\sim t^{-0.5}$ in what is known as a *hydrodynamic tail*.
- In Sec. 5.6, comparing the saturation timescales of local mean densities and fluctuations has revealed a strong separation of equilibration timescales in large subsystems, typical for systems governed by hydrodynamic processes.

These observations suggest that FHD could provide not only a qualitative but also a quantitative description of out-of-equilibrium quantum systems. Strikingly, this would mean that not only the equilibrium dynamics but also the non-equilibrium dynamics after a quench (which we measure) must be fully determined by a single quantity – the linear-response diffusion constant. The strategy for quantitatively testing the predictions of FHD will be to extract this diffusion constant from our experimental data and compare it to computed values from the literature. Crucially, while we can obtain the diffusion constant from a far-from-equilibrium measurement, the reference values from the literature were computed in an equilibrium setting. Hence, by showing quantitative agreement between experimental and theoretical values, we build on an intriguing relationship between the equilibrium properties (the diffusion constant) of the system and its non-equilibrium fluctuations. This extends the notion of fluctuation-dissipation relations to far-from-equilibrium scenarios.

Extracting the diffusion constant from fluctuation growth

One way to obtain the diffusion constant D is to fit the chaotic fluctuation growth using an FHD prediction with D as a free fit parameter. In Sec. 2.4 we have discussed a simple derivation of the time evolution of the particle number variance in large subsystems at short times (cf. Eq. 2.45). This result can be further refined and adapted to a ladder geometry through a hydrodynamic description of quantum operator evolution [279]. As detailed in the supplementary information of Ref. [16], the final fit function for the variance at short times ($t \ll (La)^2/D$) reads:

$$\mathrm{Var}(\mathcal{N}_L(t))_{\mathrm{CDW}} = A\sqrt{\frac{2Dt}{\pi\, a^2}} + c. \tag{5.17}$$

Here, A is a scaling factor and c is an offset parameter. They take account for the fact that due to defects in the pre-quench CDW, the fluctuations at $t = 0$ are non-zero and the overall growth amplitude is diminished. The prefactor A is given by the difference between the susceptibility χ (or the variance of

a randomly occupied single site, cf. Eq. 5.6) and the measured variance of single site $t = 0$, averaged over all sites in the system:

$$A = 4\,(\chi - \langle \mathrm{Var}(\hat{n}_{\alpha,i})\rangle_{\alpha,i}). \tag{5.18}$$

The factor 4 normalizes the expression to 1. Under ideal conditions with a perfect initial state, the experimental variance should vanish and, since $\chi(\bar{n} = 0.5) = 0.25$ (Eq. 5.6), we get $A = 1$.

Fig. 5.11 shows the time evolution of the particle number variance for a subsystem of size $L = 16$. Because of its large size this subsystem thermalizes on timescales far beyond what we can observe in our experiment and we do not see the fluctuations saturate. However, it is the growth on short timescales before saturation where the prediction from FHD is expected to hold. Fitting the variance data in Fig. 5.11 using Eq. 5.17 with free fit parameters D and c yields $D = 1.11(25)\,Ja^2/\hbar$.

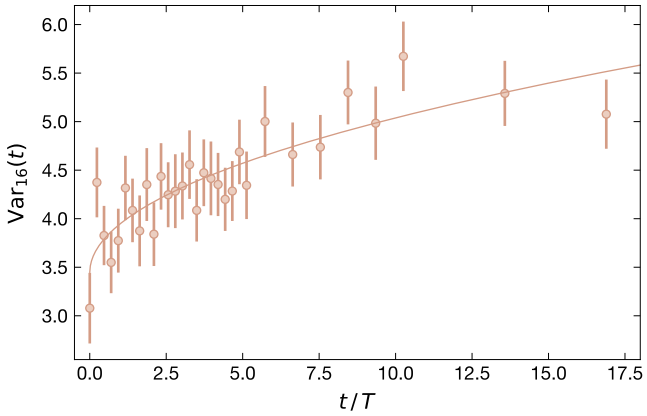

Figure 5.11 | Extracting the diffusion constant from the variance time evolution. Atom number variance for a subsystem of size $L = 16$ as a function of the evolution time after the quench. The solid line is a fit to the experimental data using the FHD prediction for the time evolution of the atom number variance (Eq. 5.17) and yields $D = 1.11(25)\,Ja^2/\hbar$. Error bars denote the standard deviation.

Extracting the diffusion constant from density-density correlation spreading

Another way to obtain the diffusion constant D is to fit the measured density-density correlations in the chaotic case (cf. Fig. 5.8 and Fig. 5.12a) using the FHD prediction with D as a free fit parameter. Disregarding the autocorrelator ($d = 0$), the fit function is given by Eq. 2.40 with an added offset c and a generic amplitude A:

$$C_d^{III} = A\frac{a\,e^{-\frac{d^2a^2}{8Dt}}}{2\sqrt{8\pi Dt}} + c. \tag{5.19}$$

It describes a Gaussian profile with an envelope that grows polynomially according to:

$$\sigma_{\mathrm{env}}(t) = \sqrt{4Dt/a^2}. \tag{5.20}$$

The free fit parameters are c, A and the diffusion constant D. The fitted date includes only (non-local) correlations belonging to distances $1 \leq d \leq 20$, excluding the autocorrelator. The latter is a local quantity with different dynamics, approaching a value related to the susceptibility of the system instead of decaying to zero as an hydrodynamic tail (cf. Sec. 2.4). We obtain a diffusion constant of $D = 0.88(5)\,Ja^2/\hbar$

Source	D ($Ja^2/\hbar$)
from $\mathrm{Var}_{L=16}(t)$ (measured, Fig. 5.11)	1.11(25)
from $C_d^{III}(t)$ (measured, Fig. 5.12)	0.88(5)
from [280] (theory)	0.95
from [281] (theory)	≈ 0.97

Table 5.2 | Comparison of measured diffusion constants with theory. The measured linear-response diffusion constants are in very good agreement with theory values taken from linear-response studies in the literature. Remarkably, we extract D (an equilibrium property) from observing the fluctuation dynamics after a quench in a far-from-equilibrium setting. The good agreement suggests that FHD provides not only a qualitative but also a quantitative description of our closed chaotic quantum system.

Fig. 5.12 juxtaposes the experimentally measured density-density correlations and the fit applied to the data. Note that the uncertainty of the fitted diffusion constant is smaller compared to that of the value obtained from the variance time evolution fit. This is because, if we use the entire correlation cone for fitting (rather than the variance which combines many correlators into a single quantity, see Eq. D.1), the number of individual correlators and, thus, the amount of information available to the fit is larger.

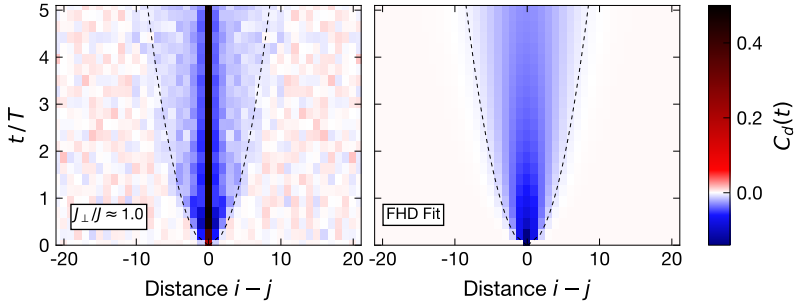

Figure 5.12 | Extracting the diffusion constant from the density-density correlations. a, Rung density-density correlations as a function of evolution time after the quench for the chaotic case with $J_\perp/J \approx 1$ **b**, Fit to the experimental data in (**a**) (distances $1 \leq d \leq 20$) using the prediction from FHD, yielding a diffusion constant of $D = 0.88(5)\, Ja^2/\hbar$. The dashed curves indicates the $2\,\sigma_{\mathrm{env}}$-envelope of the Gaussian fit function (Eq. 5.20).

Discussion

Both values for the linear-response diffusion constant fitted above from non-equilibrium data are in good agreement with computed values reported in the literature in the context of linear-response theory ($D = 0.95\, Ja^2/\hbar$ [280], $D \approx 0.97\, Ja^2/\hbar$ [281]), see Tab. 5.2 for a summary. This is strong evidence that the classical FHD description indeed applies to our chaotic quantum system and is able to describe its far-from-equilibrium behavior starting from an infinite-temperature state. This means that the non-equilibrium dynamics are determined by a single quantity – the equilibrium diffusion constant of the system. Diffusion constants describing quantum many-body systems are hard to compute numerically. In our experiment we obtain this quantity with high precision within a few hours of data taking.

Most generally, the diffusion constant depends on the density and the temperature T of the initial state. Further, the dynamics of the density can be coupled to the dynamics of the energy ϵ in the system through thermoelectric coupling, such that $D = D(n, \epsilon, T)$. The setting of this experiment is a ladder system at half filling in which an infinite-temperature initial state time-evolves after a quench. At half

filling, linear thermoelectric coupling can be ruled out due to particle-hole symmetry and must enter non-linearily through the transport coefficients. However, at infinite temperature, a $\epsilon \leftrightarrow -\epsilon$ symmetry holds, such that $D(\varepsilon, n) \sim D(n) + \mathcal{O}(\varepsilon^2)$ and any hydrodynamic corrections resulting from that are expected to be subleading [16]. Since the initial density variation is short-spaced, the average filling in the entire system approaches ≈ 0.5 very quickly. Thus, the diffusion constant we measure is the infinite-temperature half-filling constant. Repeating the measurements for initial states of finite temperature in systems of different fillings requires additional corrections to the simple FHD model describing this system. Observing and characterizing these quantitatively, however, is beyond the scope of this work.

CHAPTER 6

Characterization of experimental imperfections

This Chapter mainly presents benchmark measurements characterizing the experimental conditions under which the results in Chapter 5 were obtained. We identify potential sources of systematic errors, including atom loss, disorder in the lattice potentials and finite-size effects and assess how these imperfections affect the experimental data. In addition, we show that the challenging imaging resolution leads to correlated reconstruction errors and describe a method for correcting them in the density-density correlations.

6.1 Atom loss

Atom loss occurs due to parametric heating in the optical lattice or the dipole traps due to scattering events involving the trapping light [282]. Atoms are also lost due to collisions with residual gas particles in the imperfect vacuum [283]. Further, if we are insufficiently deep in the hard-core limit, doublons can form [284]. These are then lost due to light-assisted collisions during imaging and, therefore, contribute to a decrease of the visible atom number. While atom loss due to the vacuum lifetime is independent of the lattice parameters, heating and doublon generation tend to be enhanced in shallower lattice potentials when the parametric resonances are smaller, the particles can move and interact and the on-site interaction energy U is reduced due to weaker confinement. In our experiment, the lifetime of the atoms deep in the MI regime is typically on the order of seconds, while in post-quench conditions with $J, J_\perp/h \approx 100\,\mathrm{Hz}$ (cf. Sec. 5.2) it is reduced to just hundreds of milliseconds. Atom loss due to thermal hopping during the exposure time of the imaging process is not considered here, see Sec. 3.4 for details.

Fig. 6.1 shows the atom number N_{atom} (normalized to the initial state) as a function of the evolution time after the quench for $J_\perp/J \approx 0.0, 0.5, 1.0$. We use an exponential fit to extract the lifetime τ (only including data points with $t > T$). The fit yields $\tau = 650(120), 420(50)$ and $330(44)\,\mathrm{ms}$ for $J_\perp/J \approx 0.0, 0.5, 1.0$, respectively, suggesting that atoms in the coupled ladder (shallower lattice potentials) are more susceptible to heating. Another important observation is the sharp drop immediately after $t = 0$ in the $J_\perp/J \approx 1$ data. It is most likely caused by the non-zero doublon fraction which emerges shortly after the lattice depth is quenched down, taking us further away from the hard-core limit to $U/J \approx 7$. For all values of $J_\perp/J$ considered in this work, we made sure that the total atom loss after the quench does not exceed 10%. This limits our experiments to a maximum evolution time of approximately 18 tunnelling times.

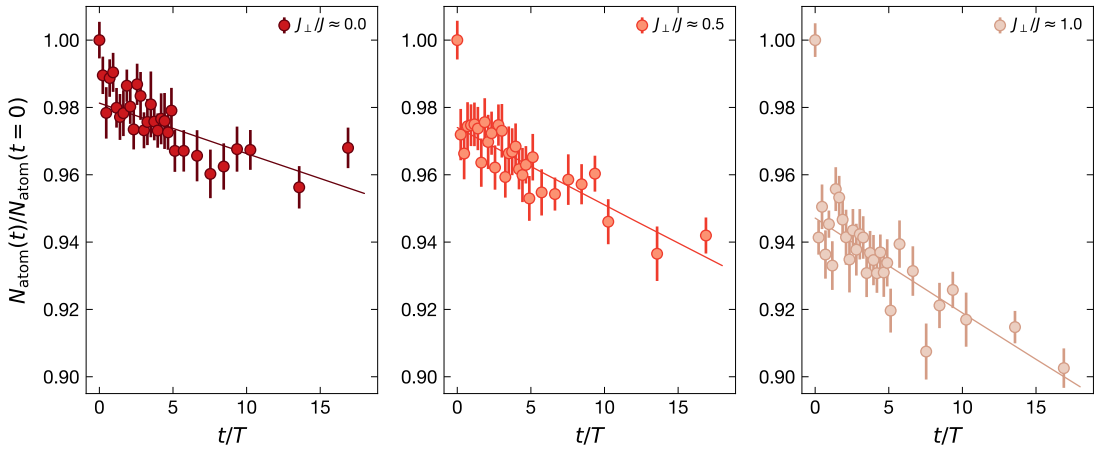

Figure 6.1 | Atom loss during the time evolution after the quench. Fraction of remaining atoms in the ROI as a function of evolution time. The solid lines are exponential fits for obtaining lifetimes. The sudden drop of the atom number directly after the quench (particularly visible for the fully coupled ladder with $J_\perp/J \approx 1$) is attributed to an enhanced doublon fraction which is lost due to parity projection and results in apparent atom loss. Error bars denote the standard error.

6.2 Disorder

Free fermion simulations

The potential landscape realizing the quantum ladder systems in not perfectly homogeneous. On the one hand, imperfect overlapping of the lattice beams with their retro-counterparts as well as the shallow vertical lattice light introduce harmonic confinement that bend the ladders away from the center of the ROI. As described in Section 4.6, we can remove this harmonic confinement using a DMD. On the other hand, wavefront errors in the lattice beams as well as uncontrolled back-reflections on optical surfaces can cause small-scale disorder of a more random kind that cannot be easily compensated with programmable potentials, especially given our short-spaced optical lattices. In order to study the impact of potential disorder and better characterize its presence in our system, we perform benchmark simulations for the integrable case ($J_\perp/J = 0$). Here, we can take advantage of the fact that the hard-core Bose-Hubbard Hamiltonian in Eq. 5.1 can be mapped onto free-fermions (see Appendix C for details), allowing to efficiently compute the time evolution of local observables and non-local correlators. The simulation is performed in one dimension with $N = 50$ sites and open boundary conditions. Mimicking the evaluation of the actual experimental data, we consider the innermost 40 sites as our ROI, leaving a buffer zone of five sites on either side. If not stated otherwise, the simulation results shown below are averaged over 600 runs with initial states randomly sampled from the experimental filling probabilities in even and odd rows of the CDW initial state (cf. Sec. 4.5).

The exact type of the small-scale disorder in our system is not known. Thus, we consider both white noise (random and uncorrelated) and Aubry-André-type disorder (deterministic). White noise is modelled by introducing on-site energy shifts V_i (cf. Eq. C.10) that are randomly sampled from an interval $[-\Delta, \Delta]$, where Δ quantifies the disorder strength. In contrast, Aubry-André disorder [285] consists of a periodic sine potential (wavelength λ_{AA}, phase ϕ) modelled by:

$$V_i = \Delta \sin\left(2\pi i/\lambda_{\mathrm{AA}} + \phi\right). \tag{6.1}$$

The phase ϕ is randomly sampled from an interval $[0, 2\pi]$ and Δ is the disorder amplitude.

Mean imbalance. – In presence of local small-scale disorder the local tunneling behavior will vary from site to site. As a consequence, imbalance oscillations in the ROI (cf. Section 5.3) are expected to dephase and the mean imbalance (averaged over the ROI) will decay faster. We simulate the time evolution of the mean imbalance and fit the traces using Eq. 5.4 to obtain the decay constant τ. In Fig. 6.2a we plot τ as a function of disorder strength Δ for white noise and Aubry-André-type disorder. For reference, the horizontal line indicates the experimentally measured decay constant (cf. Sec. 5.3). From the intersection of the simulated decay constants with the experimental reference value we find that the measured imbalance decay is consistent with a disorder strength of about $\Delta \approx J$, irrespective of what type of disorder is present. In the following, we will assume white noise for simplicity. The effect of white noise of strength $\Delta = J$ is shown in Fig. 6.2b which compares the experimental time evolution of the imbalance with simulated traces, both with and without disorder. One can see that the presence of white noise disorder enhances the damping of the mean imbalance in the ROI and that the experimental data is consistent with a disorder strength of $\Delta = J$.

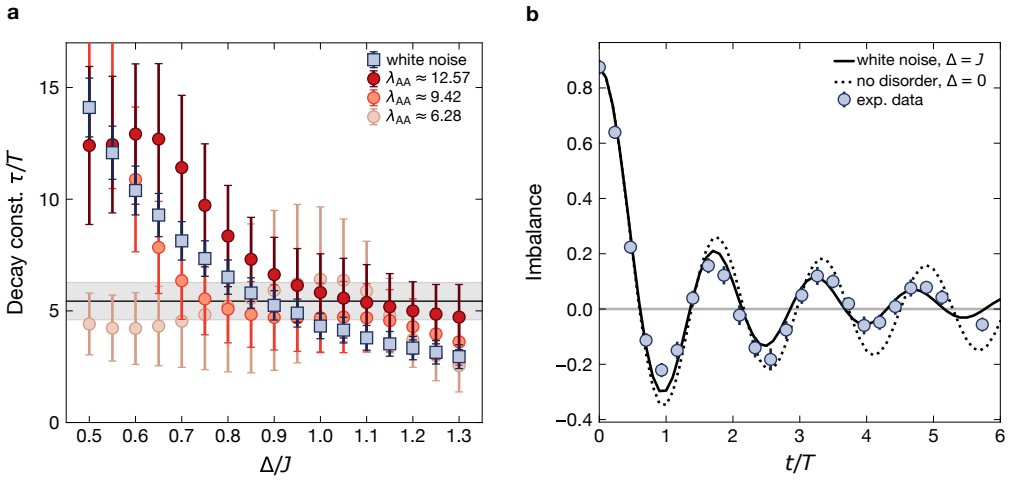

Figure 6.2 | Estimation of the disorder strength in the experiment. A free-fermion approach is used to simulate the decay of a CDW initial state in presence of different disorder types and strengths ($J_\perp/J = 0$). **a**, Decay constant of the imbalance time evolution as a function of disorder strength for white noise disorder as well as for Aubry-André-type disorder of various wavelengths λ_{AA} (in units of lattice sites). The black horizontal line and shaded region show the experimentally measured decay constant (cf. Fig. 5.4) and its uncertainty. Error bars denote the fit error. The intersection of the experimental value with the simulated traces allows to estimate that the disorder strength in the experiment is about $\Delta \approx J$. **b**, Simulated time evolution of the imbalance for white noise disorder ($\Delta = J$) and no disorder ($\Delta = 0$) in comparison with the experimental imbalance data for $J_\perp/J = 0$.

Density-density correlations. – Fig. 6.3a shows the density-density correlations obtained from the free fermion simulations as a function of distance and time, in analogy with the experimental data depicted in Fig. 5.12. In presence of random white noise disorder of strength $\Delta \approx J$, the internal structure of the cone is washed out, particularly after longer evolution times ($t > 3T$). While the maximum speed of correlation spreading (the envelope of the cone) is unaffected, the density-density correlations seem to partially concentrate at shorter distances, indicating a higher degree of Anderson localization [286–288].

Anderson localization length. – The amount of Anderson localization present in the system is quantified by the Anderson localization length ξ_{1d} which corresponds to the typical distance over which density-density correlations can spread. We can relate ξ_{1d} and the disorder amplitude Δ using additional free fermion simulations as follows: Instead of a CDW, we choose an initial state $\psi(t = 0)$ representing a single particle placed in the center of the overall system. In order to mitigate finite-size effects, the overall system size is set to $L_{tot} = 151$. When released from its starting position the particle

will delocalize over time. The amount of single-particle delocalization in $\psi(t)$ can be quantified using the inverse participation ratio (IPR):

$$\mathrm{IPR} = \left(\sum_{i}^{L_{\mathrm{tot}}} \langle n_i \rangle^2 \right)^{-1}, \tag{6.2}$$

where $\langle n_i \rangle$ is the mean occupation of site i. The IPR is related to $\xi_{1\mathrm{d}}$ via [289]:

$$\mathrm{IPR} = \coth(1/\xi_{1\mathrm{d}}) \tanh(L_{\mathrm{tot}}/\xi_{1\mathrm{d}}), \tag{6.3}$$

allowing to obtain $\xi_{1\mathrm{d}}$. For a white-noise disorder of strength $\Delta = J$ we find $\xi_{1\mathrm{d}} = 18$ lattice sites. It is the lengthscale over which we expect the inner structure of the correlation cone to wash out and the correlations to concentrate at short distances (cf. Fig. 6.2a).

Fluctuations. – Following Section 5.4, we also compute the particle number fluctuations in subsystems of different length L, as shown in Fig. 6.3b. Again, assuming white noise disorder of strength $\Delta \approx J$, we find excellent agreement between the simulated traces (solid lines) and the experimental data (markers). For comparison, Fig. 6.3b also shows the simulated variance evolution in absence of disorder (dashed lines), revealing how disorder decreases the saturation value of the fluctuation amplitude, particularly in large subsystems. This illustrates how Anderson localization due to disorder prevents the system from fully reaching global equilibrium (in an ETH sense) and suppresses the thermalization of non-local observables. The simulation also takes into account defects in the initial state, which have a small impact on the saturation value of the variance but mainly lead to an offset at $t = 0$. This is important for finding agreement between the simulated and experimental traces at short evolution times.

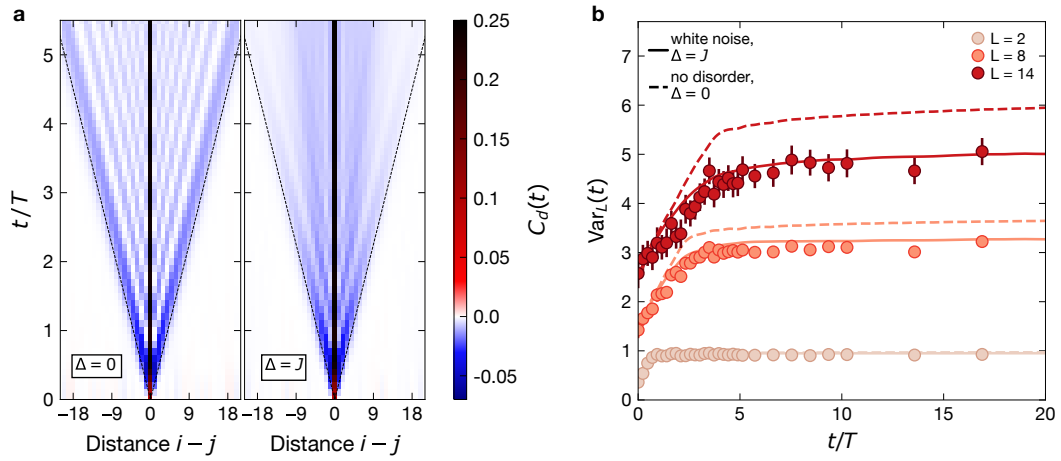

Figure 6.3 | Impact of disorder on density-density correlations and particle number fluctuations. a, Simulated density-density correlations for the ballistic case ($J_\perp/J = 0$) without (left panel) and with (right panel) white noise disorder of strength $\Delta = J$. In presence of disorder, the inner structure of the cone is washed out and correlations concentrate at shorter distances. The dashed line indicates the Lieb-Robinson velocity $4\,J\,a_{\mathrm{short}}/\hbar$ which corresponds to the envelope of the ballistic cone. **b**, Atom number variance growth in the ballistic case ($J_\perp/J = 0$) for three different subsystem sizes $L = 2, 8, 14$. The data points are the experimental data, the solid lines show the simulated free fermion prediction in presence of white noise disorder ($\Delta = J$) and the dashed lines correspond to the simulated free fermion prediction without disorder.

Spatial imbalance decay profile

In Sec. 5.3 we discuss the time evolution of the mean imbalance averaged over the entire ROI. However, due to disorder or, more generally, due to inhomogeneities in the potential landscape, the damping of the imbalance oscillations will vary spatially. We can get an idea of how disorder is distributed in the system by splitting the ROI into small tiles of 2×2 sites and, for each tile, fit the decay constant of the mean imbalance averaged over the tile, similar to the fitting procedure in Sec. 5.3. Fig. 6.4a shows the fitted decay constants as a function of the two-dimensional position of the tile in the ROI (here, $J_\perp/J = 0.5$). It reveals a stripy pattern, suggesting that there are regions in the short lattice with more disorder and others with less disorder. As seen in the histogram in Fig. 6.4b, the decay constants are spread over large range between 1 and 5 tunnelling times. We suspect that the disorder causing these spatial variations originates primarily from the vertical lattice.

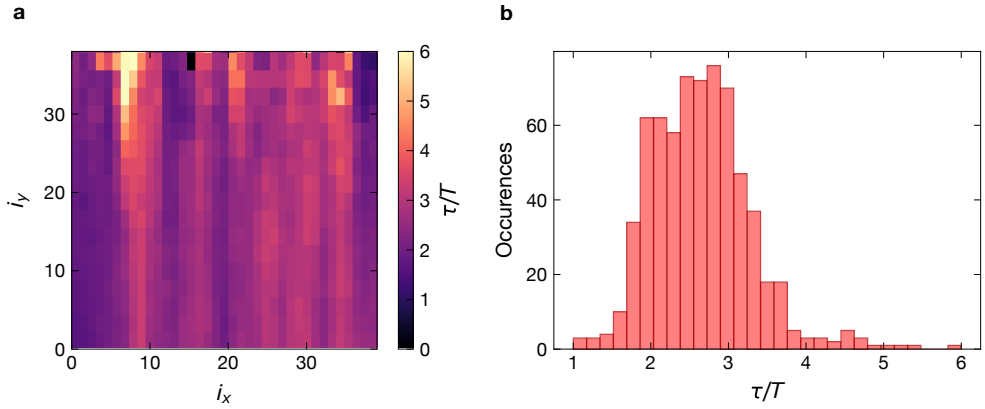

Figure 6.4 | Map of the imbalance decay constant in the ROI. a, Spatially resolved fitted decay constant of the imbalance time evolution in the ROI (for $J_\perp/J = 0.5$), averaged over small quadratic regions (tiles) with a size of 2 lattice sites. Due to locally varying disorder in the system, the decay constant varies spatially. **b**, Histogram of the fitted decay constants.

Spatial tunnel oscillations profile

Inhomogeneities can tilt the double wells in the superlattice potential. We can characterize the double well tilts by performing tunnel oscillations in isolated double wells. For that purpose, we prepare a CDW initial state (cf. Fig. 4.2b) in a tilted superlattice, such that all atoms are on the same side of the double wells. Subsequently, we remove the tilt, quench on the dynamics by abruptly setting J_{dw}/h to about 90 Hz and observe the tunnel oscillations. Any tilt introducing an energy difference Δ_{dw} between the two sites will lead to an increase of the tunnel oscillation frequency, according to [83]:

$$f = \frac{1}{h}\sqrt{\bar{f}^2 + \Delta_{\mathrm{dw}}^2}, \tag{6.4}$$

where $\bar{f} = 2J_{\mathrm{dw}}$ is the unperturbed frequency for $\Delta_{\mathrm{dw}} = 0$. Thus, by measuring the spatial profile of the oscillation frequency inside the ROI, we obtain a map of the double well tilts in the superlattice potential, similar to what is shown in Fig. 4.16. However, in order to become sensitive to our disorder energy scale, J_{dw} should be on the order of Δ. We perform this experiment along both lattice axes, starting with a CDW in the corresponding direction and setting $J_{\mathrm{dw}}/h \approx 90\,\mathrm{Hz}$. Fig. 6.5 shows the measured imbalance as a function of both time and position along the lattice axes, averaged along the respective perpendicular direction. We find that while the average frequency is $\bar{f} = 179(11)$ Hz, it varies

on the order of 10%, indicating double well tilts of up to $\Delta_{\mathrm{dw}}/h = 80\,\mathrm{Hz}$, according to Eq. 6.4. This result is consistent with the disorder strength estimated in Sec. 6.2.

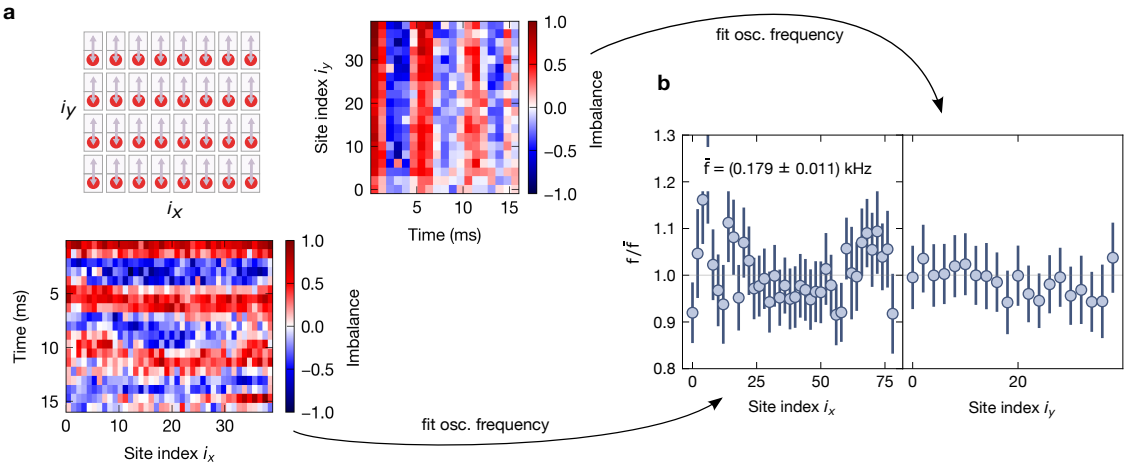

Figure 6.5 | Spatially resolved tunnel oscillations in isolated double wells. a, Imbalance as a function of space and time, averaged perpendicular and parallel to the superlattice direction. The tunnel oscillations are fitted using a sine function in order to extract the oscillation frequency. **b** Fitted oscillation frequency f as a function of spatial coordinates, revealing variations of up to $\approx 10\%$ around the mean frequency $\bar{f}$.

6.3 Finite-size effects

Experimental data

The overall length of each of the 20 ladders is about 50 sites with the box potential wall as the boundary on either side. In order to mitigate effects arising from the finite size of the system, we restrict the analysis to the 40 innermost sites, our ROI. We check whether this restriction is sufficient by performing the same data analysis for various ROIs of different sizes and comparing the results. Fig. 6.6 shows the measured time evolution of the particle number variance for three different ROI sizes, taking only the central 14, 24 and 40 sites into account, respectively. Importantly, irrespective of what type of dynamics are at play ($J_\perp/J \approx 0.0, 1.0$), the variance is independent of the chosen ROI size within the error bars. This suggests that restricting the ROI to the 40 innermost sites of each ladder is sufficient for mitigating finite-size effects.

Free fermion simulations (decoupled ladders)

The conclusion above appears surprising, particularly in the integrable configuration ($J_\perp/J = 0$) where correlations spread ballistically at the Lieb-Robinson velocity $4Ja_{\mathrm{short}}/\hbar$. It would take the correlations barely more than a single tunnelling time to propagate through the 5-sites wide buffer zone between the ROI and the edge. Yet, the impact of edge effects on the mean of the particle number variance in subsystems averaged over the entire ROI is not visible in the data. In the chaotic case ($J_\perp/J = 1$) correlations spread diffusively and the variance is expected to be even less susceptible to finite-site effects.

In order to understand this observation in more detail, we perform additional free fermion simulations (for $J_\perp/J = 0$). Following the methods in the preceding Section, we choose overall system

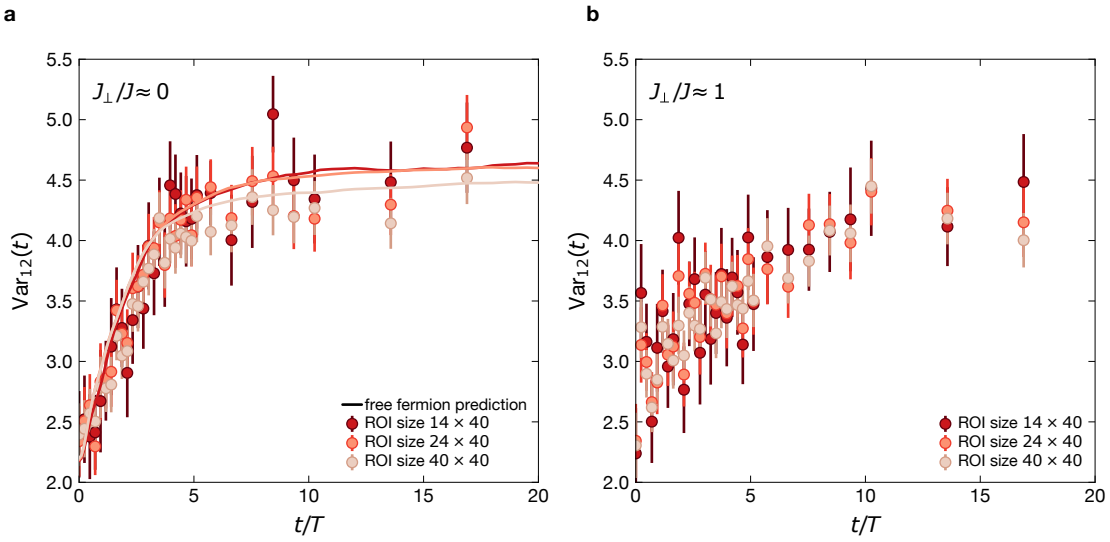

Figure 6.6 | Finite-size effects. Atom number variance as a function of time for $J_\perp/J = 0.0$ (**a**) and $J_\perp/J = 1.0$ (**b**), evaluated for different ROI sizes 12×40, 20×40 and 40×40 sites. The solid lines in (**a**) are the free-fermion prediction assuming white noise disorder of strength $\Delta = J$. We find that all traces from evaluations involving different ROI sizes agree with each other within the error bars. This indicates that our data analysis is not significantly affected by finite-size effects.

sizes of 50 and 250 sites while keeping the ROI restricted to the innermost 40 sites. The overall system size of 250 sites guarantees that even in the integrable case with ballistic correlation spreading the ROI should remain unaffected by finite-size effects within the measured time evolution range. Fig. 6.7 shows the resulting variance traces for subsystem size $L = 14$, both in presence and absence of white noise disorder of amplitude $\Delta = J$. Interestingly, without disorder, the overall system size appears to have a clear effect on the saturation value, illustrating how finite-size effects can affect the relaxation of the system. However, with disorder present, the dependence on the the overall system size almost entirely vanishes. This means that as soon as potential inhomogeneities induce Anderson localization in 1d, the impact of edge effects is diminished and the disorder strength Δ remains the dominant parameter suppressing the saturation value of the fluctuations. Note that the simulation of the particle number variance combining a finite overall system size of 50 sites and disorder of amplitude $\Delta = J$ yields excellent agreement with the experimental data (see Fig. 6.7). In contrast to the fluctuations, the imbalance is not notably affected by finite-size effects (not shown).

TDVP simulations (fully coupled ladders)

The free fermion simulations are only possible in the integrable limit where $J_\perp/J = 0.0$. However, localization and finite-size effects are expected to play out very differently when the legs of the ladders are coupled and the system is not purely 1d anymore. For instance, since density-density correlations spread diffusively, the effects of the edges could become relevant only after quadratically long times compared to the integrable configuration.

For a better intuition of how experimental imperfections affect fully coupled ladder dynamics, we run matrix product state (MPS) TDVP simulations using the open-source package TeNPy [290], both with and without white noise disorder of amplitude $\Delta = J$. Due to large computational costs, the simulations are restricted to fairly small system sizes, at most $L_{\mathrm{sys}} = 11$ containing 22 sites. Thus,

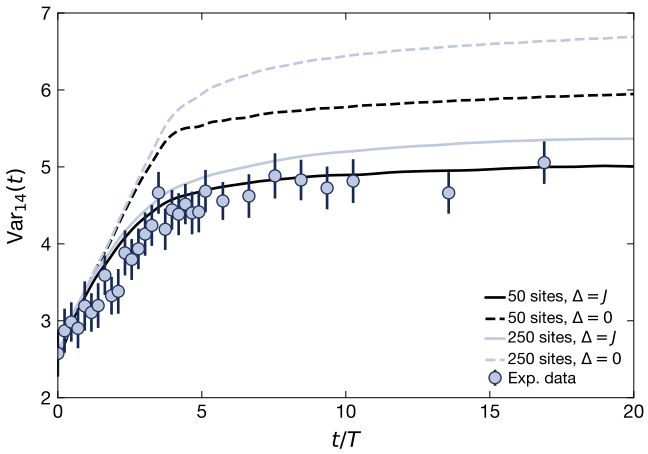

Figure 6.7 | Interplay of disorder and finite-size effects. Time evolution of the atom number variance in a subsystem of size $L = 14$ for $J_\perp/J = 0.0$. The dashed lines are free fermion simulations for an overall system size of 50 and 250 sites in absence of disorder, the solid lines include white noise disorder with amplitude $\Delta = J$. The experimental data (data points) is matched best by the simulations that include disorder. Notably, in presence of disorder the impact of finite-size effects is reduced.

instead of directly simulating experimental system sizes ($L_{\mathrm{sys}} \gtrsim 40$), we need to derive conclusions from how finite-size effects scale in the numerically accessible L_{sys}-regime and extrapolate to $L_{\mathrm{sys}} > 11$.

Fig. 6.8a shows the saturation value of the atom number variance in a subsystem of size $L = \lfloor N_{\mathrm{sys}}/2 \rfloor$ as a function of the overall system size L_{sys}. The dashed lines indicate the infinite-temperature saturation value Var_L^∞ expected from ETH. We find that the saturation value of the variance is strongly suppressed compared to the infinite temperature value Var_L^∞, even in the absence of disorder ($\Delta = 0$). This might suggest that thermalization of the fluctuations is partially inhibited. The out-of-equilibrium dynamics in finite-size systems is an ongoing research topic and it is not well understood how ETH applies to subsystems which constitute a significant part of the overall system [291–293]. Exploring this phenomenon in more detail could be an interesting direction for future experimental efforts.

Besides finite-size effects, the saturation values in Fig. 6.8 are also decreased by disorder. In 2d, the free fermion mapping fails and the hard-core dynamics cannot be mapped to single-particle physics anymore. Thus, instead of Anderson localization, many-body-localization (MBL) needs to be considered as the mechanism behind the system's failure to reach global equilibrium in presence of disorder. However, the stability of MBL in higher dimensions has been fiercely debated [294–296]. If the subsystem size is fixed to $L = 3$ and only the overall system size is increased ($L_{\mathrm{sys}}/L \to 0$) we see the variance saturation value approaching the thermal value, as shown in Fig. 6.8b. Both with and without disorder, extrapolating $L_{\mathrm{sys}} \to \infty$ suggests that the system would thermalize if not limited by finite-site effects, consistent with our expectation that the ladder dynamics should be less affected by disorder.

In the experiment, the size of the largest subsystem in which the saturation of fluctuations is observed ($L = 10$) makes up about $L/L_{\mathrm{sys}} = 1/5$ of the overall system size with $L_{\mathrm{sys}} = 50$. In the simulations, the ratio $L/L_{\mathrm{sys}} = 1/5$ is fulfilled for $L \approx 3$ (see Fig. 6.8b). In presence of disorder, the simulated saturation value obtained for $L = 3$ is approximately 25% reduced compared to the infinite-temperature value. This roughly matches the 20% suppression found in the experimental data for a subsystem size $L = 10$, indicating that finite-size effects are a likely cause for the reduced variance saturation values measured for $J_\perp/J \approx 1.0$.

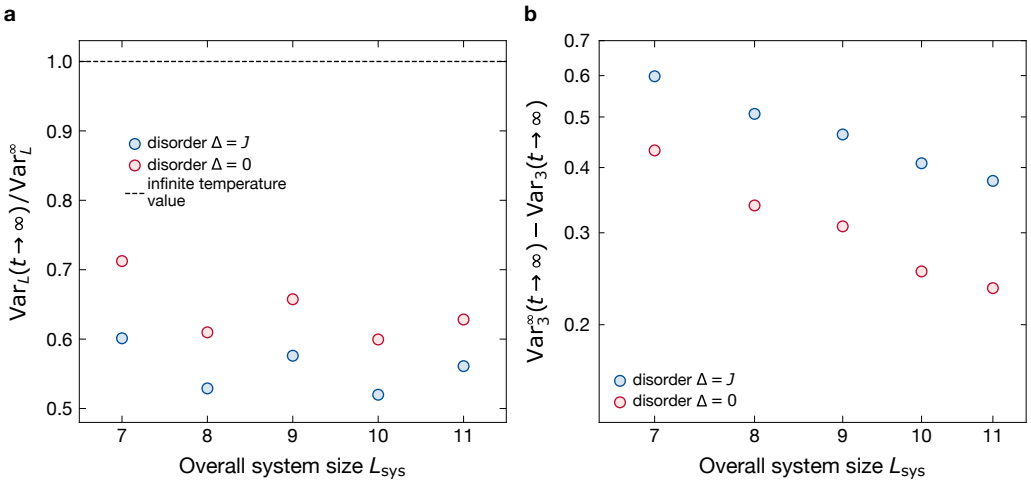

Figure 6.8 | TDVP simulation of small fully coupled ladders. a, Saturation value of the atom number fluctuations (normalized to the ETH expectation value) for a subsystem of size $L = N_{sys}/2$ as a function of the overall system size N_{sys}. The simulations were performed in a fully coupled ladder ($J_\perp/J = 1.0$) with and without white noise disorder of strength $\Delta = J$. The dashed line indicates the saturation value expected from ETH. **b**, Deviations of the simulated saturation values from the ETH expectation for a $L = 3$ subsystem as a function of the overall system size N_{sys}, with and without disorder. They appear to approach zero in the infinite-size limit $N_{sys} \to \infty$.

6.4 Correcting for reconstruction errors

When reconstructing the fluorescence images using machine learning techniques (cf. Sec. 4.3), we work in an extreme resolution regime where the spacing which we want to resolve is more than a factor of two smaller compared to the resolution provided by our high-NA objective. Yet, we have shown that we achieve a reconstruction fidelity of at least $\mathcal{F} \gtrsim 96\%$. In general, the errors made by the network could be of a systematic rather than a random kind, leading to artificial spatial correlations: For instance, if an atom is detected on a particular site, there might be an enhanced probability that an atoms is wrongly detected on adjacent sites, even though it is unoccupied. Measurement artefacts like this are highly undesirable and their magnitude (probably on the order of $1 - \mathcal{F}$) easily interferes with the true correlations of the physics that we aim to observe.

We can detect the presence of reconstruction-caused unphysical correlations by probing product states which are not expected to exhibit any true correlations (for $|d| > 0$) emerging from the physics of the state. Examples include:

- the CDW initial state (as described in Sec. 4.2) which we obtain by loading the atoms into a tilted superlattice configuration, ideally leading to unity filling in every second row and zero filling in every other row. The experimental mean filling is $\bar{n}_{\mathrm{initial}} = 0.44(2)$ with an imbalance of $\mathcal{I}_{\mathrm{initial}} = 0.91(7)$.
- a random state with filling of approximately 0.5, prepared by loading a near-unity filling Mott insulator (in $|F = 3, m_F = 3\rangle$), followed by a microwave pulse which flips about half of the atoms from $|F = 3, m_F = 3\rangle$ to $|F = 4, m_F = 4\rangle$. Finally, a blow out pulse on the $|6s_{1/2}\ F = 4, m_F = 4\rangle \leftrightarrow |6p_{3/2}\rangle$ transition is applied and only the atoms in $|F = 3, m_F = 3\rangle$ remain. The average filling is $\bar{n}_{\mathrm{random}} = 0.48(2)$ and the imbalance becomes $\mathcal{I}_{\mathrm{random}} = 0.00(13)$.

By taking many snapshots of these states we can compute the connected density-density correlations as a function of distance $d = |i - j|$, as shown in Fig. 6.9 (cf. Eq. 2.23). Against all expectations for product states, we do find non-zero correlation amplitudes for $d > 0$, particularly for $d = 1$ and

$d = 2$. Therefore, we can attribute these correlations to systematic errors in the machine-learning based reconstruction process. This appears credible in light of the fact that the point spread function (PSF) is so large compared to the lattice spacing that the fluorescence signal of an individual atom leaks into the area belonging to neighboring sites of both first and second order. The measured values for $d = 1$ in Fig. 6.9 suggest that, for the CDW state, the detection of an atom on a site increases the chance that adjacent sites are incorrectly classified as unoccupied. In turn, for the random half filling state, finding an atom on a site increases the chance that an adjacent unoccupied site is incorrectly classified as occupied. Hence, the systematic errors made by the reconstruction algorithm appear to depend on the particular occupation pattern of the state.

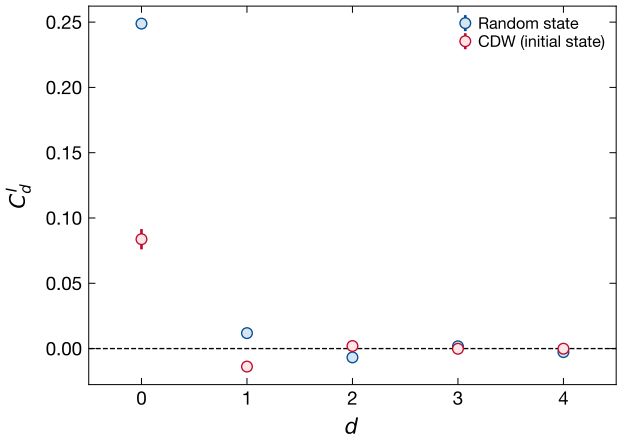

Figure 6.9 | Density-density correlations caused by the reconstruction algorithm. Spatial correlation profile C_d^I of the CDW initial state (high imbalance ~ 0.9) and a random state with near-zero imbalance, obtained from ca. 40 and 70 fluorescence images, respectively. Error bars denote the standard deviation. Both states are not expected to possess any density-density correlations for $|d| > 0$. Thus, any measured correlations can be attributed to systematic errors in the reconstruction process.

In order to remove the unphysical correlations from the measured density-density correlations, we assume that their profile only depends on the imbalance of the visible occupation pattern, such that we can write:

$$\vec{C}_{\text{corrected}} = \vec{C}_{\text{measured}} - \vec{C}_{\text{correction}}(\mathcal{I}). \tag{6.5}$$

Here, the components of the vectors contain the density-density correlation amplitudes $\{C_d\}$ belonging to the distances $d = 0, \ldots, |i - j|$. Importantly, the imbalance itself is not affected by the unphysical correlations.

Let $\vec{C}_{\text{initial}}$ and $\vec{C}_{\text{random}}$ be the correlation profiles we find for the CDW initial product state with $I_{\text{initial}} = 0.91(7)$ and for the random state with $\mathcal{I}_{\text{random}} = 0.00(13)$, respectively. Then we can use them as corrections $\vec{C}_{\text{correction}}(I_{\text{initial}}) = \vec{C}_{\text{initial}}$ and $\vec{C}_{\text{correction}}(I_{\text{random}}) = \vec{C}_{\text{random}}$. For all other imbalance values, we obtain corrections by linearly interpolating between the two measured ones. The imbalance-dependent correction profile in Eq. 6.5 can then be expressed as:

$$\vec{C}_{\text{correction}}(\mathcal{I}) = \vec{C}_{\text{random}} + \frac{\mathcal{I}}{\mathcal{I}_{\text{initial}}} \left(\vec{C}_{\text{initial}} - \vec{C}_{\text{random}} \right). \tag{6.6}$$

Similarly, we can derive corrections for C_d^{II} and C_d^{III}.

We apply Eq. 6.5 only for $|d| = 1, 2$. For C_d^{II} we, additionally, correct $d = 0$. This is because $C_{d=0}^{II}$ is the density-density correlation between two adjacent sites in different legs of the ladder, corresponding

to a real-space distance of one. Fig. 6.10 shows the density-density correlation cones before applying the correction. In comparison with the corrected density-density correlations in Fig. 5.8, one can see how the stripe-like artefact, particularly present in the $d = 1$ correlations, vanishes resulting in a cleaner cone. This correction then also benefits the variance time evolution data which is calculated from the density-density correlations, as noted in Appendix D.

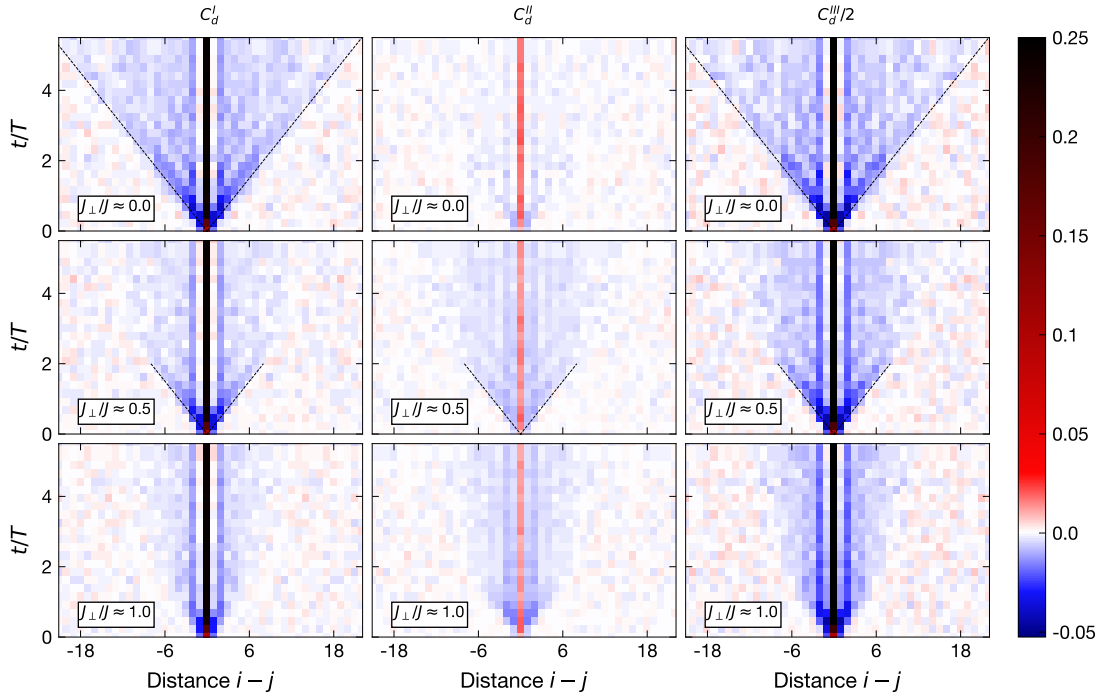

Figure 6.10 | Density-density correlations without correction of reconstruction artefacts. Density-density correlations along the legs of the ladder (C_d^I, left column), between the legs of the ladder (C_d^{II}, center column) and correlations of the total atom number in the rungs along the ladder (C_d^{III}, right column) for $J_\perp/J \approx 0.0, 0.5, 1.0$ (top, center and bottom row, respectively), shown as a function of distance $d = i - j$ and evolution time. This is the raw data before the reconstruction correction (see Eq. 6.5) is applied. The corrected density-density correlations are shown in Fig. 5.8.

CHAPTER 7

Thouless pumps and bulk-boundary correspondence in higher-order symmetry-protected topological phases

The previous two Chapters have focused on quench experiments for studying the emergence of hydrodynamics in chaotic quantum systems. In particular, Sec. 5.1 has shown how we employ optical superlattices for (a) realizing a tunable ladder Hamiltonian with dynamics adjustable from integrable to chaotic; and (b) for preparing a short-spaced charge density wave as an initial state. In this Chapter we move away from infinite temperature physics after a quench and, instead, turn our attention to the ground state properties of a half-filled superlattice potential: This simple setting can realize the bosonic analog of the Su-Schrieffer-Heeger (SSH) model [297] with highly interesting topological properties. The final chapter of this thesis is about theoretical work which sheds light on the bulk-edge-correspondence in higher-order symmetry-protected topological phases [116]. These are in reach of current quantum simulation capabilities and might even pose an interesting research direction for our own experiment.

In the following, we will explore the relationship between quantized edge states and bulk topological invariants in topological phases of matter, particularly focusing on HOSPT phases. We will, for the first time, present a solid theoretical framework which addresses the elusive connection between quantized charge transport and bulk-boundary correspondence in HOSPT phases. We demonstrate that Thouless pumps, which are cyclic adiabatic processes that result in quantized charge transport, can be described by a set of four Chern numbers. These Chern numbers measure quantized bulk charge transport in a direction-dependent manner and can predict the sign and value of fractional corner charges in HOSPT phases. Our results show that the topologically nontrivial phase can be characterized by both quadrupole and dipole configurations, contributing to recent debates about the multipole nature of the HOSPT bulk. As a particular example, we will focus on the 2d superlattice Bose-Hubbard model (2d-SL-BHM) which is naturally realized by placing atoms in a 2d optical superlattice potential.

7.1 Modern theory of polarization

When a dielectric material is placed in an electric field it becomes polarized due to charge displacement inside the material in response to the field. As a consequence, opposite surfaces of the material are subject to charge accumulation and depletion, such that measuring the surface allows to obtain information about the state of the bulk. This principle underlies many important applications and phenomena including piezoelectricity, dielectric capacitors, liquid crystal displays (LCD) and communication systems [298]. While seemingly simple, understanding bulk polarization in solids was not possible

using simple dipole moments. Instead, a powerful theory was developed in the 90s which relates the macroscopic polarization of a solid to properties of the underlying bloch bands: It is known as the *modern theory of polarization* (MTP) [104, 299].

For a discrete set of charges (like atoms forming a molecule), the dipole moment can be defined as [300]:

$$\mathbf{d} = \sum_i q_i \mathbf{r}_i, \tag{7.1}$$

where $\{q_i\}$ are the charges at positions $\{\mathbf{r}_i\}$. For a continuous charge distribution $n(\mathbf{r})$ we can write:

$$\mathbf{d} = \int e\, n(\mathbf{r})\, \mathbf{r} d\mathbf{r}, \tag{7.2}$$

where e is the elementary charge.

Using the dipole moment as a definition for polarization becomes problematic as soon as not an isolated charge distribution but a solid is considered. In a periodic system the polarization will generally depend on the choice of the unit cell, causing the polarization to be multi-valued, and only polarization difference has a meaning [300]. Using a quantum mechanical description, King-Smith and Vanderbilt provided a more rigorous definition and showed that the bulk polarization is directly related to the Berry phase γ_L of the bloch bands, i.e. [104]:

$$P_{\text{el}} = \lim_{L\to\infty} \frac{e}{2\pi} \gamma_L, \tag{7.3}$$

in the thermodynamic limit where L is the system size.

In the case of interacting many-body systems, Resta later related this polarization to the expectation value of the many-body position operator $\hat{R}$ in a periodic system [299]:

$$P_{el} = \lim_{L\to\infty} \frac{e}{2\pi} \text{Im} \log \langle \psi_0 | e^{\frac{2\pi i}{L}\hat{R}} | \psi_0 \rangle, \tag{7.4}$$

where $|\psi_0\rangle$ is the many-body ground state wavefunction. Eq. 7.4 is in line with the intuition that any change of polarization requires a physical displacement of charge, as suggested by the definition of the dipolar moment in Eq. 7.2. While MTP is a general theory meant to describe polarizable materials, in the following we will focus on insulators with non-trivial topology. A hallmark of topological matter is the emergence of quantized boundary states which are a consequence of the topological difference between the bulk and the outside. Using MTP these quantized states can be related to quantized polarization in the bulk.

7.2 Topological order

Much of our understanding of electron many-body phases roots in two notions of the so-called Landau paradigm: First, the integrity of electrons as quasiparticles above the quantum many-body ground state is preserved. Second, the different phases of matter are distinguished by a local-order parameter, which quantifies the amount of local symmetry breaking [301]. An example for such an order parameter is the net magnetization in a ferromagnet, which becomes non-zero below a critical temperature, indicating the appearance of order.

Over the past four decades, this concept of phase transitions has been challenged by experimental and theoretical work on strongly-correlated states of matter with non-trivial topology. A prominent example that lacked a consistent description by the Landau paradigm is the fractional quantum Hall effect [302]. For instance, the excitations above the Laughlin ground state are actually described by

quasiparticles with fractional charge and fundamentally different braiding statistics. Further, such topological phases exhibit long-range entanglement that cannot be captured by a local-order parameter. Instead, the order is a global property of the many-body ground state wave function and described by a robust quantity, called the topological invariant.

The concept of topological phases is defined as follows [303]: If two gapped states ψ_1 and ψ_2 (ground states of a Hamiltonian $H(\lambda)$ for $\lambda = \lambda_1, \lambda_2$, respectively) cannot be transformed into each other adiabatically [304] without closing the gap, they must belong to different topological phases, described by a different values of a topological invariant. This is called *intrinsic* topological order and illustrated in Fig. 7.1a, showing disconnected gapped regions in the parameter space of a model Hamiltonian. For instance, quantum Hall states fall into this category and crossing from one state to another is impossible without closing the many-body gap [305].

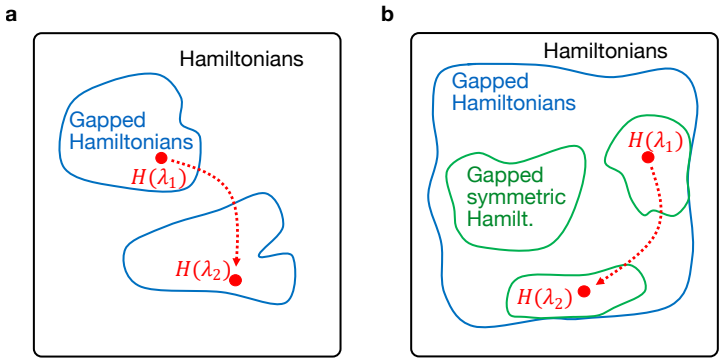

Figure 7.1 | Topological phases and symmetry-protected topological phases. a, Two gapped ground states of an Hamiltonian *H* belong to the same topological phase if they can be adiabatically transformed into each other without closing the many-body gap. **b** Two gapped ground states of an Hamiltonian *H* belong to the same symmetry-protected topological phase if they can be adiabatically transformed into each other without closing the many-body gap or breaking the protecting symmetry (or both).

The boundary between two different topological phases (like the system and the vacuum surrounding it) is where the gap closes, leading to zero-energy states that are one dimension lower than the bulk of the system. Recently, higher-order topological insulators were discovered [86, 87] featuring electric multipole moments [86, 87, 109–111, 113–115]. With open boundary conditions, n-dimensional materials of this kind with topology of order m will possess $(n - m)$ dimensional boundary states, as demonstrated on many platforms including real solids and classical metamaterials [88–98].

Symmetry-protected topological phases

The classification of topological phases becomes even richer if symmetries are taken into account, prompting the definition of so-called SPT phases. Important examples include time-reversal symmetry, particle-hole symmetry and crystal-group symmetries [306]. Restricting ourselves to classes of symmetric Hamiltonians and adiabatic transformations which fulfill a symmetry, we can adapt the definition of topological phases above as follows: If two gapped states ψ_1 and ψ_2 (ground states of an Hamiltonian $H(\lambda)$ for $\lambda = \lambda_1, \lambda_2$, respectively) cannot be transformed into each other adiabatically without closing the gap *or* breaking the symmetry (or both), they must belong to different SPT phases, described by a different values of a topological invariant. This definition is illustrated in Fig. 7.1b. The higher-order variants of SPT phases are called HOSPT phases.

In the following section, we will discuss a simple model exhibiting SPT phases protected by inversion

symmetry: first the 1d bosonic superlattice Bose-Hubbard model to illustrate important concepts such as the Berry phase which serves as a topological invariant as well as Thouless pumps inducing quantized charge transport. Then, we will move on with the 2d bosonic superlattice Bose-Hubbard model and generalize these concepts to HOSPT phases. This is the main contribution of this Chapter.

7.3 SPT phases in the 1d superlattice Bose-Hubbard model

One of the perhaps simplest models exhibiting non-trivial topological phases is the famous Su-Schrieffer-Heeger (SSH) model [297], originally developed to describe the conductivity in polymer chains. In 1d, it describes a chain of lattice sites coupled by alternating couplings t and $1-t$ with $t \in [0,1]$, as depicted in Fig. 7.2a. In the context of quantum simulation with ultracold atoms, this model can be realized by placing fermions in a 1d optical superlattice potential (at half filling), which naturally comes with two different tunnel strengths. Instead of fermionic atoms, one can also use bosonic atoms if the hard-core condition is fulfilled ($U \to \infty$) [306]. The Hamiltonian describing the 1d superlattice Bose-Hubbard model (1d-SL-BHM) reads:

$$\hat{H} = -\sum_{j \text{ odd}} \left(t\, \hat{a}_j^\dagger \hat{a}_{j+1} + \text{h.c.} \right) - \sum_{j \text{ even}} \left((1-t)\, \hat{a}_j^\dagger \hat{a}_{j+1} + \text{h.c.} \right) + \frac{U}{2} \sum_j n_j (n_j - 1) + H_\Delta \tag{7.5}$$

with operators and symbols as defined below Eq. 5.1. The last term $\hat{H}_\Delta$ is given by:

$$\hat{H}_\Delta = -\sum_{j \text{ odd}} \hat{n}_j\, \Delta + \sum_{j \text{ even}} \hat{n}_j\, \Delta, \tag{7.6}$$

and describes additional energy shifts of amplitude Δ of opposite sign on odd and even sites. These shifts emergence if the phase of the optical superlattice is tuned away from the symmetric configuration.

Phase diagram

The topological phase diagram of the 1d-SL-BHM is shown in Fig. 7.2b (at half filling in the hard-core limit). Let us first consider the special case of $\Delta = 0$ and $t = 0.5$, such that both tunnel strengths are equal. In this case the Hamiltonian describes an ordinary 1d lattice half-filled with hard-core bosons, i.e. a gapless superfluid phase. At any other point in the phase diagram, the Hamiltonian is gapped. As long as $\Delta = 0$, the model is inversion symmetric [307], giving rise to two SPT phases. For $t < 0.5$ and $t > 0.5$ the inversion symmetry axis is in the middle of either the even or the odd bonds, respectively (Fig. 7.2b). In order to get from one to the other configuration it is necessary to either cross the gapless region around $t = 0.5$ (by adjusting t) or to circumvent the gapless region by tuning Δ away from zero. However, by doing the latter, one breaks inversion symmetry. Hence, the (green) lines corresponding to $\Delta = 0, t < 0.5$ and $\Delta = 0, t > 0.5$ can be considered two SPT phases protected by inversion symmetry, called the *trivial* (SPT 1) and the *topological* phase (SPT 2), respectively.

While the two phases are topologically different, which one deserves to be called the trivial one only matters in finite systems as visualized in Fig. 7.2b: If (in SPT 1) the coupling is such that each site in the chain is strongly coupled to an adjacent site, the number of atoms matches the number of dimers and each dimer will be occupied by one delocalized atom. However, if (in SPT 2) the two edge sites of the chain are not part of a dimer, then the number of atoms in the finite system exceeds the number of dimers by one. As a consequence, the excessive atom will either occupy the left or the right edge instead of being localized in a dimer. This constitutes a zero-energy edge state, a smoking gun of

non-trivial topology. The mean occupation of the edge site will differ by either $1/2$ or $-1/2$ from the average filling of the system $\bar{n} = 1/2$. Thus, the edge charge is called *fractional* [84].

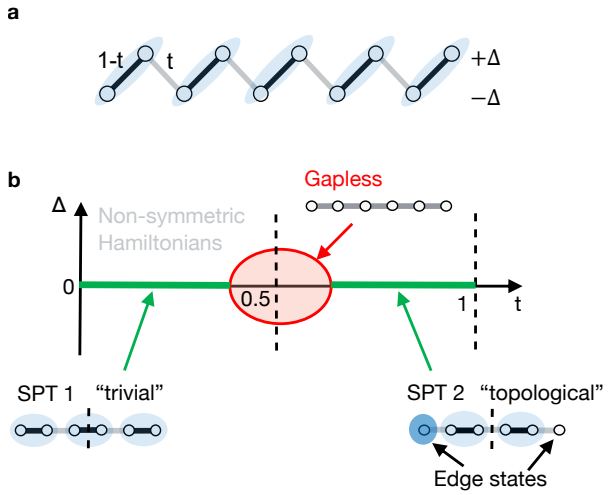

Figure 7.2 | The 1d superlattice Bose-Hubbard model. a, The 1d superlattice Bose-Hubbard model (1d-SL-BHM) as realized by an optical superlattice with two tunnel strengths t and $1 - t$ in alternation and local energy shifts Δ of opposite sine on even and odd sites. **b** Topological phase diagram of the 1d-SL-BHM revealing two distinct topological phases protected by inversion symmetry. The blue orbitals indicate the position and delocalization of the atoms in the two SPT phases.

Thouless pumps

A Thouless pump is an adiabatic process along a closed path in the parameter space of the Hamiltonian, transporting charge [107, 108]. In a topologically non-trivial system charge transport is quantized and illustrates a key concept of topology known as *bulk-boundary correspondence*.

Consider a pump cycle in the 1d-SL-BHM defined by:

$$\begin{aligned} t(\lambda) &= \frac{1}{2}\left(1 - \cos(\lambda)\right) \\ \Delta(\lambda) &= \sin(\lambda), \end{aligned} \tag{7.7}$$

where $\lambda \in [0, 2\pi)$ controls the progress of the pump. In the phase diagram, the path of the pump is a circle around the gapless region in the center ($t = 0.5, \Delta = 0$), starting in SPT 1, crossing SPT 2 after the first half ($\lambda = \pi$) and, finally, returning to the starting point in SPT 1 ($\lambda = 2\pi$), as visualized in Fig. 7.3. The blue orbitals indicate how the position of the atoms and their spatial delocalization changes as the pump progresses. At $\lambda = 0$, the initial density distribution is the ground state of SPT 1 with exactly one atom per dimer. Notably, after the first half of the pump is completed ($\lambda = \pi$) and the the state has been transferred from SPT 1 to SPT 2, the number of dimers is reduced by one, leading to one fully occupied and one empty edge state. Charge has been displaced to the right in the chain and starts to *pile up* on one side, manifesting as a topological edge state with fractional charge $|c| = 1/2$. This edge charge can be considered as the consequence of polarization in bulk which has built up due to the Thouless pump. In the second half of the pump ($\lambda > \pi$) the charge accumulation continues until, when the cycle is completed, exactly one charge has moved to the next dimer. Thus, the charge

transfer is quantized, reflecting the quantized nature of the topological invariant which characterizes the topology of the bulk, as detailed below [106, 308].

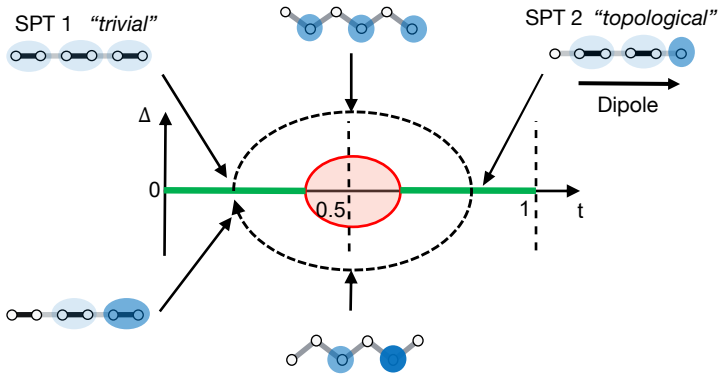

Figure 7.3 | Thouless pump in the 1D-SL-BHM. Adiabatically transforming the Hamiltonian along a closed path (dashed line) around the gapless region (red area) leads to quantized charge transport which characterizes the topology of the bulk. The blue orbitals indicate the delocalization and position of individual atoms.

Topological invariants and bulk-boundary correspondence

The Thouless pump above demonstrates how switching from one topological phase to another is accompanied by a quantized change of the polarization in the bulk, leading to quantized charge accumulation (or depletion) at the edge. This suggests that the tools provided by MTP [104] could be useful for defining a topological invariant to distinguish between different phases – much like the order parameter in the Landau-Ginzburg theory. One of the most important results of MTP is that the bulk polarization is a manifestation of the Berry phase, a geometric phase picked up by the ground state wavefunction during an adiabatic cycle due to the curvature of the band structure [103, 299, 309]. In fact, a change of the Berry phase indicates a change of the bulk polarization (cf. Eq. 7.3). For the 1d-SL-BHM with periodic boundary conditions (PBC) the Berry phase can be defined by [84]:

$$\gamma = \int_0^{2\pi} d\phi \, \langle \psi(\phi) | i\partial_\phi | \psi(\phi) \rangle, \tag{7.8}$$

where $|\psi\rangle$ is the (ground state) many-body wavefunction and ϕ is a complex tunnelling phase attached to one of the bonds, as depicted in Fig. 7.4a. Adding a phase ϕ to one of the bonds (*local twist*) is equivalent to piercing a flux of ϕ through the ring formed by the periodic system. Intuitively, the flux change during the integral in Eq. 7.8 then induces to an effective electric field along the ring which probes charge transport. Evaluating Eq. 7.8 for the trivial and topological SPT, for instance, yields $\gamma_0 = 0$ and $\gamma_1 = \pi$, respectively. While the exact values depend on the details of the path chosen in Eq. 7.8, the phase difference

$$\Delta\gamma = \gamma_1 - \gamma_0 = \pi \tag{7.9}$$

is gauge invariant and quantized due to the inversion symmetry of the system. Thus, the Berry phase is able to distinguish between the two topological phases of the 1d-SL-BHM, serving as a topological invariant. Following Eq. 7.3, the Berry phase difference in Eq. 7.9 suggests that the bulk polarization difference is $\Delta P_{el} = e/2$. This is precisely the absolute amount of charge that accumulates as an edge

states on both sides with OBC (relative to the mean filling of $\bar{n} = 0.5$) when a Thouless pump takes the system from SPT 1 to SPT 2.

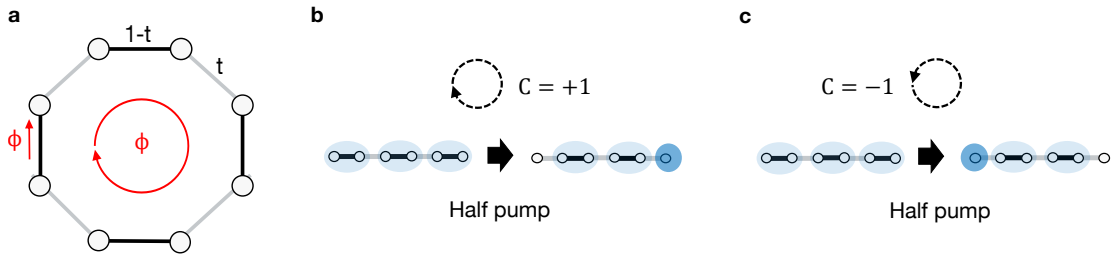

Figure 7.4 | **Berry phase and Chern number. a**, The Berry phase is obtained by inserting a flux through the 1d system with periodic boundary conditions, adiabatically ramp the flux up to 2π and measuring the geometric phase picked up by the ground state wavefunction. **b**, The Chern number integrates the Berry phase up along the path of the Thouless pump, indicating the total transported charge. For a clockwise pump we obtain $C = +1$ and **c** , for a counter-clockwise pump we obtain $C = -1$.

Generally, the total amount of transported charge within one full pump cycle is measured by the *Chern number* [310]:

$$C = \oint_0^{2\pi} \frac{d\lambda}{2\pi} \partial_\lambda \gamma(\lambda), \tag{7.10}$$

which integrates the change of the Berry phase along the closed path of the Thouless pump, parametrized by $\lambda \in [0, 2\pi)$. For the Thouless pump defined by Eq. 7.7, we obtain $C = +1$ when λ runs from 0 to 2π and $C = -1$ when λ runs from 2π to 0, indicating quantized charge transport along the chain (cf. Fig. 7.4b,c). The charge transported by half a Thouless pump is then given by $C/2$ [311]. Thus, the Berry phase and the Chern number establishes a connection between the polarization of the bulk and the zero-energy edge states which, in 1d, is called the *bulk-edge correspondence*.

7.4 HOSPT phases in the 2d superlattice Bose-Hubbard model

Starting from the 1d-SL-BHM, the simplest way to get a system featuring higher-order topology is to generalize the model to 2d, yielding the 2d-SL-BHM, as depicted in Fig. 7.5a. In a square geometry with open boundary conditions (OBC) the Hamiltonian reads [116]:

$$\hat{H}^{\mathrm{OBC}} = -\Big[\sum_{x=-D}^{D-1}\sum_{y=-D}^{D}\left(t(x)\,\hat{a}_{x,y}^\dagger \hat{a}_{x+1,y} + \mathrm{h.c.}\right) + x \leftrightarrow y\Big] + \frac{U}{2}\sum_{x,y=-D}^{D}\hat{n}_{x,y}(\hat{n}_{x,y} - 1), \tag{7.11}$$

where $D = (L-1)/2$ and $\hat{a}_{x,y}^\dagger$ ($\hat{a}_{x,y}$) are the creation (annihilation) operators for site (x, y). The other symbols are defined below Eq. 5.1. Like in 1d, the hard-core limit ensures equivalence to the 2d SSH model. While in the 1d-SL-BHM sites either belong to the 1d bulk or the 0d edges, the 2d-SL-BHM has sites in three different categories: those in the 2d bulk (part in strongly coupled plaquettes), those along the edges (organized in strongly coupled 1d dimers) and those in the 0d corners. The staggered tunnel couplings $t(\zeta), \zeta \in \{x, y\}$ are defined by

$$t(\zeta) = \begin{cases} 1-t & \text{for } \zeta \in \{-D, -D+2, \dots, D-1\} \\ t & \text{for } \zeta \in \{-D+1, -D+3, \dots, D-2\} \end{cases} \tag{7.12}$$

where, just like in the 1d-SL-BHM, $t \in [0,1]$ controls the transition from a trivial phase ($t = 0$) to a topological phase ($t = 1$). As seen in Fig. 7.5b The phase diagram looks identical to that of the 1d-SL-BHM with the notable difference that the SPT phases are now of second order, making them HOSPT phases. Instead of a bulk-edge correspondence, the non-trivial phase will feature a bulk-corner correspondence with a corner state indicating a multi-pole-like polarization of the bulk.

In the definition of the model (Eq. 7.11), the origin of the coordinate system lies in the center of the system and is the symmetry point of a C_4 symmetry. This rotational symmetry takes the role that inversion symmetry played in the 1d-SL-BHM. In addition to C_4-symmetry, the hard-core limit $U \to \infty$ leads to an additional $\mathcal{Z}_2$ symmetry $\hat{a}^\dagger_{x,y} \leftrightarrow \hat{a}_{x,y}$, which can be used to proof that the Berry phase can serve as a quantized topological invariant (see Sec. 7.6). In the following Sections, we will generalize the concepts of Berry phases, Thouless pumps and Chern numbers (introduced in Sec. 7.3) to the higher-order case of the 2d-BHM-SL. Goal of this Chapter is to find a description of the bulk polarization in HOSPT phases and understand the higher-order bulk-boundary correspondence, relating bulk properties to the corner charges.

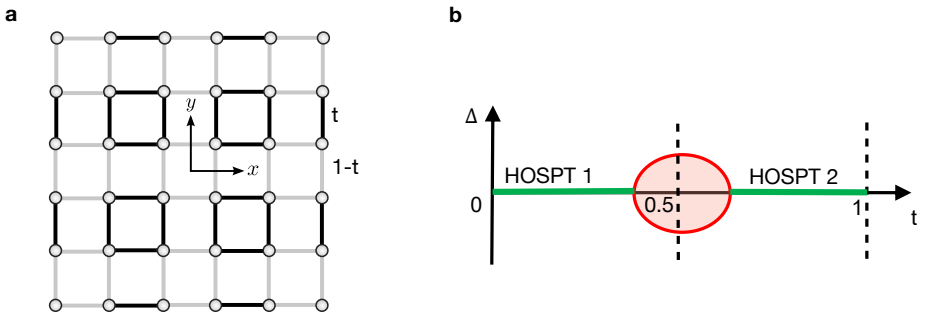

Figure 7.5 | The 2d superlattice Bose-Hubbard model. a, The 2d-SL-BHM on a square lattice is characterized by alternating tunnel strengths t and $1-t$ in both directions, leading to strongly coupled plaquettes in the bulk, strongly coupled dimers along the edges and zero dimensional corners. It is naturally implemented by ultracold atoms in a 2d superlattice potential at half filling. **b**, Phase diagram of the 2d-SL-BHM showing two HOSPT phases separated by a gapless region, similar to the phase diagram of the 1d-SL-BHM.

7.5 Higher-order Thouless pumps

In the 1d-SL-BHM, the effects of a Thouless pump are limited by the simple geometry of the system: After all, charge can be transported only to the left or to the right side of the chain, creating one particle edge state and one hole edge state on opposite ends. As we will see in this Section, the 2d case is more complex as there are four corners capable of carrying four corner states in total. Which of these end up carrying a positive (negative) corner charge depends on the particular Thouless pump applied.

In order to define Thouless pumps in the 2d-SL-BHM, we add on-site energy shifts of amplitude Δ to each site in the system, similar to the 1d case. In particular, we choose the two patterns shown in the left panels of Fig. 7.6: One where each plaquette in the system receives shifts with the same sign on

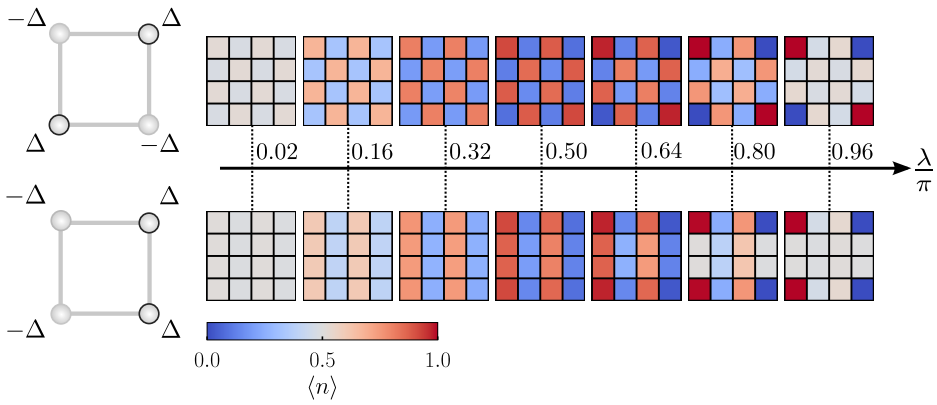

Figure 7.6 | Higher-order Thouless pumps in the 2d-SL-BHM. Time evolution of the mean density in a 4×4 system during a diagonal (upper panel) and a non-diagonal (lower panel) half-Thouless pump calculated using exact diagonalization. After completing half of the cycle, the non-trivial HOSPT exhibits a quadrupole and a dipole corner charge configuration, respectively. The drawings on the left show the arrangement of additional on-site potentials in each plaquette: The diagonal Thouless pump requires shifts of equal sign on diagonally opposite sites, while the non-diagonal Thouless pump requires shifts of the same sign on the same side.

opposite corners (diagonal), and one where each plaquette receives shifts with the same sign on the same side of the plaquette (non-diagonal). The corresponding Hamiltonian reads:

$$\begin{aligned} \hat{H}^{\text{diag.}} &= \hat{H}^{\text{OBC}} + \Delta \sum_{x,y=-D}^{D} \hat{n}_{x,y}(-1)^{(x+D)+(y+D)} \\ \hat{H}^{\text{non-diag.}} &= \hat{H}^{\text{OBC}} - \Delta \sum_{x,y=-D}^{D} \hat{n}_{x,y}(-1)^{(x+D)}. \end{aligned} \tag{7.13}$$

The pump progress is parametrized by $\lambda \in [0, 2\pi)$ which controls t and Δ as expressed by Eq. 7.7. Both the diagonal and the non-diagonal pump take the system around the gapless region in the center of the phase diagram ($t = 0.5, \Delta = 0$), starting in HOSPT 1, crossing HOSPT 2 and eventually arriving back at HOSPT 1 (cf. Fig. 7.5b). In the course of that, C_4-symmetry is broken (as $\Delta \neq 0$), except at the two points where HOSPT 1 and HOSPT 2 are passed which happens at $\lambda = 0$ and $\lambda = \pi$, respectively.

The right panels in Fig. 7.6 show the density evolution during the first half of both the diagonal and the non-diagonal pump, calculated using exact diagonalization in a $L \times L = 4 \times 4$ system at half filling (total atom number $N = L^2/2$) with OBC. The initial state ($\Delta = 0$ and $t = 0$ at $\lambda = 0$) is the ground state of the Hamiltonian in the trivial phase (HOSPT 1) with two delocalized particles per plaquette. At the beginning of the pump the charge accumulates in the sites which are subject to an on-site energy shift of $-\Delta$. Once the first quarter of the pump cycle is complete ($\lambda = \pi/2$), the density starts to even out in the bulk and along the edges of the system. Only at the corner sites the density continues to increase or decrease to 1 and 0, respectively, until HOSPT 2 is reached at $\lambda = \pi/2$. These are the corner states that emerge as the consequence of charge transport in the bulk. Both pumps have in common that they produce two particle corner state with fractional charge $+1/2$ and two hole corner states with fractional charge $-1/2$. However, their arrangement differs and depends on the type of the pump: For the diagonal pump we obtain corner states in a quadrupole configuration, while the non-diagonal pump produces corner states in a dipole configuration.

7.6 Higher-order Berry phase

In order to analytically describe the relationship between the fractional corner charge and the polarization of the bulk, we first define topological invariants for HOSPT phases by generalizing the Berry phase approach introduced in Sec. 7.3. Then, as a next step, we use these Berry phases to construct Chern numbers and track the amount of charge transported during the Thouless pumps in a direction-dependent fashion.

Corner periodic boundary conditions

As in the 1d case, we want to define the Berry phase by *locally twisting* the system, i.e. by adding complex tunnelling phases which are adiabatically increased from 0 to 2π (cf. Sec. 7.3). Recently, one way to do that was shown by Araki et al. [312] who defined a unitary transformation acting on a single plaquette in the center of the system and adding complex phases to the four bonds. However, while the transformation was chosen such that no flux is pierced through the central plaquette, adjacent plaquettes do receive non-zero flux. This turns out to be problematic in infinite systems ($L \to \infty$), as in the thermodynamic limit flux in the bulk can lead to gap closings [311]. In order to avoid this problem we need to find a way to define the Berry phase *without* introducing flux anywhere in the bulk. In the following, we show how the idea of Araki et al. [312] can be moved to the outside away from the bulk by introducing *corner periodic boundary conditions* (CPBC).

For CPBC we require additional couplings between the corners of the system as defined by:

$$\hat{H}^{\mathrm{C}} = -t\left(\hat{a}_{c_1}^{\dagger}\hat{a}_{c_2} + \hat{a}_{c_2}^{\dagger}\hat{a}_{c_3} + \hat{a}_{c_3}^{\dagger}\hat{a}_{c_4} + \hat{a}_{c_4}^{\dagger}\hat{a}_{c_1}\right), \tag{7.14}$$

with c_i denoting the coordinates of the i-th corner, i.e. $c_1 = (-D, D)$, $c_2 = (-D, -D)$, $c_3 = (D, -D)$ and $c_4 = (D, D)$ with $D = L/2 - 1/2$. The total Hamiltonian with CPBC is:

$$\hat{H}^{\mathrm{CPBC}} = \hat{H}^{\mathrm{OBC}} + \hat{H}^{\mathrm{C}}. \tag{7.15}$$

As a consequence of the additional couplings in Eq. 7.14, the four corner sites form an additional plaquettes and the couplings between the corners form super-cells delimited by the edges of the bulk and the corner-corner bonds, as depicted in Fig. 7.7a.

Definition of the Berry phase

For defining Berry phases, we introduce flux in the super-cells *outside* the bulk of the system as follows: For each corner we can write down a unitary transformation which applies only to $\hat{H}_C$ (see Eq. 7.14):

$$\hat{H}_i^{\mathrm{C}}(\theta) = \hat{U}_i^{\dagger}(\theta)\,\hat{H}^{\mathrm{C}}\,\hat{U}_i(\theta), \tag{7.16}$$

adding a complex tunnel phase θ to the two corner-to-corner bonds meeting at the corner i. Here, $\hat{U}_i(\theta) = e^{i\hat{X}_i(\theta)}$, $\hat{X}_i(\theta) = \theta\ \hat{n}_{c_i}$ and $\hat{n}_{c_i}$ is the particle number operator for the i-th corner site. As a consequence, the corresponding super-cells (delimited by the corner-to-corner couplings and the edge of the bulk) are threaded by a flux $\Phi = \theta$, as visualized in Fig 7.7. Since there are four corners in the system $i = 1, 2, 3, 4$, we can define four unitary transformations $\hat{U}_1, \hat{U}_2, \hat{U}_3, \hat{U}_4$, leading to four (transformed) Hamiltonians $\hat{H}_i(\theta) = \hat{H}_i^{\mathrm{C}}(\theta) + \hat{H}^{\mathrm{OBC}}$ with $i = 1, 2, 3, 4$, see Fig 7.7b. Note that these transformations are related to each other through the same C_4-symmetry that also gives rise to the HOSPT phases, i.e.

$$C_4^{-1}\,\hat{U}_i(\theta)\,C_4 = \hat{U}_{i+1}(\theta). \tag{7.17}$$

The Berry phases γ_i ($i = 1, 2, 3, 4$) corresponding to the four gauge transformations are then defined by

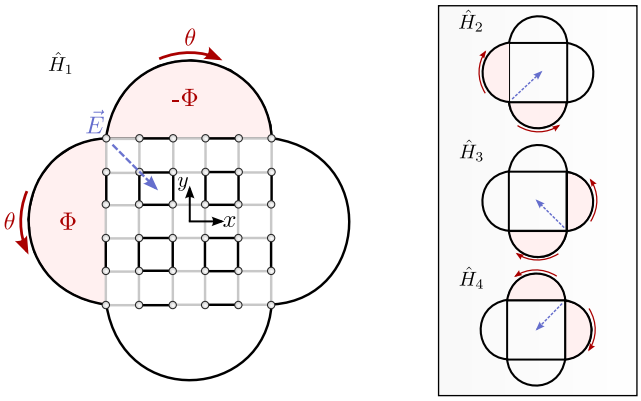

Figure 7.7 | Definition of the higher-order Berry phases. 2d-SL-BHM with CPBC for defining Berry phases while avoiding flux in the bulk. For each corner we can define unitary transformations $\hat{U}_i$ ($i = 1, 2, 3, 4$) adding complex tunnelling phases ϑ to the adjacent corner-to-corner couplings and threading flux $\Phi = \vartheta$ through the corresponding super-cells. The resulting Hamiltonians are H_i ($i = 1, 2, 3, 4$). The Berry phases effectively act as charge flow sensors, sensitive to the direction of the electric field induced when the flux is varied (blue arrows).

the integral in Eq. 7.8, just like in the 1d case. Fig. 7.8 shows γ_1 as a function of the tunnel strength t in the 2d-SL-BHM, as calculated from exact diagonalization in a $L \times L = 4 \times 4$ system at half filling with CPBC. One finds that γ_1 is zero in the trivial phase (HOSPT 1) and instantly jumps to π when $t > 0.5$ in HOSPT 2, showing clear quantization. The same is observed for the other three Berry phases γ_1, γ_2 and γ_3 (not shown). One can use the $\mathbb{Z}_2$-symmetry of the system (cf. Eq. 7.18) to prove that the Berry phases must be quantized as:

$$\gamma_i \in \pi\, \mathbb{Z}, \tag{7.18}$$

see [16] for details. The insets in Fig. 7.8 show the site-resolved density expectation values in HOSPT 1 and HOSPT 2 with CPBC and at half filling plus two additional particles. In the topological phase (HOSPT 2) these additional particles prefer to occupy the plaquettes rather than the edge dimers, leading to an inhomogeneous density distribution that is distinguishable from the homogeneous distribution in HOSPT 1.

7.7 Chern number tuples

We can now use the Berry phases defined in Sec. 7.6 to understand and quantify the charge transport driven by the higher-order Thouless pumps introduced in Sec. 7.5. Here we take advantage of the fact that the adiabatic flux insertion carried out by the unitary transformation $\hat{U}_i$ in Eq. 7.16 relates to the current flowing diagonally through the corner i (see [116] for a proof):

$$\hat{J}_i = \partial_\theta \hat{H}_i(\theta)|_{\theta=0}, \tag{7.19}$$

Thus, integrating up the Berry phases γ_i up an adiabatic path means integrating up the corner current and is expected to yield the total change of the corner charges Δq_{c_i}:

$$\Delta q_{c_i} = -\frac{\Delta \gamma_i}{2\pi}. \tag{7.20}$$

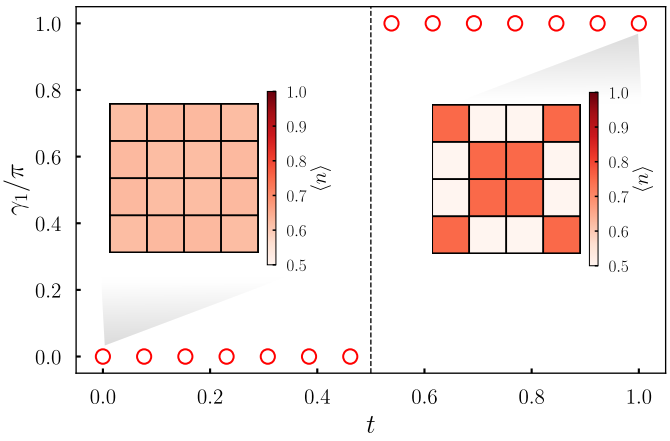

Figure 7.8 | **Higher-order Zak (Berry) phase.** One of the four Berry phases γ_1 as a function of the tunneling parameter t in a system with CPBC ($L = 4$) at half-filling ($N = L^2/2$). Insets: density expectation values in the trivial and the non-trivial HOSPT for $N = L^2/2 + 2$.

This establishes a connection between the properties of the bulk (captured by the topological invariant) and the boundary states of the system (the corner charge). As the Berry phases are quantized by $C_4 \times \mathbb{Z}_2$-symmetry, the corner charges must be quantized, too.

As a concrete example, we apply this formalism to the two Thouless pumps introduced in Sec. 7.5 and track the charge transport both in the diagonal and the non-diagonal configuration (cf. Sec. 7.5). For each Berry phase γ_i ($i = 1, 2, 3, 4$) we can define a Chern number $\mathcal{C}_i$ according to Eq. 7.10, which, following Eq. 7.20 is the total charge transported toward ($\mathcal{C}_i < 0$) or away from ($\mathcal{C}_i > 0$) corner i.

Fig. 7.9 shows all four Berry phases γ_i ($i = 1, 2, 3, 4$) as a function of $\lambda \in [0, 2\pi)$ which controls the progress of the diagonal (a) and non-diagonal (b) pump. Integrating up the Berry phase evolution yields the a tuple of four Chern numbers ($\mathcal{C}_1$, $\mathcal{C}_2$, $\mathcal{C}_3$, $\mathcal{C}_4$) as illustrated in the left panels. We get $\mathcal{C}^{\text{diag.}} = (-1, 1, -1, 1)$ for the diagonal and $\mathcal{C}^{\text{non-diag.}} = (-1, -1, +1, +1)$ for the non-diagonal pump. The charge transport directions suggested by the Chern numbers is consistent with time evolution of the density discussed in (cf. Sec. 7.5): Whenever charge flows toward (away from) a corner a particle (hole) corner state with positive (negative) fractional charge emerges. Since the Berry phases are quantized, the Chern numbers must be, too, and take integer values for a full pump cycle. Thus, for a half pump which takes the system from one HOSPT to the other, the charge accumulated is $\Delta q_{c_i} = -\mathcal{C}_i/2$, yielding fractional corner charges of $+1/2$ or $-1/2$ in HOSPT 2, depending on the sign of $\mathcal{C}_i$.

Importantly, the Chern number tuples fully characterize the polarization of the bulk and are able to describe both quadrupole and dipole configurations in the non-trivial HOSPT, distinguishing between these two configurations. This sheds new light on previous attempts to describe the bulk of HOSPT phases using a pure quadrupole operator [110]. In general, one requires three out of four Chern numbers for a full characterization of the bulk as the fourth Chern number can be deduced from symmetry.

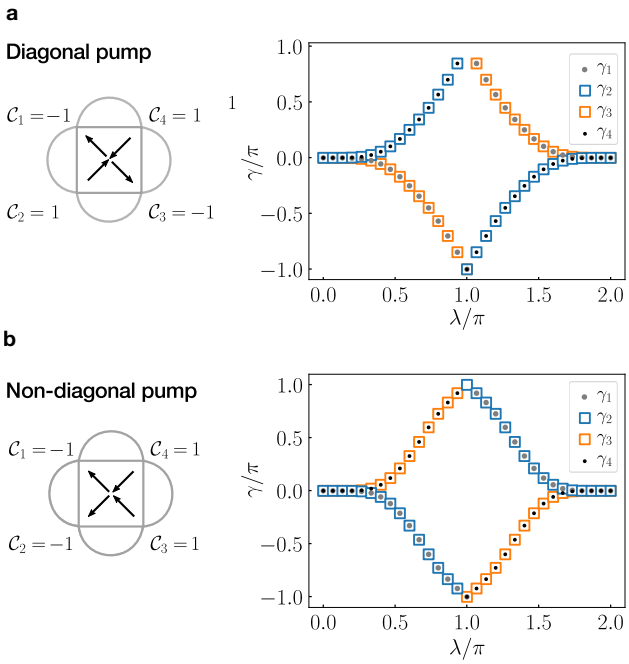

Figure 7.9 | **Chern numbers for tracking charge transport in higher-order Thouless pumps. a**, Diagonal pump. **b**, Non-diagonal pump. Right panels: Evolution of the higher-order Berry phases as a function of $\lambda \in [0, 2\pi)$ which controls the progress of the pump, calculated using exact diagonalization in a $L \times L = 4 \times 4$ system at half filling with OBC. Left panels: Chern numbers $\mathcal{C}_i$ calculated from integrating the change of the Berry phases according to Eq. 7.10. Each Chern number $\mathcal{C}_i$ is related to the the current $\hat{\mathcal{J}}_i$ (cf. Eq. 7.19) that is flowing toward ($\mathcal{C}_i < 0$) or away ($\mathcal{C}_i > 0$) from corner i.

Conclusion & Outlook

Emergence of fluctuating hydrodynamics in chaotic quantum systems

This thesis has presented quantum quench experiments for testing the qualitative and quantitative predictions of FHD in chaotic quantum many-body systems. Bosonic ultracold ^{133}Cs atoms in optical superlattices have served as a quantum simulation platform, realizing the Bose-Hubbard model at half filling in large ladder geometries (2×50 sites). Ladders allow to tune the dynamics from integrable to chaotic by adjusting the ratio of tunnelling strengths perpendicular to and along the ladder $J_\perp/J$. By measuring the post-quench relaxation of the system with single-site resolution, we have arrived at the following results:

- For the first time, we have directly observed a crossover from integrable to chaotic dynamics, demonstrating the breakdown of ballistic correlations when the legs of the ladder are coupled.
- As the dynamics are tuned from integrable to chaotic, the local mean density relaxes faster, while fluctuation growth slows down. Thus, there is a separation of equilibration timescales between local expectation values and large-scale fluctuations. The growth speed as a function of subsystem size in the integrable (chaotic) case is consistent with ballistic (diffusive) dynamics, as is the spreading of density-density correlations.
- In the chaotic case, the post-quench time-evolution of the fluctuations is macroscopically described by FHD. This indicates that a single coefficient, the linear-response diffusion constant, determines the entire out-of-equilibrium behavior and that the non-equilibrium fluctuation dynamics of a chaotic quantum system is intimately connected to the equilibrium diffusion constant via a noisy diffusion equation.
- We have shown that the time evolution of the subsystem fluctuations and the density-density correlations can be used to obtain the diffusion constant. This demonstrates that an important and difficult-to-obtain equilibrium property of the system can be extracted by observing far-from-equilibrium dynamics. This is a new paradigm, evading expensive numerical approaches or difficult experiments in the near-equilibrium regime. Our finding that the measured values are in agreement with linear-response calculations from the literature underlines that FHD describes our system not only qualitatively but also quantitatively.

Importantly, the pre-quench initial state was chosen to be a small-spaced CDW. This ensures that the initial density quickly becomes homogeneous and the dynamics are governed by the diffusion constant at uniform density (half filling) and the hydrodynamic spreading of fluctuations. In general, the diffusion constant is density-dependent. Thus, using an initial state with large-scale density variations like a domain wall would lead to more complicated dynamics (requiring corrections to the hydrodynamic model) and render the extraction of the diffusion constant more difficult. Our main finding that the macroscopic description provided by FHD applies to chaotic quantum many-body systems has far-reaching consequences: It means that despite the complexity unfolding at the microscopic level, the

coarse-grained dynamics are simple. Intriguingly, from a macroscopic perspective, the consequences of many-body entanglement are sufficiently random that a generic random noise term in the diffusion equation is sufficient to account for them. While our experiment has studied FHD in a specific setting (hard-core ladder systems at half filling), FHD is expected to provide a universal description for all chaotic quantum systems. Although we cannot rigorously prove this claim (just as ETH is a hypothesis, too), we provide important arguments and derivations in favor of it in the supplementary information of Ref. [16]. In particular, we provide additional numerical evidence based on studying a noisy staggered-anisotropy XXZ model in different chaotic configurations.

Our experimental results (cf. Chapter 5) provide first strong evidence that far-from-equilibrium fluctuation growth is a quantitative probe of equilibrium transport in the context of FHD – a relationship to be further studied in future experiments. We have established new tools for exploring the transport properties of quantum systems which are out of reach for current numerical capabilities. For instance, while we have populated ladder systems with *hard-core* bosons [254, 255, 257], future work could study the dynamics with finite interactions and explore how integrability is broken in 1d systems as a consequence of that [258, 261, 271]. The chaotic ladder thermalizes in line with the eigenstate thermalization hypothesis: However, the tools presented in this work in combination with the large system sizes might also be useful for studying systems where thermalization fails. These include prethermalization effects [72, 313, 314] as well as many-body localization (MBL) in 1d and 2d, building on earlier experiments [70, 315]. Further, the ability to prepare specific initial product states allows to observe dynamics possibly restricted to certain sectors of the Hilbert space. This benefits the experimental realization of constrained dynamics like Hilbert space fragmentation and many-body scars [75, 77, 78, 316, 317]. Also the emergence of generalized hydrodynamics in integrable systems has recently attracted more interest [318, 319]. In this work we have focused on the mean local density and the fluctuations in subsystems of various sizes. However, in principle, our quantum gas microscope allows to measure the FCS [320] (cf. Sec. 1.2). Higher moments beyond fluctuations and their equilibration timescales could yield information about further corrections to the hydrodynamic model which provides the macroscopic description of our quantum many-body system [321]. Finally, the role of finite-size effects on thermalization of these moments in finite quantum systems is not well understood and could pose another interesting direction for further experimental and theoretical studies [292].

Bulk-boundary correspondence in higher-order symmetry-protected topological phases

In Chapter 7 we have theoretically studied the quantized charge transport in HOSPT phases, using the 2d superlattice Bose-Hubbard model (2d-SL-BHM) as an example. We have shown how the (multi-pole) bulk polarization can be understood using a tuple of four Berry phases, each of which is associated with the current flowing through a different corner. These can be defined using CPBC, a necessary step in order to ensure that no flux is introduced in the bulk and that the gap does not close in the thermodynamic limit. The Berry phases can then be used to define Chern numbers and track the charge transport during higher-order Thouless pumps which produce quantized fractional corner charges in either dipole or quadrupole configuration, depending on the details of the pump. This establishes a bulk-boundary correspondence in HOSPT phases and provides an intuitive understanding of topologically non-trivial matter from the point of the modern theory of polarization.

The analytical methods developed in this study are expected to be applicable to a large variety of systems protected by other crystalline symmetries [98, 322], or systems that generally differ in terms of filling or geometry [323]. For instance, in the 2d-SL-BHM at quarter filling we expect the emergence of corner states with fractional charges of more exotic values. Another interesting direction concerns higher-order topology in quasicrystals [324, 325] which feature forbidden rotational symmetries like C_5 or C_8.

Experimental upgrades

As discussed in Chapter 6, the quality of our data is limited by disorder in the superlattice potential as well as by the challenging resolution regime that we are working in. In order to minimize or eliminate these shortcomings for future experiments, we are working on various hardware upgrades:

- For maximizing the on-site interaction strength U and being able to increase the tunnelling strength J while keeping U/J large, we are setting up a new vertical lattice. In the new version, the two beams creating the lattice will interfere under a steeper angle, providing more vertical confinement while keeping the horizontal confinement low. A larger on-site interaction strength means less sensitivity to disorder and temperature and is expected to extend the observation time after the quench.
- In order to improve the resolution of our imaging system we are planning to replace the objective and the imaging setup with a more carefully tested objective, hoping to decrease the resolution-to-spacing ratio β from 2.2 to 1.8. This should reduce the amount of systematic reconstruction errors (cf. Sec. 6.4) and improve the overall data quality.
- In order to not only detect but also manipulate the system at the level of individual atoms with single-site resolution, we will add a blue $\lambda = 455\,\mathrm{nm}$ addressing beam through the bottom objective [138]. This requires excellent magnetic field stability, which is ensured by an active stabilization setup [224].
- Finally, for the purpose of achieving higher initial state quality, particularly concerning Mott insulators and CDWs, we are planning to implement an immersion cooling scheme proposed in Ref. [74].

With these changes, we are looking forward to novel state-of-the-art quantum simulation experiments and to further exploring the intriguing physics of quantum thermalization and interacting topological matter.

***

Appendices

Appendix A Macroscopic fluctuation theory

In equilibrium systems, fluctuations of observables are given by the Boltzmann-Gibbs canonical distribution. In near-equilibrium (in the context of linear response theory) they are described by the Onsager-Machlup functional [326, 327]. In far-from-equilibrium systems, it is believed that large deviation functions can provide a useful description [328]. In this context, MFT was developed to describe large deviations in a variety of diffusive systems and solve the system for quantities relevant in FHD [210].

Just as in the previous section, imagine a system with a macroscopic density profile $\bar{n}(x,t)$ is supposed to go from an initial state $\bar{n}_0(x) = \bar{n}(x, t = 0)$ at to a final state $\bar{n}(x, t = t_f)$. A central statement of MFT is that the probability of the system doing precisely that by taking a certain path $\bar{n}(x,t)$ is given by:

$$I_{[t_0,t_f]}[\bar{n}(x,t)] \sim \exp\left(-\epsilon^{-1}\int_{t_0}^{t_f} dt \int dx\ \frac{\bar{j}(x,t)+F}{2A}\right), \tag{A.1}$$

called large deviation function. Here, F is the equation of state and ϵ is a constant introducing an Euclidean metric, playing the role of the Planck constant. Eq. A.1 can be considered a generalization of the Einstein relation describing density fluctuation in equilibrium: Since the expression describes a *transition* probability it also applies to any non-equilibrium situation [329]. In order determine the probability to find the system in $\bar{n}_f(x, t = t_f)$ considering that it was in $\bar{n}_i(x, t = t_i)$ it is necessary to integrate Eq. A.1 over all intermediate configurations allowed by the continuity equation. This corresponds to the minimization of an action:

$$S = \int dtdx \left[\frac{\bar{j}(x,t)+F}{2A} + p(\dot{\bar{n}}(x,t) + \partial_x j(x,t))\right]. \tag{A.2}$$

Here, p is a Lagrange multiplier field ensuring that the integral fulfills the continuity equation. Solving this optimization problem yields the optimal path $\bar{n}(x,t)$ and Eq. A.1 allows to obtain the full statistics of $\bar{n}(x,t)$ or any other quantity, if adapted. The distribution of an observable can provide deeper insights into the thermalization of chaotic systems [15, 210] beyond simple diffusion and possibly point at additional terms to be included in the equation of state (cf. Eq. 2.7).

Appendix B Fidelity estimation from double imaging

In order to estimate the reconstruction fidelity $\mathcal{F}$, we take two fluorescence images of the same cloud in succession and compare the reconstruction results. For modelling this process, let us think of an arbitrary site in the image: The events (along with their probabilities) leading to a change of the true occupation between the two images and the measured occupation in each of the two images can be summarized in a three-step model [83]:

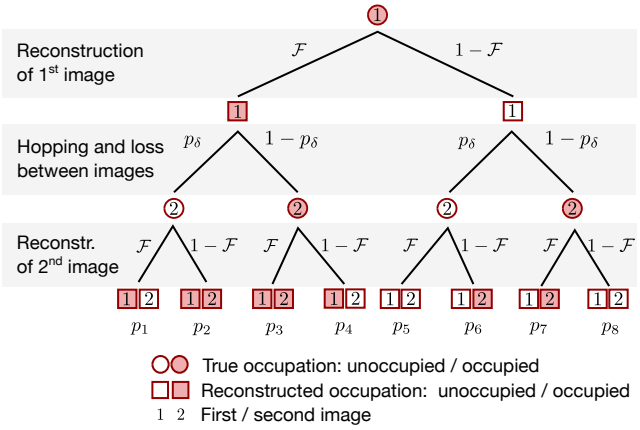

Figure B.1 | Double imaging as a three-step Bernoulli trial. Probability tree for calculating the measured occupation difference between the first and the second fluorescence image, taking reconstruction errors (probability $1-\mathcal{F}$) as well as hopping and loss events (combined probability p_δ) into account. The tree describes how the true and detected occupation of an arbitrary site is altered by imaging and reconstruction. The round and square markers indicate the true and reconstructed occupation, respectively. Red and white stand for occupied and unoccupied. The probabilities $p_1, \dots, p_8$ belong to the eight ends of the probability tree.

1. Taking the first image and reconstructing it with a fidelity $\mathcal{F}$, i.e. there is a chance of $\mathcal{F}$ that the true occupation is detected correctly and a chance of $1-\mathcal{F}$ that the wrong occupation is detected.

2. Hopping and loss occurring during and between the two images and leading to changes of the true occupation with probability p_δ.

3. Taking the first image and reconstructing it with a fidelity $\mathcal{F}$, i.e. there is a chance of $\mathcal{F}$ that the true occupation is detected correctly and a chance of $1-\mathcal{F}$ that the wrong occupation is detected.

Concatenating these steps leads to the probability tree shown in Fig. B.1 which reduces the double imaging process to a Bernoulli trial. It holds under the assumption that p_δ is not too large. In step 2, p_δ is the probability that the true occupation of a site in the second image is different from the true occupation in the first image due to hopping or loss events (probabilities p_{hop} and p_{loss} within the exposure time, respectively). It is proportional to the mean density in the system n:.

$$p_\delta(n) = n\,(p_{\text{loss}} + 2\,p_{\text{hop}}) \tag{B.1}$$

Since hopping events always leads to an occupation change of two sites, the associated probability needs to be weighted with a factor of two.

The probability tree in Fig. B.1 has eight outcomes corresponding to the probabilities $p_1, \dots, p_8$. For instance, the probability $p_1 = \mathcal{F}\ p_\delta\ \mathcal{F}$ corresponds to the case where both images are reconstructed correctly but the two occupations are differ due to a hopping or loss event. The probability $p_2 = \mathcal{F}\ p_\delta\ (1-\mathcal{F})$ corresponds to the case where the two reconstructed occupations match even though there was a hopping or loss event, as the reconstruction of the second image is incorrect.

In the experiment we can measure the probability δ for a different occupation in the second image compared to the first image. Of the eight ends of the probability tree, only four (p_1, p_4, p_6 and p_7) contribute to this scenario. Thus, we can write:

$$\begin{aligned}\delta &= p_1 + p_4 + p_6 + p_7 \\ &= \mathcal{F}^2\, p_\delta(n) + \mathcal{F}\,(1-\mathcal{F})\,(1-p_\delta(n)) + (1-\mathcal{F})^2\, p_\delta(n) + (1-\mathcal{F})\mathcal{F}\,(1-p_\delta(n)).\end{aligned} \tag{B.2}$$

We are interested in computing the reconstruction fidelity $\mathcal{F}$. Solving for this variable yields:

$$\mathcal{F} = \frac{1}{2}\left(1 + \sqrt{\frac{1-2\delta}{1-2\,p_\delta(n)}}\right). \tag{B.3}$$

In the limit of vanishing hopping and loss rate ($p_\delta = 0$), Eq. B.3 can be simplified to:

$$\mathcal{F} = \frac{1}{2}\left(1 + \sqrt{1-2\delta}\right). \tag{B.4}$$

This result suggest that if there no occupation difference between the first and the second image is measured ($\delta = 0$), the reconstruction fidelity is perfect ($\mathcal{F} = 1$), neglecting hopping and loss events. In turn, if the reconstruction result of the second image is so different that effectively two random images are being compared $\delta = 0.5$, Eq. B.4 would yield $\mathcal{F} = 0.5$ (the worst possible value). In presence of hopping and loss events, the measured occupation difference δ would lead to an underestimation the reconstruction fidelity. Eq. B.3 takes that into account and corrects the reconstruction fidelity accordingly.

Appendix C Free fermion approach

Decoupled ladders ($J_\perp/J = 0$) occupied by hard-core bosons are an integrable quantum system. This is because the many-body problem of hard-core bosons can be mapped to a single-body problem of spinless fermions. We take advantage of this mapping to carefully study the impact of disorder aas well as finite-size effects and benchmark the experiment.

Jordan-Wigner transformation

On a discrete lattice, the bosonic field operators generally satisfy the commutation relations:

$$[\hat{a}_i, \hat{a}_j] = 0, \;\; [\hat{a}_i^\dagger, \hat{a}_j^\dagger] = 0, \;\; [\hat{a}_i, \hat{a}_j^\dagger] = \delta_{ij} \tag{C.1}$$

For hard-core bosons (the on-site interaction energy $U \to \infty$) one can adapt these relations to take account for the fact the the same lattice site cannot be occupied by more than one particle, leading to mixed commutation relations [255]:

$$[\hat{a}_i, \hat{a}_j] = 0, \;\; [\hat{a}_i^\dagger, \hat{a}_j^\dagger] = 0, \;\; [\hat{a}_i, \hat{a}_j^\dagger] = \delta_{ij} \;\; \text{for } i \neq j, \tag{C.2}$$

$$\{\hat{a}_i, \hat{a}_i\} = 0, \;\; \{\hat{a}_i^\dagger, \hat{a}_i^\dagger\} = 0, \;\; \{\hat{a}_i, \hat{a}_i^\dagger\} = 1 \tag{C.3}$$

Substituting the bosonic field operators in the Bose-Hubbard Hamiltonian (Eq. 1.5 or Eq. 5.1 with $J_\perp/J = 0$) with the hard-core versions eliminates the interaction term that scales with U:

$$\hat{H}_{\text{BHM,hardcore}} = -J\left(\sum_i \hat{a}_i^\dagger \hat{a}_{i+1} + \text{h.c.}\right). \tag{C.4}$$

The hard-core boson problem can now be mapped onto a spinless fermion problem using the Jordan-Wigner transformation [330]:

$$\hat{c}_i^\dagger = \prod_{j<i}(1-2\hat{a}_j^\dagger\hat{a}_j)\hat{a}_i^\dagger \tag{C.5}$$

The operator $(1-2\hat{a}_j^\dagger\hat{a}_j)$ only takes the values $+1$ and -1, depending on whether the site i is unoccupied or occupied, respectively. Thus, the product $\prod_{j<i}(1-2a_j^\dagger\hat{a}_j)$ yields ±1, depending how many sites with index $j<i$ (to the left of site i) are occupied. If the number of occupied sites is even, we get $\hat{c}_i^\dagger = \hat{a}_i^\dagger$, otherwise $\hat{c}_i^\dagger = -\hat{a}_i^\dagger$. This ensures that $\hat{c}_i^\dagger$ and $\hat{c}_i$ obey the fermionic anticommutation relations:

$$\{\hat{c}_i, \hat{c}_j\} = 0, \;\; \{\hat{c}_i^\dagger, \hat{c}_j^\dagger\} = 0, \;\; \{\hat{c}_i, \hat{c}_j^\dagger\} = \delta_{ij}. \tag{C.6}$$

Applying this Jordan-Wigner transformation to the one-dimensional bosonic Hamiltonian (cf. Eq. C.4) yields:

$$\hat{H}_{\mathrm{ff}} = -J\left(\sum_i \hat{c}_i^\dagger\hat{c}_{i+1} + \mathrm{h.c.}\right). \tag{C.7}$$

Analytical predictions without disorder

The free fermion Hamiltonian can be diagonalized using a Fourier transform, as detailed in [267]. For a CDW initial state state of the form $\psi_0 = |...\,10101010\,...\rangle$ the imbalance (cf. 4.6) will time-evolve as:

$$\mathcal{I}(t) = \mathcal{J}_0\,(4tJ/\hbar)\,. \tag{C.8}$$

Here, $\mathcal{J}_0$ is the zeroth Bessel function of the first kind [267] which decays polynomially as $\mathcal{I}(t) \sim t^{-\frac{1}{2}}$. For the equal-time density-density correlations between sites with indices j and k one finds:

$$\langle\hat{n}_j(t)\hat{n}_k(t)\rangle - \langle\hat{n}_j(t)\rangle\langle\hat{n}_k(t)\rangle = \frac{1}{4}\delta_{j,k} - \frac{1}{4}\mathcal{J}_{j-k}(4tJ/\hbar)^2, \tag{C.9}$$

where $\delta_{j,k}$ is the Kronecker delta [267]. This expression suggests that the correlations are spreading ballistically with a maximum velocity of $4J/\hbar$, also known as the Lieb-Robinson velocity [176]. This corresponds to twice the group velocity $2J/\hbar$ of the free fermions [176, 274, 275]. Eq. C.8 is plotted in Fig. 6.2b (dashed lines),Eq. C.9 in Fig. 6.3a (left panel).

Numerics for benchmarking disorder

For the purpose of benchmarking the impact of disorder, we extend Eq. C.7 by introducing energy shifts V_i at site $i = 1, \cdot, L$ as follows:

$$\hat{H}_{\mathrm{ff}} = -J\left(\sum_i \hat{c}_i^\dagger\hat{c}_{i+1} + \mathrm{h.c.}\right) + \sum_i V_i\hat{n}_i. \tag{C.10}$$

In order to compute the time evolution of the CDW initial state under Eq. C.10, we first compute the unitary time evolution operator

$$\hat{U}(t) = e^{-i\hat{H}_{\mathrm{ff}}t/\hbar}. \tag{C.11}$$

Note that, in contrast to the original Hamiltonian in Eq. C.4 which, in the Fock basis, has $d \times d$ entries

(where d is the number of Hilbert space dimensions), $\hat{H}_{\mathrm{ff}}$ has just $L_{\mathrm{sys}} \times L_{\mathrm{sys}}$ with L_{sys} being the overall system size. It can be shown that the local occupation at site i is then given by [267]:

$$\langle n_i(t) \rangle = \sum_{\{n_q\}} \hat{U}_{i n_q} \hat{U}^{\dagger}_{n_q i} \tag{C.12}$$

,
where n_q denotes the indices of all initially occupied sites. Similarly,

$$\langle \hat{n}_j(t) \hat{n}_k(t) \rangle = \sum_{\{n_q\},\{n_p\}} \left(\hat{U}_{j n_q} \hat{U}^{\dagger}_{n_q j} \hat{U}_{k n_p} \hat{U}^{\dagger}_{n_p k} - \hat{U}_{j n_q} \hat{U}^{\dagger}_{n_q k} \hat{U}_{k n_p} \hat{U}^{\dagger}_{n_p j} \right). \tag{C.13}$$

Combining Eq. C.12 and Eq. C.13 then allows to compute the connected density-density correlator

$$C_d(t) = \langle \hat{n}_i(t) \hat{n}_j(t) \rangle - \langle n_i(t) \rangle \langle n_j(t) \rangle. \tag{C.14}$$

We typically run several hundred simulations with randomly sampled disorder potentials and randomly sampled initial states (taking into account the experimental preparation fidelity), compute the disconnected density-density correlator in Eq. C.13 for each run separately and then average over all correlator values to get the mean disconnected correlator. This yields the first term in Eq. C.13. For the second term we average the densities directly over all simulation runs. Both terms together yield the connected density-density correlator in Eq. C.14.

Appendix D Relationship between subsystem fluctuations and density-density correlations

In Chapter 5 we discuss the measured time evolution of particle number fluctuations in subsystems of length L (Sec. 5.4) and of the density density correlations (Sec. 5.5). One can find expressions that convert these two observables into each other.

The variance of the total atom number in a subsystem of length L is defined as:

$$\mathrm{Var}_L(t) = \left\langle (\hat{n}_{1,1} + \hat{n}_{2,1} + \cdots + \hat{n}_{1,L} + \hat{n}_{2,L})^2 \right\rangle - \left\langle \hat{n}_{1,1} + \hat{n}_{2,1} + \cdots + \hat{n}_{1,L} + \hat{n}_{2,L} \right\rangle^2 \tag{D.1}$$

Expanding this expression and using the definition of the connected density-density-correlator:

$$C^{\alpha,\beta}_{i,j} = \left\langle \hat{n}_{\alpha,i} \hat{n}_{\beta,j} \right\rangle - \left\langle \hat{n}_{\alpha,i} \right\rangle \left\langle \hat{n}_{\beta,j} \right\rangle, \tag{D.2}$$

for two sites i, j in legs $\alpha, \beta = 1, 2$, yields:

$$\mathrm{Var}_L(t) = \sum_{i,j=1}^{L} \left(C^{1,1}_{i,j} + C^{1,2}_{i,j} + C^{2,1}_{i,j} + C^{2,2}_{i,j} \right). \tag{D.3}$$

This expression related the particle number variance of a subsystem with length L to a sum of density-density correlators up to distance $d = |i - j| = L$.

The correlators in Eq. D.3 can be further expanded and sorted by distance, yielding:

$$\sum_{i,j=1}^{L} C^{1,1}_{i,j} = L\, C^{1,1}_0 + 2\,(L-1)\, C^{1,1}_1 + 2\,(L-2)\, C^{1,1}_2 + \cdots + 2\, C^{1,1}_{L-1}, \tag{D.4}$$

with $C^{\alpha,\beta}_d$ defined as in Eq. 5.11. Eq. D.4 allows to compute the subsystem variances directly from

the density-density correlation cone. In fact, this is what we do since the density-density correlation data can be corrected more easily for systematic reconstruction errors (cf. Sec. 6.4).

References

[1] P. W. Anderson, *More Is Different*, Science **177**, 393 (1972) (see p. 1).

[2] M. K. Verma, *Microscopic Laws vs. Macroscopic Laws: Perspectives from Kinetic Theory and Hydrodynamics*, Trans Indian Natl. Acad. Eng. **5**, 491 (2020) (see p. 1).

[3] A. Y. Grama, J. Fogarty, H. Aktulga, and S. Pandit, *N-Body Computational Methods*, in *Encyclopedia of Parallel Computing*, edited by D. Padua (Springer US, Boston, MA, 2011), 1259 (see p. 1).

[4] X. Liang, M. Li, Q. Xiao, J. Chen, C. Yang, H. An, and L. He, *Deep learning representations for quantum many-body systems on heterogeneous hardware*, Mach. Learn.: Sci. Technol. **4**, 015035 (2023) (see p. 1).

[5] E. Guyon, J. P. Hulin, L. Petit, and C. D. Mitescu, *Physical Hydrodynamics*, 2nd ed. (Oxford University Press, Oxford, 2015) (see p. 1).

[6] Romain Vasseur, *"Anomalous hydrodynamics of low dimensional quantum systems "*, YouTube, 2023 (see p. 1).

[7] P. Romatschke and U. Romatschke, *Relativistic Fluid Dynamics In and Out of Equilibrium – Ten Years of Progress in Theory and Numerical Simulations of Nuclear Collisions*, arXiv:1712.05815 (2019) (see p. 1).

[8] E. Gourgoulhon, *An introduction to relativistic hydrodynamics*, EAS Publications Series **21**, 43 (2006) (see p. 1).

[9] V. E. Hubeny, S. Minwalla, and M. Rangamani, *The fluid/gravity correspondence*, arXiv:1107.5780 (2011) (see p. 1).

[10] S. Massaglia, G. Bodo, P. Rossi, S. Capetti, and A. Mignone, *Making Faranoff-Riley I radio sources - I. Numerical hydrodynamic 3D simulations of low-power jets*, A&A **596**, A12 (2016) (see p. 1).

[11] P. J. W. Moll, P. Kushwaha, N. Nandi, B. Schmidt, and A. P. Mackenzie, *Evidence for hydrodynamic electron flow in PdCoO2*, Science **351**, 1061 (2016) (see p. 1).

[12] D. A. Bandurin, I. Torre, R. K. Kumar, M. Ben Shalom, A. Tomadin, A. Principi, G. H. Auton, E. Khestanova, K. S. Novoselov, I. V. Grigorieva, L. A. Ponomarenko, A. K. Geim, and M. Polini, *Negative local resistance caused by viscous electron backflow in graphene*, Science **351**, 1055 (2016) (see p. 1).

[13] B. N. Narozhny, *Hydrodynamic approach to two-dimensional electron systems*, Riv. Nuovo Cim. **45**, 661 (2022) (see p. 1).

[14] A. Sommer, M. Ku, G. Roati, and M. W. Zwierlein, *Universal spin transport in a strongly interacting Fermi gas*, Nature **472**, 201 (2011) (see p. 1).

[15] D. Wei, A. Rubio-Abadal, B. Ye, F. Machado, J. Kemp, K. Srakaew, S. Hollerith, J. Rui, S. Gopalakrishnan, N. Y. Yao, I. Bloch, and J. Zeiher, *Quantum gas microscopy of Kardar-Parisi-Zhang superdiffusion*, Science **376**, 716 (2022) (see pp. 1, 46, 56, 71, 78, 117).

[16] J. F. Wienand, S. Karch, A. Impertro, C. Schweizer, E. McCulloch, R. Vasseur, S. Gopalakrishnan, M. Aidelsburger, and I. Bloch, *Emergence of fluctuating hydrodynamics in chaotic quantum systems*, arxiv:2306.11457 (2023) (see pp. 1, 5, 83, 86, 109, 114).

[17] P. S. Weiß, *Quantum Fluctuations and Hydrodynamic Noise in Low Dimensions*, (see pp. 1, 21).

[18] B. Bertini, M. Collura, J. De Nardis, and M. Fagotti, *Transport in Out-of-Equilibrium XXZ Chains: Exact Profiles of Charges and Currents*, Phys. Rev. Lett. **117**, 207201 (2016) (see pp. 1, 24).

[19] O. A. Castro-Alvaredo, B. Doyon, and T. Yoshimura, *Emergent Hydrodynamics in Integrable Quantum Systems Out of Equilibrium*, Phys. Rev. X **6**, 041065 (2016) (see pp. 1, 23, 24).

[20] J.-S. Caux, B. Doyon, J. Dubail, R. Konik, and T. Yoshimura, *Hydrodynamics of the interacting Bose gas in the Quantum Newton Cradle setup*, SciPost Physics **6**, 070 (2019) (see pp. 1, 24).

[21] L. D. Landau, L. P. Pitaevskii, and E. M. Lifshitz, *Statistical Physics, Part 1, 3rd Revised and Enlarged Edition*, 3rd Edition (Butterworth Architecture, Oxford, New York, 1980) (see p. 1).

[22] M. Bixon and R. Zwanzig, *Boltzmann-Langevin Equation and Hydrodynamic Fluctuations*, Phys. Rev. **187**, 267 (1969) (see p. 1).

[23] R. F. Fox and G. E. Uhlenbeck, *Contributions to Non-Equilibrium Thermodynamics. I. Theory of Hydrodynamical Fluctuations*, The Physics of Fluids **13**, 1893 (1970) (see p. 1).

[24] K. T. Mashiyama and H. Mori, *Origin of the Landau-Lifshitz hydrodynamic fluctuations in nonequilibrium systems and a new method for reducing the Boltzmann equation*, J Stat Phys **18**, 385 (1978) (see p. 1).

[25] J. M. Ortiz de Zárate and J. V. Sengers, *Hydrodynamic fluctuations in fluids and fluid mixtures*, first edition (Elsevier, Amsterdam Heidelberg, 2006) (see p. 2).

[26] H. B. Callen and T. A. Welton, *Irreversibility and Generalized Noise*, Phys. Rev. **83**, 34 (1951) (see p. 2).

[27] R. Kubo, *The fluctuation-dissipation theorem*, Rep. Prog. Phys. **29**, 255 (1966) (see pp. 2, 28).

[28] I. Bloch, J. Dalibard, and W. Zwerger, *Many-body physics with ultracold gases*, Rev. Mod. Phys. **80**, 885 (2008) (see p. 2).

[29] N. Gemelke, X. Zhang, C.-L. Hung, and C. Chin, *In situ observation of incompressible Mott-insulating domains in ultracold atomic gases*, Nature **460**, 995 (2009) (see p. 2).

[30] J. R. Dorfman, T. R. Kirkpatrick, and J. V. Sengers, *Generic Long-Range Correlations in Molecular Fluids*, Annual Review of Physical Chemistry **45**, 213 (1994) (see p. 2).

[31] L. Bertini, A. De Sole, D. Gabrielli, G. Jona-Lasinio, and C. Landim, *Macroscopic fluctuation theory*, Rev. Mod. Phys. **87**, 593 (2015) (see pp. 2, 25).

[32] G. Falkovich, K. Gawedzki, and M. Vergassola, *Particles and fields in fluid turbulence*, Rev. Mod. Phys. **73**, 913 (2001) (see p. 2).

[33] P. I. Hurtado, C. Pérez-Espigares, J. J. del Pozo, P. L. Garrido, and J. L. Lebowitz, *Symmetries in fluctuations far from equilibrium*, Proceedings of the National Academy of Sciences of the United States of America **108**, 7704 (2011) (see p. 2).

[34] A. Naji, P. J. Atzberger, and F. L. H. Brown, *Hybrid Elastic and Discrete-Particle Approach to Biomembrane Dynamics with Application to the Mobility of Curved Integral Membrane Proteins*, Phys. Rev. Lett. **102**, 138102 (2009) (see p. 2).

[35] C. C. Chow and M. A. Buice, *Path Integral Methods for Stochastic Differential Equations*, The Journal of Mathematical Neuroscience (JMN) **5**, 8 (2015) (see p. 2).

[36] S. F. Jones, G. M. Evans, and K. P. Galvin, *Bubble nucleation from gas cavities — a review*, Advances in Colloid and Interface Science **80**, 27 (1999) (see p. 2).

[37] D. Kashchiev and G. M. van Rosmalen, *Review: Nucleation in solutions revisited*, Crystal Research and Technology **38**, 555 (2003) (see p. 2).

[38] M. Gallo, F. Magaletti, and C. M. Casciola, *Fluctuating hydrodynamics as a tool to investigate nucleation of cavitation bubbles*, Int. J. CMEM **6**, 345 (2017) (see p. 2).

[39] A. M. Kaufman, M. E. Tai, A. Lukin, M. Rispoli, R. Schittko, P. M. Preiss, and M. Greiner, *Quantum thermalization through entanglement in an isolated many-body system*, Science **353**, 794 (2016) (see pp. 2, 9–11, 18, 71).

[40] M. Rispoli, A. Lukin, R. Schittko, S. Kim, M. E. Tai, J. Léonard, and M. Greiner, *Quantum critical behaviour at the many-body localization transition*, Nature **573**, 385 (2019) (see pp. 2, 10).

[41] J. M. Deutsch, *Quantum statistical mechanics in a closed system*, Phys. Rev. A **43**, 2046 (1991) (see pp. 2, 17).

[42] M. Srednicki, *Quantum Chaos and Statistical Mechanicsa*, Annals of the New York Academy of Sciences **755**, 757 (1995) (see pp. 2, 17).

[43] P. Glorioso, J. Guo, J. F. Rodriguez-Nieva, and A. Lucas, *Breakdown of hydrodynamics below four dimensions in a fracton fluid*, Nat. Phys. **18**, 912 (2022) (see p. 2).

[44] F. Carollo, J. P. Garrahan, I. Lesanovsky, and C. Pérez-Espigares, *Fluctuating hydrodynamics, current fluctuations, and hyperuniformity in boundary-driven open quantum chains*, Phys. Rev. E **96**, 052118 (2017) (see p. 2).

[45] E. McCulloch, J. De Nardis, S. Gopalakrishnan, and R. Vasseur, *Full Counting Statistics of Charge in Chaotic Many-body Quantum Systems*, arXiv:2302.01355 (2023) (see pp. 2, 9, 30).

[46] S. R. White, *Density matrix formulation for quantum renormalization groups*, Phys. Rev. Lett. **69**, 2863 (1992) (see p. 2).

[47] S. R. White, *Density-matrix algorithms for quantum renormalization groups*, Phys. Rev. B **48**, 10345 (1993) (see p. 2).

[48] U. Schollwöck, *The density-matrix renormalization group*, Rev. Mod. Phys. **77**, 259 (2005) (see p. 2).

[49] U. Schollwöck, *The density-matrix renormalization group in the age of matrix product states*, Annals of Physics, January 2011 Special Issue **326**, 96 (2011) (see p. 2).

[50] R. P. Feynman, *Simulating physics with computers*, Int J Theor Phys **21**, 467 (1982) (see p. 2).

[51] A. Trabesinger, *Quantum simulation*, Nature Phys **8**, 263 (2012) (see p. 2).

[52] J. Preskill, *Quantum Computing in the NISQ era and beyond*, Quantum **2**, 79 (2018) (see p. 2).

[53] I. Bloch, *Quantum simulations come of age*, Nature Phys **14**, 1159 (2018) (see pp. 2, 10).

[54] C. Gross and I. Bloch, *Quantum simulations with ultracold atoms in optical lattices*, Science **357**, 995 (2017) (see pp. 2, 10).

[55] N. Yao, *Quantum Simulation: Advances, Platforms, and Applications*, in *Frontiers of Engineering: Reports on Leading-Edge Engineering from the 2018 Symposium* (National Academies Press (US), 2019) (see p. 2).

[56] W. S. Bakr, J. I. Gillen, A. Peng, S. Fölling, and M. Greiner, *A quantum gas microscope for detecting single atoms in a Hubbard-regime optical lattice*, Nature **462**, 74 (2009) (see pp. 2, 8).

[57] J. F. Sherson, C. Weitenberg, M. Endres, M. Cheneau, I. Bloch, and S. Kuhr, *Single-atom-resolved fluorescence imaging of an atomic Mott insulator*, Nature **467**, 68 (2010) (see pp. 2, 10).

[58] C. Gross and W. S. Bakr, *Quantum gas microscopy for single atom and spin detection*, Nat. Phys. **17**, 1316 (2021) (see pp. 2, 41).

[59] M. Cheneau, P. Barmettler, D. Poletti, M. Endres, P. Schauß, T. Fukuhara, C. Gross, I. Bloch, C. Kollath, and S. Kuhr, *Light-cone-like spreading of correlations in a quantum many-body system*, Nature **481**, 484 (2012) (see pp. 2, 9, 19, 79).

[60] J. Koepsell, D. Bourgund, P. Sompet, S. Hirthe, A. Bohrdt, Y. Wang, F. Grusdt, E. Demler, G. Salomon, C. Gross, and I. Bloch, *Microscopic evolution of doped Mott insulators from polaronic metal to Fermi liquid*, Science **374**, 82 (2021) (see pp. 2, 9).

[61] N. O. Abeling, *Microscopic foundation of the Eigenstate Thermalization Hypothesis*, PhD Thesis, Georg-August-Universität Göttingen (2023) (see p. 2).

[62] M. Tajik, M. Gluza, N. Sebe, P. Schüttelkopf, F. Cataldini, J. Sabino, F. Møller, S.-C. Ji, S. Erne, G. Guarnieri, S. Sotiriadis, J. Eisert, and J. Schmiedmayer, *Experimental observation of curved light-cones in a quantum field simulator*, Proceedings of the National Academy of Sciences **120**, e2301287120 (2023) (see pp. 2, 9, 79).

[63] I. Bloch, J. Dalibard, and S. Nascimbène, *Quantum simulations with ultracold quantum gases*, Nature Phys **8**, 267 (2012) (see pp. 2, 7).

[64] A. Mazurenko, C. S. Chiu, G. Ji, M. F. Parsons, M. Kanász-Nagy, R. Schmidt, F. Grusdt, E. Demler, D. Greif, and M. Greiner, *A cold-atom Fermi–Hubbard antiferromagnet*, Nature **545**, 462 (2017) (see pp. 2, 9).

[65] M. Aidelsburger, M. Atala, S. Nascimbène, S. Trotzky, Y.-A. Chen, and I. Bloch, *Experimental Realization of Strong Effective Magnetic Fields in an Optical Lattice*, Phys. Rev. Lett. **107**, 255301 (2011) (see pp. 2, 35).

[66] J. Léonard, S. Kim, J. Kwan, P. Segura, F. Grusdt, C. Repellin, N. Goldman, and M. Greiner, *Realization of a fractional quantum Hall state with ultracold atoms*, Nature **619**, 495 (2023) (see p. 2).

[67] S. Trotzky, Y.-A. Chen, A. Flesch, I. P. McCulloch, U. Schollwöck, J. Eisert, and I. Bloch, *Probing the relaxation towards equilibrium in an isolated strongly correlated one-dimensional Bose gas*, Nature Phys **8**, 325 (2012) (see pp. 2, 10, 61, 71, 74).

[68] M. Schreiber, S. S. Hodgman, P. Bordia, H. P. Lüschen, M. H. Fischer, R. Vosk, E. Altman, U. Schneider, and I. Bloch, *Observation of many-body localization of interacting fermions in a quasirandom optical lattice*, Science **349**, 842 (2015) (see pp. 2, 10, 61, 74).

[69] H. P. Lüschen, P. Bordia, S. Scherg, F. Alet, E. Altman, U. Schneider, and I. Bloch, *Observation of Slow Dynamics near the Many-Body Localization Transition in One-Dimensional Quasiperiodic Systems*, Phys. Rev. Lett. **119**, 260401 (2017) (see pp. 2, 10).

[70] A. Lukin, M. Rispoli, R. Schittko, M. E. Tai, A. M. Kaufman, S. Choi, V. Khemani, J. Léonard, and M. Greiner, *Probing entanglement in a many-body–localized system*, Science **364**, 256 (2019) (see pp. 2, 9, 10, 114).

[71] T. Kohlert, S. Scherg, X. Li, H. P. Lüschen, S. Das Sarma, I. Bloch, and M. Aidelsburger, *Observation of Many-Body Localization in a One-Dimensional System with a Single-Particle Mobility Edge*, Phys. Rev. Lett. **122**, 170403 (2019) (see pp. 2, 10).

[72] A. Rubio-Abadal, M. Ippoliti, S. Hollerith, D. Wei, J. Rui, S. L. Sondhi, V. Khemani, C. Gross, and I. Bloch, *Floquet prethermalization in a Bose-Hubbard system*, Phys. Rev. X **10**, 021044 (2020) (see pp. 2, 10, 114).

[73] Y. Takasu, T. Yagami, H. Asaka, Y. Fukushima, K. Nagao, S. Goto, I. Danshita, and Y. Takahashi, *Energy redistribution and spatiotemporal evolution of correlations after a sudden quench of the Bose-Hubbard model*, Science Advances **6**, eaba9255 (2020) (see pp. 2, 10, 79).

[74] B. Yang, H. Sun, R. Ott, H.-Y. Wang, T. V. Zache, J. C. Halimeh, Z.-S. Yuan, P. Hauke, and J.-W. Pan, *Observation of gauge invariance in a 71-site Bose–Hubbard quantum simulator*, Nature **587**, 392 (2020) (see pp. 2, 10, 115).

[75] S. Scherg, T. Kohlert, P. Sala, F. Pollmann, B. Hebbe Madhusudhana, I. Bloch, and M. Aidelsburger, *Observing non-ergodicity due to kinetic constraints in tilted Fermi-Hubbard chains*, Nat Commun **12**, 4490 (2021) (see pp. 2, 10, 114).

[76] Z.-Y. Zhou, G.-X. Su, J. C. Halimeh, R. Ott, H. Sun, P. Hauke, B. Yang, Z.-S. Yuan, J. Berges, and J.-W. Pan, *Thermalization dynamics of a gauge theory on a quantum simulator*, Science **377**, 311 (2022) (see pp. 2, 10).

[77] T. Kohlert, S. Scherg, P. Sala, F. Pollmann, B. Hebbe Madhusudhana, I. Bloch, and M. Aidelsburger, *Exploring the Regime of Fragmentation in Strongly Tilted Fermi-Hubbard Chains*, Phys. Rev. Lett. **130**, 010201 (2023) (see pp. 2, 10, 114).

[78] G.-X. Su, H. Sun, A. Hudomal, J.-Y. Desaules, Z.-Y. Zhou, B. Yang, J. C. Halimeh, Z.-S. Yuan, Z. Papić, and J.-W. Pan, *Observation of many-body scarring in a Bose-Hubbard quantum simulator*, Phys. Rev. Res. **5**, 023010 (2023) (see pp. 2, 10, 114).

[79] J. Léonard, S. Kim, M. Rispoli, A. Lukin, R. Schittko, J. Kwan, E. Demler, D. Sels, and M. Greiner, *Probing the onset of quantum avalanches in a many-body localized system*, Nat. Phys. **19**, 481 (2023) (see pp. 2, 10).

[80] X. Zhang, E. Kim, D. K. Mark, S. Choi, and O. Painter, *A superconducting quantum simulator based on a photonic-bandgap metamaterial*, Science **379**, 278 (2023) (see p. 2).

[81] W.-Y. Zhang et al., *Scalable Multipartite Entanglement Created by Spin Exchange in an Optical Lattice*, Phys. Rev. Lett. **131**, 073401 (2023) (see pp. 2, 9, 60).

[82] T. M. Klostermann, *Construction of a caesium quantum gas microscope*, PhD Thesis, Ludwig-Maximilians-Universität München (2022) (see pp. 3, 34, 36, 41–43, 46, 55).

[83] A. Impertro, J. F. Wienand, S. Häfele, H. von Raven, S. Hubele, T. Klostermann, C. R. Cabrera, I. Bloch, and M. Aidelsburger, *An unsupervised deep learning algorithm for single-site reconstruction in quantum gas microscopes*, Nat. Comm. Phys. **6**, 1 (2023) (see pp. 3, 5, 50, 52, 91, 117).

[84] F. Grusdt, M. Höning, and M. Fleischhauer, *Topological Edge States in the One-Dimensional Superlattice Bose-Hubbard Model*, Phys. Rev. Lett. **110**, 260405 (2013) (see pp. 3, 103, 104).

[85] J. Bibo, I. Lovas, Y. You, F. Grusdt, and F. Pollmann, *Fractional corner charges in a two-dimensional superlattice Bose-Hubbard model*, Phys. Rev. B **102**, 041126 (2020) (see p. 3).

[86] W. A. Benalcazar, B. A. Bernevig, and T. L. Hughes, *Quantized electric multipole insulators*, Science **357**, 61 (2017) (see pp. 3, 101).

[87] W. A. Benalcazar, B. A. Bernevig, and T. L. Hughes, *Electric multipole moments, topological multipole moment pumping, and chiral hinge states in crystalline insulators*, Phys. Rev. B **96**, 245115 (2017) (see pp. 3, 4, 101).

[88] M. Serra-Garcia, V. Peri, R. Süsstrunk, O. R. Bilal, T. Larsen, L. G. Villanueva, and S. D. Huber, *Observation of a phononic quadrupole topological insulator*, Nature **555**, 342 (2018) (see pp. 3, 101).

[89] S. Imhof, C. Berger, F. Bayer, J. Brehm, L. W. Molenkamp, T. Kiessling, F. Schindler, C. H. Lee, M. Greiter, T. Neupert, and R. Thomale, *Topolectrical-circuit realization of topological corner modes*, Nat. Phys. **14**, 925 (2018) (see pp. 3, 101).

[90] H. Xue, Y. Yang, F. Gao, Y. Chong, and B. Zhang, *Acoustic higher-order topological insulator on a kagome lattice*, Nature Materials **18**, 108 (2018) (see pp. 3, 101).

[91] C. W. Peterson, W. A. Benalcazar, T. L. Hughes, and G. Bahl, *A quantized microwave quadrupole insulator with topologically protected corner states*, Nature **555**, 346 (2018) (see pp. 3, 101).

[92] X. Ni, M. Weiner, A. Alù, and A. B. Khanikaev, *Observation of higher-order topological acoustic states protected by generalized chiral symmetry*, Nature Materials **18**, 113 (2019) (see pp. 3, 101).

[93] S. Mittal, V. V. Orre, G. Zhu, M. A. Gorlach, A. Poddubny, and M. Hafezi, *Photonic quadrupole topological phases*, Nature Photonics **13**, 692 (2019) (see pp. 3, 101).

[94] J. Bao, D. Zou, W. Zhang, W. He, H. Sun, and X. Zhang, *Topoelectrical circuit octupole insulator with topologically protected corner states*, Phys. Rev. B **100**, 201406 (2019) (see pp. 3, 101).

[95] X. Ni, M. Li, M. Weiner, A. Alù, and A. B. Khanikaev, *Demonstration of a quantized acoustic octupole topological insulator*, Nature Communications **11**, 2108 (2020) (see pp. 3, 101).

[96] A. Dutt, M. Minkov, I. A. D. Williamson, and S. Fan, *Higher-order topological insulators in synthetic dimensions*, Light Sci Appl **9**, 131 (2020) (see pp. 3, 101).

[97] R. Noguchi et al., *Evidence for a higher-order topological insulator in a three-dimensional material built from van der Waals stacking of bismuth-halide chains*, Nature Materials **20**, 473 (2021) (see pp. 3, 101).

[98] W. A. Benalcazar, J. Noh, M. Wang, S. Huang, K. P. Chen, and M. C. Rechtsman, *Higher-order topological pumping and its observation in photonic lattices*, Phys. Rev. B **105**, 195129 (2022) (see pp. 3, 4, 101, 114).

[99] B. Xie, H.-X. Wang, X. Zhang, P. Zhan, J.-H. Jiang, M. Lu, and Y. Chen, *Higher-order band topology*, Nature Reviews Physics **3**, 520 (2021) (see p. 3).

[100] W. Zhang, X. Xie, H. Hao, J. Dang, S. Xiao, S. Shi, H. Ni, Z. Niu, C. Wang, K. Jin, X. Zhang, and X. Xu, *Low-threshold topological nanolasers based on the second-order corner state*, Light Sci Appl **9**, 109 (2020) (see p. 3).

[101] H.-R. Kim, M.-S. Hwang, D. Smirnova, K.-Y. Jeong, Y. Kivshar, and H.-G. Park, *Multipolar lasing modes from topological corner states*, Nature Communications **11**, 5758 (2020) (see p. 3).

[102] M.-S. Wei, M.-J. Liao, C. Wang, C. Zhu, Y. Yang, and J. Xu, *Topological laser with higher-order corner states in the 2-dimensional Su-Schrieffer-Heeger model*, Opt. Express, OE **31**, 3427 (2023) (see p. 3).

[103] J. Zak, *Berrys Phase For Energy-bands In Solids*, Phys. Rev. Lett. **62**, 2747 (1989) (see pp. 3, 104).

[104] R. D. King-Smith and D. Vanderbilt, *Theory of polarization of crystalline solids*, Phys. Rev. B **47**, 1651 (1993) (see pp. 3, 100, 104).

[105] R. Resta, *Polarization as a Berry Phase*, Europhys. News **28**, 18 (1997) (see p. 3).

[106] D. J. Thouless, *Quantization of particle transport*, Phys. Rev. B **27**, 6083 (1983) (see pp. 4, 104).

[107] Q. Niu and D. J. Thouless, *Quantised adiabatic charge transport in the presence of substrate disorder and many-body interaction*, Journal of Physics A: Mathematical and General **17**, 2453 (1984) (see pp. 4, 103).

[108] R. Citro and M. Aidelsburger, *Thouless pumping and topology*, Nat Rev Phys **5**, 87 (2023) (see pp. 4, 103).

[109] B. Kang, K. Shiozaki, and G. Y. Cho, *Many-body order parameters for multipoles in solids*, Phys. Rev. B **100**, 245134 (2019) (see pp. 4, 101).

[110] S. Ono, L. Trifunovic, and H. Watanabe, *Difficulties in operator-based formulation of the bulk quadrupole moment*, Phys. Rev. B **100**, 245133 (2019) (see pp. 4, 101, 110).

[111] W. A. Wheeler, L. K. Wagner, and T. L. Hughes, *Many-body electric multipole operators in extended systems*, Phys. Rev. B **100**, 245135 (2019) (see pp. 4, 101).

[112] I. Petrides and O. Zilberberg, *Higher-order topological insulators, topological pumps and the quantum Hall effect in high dimensions*, Phys. Rev. Research **2**, 022049 (2020) (see p. 4).

[113] H. Watanabe and S. Ono, *Corner charge and bulk multipole moment in periodic systems*, Phys. Rev. B **102**, 165120 (2020) (see pp. 4, 101).

[114] S. Ren, I. Souza, and D. Vanderbilt, *Quadrupole moments, edge polarizations, and corner charges in the Wannier representation*, Phys. Rev. B **103**, 035147 (2021) (see pp. 4, 101).

[115] B. Kang, W. Lee, and G. Y. Cho, *Many-Body Invariants for Chern and Chiral Hinge Insulators*, Phys. Rev. Lett. **126**, 016402 (2021) (see pp. 4, 101).

[116] J. F. Wienand, F. Horn, M. Aidelsburger, J. Bibo, and F. Grusdt, *Thouless Pumps and Bulk-Boundary Correspondence in Higher-Order Symmetry-Protected Topological Phases*, Phys. Rev. Lett. **128**, 246602 (2022) (see pp. 5, 99, 105, 109).

[117] A. Impertro, S. Karch, J. F. Wienand, S. Huh, C. Schweizer, I. Bloch, and M. Aidelsburger, *Local readout and control of current and kinetic energy operators in optical lattices*, arXiv:2312.13268 (2023) (see pp. 5, 9).

[118] T. Klostermann, C. R. Cabrera, H. von Raven, J. F. Wienand, C. Schweizer, I. Bloch, and M. Aidelsburger, *Fast long-distance transport of cold cesium atoms*, Phys. Rev. A **105**, 043319 (2022) (see pp. 5, 36, 46).

[119] P. S. Jessen and I. H. Deutsch, *Optical Lattices*, in *Advances In Atomic, Molecular, and Optical Physics*, Vol. 37, edited by B. Bederson and H. Walther (Academic Press, 1996), 95 (see p. 7).

[120] M. Greiner and S. Fölling, *Optical lattices*, Nature **453**, 736 (2008) (see p. 7).

[121] R. Grimm, M. Weidemüller, and Y. B. Ovchinnikov, *Optical Dipole Traps for Neutral Atoms*, in *Advances In Atomic, Molecular, and Optical Physics*, Vol. 42, edited by B. Bederson and H. Walther (Academic Press, 2000), 95 (see pp. 7, 8).

[122] E. Haller, J. Hudson, A. Kelly, D. A. Cotta, B. Peaudecerf, G. D. Bruce, and S. Kuhr, *Single-atom imaging of fermions in a quantum-gas microscope*, Nature Phys **11**, 738 (2015) (see p. 8).

[123] A. Bohrdt, *Probing strongly correlated many-body systems with quantum simulation*, PhD Thesis, Technische Universität München (2021) (see p. 8).

[124] Y. V. Nazarov and M. Kindermann, *Full counting statistics of a general quantum mechanical variable*, Eur. Phys. B **35**, 413 (2003) (see p. 9).

[125] N. Malossi, M. M. Valado, S. Scotto, P. Huillery, P. Pillet, D. Ciampini, E. Arimondo, and O. Morsch, *Full Counting Statistics and Phase Diagram of a Dissipative Rydberg Gas*, Phys. Rev. Lett. **113**, 023006 (2014) (see p. 9).

[126] J.-M. Stéphan and F. Pollmann, *Full counting statistics in the Haldane-Shastry chain*, Phys. Rev. B **95**, 035119 (2017) (see p. 9).

[127] I. Lovas, B. Dóra, E. Demler, and G. Zaránd, *Full counting statistics of time-of-flight images*, Phys. Rev. A **95**, 053621 (2017) (see p. 9).

[128] M. Collura, F. H. L. Essler, and S. Groha, *Full counting statistics in the spin-1/2 Heisenberg XXZ chain*, J. Phys. A: Math. Theor. **50**, 414002 (2017) (see p. 9).

[129] S. Humeniuk and H. P. Büchler, *Full Counting Statistics for Interacting Fermions with Determinantal Quantum Monte Carlo Simulations*, Phys. Rev. Lett. **119**, 236401 (2017) (see p. 9).

[130] P. Calabrese, M. Collura, G. D. Giulio, and S. Murciano, *Full counting statistics in the gapped XXZ spin chain*, Europhys. Lett. **129**, 60007 (2020) (see p. 9).

[131] P. Devillard, D. Chevallier, P. Vignolo, and M. Albert, *Full counting statistics of the momentum occupation numbers of the Tonks-Girardeau gas*, Phys. Rev. A **101**, 063604 (2020) (see p. 9).

[132] T. D. Honeychurch and D. S. Kosov, *Full counting statistics for electron transport in periodically driven quantum dots*, Phys. Rev. B **102**, 195409 (2020) (see p. 9).

[133] G. Hercé, J.-P. Bureik, A. Ténart, A. Aspect, A. Dareau, and D. Clément, *Full counting statistics of interacting lattice gases after an expansion: The role of the condensate depletion in the many-body coherence*, arXiv:2207.14070 (2022) (see p. 9).

[134] B. Bertini, P. Calabrese, M. Collura, K. Klobas, and C. Rylands, *Nonequilibrium Full Counting Statistics and Symmetry-Resolved Entanglement from Space-Time Duality*, arXiv:2212.06188 (2023) (see p. 9).

[135] R. Islam, R. Ma, P. M. Preiss, M. Eric Tai, A. Lukin, M. Rispoli, and M. Greiner, *Measuring entanglement entropy in a quantum many-body system*, Nature **528**, 77 (2015) (see p. 9).

[136] A. M. Kaufman, M. C. Tichy, F. Mintert, A. M. Rey, and C. A. Regal, *Chapter Seven - The Hong–Ou–Mandel Effect With Atoms*, in *Advances In Atomic, Molecular, and Optical Physics*, Vol. 67, edited by E. Arimondo, L. F. DiMauro, and S. F. Yelin (Academic Press, 2018), 377 (see p. 9).

[137] T. Brydges, A. Elben, P. Jurcevic, B. Vermersch, C. Maier, B. P. Lanyon, P. Zoller, R. Blatt, and C. F. Roos, *Probing Rényi entanglement entropy via randomized measurements*, Science **364**, 260 (2019) (see p. 9).

[138] C. Weitenberg, M. Endres, J. F. Sherson, M. Cheneau, P. Schauß, T. Fukuhara, I. Bloch, and S. Kuhr, *Single-spin addressing in an atomic Mott insulator*, Nature **471**, 319 (2011) (see pp. 9, 115).

[139] E. B. Sonin, *Transverse forces on vortices in superfluids in a periodic potential*, Phys. Rev. B **94**, 054521 (2016) (see p. 9).

[140] D. Jaksch, C. Bruder, J. I. Cirac, C. W. Gardiner, and P. Zoller, *Cold Bosonic Atoms in Optical Lattices*, Phys. Rev. Lett. **81**, 3108 (1998) (see p. 9).

[141] J. Hubbard, *Electron Correlations in Narrow Energy Bands*, Proceedings of the Royal Society of London. Series A, Mathematical and Physical Sciences **276**, 238 (1963) (see p. 9).

[142] J. Hubbard, *Electron Correlations in Narrow Energy Bands. III. An Improved Solution*, Proceedings of the Royal Society of London Series A **281**, 401 (1964) (see p. 9).

[143] E. Pavarini, J. van den Brink, E. Koch, and G. Sawatzky, *Quantum Materials: Experiments and Theory*, tech. rep. FZJ-2016-05129 (Forschungszentrum Jülich GmbH Zentralbibliothek, Verlag, 2016) (see p. 9).

[144] M. Greiner, O. Mandel, T. Esslinger, T. W. Hänsch, and I. Bloch, *Quantum phase transition from a superfluid to a Mott insulator in a gas of ultracold atoms*, Nature **415**, 39 (2002) (see p. 10).

[145] W. S. Bakr, A. Peng, M. E. Tai, R. Ma, J. Simon, J. I. Gillen, S. Fölling, L. Pollet, and M. Greiner, *Probing the Superfluid–to–Mott Insulator Transition at the Single-Atom Level*, Science **329**, 547 (2010) (see p. 10).

[146] M. Möckel, *Real-time evolution of quenched quantum systems*, PhD Thesis, Ludwig-Maximilians-Universität München (2009) (see p. 11).

[147] D. Mitra, P. T. Brown, E. Guardado-Sanchez, S. S. Kondov, T. Devakul, D. A. Huse, P. Schauß, and W. S. Bakr, *Quantum gas microscopy of an attractive Fermi–Hubbard system*, Nat. Phys. **14**, 173 (2018) (see pp. 11, 49, 71).

[148] A. Iucci and M. A. Cazalilla, *Quantum quench dynamics of the sine-Gordon model in some solvable limits*, New J. Phys. **12**, 055019 (2010) (see p. 11).

[149] S. A. Parameswaran, *Quantum Glasses at Infinite Temperature*, (see p. 11).

[150] H. Flaschka, A. C. Newell, and M. Tabor, *Integrability*, in *What Is Integrability?* Edited by V. E. Zakharov (Springer, Berlin, Heidelberg, 1991), 73 (see p. 11).

[151] R. C. Hilborn, *Chaos and Nonlinear Dynamics: An Introduction for Scientists and Engineers* (Oxford University Press, 2000) (see p. 11).

[152] J. Wang and D. Xiong, *Observation of Ballistic Thermal Transport in a Nonintegrable Classical Many-Body System*, arXiv:2402.02142 (2024) (see p. 11).

[153] A. Luikov, *Analytical Heat Diffusion Theory* (Elsevier, 2012) (see p. 11).

[154] E. Syková, *Extrasynaptic volume transmission and diffusion parameters of the extracellular space*, Neuroscience, Brain Water Homeostasis **129**, 861 (2004) (see p. 11).

[155] T. Prosen and B. Žunkovič, *Macroscopic Diffusive Transport in a Microscopically Integrable Hamiltonian System*, Phys. Rev. Lett. **111**, 040602 (2013) (see p. 11).

[156] L. D. Faddeev and L. A. Takhtajan, *Hamiltonian Methods in the Theory of Solitons*, trans. by A. G. Reyman, Reprint of the 1st ed. Berlin Heidelberg New York 1987 Edition (Springer, Berlin ; New York, 2007) (see p. 11).

[157] Z. Wang, Y. Chong, J. D. Joannopoulos, and M. Soljačić, *Observation of unidirectional backscattering-immune topological electromagnetic states*, Nature **461**, 772 (2009) (see p. 11).

[158] A. Eckardt, *Colloquium: Atomic quantum gases in periodically driven optical lattices*, Rev. Mod. Phys. **89**, 011004 (2017) (see p. 11).

[159] A. L. Retore, *Introduction to classical and quantum integrability*, J. Phys. A: Math. Theor. **55**, 173001 (2022) (see p. 11).

[160] M. P. Grabowski and P. Mathieu, *Quantum integrals of motion for the heisenberg spin chain*, Mod. Phys. Lett. A **09**, 2197 (1994) (see p. 12).

[161] S. Moshfegh, A. Ashouri, S. Mahdavifar, and J. Vahedi, *Integrable-chaos crossover in the XXZ chain with cluster interaction*, Physica A: Statistical Mechanics and its Applications **516**, 502 (2019) (see p. 12).

[162] O. Bohigas, M. J. Giannoni, and C. Schmit, *Characterization of Chaotic Quantum Spectra and Universality of Level Fluctuation Laws*, Phys. Rev. Lett. **52**, 1 (1984) (see p. 12).

[163] M. Rigol, V. Dunjko, and M. Olshanii, *Thermalization and its mechanism for generic isolated quantum systems*, Nature **452**, 854 (2008) (see pp. 12, 16).

[164] E. Fermi, *Thermodynamics* (Dover, New York, 1956) (see p. 12).

[165] L. E. Reichl, *A Modern Course in Statistical Physics*, 4. überarbeitete Edition (Wiley-VCH, Weinheim, 2016) (see p. 13).

[166] H. Park, Y. W. Kim, and J. Yi, *Entropies of the microcanonical ensemble*, AIP Advances **12**, 065226 (2022) (see p. 13).

[167] M. Baus and C. F. Tejero, *Equilibrium Statistical Physics: Phases of Matter and Phase Transitions* (Springer Science & Business Media, 2007) (see p. 14).

[168] A. Wolf, *13. Quantifying chaos with Lyapunov exponents*, in *13. Quantifying chaos with Lyapunov exponents* (Princeton University Press, 2014), 273 (see p. 14).

[169] J. L. Lebowitz and O. Penrose, *Modern ergodic theory*, Physics Today **26**, 23 (1973) (see p. 15).

[170] B. V. Chirikov, *A universal instability of many-dimensional oscillator systems*, Physics Reports **52**, 263 (1979) (see p. 15).

[171] L. D'Alessio, Y. Kafri, A. Polkovnikov, and M. Rigol, *From Quantum Chaos and Eigenstate Thermalization to Statistical Mechanics and Thermodynamics*, Advances in Physics **65**, 239 (2016) (see pp. 16–18).

[172] S. D. Geraedts, R. Nandkishore, and N. Regnault, *Many-body localization and thermalization: Insights from the entanglement spectrum*, Phys. Rev. B **93**, 174202 (2016) (see p. 17).

[173] J. M. Deutsch, H. Li, and A. Sharma, *Microscopic origin of thermodynamic entropy in isolated systems*, Phys. Rev. E **87**, 042135 (2013) (see p. 18).

[174] M. Matty, L. Lancaster, W. Griffin, and R. H. Swendsen, *Comparison of canonical and microcanonical definitions of entropy*, Physica A: Statistical Mechanics and its Applications **467**, 474 (2017) (see p. 18).

[175] J. M. Deutsch, *Thermodynamic entropy of a many-body energy eigenstate*, New J. Phys. **12**, 075021 (2010) (see p. 18).

[176] E. H. Lieb and D. W. Robinson, *The finite group velocity of quantum spin systems*, Communications in Mathematical Physics **28**, 251 (1972) (see pp. 19, 80, 120).

[177] H. Kim and D. A. Huse, *Ballistic spreading of entanglement in a diffusive nonintegrable system*, Phys. Rev. Lett. **111**, 127205 (2013) (see p. 19).

[178] M. Mezei and D. Stanford, *On entanglement spreading in chaotic systems*, J. High Energ. Phys. **2017**, 65 (2017) (see p. 19).

[179] V. Alba and P. Calabrese, *Entanglement and thermodynamics after a quantum quench in integrable systems*, Proc. Natl. Acad. Sci. U.S.A. **114**, 7947 (2017) (see p. 19).

[180] Y. O. Nakagawa, M. Watanabe, H. Fujita, and S. Sugiura, *Universality in volume-law entanglement of scrambled pure quantum states*, Nat. Commun. **9**, 1635 (2018) (see p. 19).

[181] M. Žnidarič, *Entanglement growth in diffusive systems*, Nat. Comm. Phys. **3**, 1 (2020) (see p. 19).

[182] P. A. Lagerstrom, *Laminar Flow Theory*, Reprint Edition (Princeton University Press, Princeton, NJ, 1996) (see p. 21).

[183] C. Clarke and B. Carswell, *Principles of Astrophysical Fluid Dynamics* (Cambridge University Press, Cambridge, 2007) (see p. 21).

[184] J. Dubail, *Three lectures on classical and quantum hydrodynamics applied to trapped 1d quantum gases*, Lecture Notes (see pp. 21–23).

[185] D. Wei, *Microscopy of spin hydrodynamics and cooperative light scattering in atomic Hubbard systems*, PhD Thesis, Ludwig-Maximilians-Universität München (2023) (see pp. 23, 24).

[186] R. B. Bird, W. E. Stewart, and E. N. Lightfoot, *Transport Phenomena* (John Wiley & Sons, 2006) (see p. 23).

[187] A. M. Fouad and M. M. Fouad, *A Density-Dependent Diffusion Model of an Interacting System of Brownian Particles*, arXiv:2202.05394 (2022) (see p. 23).

[188] A. Jain and P. Kovtun, *Late Time Correlations in Hydrodynamics: Beyond Constitutive Relations*, Phys. Rev. Lett. **128**, 071601 (2022) (see p. 24).

[189] A. Lucas, R. A. Davison, and S. Sachdev, *Hydrodynamic theory of thermoelectric transport and negative magnetoresistance in Weyl semimetals*, Proc. Natl. Acad. Sci. U.S.A. **113**, 9463 (2016) (see p. 24).

[190] J. M. O. d. Zarate and J. V. Sengers, *Hydrodynamic Fluctuations in Fluids and Fluid Mixtures*, 1st ed. (Elsevier Science, 2006) (see pp. 24, 25).

[191] Y. P. P. Mörters, *Brownian Motion*, 1st ed. (Cambridge University Press, Cambridge, UK ; New York, 2010) (see p. 25).

[192] X. Bian, C. Kim, and G. E. Karniadakis, *111 years of Brownian motion*, Soft Matter **12**, 6331 (2016) (see p. 25).

[193] P. L. Krapivsky, S. Redner, and E. Ben-Naim, *A Kinetic View of Statistical Physics* (Cambridge University Press, Cambridge, 2010) (see p. 26).

[194] D. S. Lemons and A. Gythiel, *Paul Langevin's 1908 paper "On the Theory of Brownian Motion" ["Sur la théorie du mouvement brownien," C. R. Acad. Sci. (Paris)* ***146*** *, 530–533 (1908)]*, American Journal of Physics **65**, 1079 (1997) (see p. 26).

[195] J. Lux, J. Müller, A. Mitra, and A. Rosch, *Hydrodynamic long-time tails after a quantum quench*, Phys. Rev. A **89**, 053608 (2014) (see pp. 27, 28, 82).

[196] J. Lux, *FLUCTUATIONS IN AND OUT OF EQUILIBRIUM: Thermalization, quantum measurements and Coulomb disorder*, (see pp. 28, 29).

[197] L. D. Landau and E. M. Lifshitz, *Fluid Mechanics: Volume 6*, 2nd ed. (Butterworth-Heinemann, Amsterdam Heidelberg, 1987) (see p. 28).

[198] M. H. Ernst, E. H. Hauge, and J. M. J. van Leeuwen, *Asymptotic Time Behavior of Correlation Functions*, Phys. Rev. Lett. **25**, 1254 (1970) (see p. 29).

[199] J. R. Dorfman and E. G. D. Cohen, *Velocity Correlation Functions in Two and Three Dimensions*, Phys. Rev. Lett. **25**, 1257 (1970) (see p. 29).

[200] Y. Pomeau and P. Résibois, *Time dependent correlation functions and mode-mode coupling theories*, Physics Reports **19**, 63 (1975) (see p. 29).

[201] M. H. Ernst, E. H. Hauge, and J. M. J. van Leeuwen, *Asymptotic time behavior of correlation functions. II. Kinetic and potential terms*, J Stat Phys **15**, 7 (1976) (see p. 29).

[202] T. R. Kirkpatrick and J. R. Dorfman, *Nonequilibrium is different*, Phys. Rev. E **92**, 022109 (2015) (see p. 29).

[203] B. J. Alder and T. E. Wainwright, *Decay of the Velocity Autocorrelation Function*, Phys. Rev. A **1**, 18 (1970) (see p. 29).

[204] T. E. Wainwright, B. J. Alder, and D. M. Gass, *Decay of Time Correlations in Two Dimensions*, Phys. Rev. A **4**, 233 (1971) (see p. 29).

[205] D. Goykolov, *ASYMMETRIC SIMPLE EXCLUSION PROCESS IN TWO DIMENSIONS*, University of Kentucky Doctoral Dissertations (2007) (see p. 30).

[206] K. Nagel and M. Schreckenberg, *A cellular automaton model for freeway traffic*, J. Phys. I France **2**, 2221 (1992) (see p. 30).

[207] L. B. Shaw, R. K. P. Zia, and K. H. Lee, *Totally asymmetric exclusion process with extended objects: A model for protein synthesis*, Phys. Rev. E **68**, 021910 (2003) (see p. 30).

[208] B. Widom, J. L. Viovy, and A. D. Defontaines, *Repton model of gel electrophoresis and diffusion*, J. Phys. I France **1**, 1759 (1991) (see p. 30).

[209] B. Derrida, E. Domany, and D. Mukamel, *An exact solution of a one-dimensional asymmetric exclusion model with open boundaries*, J Stat Phys **69**, 667 (1992) (see p. 30).

[210] K. Mallick, H. Moriya, and T. Sasamoto, *Exact Solution of the Macroscopic Fluctuation Theory for the Symmetric Exclusion Process*, Phys. Rev. Lett. **129**, 040601 (2022) (see pp. 30, 117).

[211] S. Prolhac and K. Mallick, *Current fluctuations in the exclusion process and Bethe ansatz*, J. Phys. A: Math. Theor. **41**, 175002 (2008) (see p. 30).

[212] B. Derrida and A. Gerschenfeld, *Current Fluctuations of the One Dimensional Symmetric Simple Exclusion Process with Step Initial Condition*, J Stat Phys **136**, 1 (2009) (see p. 30).

[213] B. Derrida, M. R. Evans, V. Hakim, and V. Pasquier, *Exact solution of a 1D asymmetric exclusion model using a matrix formulation*, J. Phys. A: Math. Gen. **26**, 1493 (1993) (see pp. 30, 31).

[214] L. Essen and J. V. L. Parry, *An Atomic Standard of Frequency and Time Interval: A Cæsium Resonator*, Nature **176**, 280 (1955) (see p. 33).

[215] D. A. Steck, *Cesium D Line Data*, (see pp. 33, 34).

[216] S. Rachel, *Interacting topological insulators: a review*, Rep. Prog. Phys. **81**, 116501 (2018) (see p. 33).

[217] M. Dzero, J. Xia, V. Galitski, and P. Coleman, *Topological Kondo Insulators*, Annual Review of Condensed Matter Physics **7**, 249 (2016) (see p. 33).

[218] A. Rasmussen and Y.-M. Lu, *Classification and construction of higher-order symmetry-protected topological phases of interacting bosons*, Phys. Rev. B **101**, 085137 (2020) (see p. 33).

[219] K. Kwon, K. Kim, J. Hur, S. Huh, and J.-y. Choi, *Site-resolved imaging of a bosonic Mott insulator of Li atoms*, Phys. Rev. A **105**, 033323 (2022) (see p. 33).

[220] N. Baldelli, C. R. Cabrera, S. Julià-Farré, M. Aidelsburger, and L. Barbiero, *Frustrated extended Bose-Hubbard model and deconfined quantum critical points with optical lattices at the anti-magic wavelength*, arXiv:2309.03193 (2023) (see pp. 33, 35).

[221] D. Jaksch and P. Zoller, *Creation of effective magnetic fields in optical lattices: the Hofstadter butterfly for cold neutral atoms*, New J. Phys. **5**, 56 (2003) (see p. 33).

[222] F. Gerbier and J. Dalibard, *Gauge fields for ultracold atoms in optical superlattices*, New J. Phys. **12**, 033007 (2010) (see p. 33).

[223] M. D. Frye, B. C. Yang, and J. M. Hutson, *Ultracold collisions of Cs atoms in excited Zeeman and hyperfine states*, Phys. Rev. A **100**, 022702 (2019) (see pp. 34, 35).

[224] H. v. Raven, *A new Caesium quantum gas microscope with precise magnetic field control*, PhD Thesis, Ludwig-Maximilians-Universität München (2022) (see pp. 34–37, 46, 115).

[225] P. N. Jepsen, J. Amato-Grill, I. Dimitrova, W. W. Ho, E. Demler, and W. Ketterle, *Spin transport in a tunable Heisenberg model realized with ultracold atoms*, Nature **588**, 403 (2020) (see p. 34).

[226] C. Chin, V. Vuletić, A. J. Kerman, and S. Chu, *High Resolution Feshbach Spectroscopy of Cesium*, Phys. Rev. Lett. **85**, 2717 (2000) (see p. 34).

[227] M. Gustavsson, E. Haller, M. J. Mark, J. G. Danzl, G. Rojas-Kopeinig, and H.-C. Nägerl, *Control of Interaction-Induced Dephasing of Bloch Oscillations*, Phys. Rev. Lett. **100**, 080404 (2008) (see p. 34).

[228] C. Chin, R. Grimm, P. Julienne, and E. Tiesinga, *Feshbach resonances in ultracold gases*, Rev. Mod. Phys. **82**, 1225 (2010) (see pp. 34, 63).

[229] T. Kraemer, M. Mark, P. Waldburger, J. G. Danzl, C. Chin, B. Engeser, A. D. Lange, K. Pilch, A. Jaakkola, H.-C. Nägerl, and R. Grimm, *Evidence for Efimov quantum states in an ultracold gas of caesium atoms*, Nature **440**, 315 (2006) (see p. 34).

[230] T. Kraemer, *Few-body interactions in an ultracold gas of Cesium atoms*, (see pp. 34, 55).

[231] N. Belmechri, L. Förster, W. Alt, A. Widera, D. Meschede, and A. Alberti, *Microwave control of atomic motional states in a spin-dependent optical lattice*, J. Phys. B: At. Mol. Opt. Phys. **46**, 104006 (2013) (see p. 34).

[232] M. Sajid, J. K. Asbóth, D. Meschede, R. F. Werner, and A. Alberti, *Creating anomalous Floquet Chern insulators with magnetic quantum walks*, Phys. Rev. B **99**, 214303 (2019) (see p. 34).

[233] C. Robens, J. Zopes, W. Alt, S. Brakhane, D. Meschede, and A. Alberti, *Low-Entropy States of Neutral Atoms in Polarization-Synthesized Optical Lattices*, Phys. Rev. Lett. **118**, 065302 (2017) (see p. 34).

[234] S. Knoop, F. Ferlaino, M. Berninger, M. Mark, H.-C. Nägerl, R. Grimm, J. P. D'Incao, and B. D. Esry, *Magnetically Controlled Exchange Process in an Ultracold Atom-Dimer Mixture*, Phys. Rev. Lett. **104**, 053201 (2010) (see p. 34).

[235] J. E. Sansonetti, *Wavelengths, Transition Probabilities, and Energy Levels for the Spectra of Cesium „Cs I – Cs LV…* J. Phys. Chem. Ref. Data **38** (2009) (see p. 34).

[236] J. F. Wienand, *Multi-Level Fluorescence Imaging and Degenerate Raman Sideband Cooling for a Caesium Quantum Gas Microscope*, MA thesis, Ludwig-Maximilians-Universität München (2019) (see p. 34).

[237] T. Hilker, *Spin-resolved microscopy of strongly correlated fermionic many-body states*, PhD Thesis, Ludwig-Maximilians-Universität München (2017) (see p. 34).

[238] C. Cesar, *Quantum liquid droplets in a mixture of Bose-Einstein condensates*, PhD Thesis, Universitat Politècnica de Catalunya (2018) (see p. 34).

[239] D. A. Steck, *Rubidium 87 D Line Data* (see p. 34).

[240] M. Aidelsburger, M. Atala, M. Lohse, J. T. Barreiro, B. Paredes, and I. Bloch, *Realization of the Hofstadter Hamiltonian with Ultracold Atoms in Optical Lattices*, Phys. Rev. Lett. **111**, 10.1103/physrevlett.111.185301 (2013) (see p. 35).

[241] C. Weitenberg, *Single-Atom Resolved Imaging and Manipulation in an Atomic Mott Insulator*, PhD Thesis, Ludwig-Maximilians-Universität München (2011) (see pp. 37, 42, 43, 50).

[242] M. Lohse, C. Schweizer, H. M. Price, O. Zilberberg, and I. Bloch, *Exploring 4D quantum Hall physics with a 2D topological charge pump*, Nature **553**, 55 (2018) (see pp. 39, 65).

[243] I. Pérez, *Single-Site Addressing and Imaging of Cesium Atoms in a Quantum Gas Microscope*, MA thesis, Ludwig-Maximilians-Universität München (2023) (see p. 42).

[244] G. Gauthier, I. Lenton, N. M. Parry, M. Baker, M. J. Davis, H. Rubinsztein-Dunlop, and T. W. Neely, *Direct imaging of a digital-micromirror device for configurable microscopic optical potentials*, Optica, OPTICA **3**, 1136 (2016) (see p. 42).

[245] D. Wei, *Development of a Spatially Incoherent Laser Source*, (2019) (see p. 42).

[246] S. Hubele, *Potential Shaping Using a DMD and High-Resolution Imaging of Cesium Atoms in Optical Lattices*, MA thesis, Ludwig-Maximilians-Universität München (2022) (see p. 42).

[247] K. B. Davis, M. .-. Mewes, M. R. Andrews, N. J. van Druten, D. S. Durfee, D. M. Kurn, and W. Ketterle, *Bose-Einstein Condensation in a Gas of Sodium Atoms*, Phys. Rev. Lett. **75**, 3969 (1995) (see p. 49).

[248] K. D. Nelson, X. Li, and D. S. Weiss, *Imaging single atoms in a three-dimensional array*, Nature Phys **3**, 556 (2007) (see p. 49).

[249] S. Häfele, *Deep Learning for Quantum Gas Microscopy of Cesium Atoms in Optical Lattices - Below the Resolution Limit*, MA thesis, Ludwig-Maximilians-Universität München (see p. 50).

[250] P. A. Murthy, D. Kedar, T. Lompe, M. Neidig, M. G. Ries, A. N. Wenz, G. Zürn, and S. Jochim, *Matter-wave Fourier optics with a strongly interacting two-dimensional Fermi gas*, Phys. Rev. A **90**, 043611 (2014) (see p. 55).

[251] L. Asteria, H. P. Zahn, M. N. Kosch, K. Sengstock, and C. Weitenberg, *Quantum gas magnifier for sub-lattice-resolved imaging of 3D quantum systems*, Nature **599**, 571 (2021) (see p. 55).

[252] D. J. Papoular, G. V. Shlyapnikov, and J. Dalibard, *Microwave-induced Fano-Feshbach resonances*, Phys. Rev. A **81**, 041603 (2010) (see p. 63).

[253] E. Haller, M. J. Mark, R. Hart, J. G. Danzl, L. Reichsöllner, V. Melezhik, P. Schmelcher, and H.-C. Nägerl, *Confinement-Induced Resonances in Low-Dimensional Quantum Systems*, Phys. Rev. Lett. **104**, 153203 (2010) (see p. 63).

[254] P. Donohue and T. Giamarchi, *Mott-superfluid transition in bosonic ladders*, Phys. Rev. B **63**, 180508 (2001) (see pp. 69, 114).

[255] F. Crépin, N. Laflorencie, G. Roux, and P. Simon, *Phase diagram of hard-core bosons on clean and disordered two-leg ladders: Mott insulator–Luttinger liquid–Bose glass*, Phys. Rev. B **84**, 054517 (2011) (see pp. 69–71, 114, 119).

[256] Z. Weihong, J. Oitmaa, C. J. Hamer, and R. J. Bursill, *Numerical studies of the two-leg Hubbard ladder*, J. Phys.: Condens. Matter **13**, 433 (2001) (see p. 69).

[257] A. Padhan, R. Parida, S. Lahiri, M. K. Giri, and T. Mishra, *Quantum phases of constrained bosons on a two-leg Bose-Hubbard ladder*, Phys. Rev. A **108**, 013316 (2023) (see pp. 69, 114).

[258] T. Kinoshita, T. Wenger, and D. S. Weiss, *A quantum Newton's cradle*, Nature **440**, 900 (2006) (see pp. 70, 74, 114).

[259] R. Modak, S. Mukerjee, and S. Ramaswamy, *Universal power law in crossover from integrability to quantum chaos*, Phys. Rev. B **90**, 075152 (2014) (see p. 71).

[260] B. Bertini, F. H. L. Essler, S. Groha, and N. J. Robinson, *Prethermalization and Thermalization in Models with Weak Integrability Breaking*, Phys. Rev. Lett. **115**, 180601 (2015) (see p. 71).

[261] Y. Tang, W. Kao, K.-Y. Li, S. Seo, K. Mallayya, M. Rigol, S. Gopalakrishnan, and B. L. Lev, *Thermalization near Integrability in a Dipolar Quantum Newton's Cradle*, Phys. Rev. X **8**, 021030 (2018) (see pp. 71, 114).

[262] A. J. Friedman, S. Gopalakrishnan, and R. Vasseur, *Diffusive hydrodynamics from integrability breaking*, Phys. Rev. B **101**, 180302 (2020) (see p. 71).

[263] V. B. Bulchandani, D. A. Huse, and S. Gopalakrishnan, *Onset of many-body quantum chaos due to breaking integrability*, Phys. Rev. B **105**, 214308 (2022) (see pp. 71, 72).

[264] A. M. Rey, *Private Communications* (see p. 71).

[265] J. R. Garrison, *Thermalization and its breakdown in isolated quantum systems*, (see p. 72).

[266] S. A. Parameswaran, *Quantum Glasses at Infinite Temperature*, (see p. 72).

[267] A. Smith, *Disorder-Free Localization*, Springer Theses (Springer International Publishing, Cham, 2019) (see pp. 74, 120, 121).

[268] L. Vidmar and M. Rigol, *Generalized Gibbs ensemble in integrable lattice models*, J. Stat. Mech. **2016**, 064007 (2016) (see p. 74).

[269] M. Lucas, L. Piroli, J. De Nardis, and A. De Luca, *Generalized deep thermalization for free fermions*, Phys. Rev. A **107**, 032215 (2023) (see p. 74).

[270] A. Bastianello, A. D. Luca, and R. Vasseur, *Hydrodynamics of weak integrability breaking*, J. Stat. Mech. **2021**, 114003 (2021) (see pp. 75, 81).

[271] F. H. L. Essler, *A short introduction to Generalized Hydrodynamics*, Physica A: Statistical Mechanics and its Applications, Lecture Notes of the 15th International Summer School of Fundamental Problems in Statistical Physics **631**, 127572 (2023) (see pp. 75, 114).

[272] I. M. Zaid, M. A. Lomholt, and R. Metzler, *How Subdiffusion Changes the Kinetics of Binding to a Surface*, Biophys J **97**, 710 (2009) (see p. 78).

[273] H. Singh, B. A. Ware, R. Vasseur, and A. J. Friedman, *Subdiffusion and Many-Body Quantum Chaos with Kinetic Constraints*, Phys. Rev. Lett. **127**, 230602 (2021) (see p. 78).

[274] A. Smith, D. L. Kovrizhin, R. Moessner, and J. Knolle, *Dynamics of a lattice gauge theory with fermionic matter—minimal quantum simulator with time-dependent impurities in ultracold gases*, Quantum Sci. Technol. **3**, 044003 (2018) (see pp. 80, 120).

[275] I. Poboiko, P. Pöpperl, I. V. Gornyi, and A. D. Mirlin, *Theory of Free Fermions under Random Projective Measurements*, Phys. Rev. X **13**, 041046 (2023) (see pp. 80, 120).

[276] D. K. Wójcik and J. R. Dorfman, *Diffusive-Ballistic Crossover in 1D Quantum Walks*, Phys. Rev. Lett. **90**, 230602 (2003) (see p. 81).

[277] S. Miyazaki, *Crossover between Ballistic and Normal Diffusion*, Progress of Theoretical Physics Supplement **161**, 270 (2006) (see p. 81).

[278] V. Eisler, *Crossover between ballistic and diffusive transport: the quantum exclusion process*, J. Stat. Mech. **2011**, P06007 (2011) (see p. 81).

[279] C. Von Keyserlingk, F. Pollmann, and T. Rakovszky, *Operator backflow and the classical simulation of quantum transport*, Phys. Rev. B **105**, 245101 (2022) (see p. 83).

[280] R. Steinigeweg, F. Heidrich-Meisner, J. Gemmer, K. Michielsen, and H. De Raedt, *Scaling of diffusion constants in the spin- 1 2 XX ladder*, Phys. Rev. B **90**, 094417 (2014) (see p. 85).

[281] T. Rakovszky, F. Pollmann, and C. W. von Keyserlingk, *Sub-ballistic Growth of R\'enyi Entropies due to Diffusion*, Phys. Rev. Lett. **122**, 250602 (2019) (see p. 85).

[282] C. Han, M. Zhou, X. Zhang, Q. Gao, Y. Xu, S. Li, S. Zhang, and X. Xu, *Carrier thermometry of cold ytterbium atoms in an optical lattice clock*, Sci Rep **8**, 7927 (2018) (see p. 87).

[283] D. S. Barker, J. A. Fedchak, J. Kłos, J. Scherschligt, A. A. Sheikh, E. Tiesinga, and S. P. Eckel, *Accurate measurement of the loss rate of cold atoms due to background gas collisions for the quantum-based cold atom vacuum standard*, AVS Quantum Science **5**, 035001 (2023) (see p. 87).

[284] W. Hofstetter, *Ultracold atoms in optical lattices: tunable quantum many-body systems*, Philosophical Magazine **86**, 1891 (2006) (see p. 87).

[285] S. Aubry and G. André, *Analyticity breaking and Anderson localization in incommensurate lattices*, Ann. Israel Phys. Soc **3**, 18 (1980) (see p. 88).

[286] P. W. Anderson, *Absence of Diffusion in Certain Random Lattices*, Phys. Rev. **109**, 1492 (1958) (see p. 89).

[287] A. Aspect and M. Inguscio, *Anderson localization of ultracold atoms*, Physics Today **62**, 30 (2009) (see p. 89).

[288] M. Pasek, G. Orso, and D. Delande, *Anderson Localization of Ultracold Atoms: Where is the Mobility Edge?* Phys. Rev. Lett. **118**, 170403 (2017) (see p. 89).

[289] A. H. Karamlou et al., *Quantum transport and localization in 1d and 2d tight-binding lattices*, npj Quantum Inf **8**, 1 (2022) (see p. 90).

[290] J. Hauschild and F. Pollmann, *Efficient numerical simulations with Tensor Networks: Tensor Network Python (TeNPy)*, SciPost Physics Lecture Notes, 005 (2018) (see p. 93).

[291] T. N. Ikeda, Y. Watanabe, and M. Ueda, *Finite-size scaling analysis of the eigenstate thermalization hypothesis in a one-dimensional interacting Bose gas*, Phys Rev E Stat Nonlin Soft Matter Phys **87**, 012125 (2013) (see p. 94).

[292] W. Beugeling, R. Moessner, and M. Haque, *Finite-size scaling of eigenstate thermalization*, Phys. Rev. E **89**, 042112 (2014) (see pp. 94, 114).

[293] K. Seetharam, P. Titum, M. Kolodrubetz, and G. Refael, *Absence of thermalization in finite isolated interacting Floquet systems*, Phys. Rev. B **97**, 014311 (2018) (see p. 94).

[294] W. De Roeck and J. Z. Imbrie, *Many-body localization: stability and instability*, Philosophical Transactions of the Royal Society A: Mathematical, Physical and Engineering Sciences **375**, 20160422 (2017) (see p. 94).

[295] F. Alet and N. Laflorencie, *Many-body localization: An introduction and selected topics*, Comptes Rendus Physique, Quantum simulation / Simulation quantique **19**, 498 (2018) (see p. 94).

[296] D. C. W. Foo, N. Swain, P. Sengupta, G. Lemarié, and S. Adam, *Stabilization mechanism for many-body localization in two dimensions*, Phys. Rev. Res. **5**, L032011 (2023) (see p. 94).

[297] W. P. Su, J. R. Schrieffer, and A. J. Heeger, *Solitons in Polyacetylene*, Phys. Rev. Lett. **42**, 1698 (1979) (see pp. 99, 102).

[298] S. Fiedziuszko, I. Hunter, T. Itoh, Y. Kobayashi, T. Nishikawa, S. Stitzer, and K. Wakino, *Dielectric materials, devices, and circuits*, IEEE Transactions on Microwave Theory and Techniques **50**, 706 (2002) (see p. 99).

[299] R. Resta, *Quantum-Mechanical Position Operator in Extended Systems*, Phys. Rev. Lett. **80**, 1800 (1998) (see pp. 100, 104).

[300] N. A. Spaldin, *A beginner's guide to the modern theory of polarization*, Journal of Solid State Chemistry **195**, 2 (2012) (see p. 100).

[301] T. Senthil, *Quantum matters: Physics beyond Landau's paradigms*, arxiv:cond-mat/0411275 (2004) (see p. 100).

[302] H. L. Stormer, D. C. Tsui, and A. C. Gossard, *The fractional quantum Hall effect*, Rev. Mod. Phys. **71**, S298 (1999) (see p. 100).

[303] X. Chen, Z.-C. Gu, and X.-G. Wen, *Local unitary transformation, long-range quantum entanglement, wave function renormalization, and topological order*, Phys. Rev. B **82**, 155138 (2010) (see p. 101).

[304] T. Kato, *On the Adiabatic Theorem of Quantum Mechanics*, Journal of the Physical Society of Japan **5**, 435 (1950) (see p. 101).

[305] B. Douçot, *Introduction to the theory of the integer quantum Hall effect*, Comptes Rendus. Physique **12**, 323 (2011) (see p. 101).

[306] F. Grusdt, *Topological phases and polaron physics in ultracold quantum gases*, PhD thesis, (2016) (see pp. 101, 102).

[307] S. Bid and A. Chakrabarti, *Topological properties of a class of Su-Schrieffer-Heeger variants*, Physics Letters A **423**, 127816 (2022) (see p. 102).

[308] D. J. Thouless, M. Kohmoto, M. P. Nightingale, and M. den Nijs, *Quantized Hall Conductance in a Two-Dimensional Periodic Potential*, Phys. Rev. Lett. **49**, 405 (1982) (see p. 104).

[309] M. Atala, M. Aidelsburger, J. T. Barreiro, D. Abanin, T. Kitagawa, E. Demler, and I. Bloch, *Direct measurement of the Zak phase in topological Bloch bands*, Nat. Phys. **9**, 795 (2013) (see p. 104).

[310] S.-s. Chern, *Characteristic Classes of Hermitian Manifolds*, Annals of Mathematics **47**, 85 (1946) (see p. 105).

[311] J. F. R. Bibo, *Higher-order and Quotient group symmetry-protected topological phenomena*, PhD Thesis, Technische Universität München (2023) (see pp. 105, 108).

[312] H. Araki, T. Mizoguchi, and Y. Hatsugai, *Berry phase for higher-order symmetry-protected topological phases*, Physical Review Research **2**, 012009 (2020) (see p. 108).

[313] M. Gring, M. Kuhnert, T. Langen, T. Kitagawa, B. Rauer, M. Schreitl, I. Mazets, D. A. Smith, E. Demler, and J. Schmiedmayer, *Relaxation and Prethermalization in an Isolated Quantum System*, Science **337**, 1318 (2012) (see p. 114).

[314] M. Ueda, *Quantum equilibration, thermalization and prethermalization in ultracold atoms*, Nat Rev Phys **2**, 669 (2020) (see p. 114).

[315] J.-y. Choi, S. Hild, J. Zeiher, P. Schauß, A. Rubio-Abadal, T. Yefsah, V. Khemani, D. A. Huse, I. Bloch, and C. Gross, *Exploring the many-body localization transition in two dimensions*, Science **352**, 1547 (2016) (see p. 114).

[316] C. J. Turner, A. A. Michailidis, D. A. Abanin, M. Serbyn, and Z. Papić, *Weak ergodicity breaking from quantum many-body scars*, Nature Phys **14**, 745 (2018) (see p. 114).

[317] S. Moudgalya, B. A. Bernevig, and N. Regnault, *Quantum many-body scars and Hilbert space fragmentation: a review of exact results*, Rep. Prog. Phys. **85**, 086501 (2022) (see p. 114).

[318] K. Fujimoto and T. Sasamoto, *Exact Solution of Bipartite Fluctuations in One-Dimensional Fermions*, arXiv:2403.18523 (2024) (see p. 114).

[319] B. Doyon, G. Perfetto, T. Sasamoto, and T. Yoshimura, *Ballistic macroscopic fluctuation theory*, SciPost Physics (see p. 114).

[320] S. Gopalakrishnan, A. Morningstar, R. Vasseur, and V. Khemani, *Distinct universality classes of diffusive transport from full counting statistics*, arXiv:2203.09526 (2023) (see p. 114).

[321] A. A. Michailidis, D. A. Abanin, and L. V. Delacrétaz, *Corrections to diffusion in interacting quantum systems*, arXiv:2310.10564 (2023) (see p. 114).

[322] H.-X. Wang, L. Liang, B. Jiang, J. Hu, X. Lu, and J.-H. Jiang, *Higher-order topological phases in tunable C_3 symmetric photonic crystals*, Photon. Res., PRJ **9**, 1854 (2021) (see p. 114).

[323] A. Jahin, Y.-M. Lu, and Y. Wang, *Many-body higher-order topological invariant for C_n-symmetric insulators*, arXiv:2401.00050 (2024) (see p. 114).

[324] R. Chen, C.-Z. Chen, J.-H. Gao, B. Zhou, and D.-H. Xu, *Higher-Order Topological Insulators in Quasicrystals*, Phys. Rev. Lett. **124**, 036803 (2020) (see p. 114).

[325] Y. Hu, S. Liu, B. Pan, P. Zhou, and L. Sun, *Second-order topological states in a sixfold symmetric quasicrystal*, Phys. Rev. B **109**, L121403 (2024) (see p. 114).

[326] L. Onsager and S. Machlup, *Fluctuations and Irreversible Processes*, Phys. Rev. **91**, 1505 (1953) (see p. 117).

[327] S. Machlup and L. Onsager, *Fluctuations and Irreversible Process. II. Systems with Kinetic Energy*, Phys. Rev. **91**, 1512 (1953) (see p. 117).

[328] H. Touchette, *The large deviation approach to statistical mechanics*, Physics Reports **478**, 1 (2009) (see p. 117).

[329] A. P. Polychronakos, *Solitons in fluctuating hydrodynamics of diffusive processes*, Phys. Rev. E **101**, 022209 (2020) (see p. 117).

[330] G. Metalidis, *Strongly correlated bosons in one-dimensional optical lattices*, MA thesis, Eindhoven University of Technology (see p. 120).

List of Figures

List of Tables

List of Abbreviations

AOD acusto-optic deflector

ASEP asymmetric simple exclusion process

BHM Bose-Hubbard model

CDW charge density wave

CPBC corner-periodic boundary conditions

DMD digital micromirror device

ED exact diagonalization

ETH eigenstate thermalization hypothesis

FCI fractional Chern insulator

FCS full counting statistics

FDT fluctuation dissipation theorem

FHD fluctuating hydrodynamics

GGE generalized Gibbs ensemble

GHD generalized hydrodynamics

HOSPT higher-order symmetry-protected topological

IPR inverse participation ratio

MBL many-body localization

MFT macroscopic fluctuation theory

MPS matrix product state

MTP modern theory of polarization

OBC open boundary conditions

PSF point spread function

RMT random matrix theory

ROI region of interest

SDE stochastic differential equation

SLD superluminescent laser diodes

SNR signal-to-noise ratio

SPT symmetry-protected topological

SSEP symmetric simple exclusion process

SSH Su–Schrieffer–Heeger

TDVP time-dependent variational principle

Acknowledgements

First of all, I would like to thank *Monika Aidelsburger* and *Immanuel Bloch* for the opportunity to pursue my PhD in this group. It has been an exciting time full of versatile challenges, fascinating physics and rewarding achievements. This is made possible by Monika's and Immanuel's passion for quantum science and their ability to spark excitement and curiosity for the big and small topics in the field. Im grateful for their ideas and helpful suggestions raised in countless meetings and hallway conversations; for letting us explore our own ideas and simply try things out; and for supporting me and my plans throughout the last five years since I joined this group as a Master student back in 2018. I highly appreciate Monika's help in securing my scholarships and for connecting me with *Monika Schleier-Smith* for the research internship I did right before my PhD.

I would like to thank all the great physicists outside our group who have collaborated with me on the great projects featured in this thesis: *Sarang Gopalakrishnan*, *Ewan McCulloch* and *Romain Vasseur* who never refused to answer any question of mine about quantum thermalization and whose impressive intuition of quantum many-body dynamics has significantly shaped my own. *Fabian Grusdt*, *Friederike Horn* and *Julian Bibo* with whom I have worked on the higher-order Thouless pump project, a prolific collaboration between three different Munich groups. *Fabian Grusdt* and *Ulrich Schollwöck* deserve special thanks for letting me join their group as part of my Marianne-Plehn-Program position.

I would like to thank all people who are or have been part of the Cesium team: *Alexander Impertro*, with whom I have lived through the full spectrum of lab emotions, ranging from utmost frustration to limitless excitement. Irrespective of how it was going in the lab, the chemistry was always right and the jokes never stopped. It was a great pleasure to travel to Switzerland last summer and give the Sommerakademie course together (after getting all the laser equipment legally across the border). *Simon Karch*, who enjoys classical music at least as much as I do, who has always something interesting and meaningful to say and who might be the chosen one capable of finally solving the machine's mysterious chronic issues. *SeungJung Huh*, *Cesar R. Cabrera* and *Christian Schweizer*, our postdocs who are or have been devoting their life to unleashing the Cesium lab's full potential and who never stop supporting the PhDs. *Scott Hubele*, *Ignacio Pérez Ramos* and *Sophie Häfele*, our motivated Master students who have done a great job at developing novel tools for the experiment and who contributed to the lab atmosphere with their interesting personalities. And *Till Klostermann* and *Hendrik von Raven*, the founding fathers of the Cesium lab, who laid the foundation for the great experiments we are able to do now, and played a crucial role in teaching me how the lab works.

I would like to thank all the other (former) group members outside the Cesium lab for sharing ideas, coming up with quick fixes to seemingly unsolvable problems, for spontaneous lunch conversations about physics-unrelated topics and for career advice. These people include *Giulio Paqualetti*, *Clara Bachorz*, *Etienne Staub*, *Tim Höhn*, *Ronen Kroeze*, *René Villela*, *David Gröters*, *Christoph Braun*, *Alexander Hesse*, *Johannes Arceri*, *Bodo Kaiser*, *Daniel Adler*, *Yilong Yang*, *David Wei*, *Pascal Weckesser*, *Karen Wintersperger*, *Simon Fölling*, *Thomas Kohlert*, *Sebastian Scherg* and *Roman Bause*. I am proud to have introduced Giulio, Alex H. and Simon K. to the "Junge Opernfreunde München" and I can look forward

to meeting them there regularly. I have also enjoyed the occasional hiking tours and BBQ events at the Isar that were organized during summertime — a tradition that should be upheld. I would also like to thank *Bodo Hecker* and *Reinhard Grottenthaler* for their unwavering support in electronic matters. And *Ildiko Kecskesi* for helping me so much with all the administrative stuff. And the *LMU machine shop specialists* for always reliably manufacturing our parts.

My PhD has been generously supported by the *Marianne-Plehn-Program* and, particularly, the *Studienstiftung des Deutschen Volkes*. Events related to this organization have repeatedly altered the course of my life, most probably for the better. Special thanks goes to the members of my defense committee, that is Monika, Sarang, *Alexander Högele* and *Thomas Birner*.

An important part of my life here in Munich is the StOrch orchestra, and I would like to thank all the wonderful people contributing to the sustainably meaningful and socially fulfilling atmosphere which makes this ensemble so special.

Last but not least I would like to thank my family and friends for being a part of my life, for providing guidance and advice when there are difficult decisions to make, and for their unconditional support and love.